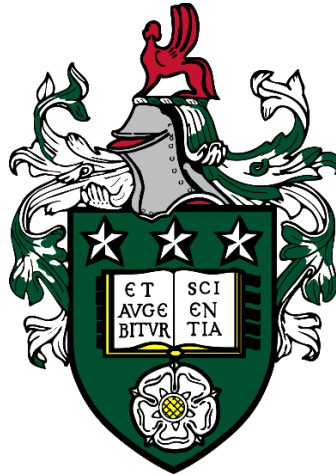# HYDROTHERMAL REE TRANSPORT IN CARBONATITES

Delia Auriane Cangelosi

Submitted in accordance with the requirements for the degree of

Doctor of Philosophy

The University of Leeds

School of Earth and Environment

December 2019

The candidate confirms that the work submitted is his/her own, except where work which has formed part of jointly-authored publications has been included. The contribution of the candidate and the other authors to this work has been explicitly indicated below. The candidate confirms that appropriate credit has been given within the thesis where reference has been made to the work of others. Contributors to jointly-authored publications are outlined below.

Chapter Three

D.A. Cangelosi: principal investigator, data collection and interpretation, main author.

S. Broom-Fendley: fieldwork supervision, discussion, manuscript review.

B.W.D. Yardley: discussion, manuscript review.

D.J. Morgan: discussion, manuscript review.

D.A. Banks: laboratory supervision, discussion, manuscript review.

Activation Laboratories Ltd**:** performed bulk rock analyses.

Chapter Four

D.A. Cangelosi: principal investigator, data collection and interpretation, main author.

B.W.D. Yardley: discussion, manuscript review.

M.P. Smith: field supervision, discussion, manuscript review.

D.J. Morgan: discussion, manuscript review.

D.A. Banks: discussion, manuscript review.

Chapter Five

D.A. Cangelosi: principal investigator, data collection and interpretation, main author.

S. Broom-Fendley: Data collecting assistance, discussion, manuscript review.

B.W.D. Yardley: discussion, manuscript review.

R.A. Jamieson: Ran the Elementar Isoprime™ isotope instrument, discussion, manuscript review.

The candidate confirms that the work submitted is her own and that appropriate credit has been given where reference has been made to the work of others.

The copy has been supplied on the understanding that it is copyright material and that no quotation from the thesis may be published without proper acknowledgement.

The right of Delia Auriane Cangelosi to be identified as Author of this thesis work has been asserted by them in accordance with the Copyright, Designs and Patents Act 1988.

Acknowledgements

Firstly, I would like to thank myself for doing such a great job.

I would also like to thank my supervisor, Prof Bruce Yardley for your <u>patience</u>, guidance and invaluable scientific discussions along the way.

I am particularly grateful to Dr Sam Broom-Fendley for your support and help.

Mostly importantly I would like to thank Bobbie for being such a good girl.

Lastly, I would like to thank Iain and my friends for being there for me and my parents for making it all possible.

Abstract

Rare earth elements (REE) have been classified as 'critical metals' by a number of international organisations due to China controlling the current market, the ever growing demand, low recycling rates, and poor substitutability of these elements. Currently, carbonatite deposits are the main source of Light REE (LREE) due to their high REE grade and easy to process minerals. Interestingly, few carbonatite deposits worldwide also show economic Heavy REE (HREE) enrichment. Often, REE economic concentrations are hosted by minerals precipitated during hydrothermal alteration, rather than the early magmatic REE minerals. However the role of hydrothermal activity in enhancing ore grades of REE carbonatite deposits is poorly understood.

This study considers two contrasting deposits, both hydrothermally reworked; the Okorusu carbonatite complex, Namibia, considered to be a 'common' carbonatite deposit, based on its LREE enriched pattern, and the Dashigou mine part of the Huanglongpu carbonatite deposit, China, which is one of the few carbonatite deposits showing a HREE enrichment, leading to an unusual flat REE pattern. The work achieved during this PhD has allowed the recognition of fundamental characteristics about hydrothermal REE reworking and beneficiation processes in carbonatite. The REE are remobilised by hydrothermal fluids from the REE-bearing magmatic minerals, which can be transported over sufficiently large distance to create an enrichment of the more altered carbonatites. This transport has been found effective at a temperature below 100 °C. The final REE pattern and content of a carbonatite strongly depends on the magmatic REE source and the nature of the hydrothermal fluid. The unusual HREE enrichment of the Huanglongpu carbonatites is attributed to a HREE enrichment at the final magmatic stage of the carbonatite and subsequent alteration by sulfate-rich hydrothermal fluids. Finally, relatively small volumes of hydrothermal fluids, such that the magmatic oxygen isotope signature is not greatly modified, are sufficient to rework magmatic REE from gangue minerals to form secondary REE mineralisation.

Contents

List of figures

Abbreviations

BSE	Back Scattered Electron
CL	Cathodoluminescence
EPMA	Electron Probe Micro Analyser
HREE	Heavy Rare Earth Elements
LA-ICP-MS	Laser Ablation Inductively Coupled Plasma Mass Spectrometry
LOD	Limit of Detection
LOI	Loss of Ignition
LREE	Light Rare Earth Elements
n.a.	not analysed
n.d.	not detected
n.i.	not identified
NERC	Natural Environment Research Council
REE	Rare Earth Elements
REO	Rare Earth Oxide
SEM	Scanning Electron Microscopy
SoS rare	Security of Supply of Rare Earth Elements
VPDB	Vienna Pee Dee Belemnite
VSMOW	Vienna Standard Mean Ocean Water

CHAPTER 1.

Introduction

1.1. PhD setting

This PhD is part of the SoS RARE project consortium project funded by NERC (Natural Environment Research Council) under the Security of Supply of Mineral Resources (SoS Minerals) research program. SoS Minerals was initiated to support the security of supply of the strategic elements that reinforce current and future green energy technologies. These elements, identified as of interest by NERC, are referred to as e-tech elements and comprise of rare earth elements (REE), cobalt, tellurium, selenium, indium and gallium. This programme aims to enhance global security of supply of the e-tech elements in two ways, (1) improved understanding of e-tech element cycling and concentration in natural systems, (2) using this information to develop improved recovery processes from primary sources in order to mitigate the environmental effects of extraction and recovery of these elements. SoS RARE is divided into four work packages, each with specific aims and objectives. This PhD is part of work package one, which focuses on the mobility of REE in solution.

The SoS RARE research team included 17 investigators from 6 UK universities and research institutes, with 10 industry partners and 8 core international research collaborators. The objective was to improve understanding of REE's concentration in natural systems (conventional deposits and ion adsorption deposits) and to develop improved recovery processes from primary sources in order to moderate the environmental effects of extraction and recovery of these elements. This PhD project addresses the understanding of REE mobility in conventional deposits, and in particular in carbonatites.

1.2. Motivation and aim of this research

Research on REE in geological systems has increased over the past decade due to the growing demand for REE in high technology applications, in particular for low carbon technologies but also for a range of everyday consumer products.

Currently the REE market depends heavily on a single source, China. They produce an estimated 71% of the global supply, this figure does not include the undocumented production (U.S. Geological Survey, 2019). Illegal mining is estimated to add about 20% to the Chinese legal production, and this also raises the problem of pollution associated to such an activity (Liu *et al.,* 2017). This reliance upon a single supplier nation, combined with low recycling rates and poor substitutability, has led to the REE to be categorised as 'critical metals' (European Commission, 2017; Wall, 2014).

The recent up turn of the REE market has led to a global interest in understanding the processes responsible for their formation and finding new REE resources. It has especially attracted interest in carbonatite-related REE systems, as they currently are the primary REE source. They display high grade and commonly show LREE enrichment compared to other potential REE deposit types (Fig. 2-1; Kynicky *et al.,* 2012; Wall 2014).

Therefore, the aim of this project is to **understand the role of hydrothermal alteration on the final REE mineralisation and identify what can affect the overall REE pattern of carbonatites.**

To address this, two hydrothermally reworked carbonatite deposits have been investigated: The Okorusu fluorspar mine, Namibia, and the Huanglongpu deposit, China. These deposits were selected due to their contrasting REE profiles and the material was sampled during fieldwork in October 2015 and in June 2016 respectively. The Okorusu carbonatite shows a typical LREE enriched profile which provides a baseline comparison with the Huanglongpu carbonatite which shows an unusually high HREE content leading to a flat REE profile.

Understanding REE mobility and beneficiation in typical carbonatites as well as in unusual carbonatites showing economic HREE concentration will contribute to better exploration targeting for deposits enriched in these critical metals, which may contribute to improvements in the current world resource availability and security.

1.3. Thesis structure

This thesis includes a literature review (Chapter 2) providing an up to date summary of the literature related to REE transport at hydrothermal conditions. The subsequent chapters are split into three distinct publications covering the overall data obtained during this PhD. Two of these are published (Chapter 3 and 4) in the Mineralogical Magazine within the special issue on Critical Metals, 2019 and the final chapter (Chapter 5) is ready for submission.

The structure of the data chapters is as follow:

Chapter 3: Cangelosi, D.A., Broom-Fendley, S., Banks, D.A., Morgan, D.J. and Yardley, B.W.D. (2020) LREE redistribution during hydrothermal alteration at the Okorusu carbonatite complex, Namibia. *Mineralogical Magazine*, **84**(1), 49-64. doi: 10.1180/mgm.2019.54.

Chapter 4: Cangelosi, D.A., Smith, M.P; Banks, D.A. and Yardley, B.W.D. (2019b) The role of sulfate-rich fluids in Heavy Rare Earth enrichment at the Dashigou carbonatite deposit, Huanglongpu, China. *Mineralogical Magazine*, **84**(1), 65-80. doi 10.1180/mgm.2019.78.

Chapter 5: Cangelosi, D.A., Broom-Fendley, S., Jamieson, R.A. and Yardley, B.W.D. (ready for submission) Pulsed hydrothermal inputs during reworking of a REE carbonatite deposit, the Okorusu complex, Namibia.

Finally, Chapter 6 discusses the key outcomes of this research and define the further work needed.

CHAPTER 2.

Literature review

2.1. Rare Earth Elements

2.1.1. Overview

The REE are defined by the International Union of Pure and Applied Chemistry (IUPAC) as 17 chemical elements in the periodic table: yttrium (Y), scandium (Sc) and the 15 lanthanides. Due to its small ionic radius, scandium is often not considered as a REE by Earth Scientists and promethium (Pr), which belongs to the lanthanide group, does not occur in nature. Pr have no stable isotope. Thus, the REE group comprises 15 lanthanides and yttrium which form a coherent group in their geochemical properties and applications including magnetics, phosphors, catalysts and ceramics.

The REE are divided into two groups, the Light Rare Earth Elements (LREE), from lanthanum to samarium and the Heavy Rare Earths Elements (HREE) from europium to lutetium (Henderson, 1984). Yttrium is considered to belong to the HREE group as the result of its ionic radius nearly equal to that of holmium (Shannon, 1976). Another term found in the literature is Middle Rare Earth Elements (MREE) referring to the REE with intermediate atomic numbers, between europium and dysprosium (Samson and Wood, 2004).

The name Rare Earth Elements is somewhat misleading, as some of these elements are not rare. In fact, cerium (Ce) and yttrium are the 25th and 30th most abundant elements by mass (Rudnick and Gao, 2003). The name was chosen in the nineteenth century to reflect the difficulties encountered by chemists in separating these elements from one another due to their chemical similarities (rare), and their occurrence as oxides rather than metals (earth).

2.1.2. Physical and chemical properties

As a group, the REE behave quite similarly, consequently, they tend to occur together in nature and are difficult to separate from one another (Paulick and Machacek, 2017). However, under some conditions or processes they exhibit differences. The characteristics of the lanthanide series arise from the filling of the f electrons shell in the atoms, from $5d^16s^2$ for lanthanum (La) to $4f^{14}5d^16s^2$ for lutetium (Lu) (Henderson, 1984; Table 2-1). It leads to the intensification of the magnetic and spectroscopic properties.

In geological environments, REE usually show a 3^+ state of oxidation, they form the oxide REE_2O_3, and are strongly electropositive. However, Ce can also display a 4^+ oxidation state and europium (Eu) a 2^+ oxidation state, formed respectively in oxidizing and reducing environment. When Eu displays a 2^+ oxidation state it behaves similarly to the cation Ca^{2+} due to their similar radius and charge. In oxidizing condition, Ce^{4+} may occur and is less soluble than Ce^{3+} (Wood, 1990). Different oxidation states for samarium (Sm), thulium (Th) and ytterbium (Yb) are known, but are rarely seen in nature (Henderson, 1984).

The main distinction between the REE is the well-known lanthanide contraction, which is a steady decrease in ionic radius from 1.06 nm for La to 0.85 nm for Lu with an increase in atomic number (Krishnamurthy and Gupta, 2015; Fig. 2-1). This phenomenon is due to the 4f electrons poor shielding of nuclear charge leading to the 6s electrons drawning towards the nucleus resulting in a smaller atomic radius for an element. As a result, a rising nuclear charge acts on the 4f electrons with the increase of the atomic number (Henderson, 1984), causing contraction of the lanthanide series. Due to this contraction, HREE exhibit a higher ionic potential (charge/radius ratio) and are expected to form stronger bonds than LREE (Lottermoser, 1992).

Another feature of the REE series is the characteristic jigsaw pattern which follows the distribution of REE in terrestrial and extra-terrestrial material; this is known as the Oddo Harkins effect, which results in even atomic number elements being more abundant than their adjacent odd atomic number elements (Allaby, 2008). This effect is established in the different binding energies, leading to relative stabilities of nuclei with paired and unpaired nucleons. This is coupled with the fact that in the Earth's crust, the LREE are more abundant than the HREE (Table 2-1).

The electronic properties of the REE engender particular absorption and emission spectra and most of the REE are strongly paramagnetic, which consequently make them useful in many applications.
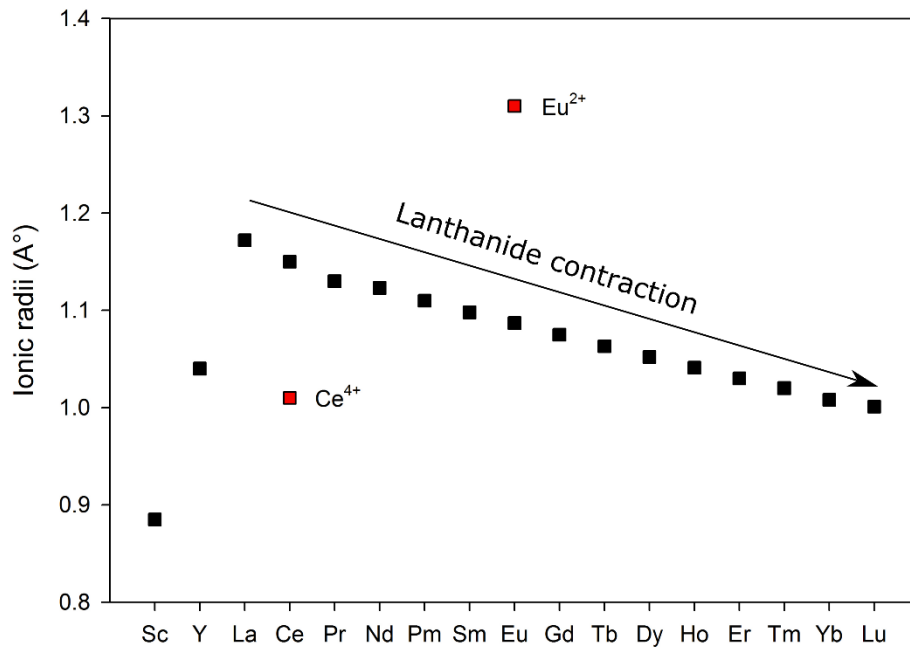
Figure 2-1: The lanthanide contraction with the ionic radii (in angstroms) of trivalent cations and Ce^{4+} and Eu^{2+} versus their atomic number. After Shannon, 1976.

Element	Symbol	Crustal abundance (ppm) [2]	Ground state configuration[3]
Scandium	Sc	22	$3d^14s^2$
Yttrium	Y	33	$4d^15s^2$
Lanthanum	La	39	$5d^16s^2$
Cerium	Ce	66.5	$4f^15d^16s^2$
Praseodymium	Pr	9.2	$4f^36s^2$
Neodymium	Nd	41.5	$4f^46s^2$
Promethium[1]	Pm		$4f^56s^2$
Samarium	Sm	7.05	$4f^66s^2$
Europium	Eu	2.0	$4f^76s^2$
Gadolinium	Gd	6.2	$4f^75d^16s^2$
Terbium	Tb	1.2	$4f^96s^2$
Dysprosium	Dy	5.2	$4f^{10}6s^2$
Holmium	Ho	1.3	$4f^{11}6s^2$
Erbium	Er	3.5	$4f^{12}6s^2$
Thulium	Tm	0.52	$4f^{13}6s^2$
Ytterbium	Yb	3.2	$4f^{14}6s^2$
Lutetium	Lu	0.8	$4f^{14}5d^16s^2$

Table 2-1: Selected properties of the REE. [1]Promethium does not occur in nature; [2]Lide (1997); [3]Henderson (1984).

2.1.3. REE mineralogy

REE are chemically similar to each other and tend to occur together within minerals in different quantities. They occur in a wide range of minerals including fluorides, halides, phosphates, silicates, carbonates and oxides (Table 2-2). By 2012, more than 200 rare earth minerals had been approved by the International Mineralogical Association, plus all the minerals that contain REE among their main constituents.

Rare earth minerals are named with a suffix representing the predominant REE in the REE site (Bayliss and Levinson, 1988; Table 2-2), e.g. monazite-(Ce). Ce is the predominant REE in the LREE-bearing minerals due to its high crustal abundance, but this is not invariably the case, monazite-(La) is known for example. On the same principle, Y should be the most abundant HREE in HREE-bearing minerals.

Rare earth elements were first identified by the chemist Johan Gadolin in 1794, from a mineral found in a feldspar mine at Ytterby, Sweden. Prior to that, in 1740 a dense reddish mineral called Bastnäs tungsten was identified in the Bastnäs base metal mining district in Sweden. But it was only after 1794, that a foundry proprietor, Wilhem Hisinger, who had been intrigued by the Bastnäs tungsten mineral from his youth, wondered if those two minerals contained the same earth. By 1804, he and another chemist Jons Berzelius, proved the same earths were present in the two minerals and found an additional earth in the Bastnäs mineral, which was later renamed cerite (Williams-Jones *et al.,* 2012).

Despite the variety of REE minerals occurring, bastnäsite, monazite and xenotime (Table 2-2) are commonly occurring REE minerals with simple mineralogy to process; hence, not surprisingly in that order are the most important ore minerals based on REE extraction. These minerals, especially bastnäsite and monazite, are found in abundance within carbonatite associated deposits with low radioactivity (low uranium and thorium content), which is an advantage for transport and processing aspect (e.g. Mariano and Mariano, 2012; Chakhmouradian, 1998). Bastnäsite is attractive as it consists of around 70 wt.% REO and shows very low level of thorium and tends to be abundant in most settings. Monazite contains approximately 70 wt.% REO, and like bastnäsite is mainly LREE dominated, but also comprises of around 5% Y_2O_3 and when derived from a carbonatite, has low thorium content (Weng *et al.,* 2013). In contrast, xenotime consists of ~ 67 wt.% REO, mostly M to HREE. Some other minerals have been extracted but in much lower quantities such as: allanite, apatite,

eudialyte, fergusonite, florencite, parisite, perovskite, pyrochlore and zircon (Krishnamurthy and Gupta, 2015).

Mineral	Formula	Wt.% REO	Other REE variants
Carbonates			
ancylite-(Ce)	$SrCe(CO_3)_2(OH).H_2O$	43	La
Fluorocarbonates			
bastnäsite-(Ce)	$CeCO_3F$	70	La, Nd, Y
huanghoite-(Ce)	$BaCe(CO_3)_2F$	40	
parisite-(Ce)	$CaCe(CO_3)_3F_2$	50	Nd
synchysite-(Ce)	$CaCe(CO_3)_2F$	51	Nd, Y
Phosphates			
cheralite-(Ce)	$Ca,Th(PO_4)_2$	variable	
churchite-(Y)	$YPO_4.2H_2O$	51	Nd
monazite-(Ce)	$CePO_4$	70	La, Nd, Sm
xenotime-(Y)	YPO_4	67	Yb
Oxides			
aeschynite-(Ce)	$(Ce,Ca,Fe,Th)(Ti,Nb)_2(O,OH)_4$	32	Nd, Y
cerianite-(ce)	CeO_2	100	
loparite-(Ce)	$(Ce,La,Nd,Ca,Sr)(Ti,Nb)O_3$	30	
yttropyrochlore-(Y)	$(Y,Na,Ca,U)_{1-2}Nb_2(O,OH)_7$	e.g. 17	
Sillicates			
allanites-(Ce)	$CaNdAl_2Fe^{2+}(SIO_4)(SI_2O_7)O(OH)$	38	La, Nd, Y
britholite-(Ce)	$(Ce,Ca,Sr)_2(Ce,Ca)_3(SIO_4,PO_4)_3(O,OH,F)$	e.g. 23	Y
eudialyte-(Ce)	$Na_{15}Ca_6Fe_3Zr_3SI(Si_{25},O_{73})(O,OH,H_2O)_3(Cl,O$	e.g. 9	
gadolinite-(Ce)	$Ce_2Fe^{2+}Be_2O_2(SIO_4)_2$	60	Y
keiviite-(Y)	$Y_2Si_2O_7$	69	Yb
Fluorides			
fluocerite-(Ce)	CeF_3	83	La

Table 2-2: Most common rare earth minerals including the rare earth oxides. After Wall, 2014.

2.2. Production and resources

The reliance upon a single and dominant supplier nation: China, combined with growing demand for these strategic elements, low recycling rates and poor substitutability, has led to REE being labelled as 'critical metals' (European Commission, 2017; Wall, 2014). REE are relatively abundant in the Earth crust (Wall, 2014), for example La and Ce respective Earth's crust abundance of 39 ppm and 66.5 ppm (Table 2-1) are a thousand times more abundant than gold with a Earth's crust abundance of 0.004 ppm (Lide, 1997). There is a variety of potential REE deposits outside China not yet mined for REE, including skarn and bauxites deposits. And a wide range of more traditional REE deposits located in Europe such as carbonatite, alkaline igneous rock and pegmatite deposits have recently been classified as REE resource (Orris and Grauch, 2002; Goodenough *et al.,* 2016, Goodenough *et al.,* 2018).

Currently, carbonatites and placer deposits are the main LREE source, while ion-absorption clays are the main HREE source worldwide (U.S. Geological Survey, 2019). The main REE deposits mined are located in China (Table 2-3), the carbonatites include the Bayan Obo deposit, Nei Mongol Autonomous Region (Fan *et al.,* 2016), the Maoniuping and the Daluxiang deposits, Sichuan Province (Xu *et al.,* 2008) and the Weishan deposit in Anhui Province (Wang et *al.,* 2019). The ion-absorption deposits are mined in various locations in the south eastern provinces (Wang *et al.,* 2018). REE deposits are usually divided into primary deposits, formed by magmatic and hydrothermal processes and secondary deposits, formed by weathering and erosions of the primary deposits and sedimentary processes. Both groups are further divided into deposit types. Carbonatite, alkaline igneous rocks and hydrothermal deposits constitute the primary deposit group; while ion adsorption, placer, laterite and bauxite deposits are part of the secondary deposits.

Location	Estimated mine production in 2017 (tons)	Reserves (tons)
China	105,000	44,000,000
United States	-	1,400,000
Australia	20,000	3,400,000
Brazil	2,000	22,000,000
Canada	-	830,000
Greenland	-	1,500,000
India	1,500	6,900,000
Malawi	-	140,000
Malaysia	300	30,000
Russia	3,000	18,000,000
South Africa	-	860,000
Thailand	1,600	NA
Vietnam	100	22,000,000
World total (tons)	**133,500**	**118,830,000**

Table 2-3: World mine production and reserves in 2017. The reserves are defined as that part of the reserve base which could be economically extracted or produced at the time of determination. After U.S. Geological Survey, 2018.

2.3. Industrial uses of Rare Earth metals

Nowadays, small quantities of REE are commonly used in everyday consumer products such as computers, smartphones and televisions (Castor and Hedrick, 2006). However, a significant part of the REE market is destined towards their use in low carbon technologies, such as wind turbines, hybrid electric vehicles, automotive catalytic converters and energy efficient fluorescent lighting (Gibson and Parkinson, 2011). They play a crucial role in environmental protection, these make them fundamental in a rapidly growing and developing world.

The market demand is currently dominated by catalysts and REE-magnets (Table 2-4), with the REE-magnets market showing the most rapid growth. Neodymium-iron-boron magnets are more powerful than alternatives for a smaller size. This has also considerably improved the weight and size of common technologic devices such as MP3 players or DVD drives. They are of critical importance too in electric vehicles, as it reduces the size and weight of the motors. REE-magnets have the potential to increase the energy efficiency, performance or longevity of many appliances. Due to the constant development of products and improvement of low carbon technology, the REE demand tends to fluctuate (Table 2-5). The popularisation of electric vehicles is believed to be the technology that will disrupt the most the REE market demand in the future years. The growth of hybrid electric vehicles and full electric vehicles is forecast for an increase of 7.8 million units in 2026 which will consequently increase the demand for Nd used in the neodymium-iron-boron magnets (Roskill, 2016).

REE uses	2016 share
Catalysts	24%
Magnets	23%
Polishing	12%
Metallurgy	8%
Batteries	8%
Glass	7%
Ceramics	6%
Phosphors	2%
Others	10%

Table 2-4: Main REE use in 2016. From Roskill, 2016.

REE	2016	2025
La	26.4%	27.4%
Ce	39.5%	37.1%
Nd	19.9%	21.7%
Sm	0.3%	0.2%
Eu	0.2%	0.1%
Gd	1.1%	1.4%
Dy	0.7%	0.8%
Tb	0.2%	0.1%
Y	7.1%	6.2%
Others	0.5%	0.7%

Table 2-5: Forecast evolution of the REE market by element from 2016 to 2025. After Roskill, 2016.

2.4. REE deposit types

In 2002, Orris and Grauch (2002) listed 822 occurrences of REE deposits worldwide and more recently over 80 REE deposits occurrences were identified in Europe, although few of these can be considered as economic at the present time (Goodenough *et al.,* 2016).

REE deposits are further categorised by geological context (Chakhmouradian and Wall, 2012; Wall, 2014; Goodenough *et al.,* 2016; Verplanck and Hitzman, 2016). The most economically important REE deposit types are those hosted by primary deposits, such as carbonatite and peralkaline rocks, and secondary deposits, mostly ion absorption deposits.

2.4.1. Alkaline igneous rock-related deposits

Alkaline igneous rocks are deficient in SiO_2 relative to Na_2O, K_2O and CaO. They range widely in composition from ultra-alkaline (silica-undersaturated) to peralkaline (silica-saturated) (Winter, 2001). Alkaline igneous complexes are characteristic of intracontinental tectonic setting; they form from alkaline-rich magma sources and crystallize sodium and potassium bearing minerals (Woolley and Kempe, 1989). The peralkaline and carbonatite subclasses are the main REE source.

Peralkaline rocks and carbonatites are the most economically significant members of the alkaline igneous group, due to their enrichment in alkali metal and high field strength elements (HFSE) such as Nb, Zr, Ta, Th, and U and REE (U.S. Geological Survey, 2010; Dostal, 2016; Verplanck *et al.*, 2016).

2.4.1.1. Carbonatite-related deposits

Carbonatites are defined in the IUGS (International Union of Geological Science) system of classification as igneous rocks composed of greater than 50 modal per cent primary carbonate (Streckeisen, 1979) and containing less than 20 wt.% SiO_2 (Le Maitre, 2002). Although they are igneous rocks, most carbonatites are polygenetic (Jones *et al.,* 2013) and show evidence of hydrothermal and metasomatic reworking, some examples are the Lofdal and Okorusu carbonatites, Namibia, the Bear Lodge carbonatite, USA, the Songwe Hill carbonatite, Malawi and the Huanglongpu carbonatite, China (Wall *et al.,* 2008; Moore *et al.,* 2015; Broom-Fendley *et al.,* 2016, Smith *et al.,* 2018).

Carbonatites were first described in 1884 by Bose from the Lower Narbada Valley of India. It was only in 1895 that a volcanic origin was proposed (Högbohm, 1895). The precise origin of carbonatite is still disputed, but currently, the parental magma is believed to come from a lithospheric or asthenospheric mantle source, based on isotopic evidence (Chakhmouradian and Zaitsev, 2012). The parental magma may be by a low-degree melting of metasomatized peridotite. But the majority of the carbonate melt does not crystallise directly from the mantle derived melt, instead it tends to form in association with contemporaneous ultramafic and alkaline silicate rock (Chakhmouradian and Zaitsev, 2012). While the majority of carbonatites are intrusive bodies, such as the Maoniuping and Daluxiang carbonatite, China, (Xu *et al.,* 2010a) some have erupted such as the Oldoinyo Lengai, Tanzania (Woolley and Church, 2005), which is the only active volcano currently erupting carbonatite lavas.

Since its last explosive activity in 2008, intermittent effusive carbonatite eruptions have been observed (Smithsonian Institution, 2019). Volumetrically speaking, carbonatites are rare compared to silicate rocks, even within the igneous complexes that host them.

Carbonatites are normally classified according to the dominant carbonate mineral and its associated chemistry, i.e. Ca, Mg or Fe-dominated (Woolley and Kempe, 1989; Le Bas, 1987; Mitchell, 2005). On this basis, carbonatites are divided into four groups: calcite carbonatite (Ca e.g. Okorusu and Huanglongpu carbonatites discussed in this thesis), magnesium carbonatite (Mg), ferrocarbonatite (Fe) and sodium carbonatite (Na) which is only identified as extrusive carbonatite observed at the Oldoinyo Lengai volcano, Tanzania (Mitchell, 2009). Jones *et al.,* (2013) proposed another independent category, the REE-carbonatite, they are characterised by a whole-rock content of $REE_2O_3 > 1\%$. Examples of deposits that can be described as REE-carbonatite include: the Bayan Obo, China (Ling *et al.,* 2013; Smith *et al.,* 2015); the Kangankunde carbonatite, Malawi (Broom-Fendley *et al.,* 2016), the Mountain Pass carbonatite, California (Castor, 2008) and the Huanglongpu carbonatite, China (Xu *et al.,* 2007, 2010b). Carbonatites can also be classified by their origin, which divides them into two main groups: primary igneous and carbothermal carbonatite. Carbothermal carbonatites are inferred to have been precipitated from a mixed CO_2-H_2O fluid at subsolidus temperature (Mitchell, 2005; Woolley and Kjarsgaard, 2008).

The most common carbonate phases in carbonatites are: calcite, dolomite, ankerite and siderite (Linnen *et al.,* 2013; Zaitsev *et al.,* 2014). Common accessory phases include: apatite, Na-pyroxene, amphibole, diopside, magnetite, phlogopite, pyrochlore, ferro-magnesian silicates and REE-bearing minerals such as xenotime, burbankite, bastnäsite, monazite and REE-fluorcarbonates. Carbonatite geochemistry is characterized by a high abundance of Sr, Ba, P and LREE.

The largest and highest grade REE deposits are associated with carbonatite complexes (Chakhmouradian and Wall, 2012; Chakhmouradian and Zaitsev, 2012; Verplanck, 2017). They are enriched in REE relative to widespread igneous rocks such as granite and basalt, and show strong LREE enrichment compared to other REE-rich rocks including peralkaline rocks. For example, the Bear Lodge carbonatite, Canada, has ten times more LREE than the peralkaline Strange Lake deposit, Canada (Fig. 2-2).
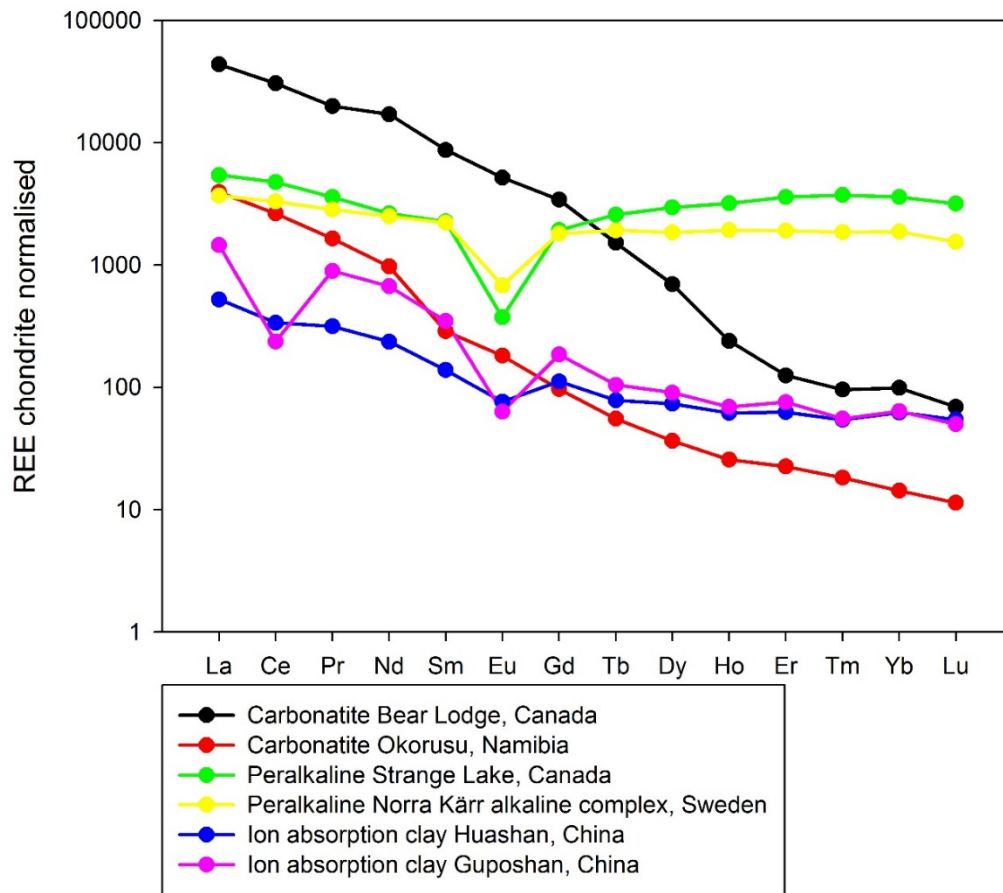
Figure 2-2: Chondrite normalised plot (McDonough and Sun, 1995) *showing representative REE profiles from a range of REE deposits. Okorusu carbonatite, sample OKC19-1 (Cangelosi et al., 2019); Bear Lodge Mountains carbonatite, sample BL71* (Moore *et al.,* 2015)*; Strange Lake peralkaline rock, average of drill core BZ10027* (Gysi and Williams-Jones, 2013)*; Norra Kärr peralkaline rock, sample PGT 407497* (Sjöqvist *et al.,* 2013)*; Huashan and Guposhan ion absorption clay, respectively sample Hua95-9 and HK-3 (Bao and Zhao, 2008).*

Carbonatite-associated REE deposits have been found in several geotectonic environments. Woolley and Kjarsgaard (2008) compiled data from 500 carbonatite occurrences and concluded that they tend to occur within stable, intra-plate tectonic settings, and are associated with major faulting and rift related doming, although other examples are also associated with orogenic activity (Woolley and Kempe, 1989; Hou *et al.,* 2006).

There are three main hypotheses for the formation of carbonatite magmas:

1) Direct melting of a CO_2-bearing peridotite mantle source (Wallace and Green, 1988; Sweeney, 1994; Harmer and Gittins, 1998; Harmer *et al.,* 1998; Ying *et al.,* 2004).

2) Extensive crystal fractionation from carbonated nephelinite or melilitite melt (Gittins, 1989; Gittins and Jago, 1998).

3) Immiscible melt separation from a CO_2-saturated silicate melt (Freestone and Hamilton, 1980; Mundsen, 1987; Kjarsgaard and Hamilton, 1988 and 1989; Brooker and Hamilton, 1990; Church and Jones, 1995; Lee and Wyllie, 1997; Dawson, 1998; Halama *et al.,* 2005; Brooker and Kjarsgaard, 2011).

Hybrids of these three different hypotheses have also been proposed (Yaxley and Brey, 2004; Wyllie, 1995; Bizimis *et al.,* 2003 and Woolley and Bailey, 2012).

The carbonatites stable isotope signature has been commonly used to understand their evolution. Because, in many cases, their isotopic compositions reflect processes that have modified the original mantle $\delta^{13}C$ and $\delta^{18}O$ values (e.g. Moore *et al.,* 2015; Trofanenko *et al.,* 2016; Broom-Fendley *et al.,* 2017b; Simandl and Paradis, 2018; Chikanda, *et al.,* 2019). The reference Primary Igneous Carbonatite (PIC) values represent the natural C and O isotopic range of mantle derived carbonatites, allowing for mantle heterogeneities. In other words, it consists of analyses of carbonatite material unaffected by weathering, or by hydrothermal alteration. Several primitive mantle values with slightly different ranges have been proposed (Taylor *et al.,* 1967; Keller and Hoefs, 1995; Demény *et al.,* 2004; Jones *et al.,* 2013; Fig. 2-3). The small deviations from PIC $\delta^{13}C$ and $\delta^{18}O$ values are typically attributed to mantle heterogeneity or variations in the source reservoir (Andersen *et al.,* 2019). An overall $\delta^{18}O$ range considering all these studies is between 5‰ to 10‰ (vs VSMOW throughout this thesis; Fig. 2-3).

Carbonatites isotopic composition signatures can be changed by a number of mechanisms (Fig. 2-3), including magmatic processes such as Rayleigh fractionation, which is manifested as an increase of $\delta^{18}O$ and $\delta^{13}C$ due to the calcite crystallising in equilibrium with a H_2O and CO_2 from a magma (Ray and Ramesh, 2000). Magma-rock interaction including sediment assimilation, tends to increase the $\delta^{18}O$ and $\delta^{13}C$ composition of the carbonatite (Santos and Clayton, 1995; Demény *et al.,* 1998). Degassing lowers the $\delta^{13}C$ values through preferential

partitioning of heavy carbon into the gas phase (Suwa *et al.,* 1975; Demény *et al.,* 1994) and tend to increase the $\delta^{18}O$ values (Demény *et al.,* 1994; Demény *et al.,* 2004). Lastly, post-magmatic alteration involving fluids such as meteoritic/geothermal waters, usually have negative $\delta^{18}O$ compositions (Hoefs, 2008). The effect on the $\delta^{18}O$ carbonatite composition is temperature dependent in this case, alteration from a water below 200 °C results in an increase of the $\delta^{18}O$ and above 200 °C it results in a decrease of the calcite $\delta^{18}O$ value (Deines, 1989; Broom-Fendley *et al.,* 2016). The different PIC fields with the processes able to alter the PIC mantle values of carbonatites are summarised in Figure 2-3.

Typically, REE carbonatites show C and O isotope compositions that have extended beyond the PIC field (Fig. 2-3), usually showing higher $\delta^{18}O$ and $\delta^{13}C$ resulting from post magmatic fluids alteration associated to the REE deposition (e.g. Downes *et al.,* 2014; Moore *et al.,* 2015; Trofanenko *et al., 2016*, Broom-Fendley *et al.,* 2016b; Andersen *et al.,* 2019).
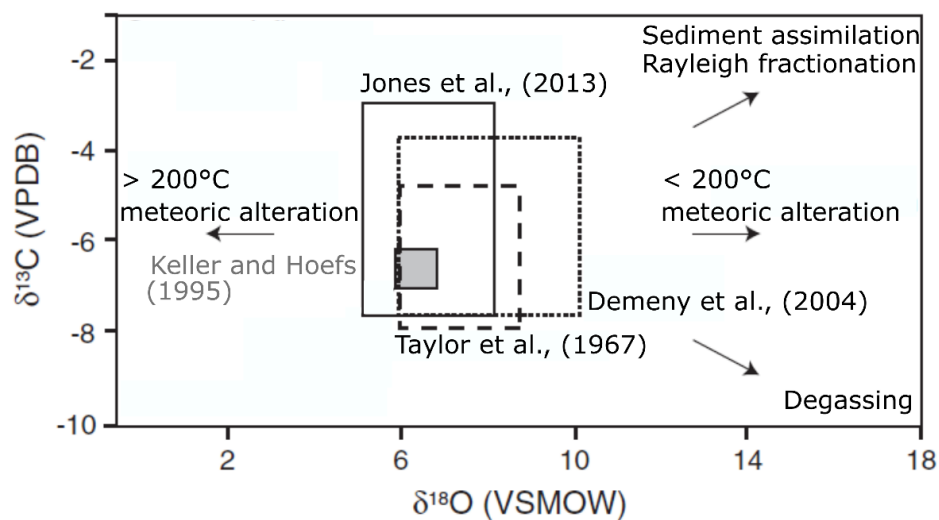
Figure 2-3. Alteration processes and their effects on the C and O isotope composition of PIC carbonatites. The different boxes represent the different PIC carbonatite ranges found in the literature (vs VPDB and VSMOW). After Broom-Fendley et al., 2016b.

Carbonatites rocks are often surrounded in part by an alkali metasomatic aureole of fenite. Fenites are formed by the metasomatism process triggered by the alkali-rich aqueous fluids circulating in the country rock and formerly expelled from the crystallising and cooling of a carbonatite melt (Le Bas, 2008). During fenetisation, the alkalis and volatiles expelled are original constituents of the magma but are not recorded in the carbonatite rocks after

crystallisation (Le Bas, 2008). Fenite composition depends on numerous parameters such as the protolith mineralogy, permeability and structure and the expelled fluid composition as well as its temperature and pressure (Platt, 1996; Le Bas, 1987). However, they typically consist of K-feldspar, albite, alkali pyroxene and alkali amphibole (Zharikov *et al.,* 2007). Although, fenite tends to host less REE than its carbonatite counterpart, they have potential to be used as an exploration tool as they can extent up to several kilometres (Elliot *et al.,* 2018). Carbonatite fenitizing fluids contain ligands such as chloride and sulfate which form complexes with the REE, enhancing their solubility. This permits the transport of these elements into the surrounding aureole where they crystallise. Hence, the composition of the fenitic aureole may act as an exploration tool indicator to determine the REE composition of the carbonatite, and potentially avoid costly drilling (Elliot *et al.,* 2018). Previously, igneous metasomatic has already been used to facilitate gold exploration in Russia (Dvornik, 2015).

2.4.1.2. Peralkaline deposits

Peralkaline rocks are characterised by a molar Na_2+K_2O greater than Al_2O_3. They range from silica-oversaturated rocks such as granitic and rhyolitic to silica-saturated rocks such as syenitic and trachyte and silica-undersaturated rocks such as nepheline syenitic to foditic. They tend to host a range of characteristic complex sodium minerals such as sodic amphiboles, sodic pyroxenes and feldspathoids (Goodenough *et al.,* 2018). Compared to carbonatite deposits, peralkaline REE deposits are less LREE enriched but tend to have higher HREE content than a typical carbonatite (Linnen and Cuney, 2005), leading to a flatter REE profile (Fig. 2-2) and typically have a rare earth oxide grade < 1 wt.% (Goodenough *et al.,* 2018). For example, the Norra Kärr alkaline complex, Sweden, shows a fairly flat REE pattern across the lanthanide series and up to 100 times more HREE than the Bear Lodge carbonatite (Fig. 2-2). A wide variety of REE-bearing minerals are typical of peralkaline intrusions including apatite, eudialyte, loparite, gittinsite, xenotime, gadolinite, monazite, bastnäsite, synchysite, iimoriite, euxenite, kainosite, mosandrite, britholite, allanite, fergusonite and zircon (U.S. geological survey, 2010; Table 2-6).

Agpaitic intrusions are characterised by a range of mostly halogen-bearing Na-Ca-HFSE minerals such as sodalite and fluorite (Marks and Markl, 2017) and are some of the most REE-enriched peralkaline rocks (Marks *et al.,* 2011). The Khibina and Lovozero deposits, Kola Peninsula in Russia are among the largest peralkaline bodies worldwide, with the Lovozero agpaitic nepheline syenite deposit being the only active REE peralkaline mine with the main REE ore being loparite (Kogarko *et al.,* 2002). But many other agpaitic nepheline syenite

related intrusions are at the exploration stage such as the Red Wine, Labrador agpaitic, Canada (Curtis and Currie, 1981; Mariano and Mariano 2012), the Kvanefjeld and the Ilímaussaq Complex, Greenland (Goodenough *et al.,* 2016).

Mineral group	Mineral	Formula
Sillicates	eudialyte	$Na_{15}Ca_6(Fe^{2+},Mn^{2+})_3Zr_3[Si_{25}O_{73}](O,OH,H_2O)_3(OH,Cl)_2$
	allanite-(Ce)	$(CaCe)(Al_2Fe^{2+})(Si_2O_7)(SiO_4)O(OH)$
	britholite-(Ce)	$(Ce,Ca)_5(SiO_4)_3OH$
	zircon	$ZrSiO_4$
	gadolinite	$Y_2Fe^{2+}Be_2Si_2O_{10}$
	gittinsite	$CaZrSi_2O_7$
	iimoriite-(Y)	$Y_2[SiO_4][CO_3]$
	kainosite-(Ce)	$Ca_2(Y,Ce)_2(Si_4O_{12})(CO_3)\cdot H_2O$
	mosandrite-(Ce)	$(Ca_3Ce)[(H_2O)_2Ca_{0.5}\square_{0.5}]Ti(Si_2O_7)_2(OH)_2(H_2O)_2$
Carbonates	bastnäsite-(Ce)	$Ce(CO_3)F$
	synchysite-(Ce)	$CaCe(CO_3)_2F$
Phosphates	monazite-(Ce)	$CePO_4$
	xenotime-(Y)	YPO_4
	apatite	$Ca_5(PO_4)_3(OH,F,Cl)$
Oxides	loparite-(Ce)	$(Ce,Na,Sr,Ca)(Ti,Nb,Ta,Fe^{3+})O_3$
	euxenite-(Y)	$(Y,Ca,Ce)(Nb,Ta,Ti)_2O_6$
	fergusonite-(Y)	$YNbO_4$

Table 2-6: Common REE minerals and REE bearing minerals in peralkaline rocks.

2.4.2. Ion absorption deposits

REE ion absorption deposit refers to the lateritic residual soil which mainly consists of clay minerals and Al and Fe oxides (Gidigasu, 1972). These deposits are formed under tropical and sub-tropical climates, where the erosion is minimal and results from the in-situ weathering of the host rock (Moldaveanu and Papangelakis, 2016). The warm temperatures and abundant rainfalls in these regions allow laterite weathering profiles to form by washing out the bases and the silicic acid and enriching the soil with aluminium silicates clays (Maji *et al.,* 2007). The REE hosted in the bedrock are mobilised into secondary minerals accumulating within the profile or they get absorbed onto the clay minerals surfaces due to the permanent negative charge, hosting from 0.05 to 0.3 wt.% REE (Chi and Tian, 2008, Goodenough *et al.*, 2018). The charge imbalance is due to isomorphous substitution of a cation by another with a lesser charge, leading to the clay ability to absorb the REE previously released by the weathering (Meunier, 2005). The REE are from the original bedrock, mainly granite (but also from pyroclastic rock and lamprophyres) containing minerals such as parisite which are easily weathered (Bao and Zhao, 2008).

Despite the rare earth oxide grade being one of the lowest of the REE related deposits (0.05 - 0.2 wt.% REO; Kynicky *et al.,* 2012, Fig. 2-2), ion absorption deposits are the world's most important source of HREE and account for 35% of the China's total REE output and about 80% of world's HREE production (Yang *et al.,* 2013). These deposits are valuable because they are very easy to mine by leaching techniques at ambient temperature and have very low U and Th contents (Bao and Zhao, 2008; Sanematsu and Watanabe 2016).

REE ion absorption deposits are mainly known from southern China (south of 28 °N), especially in the sub-tropical climates of Jiangxi, Hunan, Guangdong and Guangxi provinces including the Heling, Longnan, Guposhan and Huashan REE deposits (Fig. 2-2). They are also referred to as the South China clays (Bao and Zhao, 2008; Grauch and Mariano, 2008). They have been discovered in a few other localities, including Madagascar (Berger, 2014), Malawi (Le Couteur, 2011) and Brazil (Rocha *et al.,* 2013). However, none of these deposits show HREE content nearing the South China clays.

22

2.5. REE enrichment in natural systems

2.5.1. REE enrichment by magmatic processes

The concentration of REE in magmatic systems is a function of several processes. The source of the parental magma is key to creating economically viable deposits. A metasomatic, incompatible element enriched mantle source is needed to create a magma which will lead to a REE-deposit. The enrichment occurs through adding material to the mantle by either infiltration of another phase or diffusion (Chakhmouradian and Zaitsev, 2012). The widely observed LREE enriched pattern of carbonatites is mainly due to the LREE incompatibility in mantle minerals due to their larger size than the HREE (Krishnamurthy and Gupta, 2015), leading to the REE being preferentially incorporated into the melt during partial melting (Chakhmouradian and Zaitsev, 2012).

Further enrichment is required to reach the REE concentrations observed in igneous-related deposits regardless the origin of the magma. Fractional crystallisation is able to enrich a melt by precipitating minerals with lower REE content than the magma, leading to REE enrichment of the remaining melt (Thompson *et al.,* 1982; Chakhmouradian, 2006; Chakhmouradian *et al.,* 2017; Giebel *et al.,* 2017). One example is the Mountain Pass deposits, USA, where the carbonatite magma has crystallised abundant primary magmatic bastnäsite mineralisation (Castor, 2008).

In the case of carbonatite systems, it is likely that liquid immiscibility between silicate and carbonate melts can concentrate REE in the carbonatite melt. During silicate-carbonatite immiscibility, LREE are more compatible in the carbonatitic phase than the HREE, leading to separation of the HREE from the LREE (Chakhmouradian and Zaitsev, 2012; Veksler *et al.,* 2012).

2.5.2. REE enrichment by hydrothermal processes

Further REE enhancement can be caused by later hydrothermal activity overprinting the magmatic REE mineralisation (Williams-Jones *et al.,* 2000; Smith and Henderson 2000; Wall *et al.,* 2008; Chakhmouradian and Wall, 2012; Moore *et al.,* 2015; Broom-Fendley *et al.,* 2017). In fact, REE economic concentrations are often hosted by minerals precipitated through hydrothermal alteration, rather than the early magmatic REE minerals, well known examples are the Bayan Obo deposit, China (Smith *et al.,* 2015) and the Bear Lodge deposit, USA (Moore *et al.,* 2015). As Wall (2014) noted, economic levels of REE in carbonatite-related deposits are mainly contained in secondary minerals such as REE fluorcarbonates and monazite.

The REE mobility in hydrothermal fluids is controlled by numerous parameters, such as the nature and the stability of the REE-ligand aqueous complexes formed, but also the temperature, pH and redox conditions of the fluid among others. Hence, understanding the conditions of REE transport and deposition in hydrothermal fluids is key to understand how REE ore deposits form.

2.5.2.1. Stability of REE aqueous complexes at room temperature

The REE as a group are recognised as potentially mobile in some hydrothermal fluids in a variety of geological settings (Linnen *et al.,* 2014). As discussed earlier, a number of major REE deposits are in part hydrothermal, including the Bayan Obo deposit, China; the Bastnäs deposit, Sweden and the Fen Complex, Norway (Smith *et al.,* 2000; Holtstam *et al.,* 2007; Holtstam *et al.,* 2014; Marien *et al.,* 2017). Other examples have been described by Oreskes and Einaudi, (1990); Williams-Jones *et al.,* (2000) and Sheard *et al.,* (2012). The REE are soluble only if a suitable liquid phase is present; they move as complexes with ligands in aqueous solution, and so can migrate when the fluid circulates through the rock.

Most studies have been carried out on the stability of REE aqueous complexes at room temperature. Pearson's rule (Pearson, 1963) state that hard cations (cations with no outer shell electron) bond preferentially with hard anions thanks to an ionic bonding character, while soft cations (cations with many outer shell electrons) bond preferentially with soft anions thanks to covalent bonding. REE cations predominantly have a 3^+ charge with small ionic radii, classing them as hard cations. Due to the lanthanide contraction (Fig. 2-1), the REE are not all able to create the same strength of bond with the same ligand.

Ce^{4+} is the hardest REE cation, with an ionic potential of 3.96, and Eu^{2+} the softest, with an ionic potential of 1.53. Apart from these two ions, the lanthanide series follows a linear pattern with the ionic potential increasing with atomic number, from La^{3+} (2.56) to Lu^{3+} (3.00). Y^{3+} has a similar ionic radius than Ho^{3+}, and a comparable ionic potential (~2.88) (Williams-Jones *et al.,* 2012). According to the Pearson's rule the stability of complexes formed with hard ligands increases along the lanthanide series (from La to Lu), with Y behaviour between that of Ho and Er.

Pearson's rule predicts that cation solubility depends on the ligands present in the fluid and its temperature. He has ordered the ligands according to the stability of their aqueous complexes, only inorganic ligands are discussed here; the order of monovalent ligands with which the REE should form their most stable aqueous complexes is: F$^-$ > OH$^-$ > NO$_3^-$ > Cl$^-$ > Br$^-$. For complexes involving divalent ligands, the order is CO$_3^{2-}$ > SO$_4^{2-}$ > P$_2$O$_5^2$.

Williams-Jones (2012) has summarised the results of the several relevant studies carried on the behaviour of aqueous REE complexes at a temperature of 25 °C. He concluded that at ambient temperature, the predictions of Pearson's rule are fulfilled. Thus, the REE complexes with the hardest ligands (F$^-$ and CO$_3^{2-}$) are more stable than complexes with intermediate hardness ligand such as Cl$^-$. Furthermore, the stability of REE complexes increases with the hardness of the REE independently of the ligand (Luo and Byrne, 2001; Williams-Jones, 2012; Migdisov *et al.,* 2016). The SO$_4^{2-}$ ligand is the exception since the REE hardness does not affect the stability of REE-sulfate complexes (Migdisov and Williams-Jones, 2008). Cl$^-$ complexes at ambient temperature follow an inverse pattern; stability tends to decrease with increasing REE hardness (Luo and Byrne, 2001).

2.5.2.2. Stability of aqueous REE complexes at high temperature

Prior to modern experimental studies, looking at the REE complexation at high temperature, (up to 300 °C), stability data for REE aqueous complexes were derived from theoretical calculations based on Haas' model (1995). More recently, it has been found that for the halogen ligands, due to the behaviour of the dielectric constant of water at higher temperatures, these predictions have proved to be unsatisfactory. Higher temperature decreases the dielectric constant, in turn reducing the resistance to electron transfer, leading to a different stability than the Haas' (Haas *et al.,* 1995) extrapolated data (Cárdenas *et al.,* 2011; Williams-Jones *et al.,* 2012; Fig. 2-4).

Study of REE complexation at high temperature, has been conducted for four of the main ligands including F^-, Cl^-, SO_4^{2-} and OH^- (Migdisov and Williams-Jones, 2002, 2006; Migdisov *et al.,* 2006; Migdisov and Williams-Jones, 2007, 2008; Migdisov *et al.,* 2008, 2009; Williams-Jones, 2012; Loges *et al.,* 2013; Migdisov *et al.*, 2016). The recent experimental studies have emphasised the importance of temperature in controlling the stability of aqueous complexes; at higher temperature, complexes do not behave the same as they do at ambient temperature. The stability is connected to the formation constant of the complex formed as such: the larger the formation constant value of a complex, the more stable it is. The formation constant is an equilibrium constant for the formation of a complex in solution, it measures the strength of the interaction between the ligand and metal forming the complex. The formation constant represented in Figure 2-4 and 2-5 are calculated from $\log\beta^F = \log a_{REEF2+} - \log a_{REE3+} - \log a_{F-}$; $\log\beta^{Cl} = \log a_{REECl2+} - \log a_{Cl-} - \log a_{REE3+}$ and $\log\beta^0 = \log a_{REESO4+} - \log a_{SO42-} - \log a_{REE3+}$, with $\log a$ the charged ion representing its activity (Migdisov *et al.,* 2009).

For the REE complexes forming with fluoride, the hardest ligand, Migdisov *et al.,* (2009) showed that their stability decreases with increasing atomic number, instead of increasing. Thus $LREEF^{2+}$ are more stable at high temperature than $HREEF^{2+}$. The change in relative stability between the $LREEF^{2+}$ and the $HREEF^{2+}$ complexes occurs at around 150 °C. Overall, the stability of $REEF^{2+}$ complexes increases with increasing temperature (Fig. 2-4) and it is calculated using the activity coefficient of the charged species. $HREECl^{2+}$ complexes show a similar behaviour to $HREEF^{2+}$ complexes; their stability decreases along the lanthanide series above 150 °C. $REECl^{2+}$ complexes show a lower stability overall than $REEF^{2+}$ complexes (Fig. 2-4A-B).
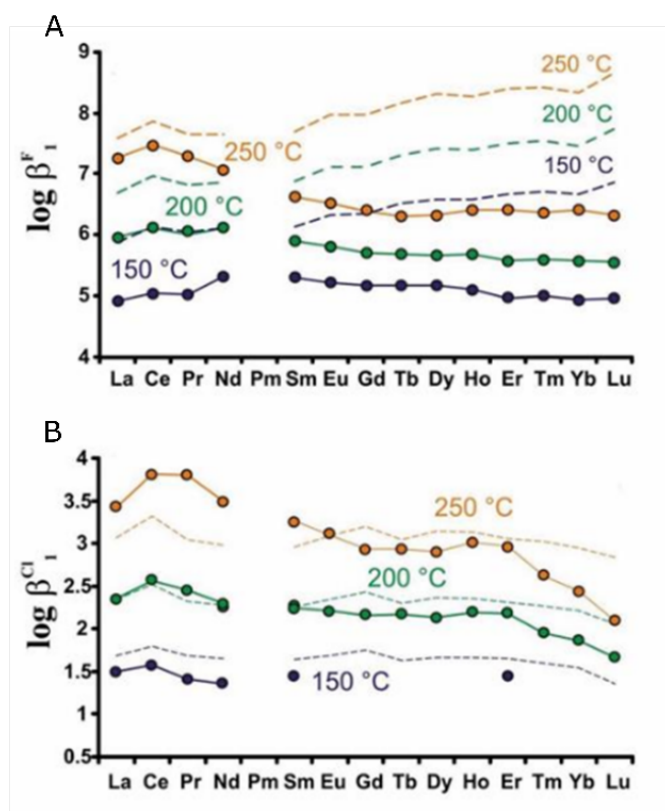
Figure 2-4: Formation constants of REEF⁻ (A) and REECl⁻ (B) complexes at high temperature, respectively for the reaction $REE^{3+} + F^- = REEF^{2+}$ and $REE^{3+} + Cl^- = REECl^{2+}$. The solid lines represent experimental data and the dashed lines theoretical estimates (Migdisov et al., 2009; Haas et al., 1995). From Williams-Jones et al., 2012.

As noted previously, $REESO_4^{2-}$ stability does not vary with atomic number at ambient temperature. All the $REESO_4^{2-}$ aqueous complexes have similar stability, but the increase in temperature leads to more stable $REESO_4^{2-}$ complexes (Fig. 2-5). The experiment on sulfate complexes were only carried on three REE (Nd, Sm and Er), however the results are in good agreement with the theoretical prediction, even if the experimental studies turned out to reveal lower stabilities than expected (Migdisov and Williams-Jones, 2008, 2014; Fig. 2-4).
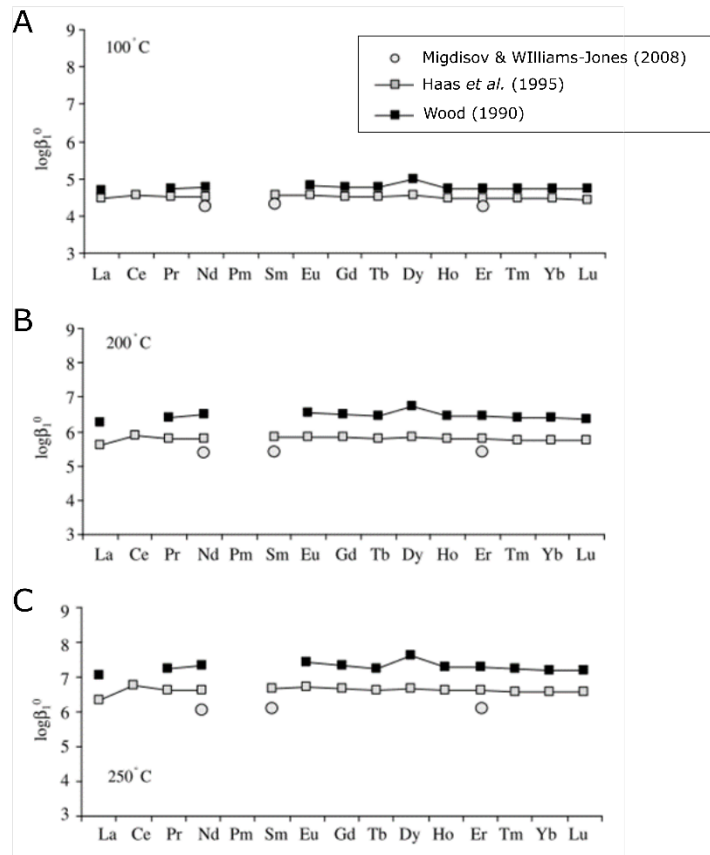
Figure 2-5. Variation of the formation constant for the reaction $REE^{3+} + SO_4^{2-} = REESO_4^+$ of REE sulfate complexes with temperature from 100 °C to 250 °C. From Migdisov and Williams-Jones, 2008.

Currently, no modern experimental work has been done, leading to a lack of thermodynamic data for the REE-bicarbonate and carbonate complexes at high temperature. They are solely based on theoretical extrapolation from low temperature (Haas *et al.,* 1995) and show differences between the behaviour of REE-bicarbonate and REE-carbonate complexes at elevated temperature. The stability of the REE-bicarbonate complexes increases with increasing temperature, whereas the stability of REE-carbonate complexes goes through a maximum at ~300 °C and then decreases with increasing temperature. However, the previous predictions made by Haas *et al.,* (1995) at high temperature have not been supported by experimental data (e.g. Fig. 2-4).

2.5.2.3. Ligands available in natural hydrothermal systems

Although temperature affects the stability of the REE aqueous complexes, the natural variables such as pH, availability of ligands and sources of the REE are also fundamental in determining REE mobility.

In recent studies (Migdisov and Williams-Jones, 2008; 2014; Migdisov *et al.,* 2016), two different types of ligand have been suggested: the ligands leading to REE transportation, and the ligands leading to REE deposition. This is based on the notion of weak and strong acid, a strong acid is virtually 100% ionised in solution while a weak acid does not fully ionise so fewer ions are available in solution to complex with the REE. HCl and H_2SO_4 are strong acids and chloride and sulfate minerals are rare because they are soluble; sulfate and chloride are therefore potentially available to complex with REE and act as transporting agents. REE-fluoride minerals (fluocerite), REE-carbonate and REE-phosphate (monazite and xenotime) are more common minerals because they are relatively insoluble; weak acids such as HF, H_2CO_3 and H_3PO_4 are unlikely to play a role in REE transport but could act as agents of deposition. Unfortunately, there is a lack of solubility data for many REE minerals. Migdisov and Williams-Jones (2014) experimental study and follow up work by Migdisov *et al.,* (2016) confirms the transport of REE as $REEF^{2+}$ complexes is unlikely to be important; they also conclude that the transport of REE by REE-carbonate or REE-bicarbonate complexes is unlikely, but further experimental data on REE-carbonate and bicarbonate speciation and on the solubility of these minerals is needed.

Migdisov and Williams-Jones (2008; 2014) investigated REE transport in chloride-rich and sulfate-rich fluids. Chloride is believed to be the main REE transporting agent and is able to transport significant amount of REE at low pH, due to its dominant occurrence in natural hydrothermal fluids and the relatively stable REE-chloride complexes they form (Fig. 2-4B). But it has been noted that some fluids can hold a sufficient amount of sulfate in solution to transport REE as $REESO_4^{2-}$ complexes at low pH and high hydrothermal temperature. The solution considered to investigate the REE transport in a sulfate-rich fluid contained 10 wt.% NaCl equivalent, 500 ppm F, 2 wt.% Na_2SO_4 equivalent and 200 ppm of Nd (based on a natural ore fluid described by Banks *et al.,* 1994). Their calculations show that sulfate complexes can yield Nd concentrations > 1 ppm for weakly acidic hydrothermal conditions (pH 3.5-5) at 400 °C (Fig. 2-6). They also demonstrated that in sulfate-bearing aqueous solutions of Nd, Sm and

Er, complexes with sulfate (REESO$_4$$^-$ and REE(SO$_4$)$_2$$^{2-}$) strongly predominate over the simple hydrated ions, and the importance of REE(SO$_4$)$_2$$^{2-}$ increases with the increasing temperature. Only few studies showing experimental data on hydrothermal REE transport using natural fluid systems are published (Williams-Jones *et al.,* 2012; Richter *et al.,* 2018) but none are using hydrothermal fluids associated to a carbonatite deposit. Compositions of carbonatite-related REE mineralising fluids were missing up to very recently from the literature (Zheng and Liu, 2019; Shu and Liu, 2019) and as a result most models use simplified fluid compositions (e.g. Song *et al.,* 2016).
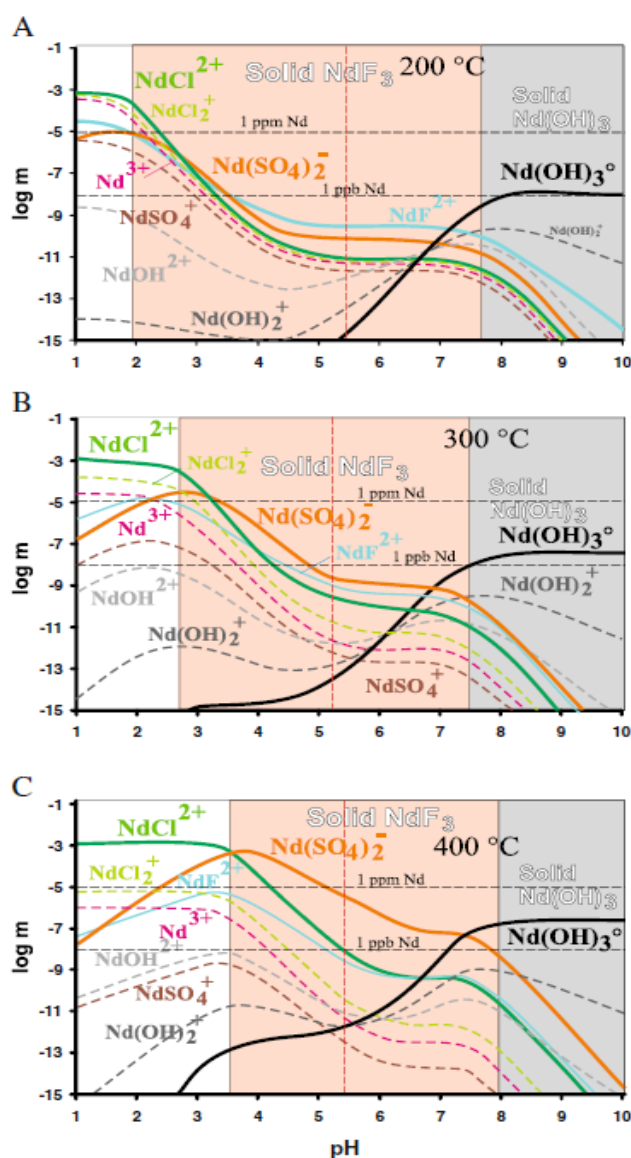
Figure 2-6: Speciation of Nd as a function of pH at 1000 bar for 200 °C, 300 °C and 400 °C. The solution considered contained 10 wt.% NaCl equivalent, 500 ppm F, 2 wt.% Na$_2$SO$_4$ equivalent and 200 ppm of Nd. From Migdisov and Williams-Jones, 2014.

2.6.   Summary

In this review we have mentioned the importance of the REE, mainly due to their application in low carbon technologies but also everyday products. The growing demand, lack of substitute and low recycling rates have pushed the REE to be classified as 'critical metals' by a number of organisations and led China, which hosts the main REE reserves, to control the world market.

In the current climate, REE deposits need to be better understood in order to be able to find new resources outside China. Carbonatite deposits are the primary LREE source and some deposits also show unusual HREE enrichment such as the Huanglongpu deposit, China, but the processes behind REE beneficiation is still poorly understood.

The REE transport at hydrothermal temperature is triggered by a few potential ligands with the main one being the most abundant in natural systems: chloride. Sulfate also shows potential in REE transport. The stability difference of the REE-ligand complexes is quite striking with the $REECl^-$ complexes stability decreasing along the lanthanide series while the $REESO_4^{2-}$ complexes show a similar stability for all the REE and an overall higher stability than the $REECl^-$ complexes.

REE enrichment is often the results of several factors, such as, the primary REE content of the magmatic carbonatite, the nature of the ligand and their concentration coupled with the conditions of the hydrothermal fluid, and the precipitation conditions of the hydrothermal minerals favouring LREE- bearing minerals or HREE-bearing minerals for example.

Carbonatite associated deposits are considerate a good candidate for REE mining due to their REE high grade and high tonnage, generally low radioactivity, and host REE minerals that are easy to process such as bastnäsite. Despite being the current leading LREE resource, more information is needed to understand how secondary processes such as hydrothermal activity is able to concentrate the REE and why secondary reworking can result in an economic HREE enrichment of some carbonatite deposits.

References

Allaby, M. (2008). A Dictionary of Earth Sciences. Oxford: Oxford University Press.

Andersen, A.K., Larson, P.B. and Cosca, M.A. (2019) C–O stable isotope geochemistry and 40Ar/39Ar geochronology of the Bear Lodge carbonatite stockwork, Wyoming, USA. *Lithos*, **324-325**, 640-660.

Banks, D.A., Yardley, B.W.D., Campbell, A.R. and Jarvis, K.E. (1994) REE composition of an aqueous magmatic fluid: A fluid inclusion study from the Capitan Pluton, New Mexico, U.S.A. *Chemical Geology*, **113**, 259-272.

Bao, Z., and Zhao, Z. (2008) Geochemistry of mineralization with exchangeable REY in the weathering crusts of granitic rocks in South China. *Ore Geology Reviews*, **33**(3-4), 519-535.

Bayliss, P. and Levinson, A.A. (1988) A system for nomenclature of rare-earth mineral species: revision and extension. *The American Mineralogist*, **73**, 422-423.

Berger, A., Janots, E., Gnos, E., Frei, R. and Bernier, F. (2014) Rare earth element mineralogy and geochemistry in a laterite profile from Madagascar. *Applied Geochemistry*, **41**, 218-228.

Binnemans, K.J., Blanpain, P.T., Van Gerven,B., Yongxiang, Y., Walton, A. and Buchert, M. (2013) Recycling of rare earths: A critical review. *Journal of Cleaner Production*, **51**, 1-22.

Bizimis M., Salters, V.J.M. and Dawson, J.B. (2003) The brevity of carbonatite sources in the mantle: evidence from Hf isotopes. *Contribution to Mineralogy and Petrology.* **145**, 281-300.

Brooker, R.A. and Hamilton, D.L. (1990) Three-liquid immiscibility and the origin of carbonatites. *Nature.* **346**, 459-462.

Brooker, R.A. and Kjarsgaard, B.A. (2011) Silicate-carbonate liquid immiscibility and phase relations in the system SiO_2-Na_2O-Al_2O_3-CaO-CO_2 at 0.1-2.5 GPa with applications to carbonatite genesis. *Journal of Petrology.* **52**, 1281-1305.

Broom-Fendley, S., Styles, M.T., Appleton, J.D., Gunn, G. and Wall, F. (2016) Evidence for dissolution-reprecipitation of apatite and preferential LREE mobility in carbonatite-derived late-stage hydrothermal processes. *The American Mineralogist*, **101**, 596-611.

Broom-Fendley, S., Heaton, T, Wall, F. and Gunn, G. (2016b) Tracing the fluid source of heavy REE mineralisation in carbonatites using a novel method of oxygen-isotope analysis in apatite: The example of Songwe Hill, Malawi. *Chemical Geology*, **440**, 275-287.

Broom-Fendley, S., Aoife, B.E., Wall, F., Gunn, G. and Dawes, W. (2017) REE minerals at the Songwe Hill carbonatite, Malawi: HREE-enrichment in late-stage apatite. *Ore Geology Reviews,* **81**, 23-41.

Cangelosi, D.A., Broom-Fendley, S., Banks, D.A., Morgan, D.J. and Yardley, B.W.D. (2019) LREE redistribution during hydrothermal alteration at the Okorusu carbonatite complex, Namibia. Mineralogical Magazine, (n.d.) 1-54.

Cárdenas C., Ayers, P., De Proft, F., Tozer, D.J. and Geerling, P. (2011) Should negative electron affinities be used in evaluating the chemical hardness? *Physical Chemistry Chemical Physics*, **13**, 2285-2293.

Castor, S.B. (2008) The Mountain Pass rare-earth carbonatite and associated ultrapotassic rocks, California. *The Canadian Mineralogist*, **46,** 779-806.

Castor, S.B. and Hedrick, J.B. (2006) Rare earth elements. Pp 1568 in: Industrial minerals and rocks: commodities, markets and uses (Kogel, J.E.editor). 7th edition, SME.

Chakhmouradian, A.R. (2006) High-field-strength elements in carbonatitic rocks: Geochemistry, crystal chemistry and significance for constraining the sources of carbonatites. *Chemical Geology*, **235**,138-160.

Chakhmouradian, A.R., Mitchell, R.H. (1998) Lueshite, pyrochlore and monazite-(Ce) from apatite-dolomite carbonatite, Lesnaya Varaka complex, Kola Peninsula, Russia. *Mineralogical Magazine*, **62**, 769-782.

Chakhmouradian, A.R. and Wall, F. (2012) Rare earth elements: Minerals, mines, magnets (and more). *Elements*, **8**, 333-340.

Chakhmouradian, A.R. and Zaitsev, A.N. (2012) Rare earth mineralization in igneous rocks: Sources and processes, *Elements*, **8,** 347-353.

Chakhmouradian, A.R., Reguir, E.P., Zaitsev, A.N., Couëslan, C., Xu, C., Kynický, J. and Yang, P. (2017) Apatite in carbonatitic rocks: Compositional variation, zoning, element partitioning and petrogenetic significance. *Lithos*, 274-275.

Chi, R and Tian, J. (2008) *Weathered Crust Elution-Deposit Rare Earth Ores*. Nova Science Publishers, New York.

Chikanda, F., Otake, T., Ohtomo, Y., Ito, A., Takaomi D. and Sato, T. (2019) Magmatic-Hydrothermal Processes Associated with Rare Earth Element Enrichment in the Kangankunde Carbonatite Complex, Malawi. *Minerals*, **9**(7), 442-464.

Cullers, R.L. and Medaris, G. (1977) Rare earth elements in carbonatite and cogenetic alkaline rocks: Examples from Seabrook Lake and Callander Bay, Ontario. *Contribution to Mineralogy and Petrology*, **65**(2), 143-153.

Church, A.A. and Jones, A.P. (1995) Silicate-Carbonate Immiscibility at Oldoinyo-Lengai. *Journal of Petrology*. **36**(4), 869-889.

Curtis LW, Currie KL (1981) Geology and Petrology of the Red Wine Alkaline Complex, Central Labrador. *Geological Survey of Canada Bulletin*, **294**, 61-72.

Dawson, J.B. (1998) Peralkaline nephelinite-natrocarbonatite relationships at Oldoinyo Lengai, Tanzania. *Journal of Petrology*, **39**(11-12), 2077-2094.

Deines, P. (1989) Stable isotope variations in carbonatite. In: Bell, K. (Ed.), Carbonatites: Genesis and Evolution. Unwin Hyman, London.

Demény, A., Ahijado, A., Casillas, R. and Vennemann, T. (1998) Crustal contamination and fluid/rock interaction in the carbonatites of Fuerteventura (Canary Islands, Spain): a C, O, H isotope study. *Lithos*, **44**, 101-115.

Demény, A., Sitnikova, M. and Karchevsky, P. (2004) Stable C and O isotope compositions of carbonatite complexes ofthe Kola Alkaline Province: phoscorite-carbonatite relation- ships and source compositions. In: Wall, F., Zaitsev, A. (Eds.), Phoscorites and Carbonatites from Mantle to Mine: The Key Example of the Kola Alkaline Province. Mineralogical Society Series, vol. 10, p. 407.

Dostal, J. (2016) Rare metal deposits associated with alkaline/peralkaline igneous rocks. Pp. 33-54 in: *Rare earth and critical elements in ore deposits* (Verplanck, P. and Hitzman, M. Editors). Society of Economic Geologists, Littleton, Colorado.

Downes, P.J., Demény, A., Czuppon, G., Jaques, A.L., Verrall, M., Sweetapple, M., Adams, D., McNaughton, N.J., Gwalani, L.G. and Griffin, B.J. (2014). Stable H–C–O isotope and trace element geochemistry of the Cummins Range Carbonatite Complex, Kimberley region, Western Australia: implications for hydrothermal REE mineralization, carbonatite evolution and mantle source regions. *Mineral Deposita* **49**, 905-932.

Dvornik, G.P. (2015) Metasomatism and gold-porphyry mineralization in potassic alkaline complexes.

Elliott, H.A.L., Wall, F., Chakhmouradian, A.R., Siegfried, P.R., Dahlgren, S., Weatherley, S., Finch, A.A., Marks, M.A.W., Dowman, E., and Deady, E. (2018) Fenites associated with carbonatite complexes: A review. Ore Geology Reviews, **93**, 38-59.

European Commission (2017) Communication from the commission to the European parliament, the council. The European economic and social committee and the committee of the regions on the 2017

list of Critical Raw Materials for the EU. COM(2017) 490.

Fan, H.R., Yang, K.F., Hu, F.F., Liu, S. and Wang, K.Y. (2016) The giant Bayan Obo REE-Nb-Fe deposit, China: Controversy and ore genesis. *Geoscience Frontiers,* **7**(3), 335-344.

Freestone, I.C. and Hamilton, D.L. (1980) The role of liquid immiscibility in the genesis of carbonatites - An experimental study. *Contribution to Mineral Petrology*, **73**(2), pp.105-1171.

Gibson, M. and Parkinson, I. (2011) Once Ignored on the Periodic Table, Don't Ignore Them Now, A Rare Earth Element Industry Overview. CIBC World Market Inc. report. CIBC World Market Inc., Toronto, Canada, pp. 41

Gidigasu, M.D. (1972) Mode of formation and geotechnical characteristics of laterite materials of Ghana in relation to soil forming factors. *Engineering Geology,* **6** (2), 79-150.

Giebel, R., Gauert, C.D.K., Marks, M.A.W., Costin, G. and Markl, G. (2017) Multi-stage formation of REE minerals in the Palabora Carbonatite Complex, South Africa. *American Mineralogist*, **102**(6), 1218-1233.

Gittins, J. (1989) The origin and evolution of carbonatite magmas. Pp 580-600 in: *Carbonatites: Genesis and Evolution* (Bell, K . Editor). Unwin Hyman, London.

Gittins, J. and Jago, B.C. (1998) Differentiation of natrocarbonatite magma at Oldoinyo Lengai volcano, Tanzania. *Mineralogical Magazine*, **62**, pp.759-768.

Goodenough, K.M., Schilling, J., Jonsson, E., Kalvig, P., Charles, N., Tuduri, J. (2016) Europe rare earth element resource potential: An overview of REE metallogenetic provinces and their geodynamic setting. *Ore Geology Reviews,* **72**, 838-856.

Goodenough, K. (2017) EURARE's website. [online]. [Accessed 15 March 2019]. Available from: http://www.eurare.eu/countries/reemap.html

Goodenough, K. M., Wall, F. and Merriman, D. (2018) The Rare Earth Elements: Demand, Global Resources, and Challenges for Resourcing Future Generations. *Natural Resources Research*, **27**(2), 201-216.

Gysi, A. P. and Williams-Jones, A. E. (2013) Hydrothermal mobilization of pegmatite-hosted REE and Zr at Strange Lake, Canada: A reaction path model. *Geochimica et Cosmochimica Acta*, **122**, 324-352.

Grauch, R. and Mariano, A. (2008) Ion-Absorption Type Lanthanide Deposits. Abstract, annual SME Conference, Salt Lake City.

Haas, J.R., Everett, L.S. and Sassani, D.C. (1995) Rare earth elements in hydrothermal systems: Estimates of standard partial molal thermodynamic properties of aqueous complexes of the rare earth elements at high pressures and temperatures. *Geochimica et Cosmochimica Acta*, **59**(21), 4329-4350.

Halama, R. et al. (2005) The Gronnedal-Ika carbonatite-syenite complex, South Greenland: carbonatite formation by liquid immiscibility. *Journal of Petrology*. **46**(1), 191-217.

Harmer, R.E. and Gittins, J. (1998) The Case for Primary, Mantle-derived Carbonatite Magma. *Journal of Petrology*. **39**(11-12), 1895-1903.

Harmer, R.E. *et al.* (1998) A deep mantle source for carbonatite magmatism; evidence from the nephelinites and carbonatites of the Buhera district, SE Zimbabwe. *Earth and Planetary Science Letters.* **158**, 131-142.

Henderson, P. (1984) Rare earth element geochemistry. Elsevier Science, Amsterdam; Oxford; New York; Tokyo.

Hoefs, J. (2008) Stable Isotope Geochemistry. Springer

Högbohm, A.G. (1895) Über das Nephelinsyenitgebiet auf derInsel Alnö. *Geol. Fören. Stockholm Förh*. **17**, 100-160.

Holtstam, D. and Andersson, U.B. (2007) The REE minerals of the bastnäs-type deposits, South-Central Sweden. *Canadian Mineralogist*, **45**, 1073-1114.

Holtstam, D., Andersson, U.B., Broman, C. and Mansfeld, J. (2014) Origin of REE mineralization in the bastnäs-type Fe–REE-(Cu–Mo–bi–Au) deposits, bergslagen, Sweden. *Mineralium Deposita*, **49**, 933-966.

Hou, Z.Q. *et al.* (2006) The Himalayan collision zone carbonatites in western Sichuan, SW China-Petrogenesis, mantle source and tectonic implication. *Earth and Planetary Science Letters,* **244**, 234-250.

Jones, A. P., Genge, M. and Carmody, L. (2013) Carbonate Melts and Carbonatites. *Reviews in Mineralogical and Geochemistry*, **75**(1), 289-322.

Keller, J. and Hoefs, J. (1995) Stable isotope characteristics of recent natrocarbonatites from Oldoinyo Lengai. In: Bell, K., Keller, J. (Eds.), Carbonatite Volcanism. Springer, pp. 113-123.

Kjarsgaard, B. and Hamilton, D.L. (1988) Liquid immiscibility and the origin of alkali-poor carbonatites. *Mineralogy Magazine*. **52**, 43-55.

Kjarsgaard, B. and Hamilton, D.L. (1989) The genesis of carbonatites by immiscibility. Pp. 388-404 in: Bell, K. ed. *Carbonatites: Genesis and Evolution.* London: Unwin Hyman,

Krishnamurthy, N and Gupta, C.K. (2015). Extractive metallurgy of rare earths (2nd edition). New York: CRC Press.

Kogarko, L.N., Williams, C.T., and Woolley, A.R. (2002) Chemical evolution and petrogenetic implications of loparite in the layered, agpaitic Lovozero complex, Kola Peninsula, Russia. *Mineralogy and Petrology*, **74**(1), 1-24.

Kynicky, J., Smith, M. P. and Xu, C. (2012) Diversity of rare earth deposits: The key example of China. *Elements*, **8**, 361-367.

Le Bas, M.J. (1987) Nephelinites and carbonatites. *Geological Society of London Special Publication*, **30**(1), 53-83.

Le Bas, M.J. (2008) Fenites associated with carbonatites. *Canadian Mineralogist*, **46**(4), 915-932.

Le Couteur, P.C. (2011) Geological Report on the Chambe Basin Area of Exclusive Prospecting License EPL0325/11 Mulanje Massif, Southern Malawi, East Africa.

Lee, W.J. and Wyllie, P.J. (1997) Liquid immiscibility between nephelinite and carbonatite from 1.0 to 2.5 GPa compared with mantle melt compositions. *Contribution to Mineralogy and Petrology*, **127**(1), 1-16.

Le Maitre, R.W. (2002) Igneous Rocks: A Classification and Glossary of Terms. Cambridge: Cambridge University Press.

Lide, D.R. (1997) *CRC handbook of chemistry and physics*. [S.l.], Springer.

Ling, M.X., Liu, Y., Williams, I.S., Teng, F.,Yang, X., Ding, X., Wei, G., Xie, L., Deng, W., and Sun, W. (2013) Formation of the world's largest REE deposit through protracted fluxing of carbonatite by subduction-derived fluids. *Scientific Reports*, **3**(1), 1776.

Linnen, R.L. and Cuney, M. (2005). Granite-related rare-element deposits and experimental constraints on Ta-Nb-W-Sn-Zr-Hf mineralization. Pp. 45-68 in: Rare Element Geochemistry and Mineral Deposits (Linnen, R.L. and Samson, I.M. editors). Geological Association of Canada Short Course Notes (17), St. John's N.L. Geological Association of Canada.

Linnen, R.L., Samson, I.M., Williams-Jones, A.E. and Chakhmouradian, A.R. (2013) Geochemistry of the rare-earth element, Nb, Ta, Hf, and Zr deposits. Pp 543-569 in: Treatise on Geochemistry: Second Edition, Elsevier.

Liu, H. Rare Earths: Shades of Grey. Can China Continue to Fuel Our Global Clean and Smart Future. Available online: http://chinawaterrisk.org/wp-content/uploads/2016/07/CWR-Rare-Earths-Shades-Of- Grey-2016-ENG.pdf (accessed on 9 July 2017).

Loges, A., Migdisov, A.A., Wagner, T., Williams-Jones, A.E. and Markl, G. (2013) An experimental study of the aqueous solubility and speciation of Y (III) fluoride at temperatures up to 250 C. *Geochimica et Cosmochimica Acta,* **123**, 403-415.

Lottermoser, B.G. (1992) Rare earth elements and hydrothermal ore formation processes *Ore Geology Reviews,* **7**, 25-41.

Luo Y.R. and Byrne R.H. (2001) Yttrium and rare earth element complexation by chloride ions at 25ºC. *Journal of Solution Chemistry*, **30**, 837-845.

Maji, S.K., Pal, A., Pal, T. and Adak, A. (2007) Adsorption thermodynamics of arsenic on laterite soil. *Journal of Surface Science and Technology*, **23** (3/4), 161-178.

Marks, M., and Markl, G. (2017) A global review on agpaitic rocks. *Earth-Science Reviews*, **173**, 229-258.

Mariano, A.N., and Mariano, A. (2012) Rare earth mining and exploration in North America. *Elements,* **8**(5), 369-376.

Marien, C., Dijkstra, A.H. and Wilkins, C. (2017) The hydrothermal alteration of carbonatite in the Fen Complex, Norway: mineralogy, geochemistry, and implications for rare earth element resource formation. Mineralogical Magazine, **82**, S115-S131.

Marks, M.A.W., Hettmann, K., Schilling, J., Frost, B.R. and Markl, G. (2011) The mineralogical diversity of alkaline igneous rocks: Critical factors for the transition from miaskitic to agpaitic phase assemblages. *Journal of Petrology*, **52**(3), 439-455.

McDonough, W.F. and Sun, S. (1995) The composition of the earth. *Chemical Geology*, **120**, 223-253.

Meunier, A. (2005) Clays. Springer, Berlin.

Migdisov, A., Williams-Jones, A.E., Brugger, J. and Caporuscio, F.A. (2016) Hydrothermal transport, deposition, and fractionation of the REE: Experimental data and thermodynamic calculations. *Chemical Geology,* **439**, 13-42.

Migdisov, A.A., Reukov, V. and Williams-Jones, A.E. (2006) A spectrophotometric study of neodymium (III) complexation in sulfate solutions at elevated temperatures. *Geochimica et Cosmochimica Acta*, **70**, 983-992.

Migdisov, A.A. and Williams-Jones, A.E. (2007) An experimental study of the solubility and speciation of neodymium (III) fluoride in F-bearing aqueous solutions. *Geochimica et Cosmochimica Acta,* **71,** 3056-3069.

Migdisov, A.A. and Williams-Jones, A.E. (2008) A spectrophotometric study of Nd(III), Sm(III) and Er(III) complexation in sulfate-bearing solutions at elevated temperatures. *Geochimica et Cosmochimica Acta,* **72**, 5291-5303.

Migdisov, A.A. and Williams-Jones, A.E. (2002) A spectrophotometric study of neodymium (III) complexation in chloride solutions. Geochimica et Cosmochimica Acta, **66**, 4311-4323.

Migdisov, A.A. and Williams-Jones, A.E. (2006) A spectrophotometric study of erbium (III) speciation in chloride solutions at elevated temperatures. *Chemical Geology,* **234**, 17-27.

Migdisov, A.A. and Williams-Jones, A.E. 2014. Hydrothermal transport and deposition of the rare earth elements by fluorine-bearing aqueous liquids. *Mineralium Deposita*. **49**, 987-997.

Migdisov, A.A., Williams-Jones, A.E. and Wagner, T. (2009) An experimental study of the solubility and speciation of the Rare Earth Elements (III) in fluoride- and chloride-bearing aqueous solutions at temperatures up to 300 °C. *Geochimica et Cosmochimica Acta*, **73**, 7088-7109.

Mitchell, R.G. (2005) Carbonatites and carbonatites and carbonatites. *The Canadian Mineralogist,* **43**, 2049-2068.

Mitchell, R. H. (2009) Peralkaline nephelinite-natrocarbonatite immiscibility and carbonatite assimilation at Oldoinyo Lengai, Tanzania. *Contributions to Mineralogy and Petrology*, **158**(5), 589-598.

Moldoveanu, G. and Papangelakis, V. (2016) An overview of rare-earth recovery by ion-exchange leaching from ion-adsorption clays of various origins. *Mineralogical Magazine*, **80**(1), 63-76.

Moore, M. Chakhmouradian, A.R., Mariano, A.N. and Sidhu, R. (2015) Evolution of rare-earth mineralization in the Bear Lodge carbonatite, Wyoming: Mineralogical and isotopic evidence. *Ore Geology Reviews*, **64**, 499-521.

Mundsen, H.E.F. 1987. Evidence of liquid immiscibility in the upper mantle. *Nature,* **327**, 692-695.

Orris, G. J. and Grauch, R. I. (2002) Rare Earth Element Mines, Deposits, and Occurrences. U.S. GEOLOGICAL SURVEY open-file report 02-189.

Oreskes, N. and Einaudi, M.T. (1990) Origin of Rare Earth Element-Enriched Hematite Breccias at the Olympic Dam Cu-U-Au-Ag Deposit, Roxby Downs, South Australia. *Economic Geology*, **85**, 1-28.

Paulick, H. and Machacek, E. (2017) The global rare earth element exploration boom: An analysis of resources outside of China and discussion of development perspectives. Resources Policy, **52**, 134-

153.

Pearson, R.G. (1963) Hard and soft acids and bases. *Journal of the American Chemical Society,* **85**, 3533-3539.

Platt, R.G. (1996) The ijolite-series rocks. Pp. 101-122 in: Undersaturated alkaline rocks: mineralogy, petrogenesis, and economic potential (Mitchell, R.H. Editor). Mineralogical Association of Canada Short Course Series. Mineralogical Association of Canada.

Rocha, A., Schissel, D., Sprecher, A., de Tarso, P. and Goode, J. (2013) Process development for the Serra Verde weathered crust elution-deposited rare earth deposit in Brazil. Proceedings of the 52rd Conference of Metallurgists.

Richter, L., Diamond, L.W., Atanasova, P., Banks, D.A. and Gutzmer, J. 2018. Hydrothermal formation of heavy rare earth element (HREE)– xenotime deposits at 100°C in a sedimentary basin. *Geology*, **46**(3), 263-266.

Roskill, R. (2016). Rare earths: Global industry, markets and out- look (16th edition), London.

Rudnick, R., and Gao, S. (2003) Composition of the continental crust. Pp. 1-64 in: *Treatise on Geochemistry* (Holland, H.D., Turekian, K.K. Editors). Elsevier-Pergamon, Oxford.

Samson, I.M., and Wood, S.A. (2004) The rare earth elements: behaviour in hydrothermal fluids and concentration in hydrothermal mineral deposits, exclusive of alkaline settings. Pp 269-298 in: *Rare-element geochemistry and mineral deposits* (Linnen, R.l. and Samson, I.M Editor). Geological Association of Canada Short Course Notes Volume 17. Geological Association Of Canada.

Sanematsu, K. and Watanabe, Y. (2016) Characteristics and genesis of ion adsorption-type rare earth element deposits. Pp 55-79 in: *Rare earth and critical elements in ore deposits* (Verplanck, P. and M. Hitzman Editors).

Santos, R.V. and Clayton, R.N. (1995) Variations ofoxygen and carbon isotopes in carbonatites: a study of Brazilian alkaline complexes. *Geochimica Cosmochimica Acta,* **59**, 1339-1352.

Shannon, R.D. (1976) Revised effective ionic radii and systematic studies of interatomic distances in halides and chalcogenides. *Acta Crystallographica*, **A32**, 751-767.

Sheard E. R. et al. (2012) Controls on the concentration of zirconium, niobium and the rare earth elements in the Thor Lake rare metal deposit, Northwest Territories, Canada. *Economical Geology*, **107**, 81-104.

Shu, X. and Liu, Y. (2019) Fluid inclusion constraints on the hydrothermal evolution of the Dalucao Carbonatite-related REE deposit, Sichuan Province, China. Ore Geology Reviews, **107**, 41-57.

Simandl, G.J. and Paradis, S. (2018) Carbonatites: related ore deposits, resources, footprint, and exploration methods. *Applied Earth Science,* **127**(4), 123-152.

Sjöqvist, A., Cornell, D., Andersen, T., Erambert, M., Ek, M., Leijd, M. (2013) Three Compositional Varieties of Rare-Earth Element Ore: Eudialyte-Group Minerals from the Norra Kärr Alkaline Complex, Southern Sweden. *Minerals*, **3**(1), 94-120.

Smith M.P. and Henderson, P. (2000) Preliminary fluid inclusion constraints on fluid evolution in the Bayan Obo FeREE-Nb deposit, Inner Mongolia, China. *Economic Geology,* **95**(7), 1371-1388.

Smith, M. P., Campbell, L. S. and Kynicky, J. (2015) A review of the genesis of the world class Bayan Obo Fe-REE-Nb deposits, Inner Mongolia, China: Multistage processes and outstanding questions. *Ore Geology Reviews,* **71***, 1-12.*

Smithsonian Institution. 2019. National Museum of Natural History Global Volcanism Program [Online]. [Accessed 21 October 2019]. Available from: https://volcano.si.edu/volcano.cfm?vn=222120

Song, W.L. Xu, C., Veksler, I.V. and Kynicky, J. (2016) Experimental study of REE, Ba, Sr, Mo and W partitioning between carbonatitic melt and aqueous fluid with implications for rare metal mineralization. *Contributions to Mineralogy and Petrology,* **171,** 1-22.

Streckeisen, A.L. (1978) IUGS Subcommission on the Systematics of Igneous Rocks. Classification and Nomenclature of Volcanic Rocks, Lamprophyres, Carbonatites and Melilite Rocks. Recommendations and Suggestions. *Neues Jahrbuch für Mineralogie*, **141**, 1-14.

Taylor, H.P., Frechen, J. and Degens, E.T. (1967) Oxygen and carbon isotope studies of carbonatites from the Laacher See district, West Germany and the Alnö district, Sweden. *Geochimica Cosmochimica Acta,* **31,** 407-430.

Thompson, T.B., Pierson, J.R., and Lyttle, T. (1982) Petrology and petrogenesis of the Bokan granite complex, southeastern Alaska. *Geological Society of America Bulletin*, **93**, 898-908.

Trofanenko, J., Williams-Jones, A.E., Simandl, G.J., Migdisov, A.A. (2016) The nature and origin of the REE mineralization in the Wicheeda Carbonatite, British Columbia, Canada. *Economic Geology*, **111**, 199-223.

Sweeney, R.J. (1994) Carbonatite melt compositions in the Earth's mantle. *Earth Planetary Science Letter*, **128**(3-4), 259-270.

U.S Geological Survey (2010) A Deposit Model for Carbonatite and Peralkaline Intrusion-Related Rare Earth Element Deposits. Scientific Investigations Report 2010–5070–J.

U.S. Geological Survey (2019) *Mineral Commodity Summaries 2019, U.S. Geological Survey*.

Veksler, I.V., Dorfman, A.M., Dulski, P., Kamenetsky, V.S., Danyushevsky, L.V., Jeffries, T. and Dingwell, D. (2012) Partitioning of elements between silicate melt and immiscible fluoride, chloride, carbonate, phosphate and sulfate melts, with implications to the origin of natrocarbonatite. *Geochimica and Cosmochimica Acta*, **79**, 20-40.

Verplanck, P.L. and Hitzman, M. (2016) Rare earth and critical elements in ore deposits. Society of Economic Geologists, Littleton, Colorado.

Verplanck, P.L., Mariano, A.N. and Mariano, A.J. (2016) Rare earth element ore geology of carbonatites. Pp. 5-32 in: *Rare earth and critical elements in ore deposits* (Hitzman, M. Editor). Society of Economic Geologists, Littleton, Colorado.

Verplanck, P. L. (2017) The Role of Fluids in the Formation of Rare Earth Element Deposits. *Procedia Earth and Planetary Science*, **17**(39), 758-761.

Wall, F., Niku-Paavola, V.N., Storey, C.M. and Axel, J.T. (2008) Xenotime-(Y) from carbonatite dykes at Lofdal, Namibia: Unusually low LREE:HREE ratio in carbonatite, and the first dating of xenotime overgrowths on zircon. *Canadian Mineralogist,* **46**, 861-877.

Wall, F (2014) Rare Earth Elements. Pp. 312-340 in: Critical Metals Handbook (Gunn, A. editor). Wiley, New York, USA.

Wallace, M.E. and Green, D.H. 1988. An experimental determination of primary carbonatite magma composition. *Nature,* **335**, 343-346.

Wang, D., Zhao, Z., Yu, Y., Dai, J. and Liu, L. (2018) Exploration and research progress on ion-adsorption type REE deposit in South China. *China Geolog*y, **1**(3), 414-423.

Wang, C., Liu, J., Zhang, H., Zhang, X., Zhang, D., Xi, Z. and Wang, Z. (2019) Geochronology and mineralogy of the Weishan carbonatite in Shandong province, eastern China. *Geoscience Frontier*s, **10**(2), 769-785.

Weng, Z., Jowitt, S., Mudd, G.and Haque, N. 2013. Assessing rare earth element mineral deposit types and links to environmental impacts. *Applied Earth Science*, **122**, 83-96.

Williams-Jones, A.E., Samson, I.M. and Olivo, G.R. (2000) The genesis of hydrothermal fluorite-REE deposits in the Gallinas Mountains, New Mexico. *Economic Geology*, **95**, 327-341.

Williams-Jones, A.E., Migdisov, A.A. and Samson, I M. (2012) Hydrothermal mobilisation of the rare earth elements-a tale of "ceria" and "yttria". *Elements*, **8**, 355-360.

Winter, J.D. (2001) An introduction to igneous and metamorphic petrology. Prentice Hall, New jersey.

Wood, S.A. (1990) The aqueous geochemistry of the rare earth elements and yttrium 2. Theoretical predictions of speciation in hydrothermal solutions to 350 °C at saturation water vapour pressure. Chemistry Geology, **88**, 99-125.

Woolley, A.R. and Kempe, D.R.C. (1989) Carbonatites: nomenclature, average chemical composition. Pp. 1-14 in: *Carbonatites: Genesis and evolution* (Bell, K. editor). Unwin Hyman, London.

Woolley, A.R. and Church, A. A. (2005) Extrusive carbonatites: A brief review. *Lithos*, **85**, 1-14

Woolley, A.R. and Kjarsgaard, B.A. (2008) Paragenetic types of carbonatite as indicated by the diversity and relative abundances of assoicated silicate rocks: evidence froma global database. *The Canadian Mineralogist*, **46**, 741-752.

Woolley, A.R. and Bailey, D.K. (2012) The crucial role of lithospheric structure in the generation and release of carbonatites: geological evidence. *Mineralogy Magazine.* **76**, 259-270.

Wyllie, P.J. (1995) Experimental petrology of upper-mantle materials, process and products. *Journal Geodynamique*. **20**(4), 429-468.

Xu, C., Campbell, I.H, Allen, C.M, Huang, Z., Qi, L., Zhang, H. and Zhang, G. (2007) Flat rare earth elements patterns as an indicator of cumulate processes in the Lesser Qinling carbonatites, China. *Lithos*, **95**, 267-278.

Xu, C., Campbell, I.H., Kynicky, J, Allen, C.M., Chen, Y., Huang, Z. and Qi, L. (2008) Comparison of the Daluxiang and Maoniuping carbonatitic REE deposits with Bayan Obo REE deposit, China. *Lithos*, **106**, 12-24.

Xu, C. Wang, L., Song, W. and Wu, M. (2010a) Carbonatites in China: A review for genesis and mineralization. *Geoscience Frontiers*, **1**(1), 105-114.

Xu, C., Kynicky, K, Chakhmouradian, A.R., Qi, L and Song, W. (2010b) A unique Mo deposit associated with carbonatites in the Qinling orogenic belt, central China. *Lithos*, **118**, 50-60.

Yang, X.J., Lin, A., Li, X-L., Wu, Y., Zhou, W. and Chen, Z. (2013) China's ion-adsorption rare earth resources, mining consequences and preservation. *Environmental Development*, **8,** 131-136 .

Yaxley, G.M. and Brey, G.P. (2004) Phase relations of carbonate-bearing eclogite assemblages from 2.5 to 5.5 GPa: implications for petrogenesis of carbonatites. *Contribution to Mineralogy and Petrology*, **146**(5), 606-619.

Ying, J. et al. (2004) Geochemical and isotopic investigation of the Laiwu–Zibo carbonatites from western Shandong Province, China, and implications for their petrogenesis and enriched mantle source. *Lithos*, **75**(3-4), 413-426.

Zaitsev, A.N., Wall, F and Chakhmouradian, A.R. (2014) Rare-earth elements minerals in carbonatites of the Kola alkaline province (Northern Fennoscandia). Abstract, 1st European Rare Earth Resources Conference. Milos.

Zharikov, V.A., Pertsev, N.N., Rusinov, V.L., Callegari, E., Fettes, D.J. (2007) Metasomatism and metasomatic rocks. In: *Recommendations by the IUGS Subcommision of the Systematics of Metamorphic Rocks*. British Geological Survey.

Zheng, X. and Liu, Y. (2019) Mechanisms of element precipitation in carbonatite-related rare-earth element deposits: Evidence from fluid inclusions in the Maoniuping deposit, Sichuan Province, southwestern China. Ore Geology Reviews, 107, 218-238.

CHAPTER 3.

LREE redistribution during hydrothermal alteration at the Okorusu carbonatite complex, Namibia

Cangelosi, D.A., Broom-Fendley, S., Banks, D.A., Morgan, D.J. and Yardley, B.W.D. (2019) LREE redistribution during hydrothermal alteration at the Okorusu carbonatite complex, Namibia. *Mineralogical Magazine*, (n.d.) 1-54.

3.1. Abstract

The Cretaceous Okorusu carbonatite, Namibia, includes diopside-bearing and pegmatitic calcite carbonatites, both exhibiting hydrothermally altered mineral assemblages. In unaltered carbonatite, REE, Sr and Ba are largely hosted by calcite and fluorapatite. However, in hydrothermally altered carbonatites, small (< 50 μm) parisite-(Ce) grains are the dominant REE host, while Ba and Sr are hosted in baryte, celestine, strontianite and witherite. Hydrothermal calcite has a much lower trace element content than the original, magmatic calcite. Despite the low REE contents of the hydrothermal calcite, the REE patterns are similar to those of parisite-(Ce), and magmatic minerals and mafic rocks associated with the carbonatites. These similarities suggest that hydrothermal alteration remobilised REE from magmatic minerals, predominantly calcite, without significant fractionation or addition from an external source. Ba and Sr released during alteration were mainly reprecipitated as sulfates. The breakdown of magmatic pyrite into Fe-hydroxide is inferred to be the main source of sulfate. The behaviour of sulfur suggests that the hydrothermal fluid was somewhat oxidising and it may have been part of a geothermal circulation system. Late hydrothermal massive fluorite replaced the calcite carbonatites at Okorusu and resulted in extensive chemical change, suggesting continued magmatic contributions to the fluid system.

3.2. Introduction

The rare earth elements (REE) are well known as 'critical metals' — metals which are sourced from a restricted region and have low substitutability and recyclability (Wall, 2014; European Commission, 2017; US Geological Survey, 2018). The largest and highest grade REE deposits are associated with carbonatite complexes (Chakhmouradian and Wall, 2012; Chakhmouradian and Zaitsev, 2012; Wall, 2014; Verplanck *et al.*, 2016). While this association demonstrates that magmatic processes are required for REE concentration, the REE as a group are also mobile in some hydrothermal fluids (Linnen *et al.*, 2014), and hydrothermal activity can play a major role in the development of economic concentrations of REE (e.g. Smith *et al.*, 2000, 2016).

A number of hydrothermally modified REE deposits have been recognised in a range of geological environments (e.g. Alderton *et al.*, 1980; Lewis *et al.*, 1998; Gysi and Williams-Jones, 2013). Indeed, the type-locality for several REE minerals, Bastnäs, is a skarn deposit (Holtstam *et al.*, 2007; Holtstam *et al.*, 2014). Many carbonatites show evidence of hydrothermal reworking, which may be extensive (e.g. Wall *et al.*, 2008; Moore *et al.*, 2015; Broom-Fendley *et al.*, 2017a).

Evidence for hydrothermal mobility of REE comes from both experimental and natural studies of REE deposits (Perry and Gysi, 2018). Experimental studies indicate the solubility of REE is mainly determined by temperature and ligand availability (Williams-Jones *et al*., 2012). The stability of REE aqueous complexes with most ligands decreases along the lanthanide series, with light (L)REE (La to Sm) complexes more stable than the (H)REE (Migdisov *et al.*, 2016). Complexation by sulfate is the exception, with all REE-sulfate complexes having a similar stability (Migdisov and Williams-Jones, 2008). In most geological settings, the REE are believed to be predominantly transported as Cl^- complexes, reflecting the dominance of Cl^- over other potential ligands in most natural fluids (Banks *et al.*, 1994), as well as the greater solubility of REE-chloride complexes relative to fluoride, phosphate and carbonate complexes (Williams-Jones *et al.*, 2012).

Not all carbonatites show evidence of secondary fluid reworking. The REE can be hosted in apatite, a common carbonatite magmatic mineral for which the REE have a strong affinity (e.g. Giebel *et al.,* 2017). Apatite in carbonatites commonly contains over 1 wt.% total REE

(Bühn *et al.*, 2003; Broom-Fendley *et al.*, 2016; Chakhmouradian *et al.,* 2017). REE may also be hosted in burbankite [(Na,Ca)$_3$(Sr,Ca,REE,Ba)$_3$(CO$_3$)$_5$] which commonly forms in a magmatic environment or close to the magmatic-hydrothermal transition (Zaitsev *et al.,* 1998, 2002; Moore *et al.,* 2015; Broom-Fendley *et al.,* 2017b). Wall (2014) however, noted that in carbonatite-related deposits, economic levels of REE are mainly contained in secondary minerals such as REE fluorcarbonates and monazite. The two main mechanisms which may determine the economic viability of a carbonatite deposit for the REE are thus primary enrichment at the magmatic stage, which is predominantly controlled by apatite crystallisation, and secondary hydrothermal reworking.

In this study we investigate the mineralogy of the Okorusu Carbonatite Complex, Namibia, in order to understand the mechanism and scale of hydrothermal reworking of REE in a carbonatite. Although Okorusu is not a REE-rich carbonatite, the relatively small-scale alteration where REE contents are locally upgraded, provides an opportunity to understand the key processes. We report on how the REE are mobilised and concentrated from the magmatic to the late hydrothermal stages and investigate whether the locally elevated bulk REE contents are due to secondary enrichment from an external source or redistribution from nearby parts of the complex.

3.3. The Okorusu Carbonatite Complex

The Okorusu carbonatite complex is part of the Cretaceous Damaraland Igneous Province (~137 to 124 Ma), which is thought to be related to the Tristan da Cunha hot spot and the opening of the South Atlantic (Milner *et al.,* 1995). Okorusu has been dated to 126.6 ± 7.3 Ma (Milner *et al.,* 1995). The province comprises several intrusions of alkaline rocks and carbonatites trending northeast from the Cape Cross complex at the Atlantic coast (Fig. 3-1). Okorusu is the most north-easterly of this chain of intrusions and is located about 45 km NNE of the town of Otjiwarongo.
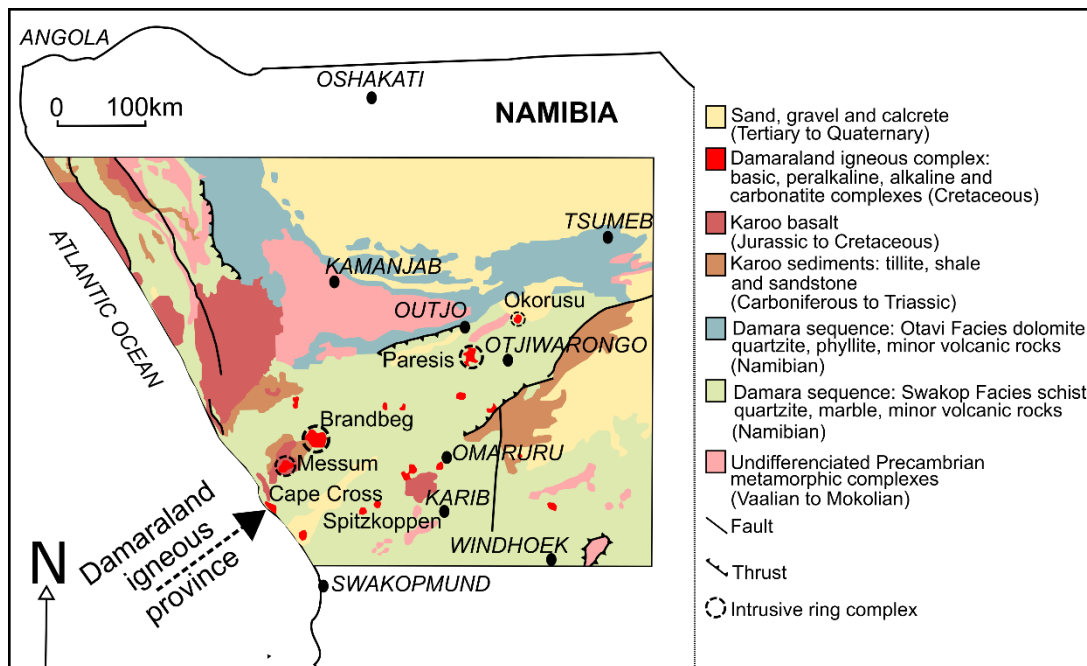
Figure 3-1: Simplified geological map of Namibia showing the Damaraland igneous province trending North-East (after the geological map of Namibia, from Schreiber et al., 1977).

The detailed geological mapping by Van Zijl (1962) shows that it comprises a ring complex approximately 5 km by 6 km, consisting of syenite, nepheline syenite and carbonatite with an associated fenite aureole and hydrothermal fluorite mineralisation (Fig. 3-2). The country rocks adjacent to the complex are intruded by mafic dykes (Table 3-1), which are themselves intruded by calcite carbonatite. The mafic dykes may be an early phase of the intruding igneous suite. The main carbonatite bodies are medium-grained (0.25 mm to 2 mm) calcite carbonatites with white/grey calcite and accessory apatite and feldspar (Van Zijl, 1962; Bühn *et al.,* 2002). Shivdasan (2002) described two additional types of carbonatite: clinopyroxene carbonatite (diopside-bearing calcite carbonatite in this study), which has a silica content ranging from 9 wt.% to 12 wt.% and on average contains ~15% volume pyroxene, and subordinate pegmatite carbonatite (pegmatitic calcite carbonatite in this study), characterised by a very coarse grain size (from 2 cm to > 20 cm), occurring as local pods or segregations within the diopside-bearing carbonatite.

The country rocks around the complex are regionally-metamorphosed sediments of the Pan-African Damara system, comprising schist, marble, conglomerate, and quartzite. Greywacke close to the carbonatites is locally fenitised to an alkali clinopyroxene-rich rock referred to as alkaline pyroxenite by Van Zijl (1962). The fenites themselves were subsequently altered by later hydrothermal activity, evidenced by fractures containing hydrothermal minerals

including fluorite, alkali feldspar, magnetite, pyrite, apatite, quartz and calcite (Van Zijl, 1962).

For two decades, Okorusu was mined to extract fluorite for the production of HF; currently the mine is in care and maintenance. Fluorite mineralisation occurs in the high-grade fenite aureole in contact with Damara marbles, in calc-silicate lithologies, and in schists (Bühn *et al.,* 2002). Fluorite ore typically forms massive replacement textures. Other hydrothermal events occurred prior to fluorite deposition: magnetite and pyrrhotite hosted in the diopside-bearing carbonatite are hydrothermally altered with marcasite or hematite replacing pyrite and later magnetite (Shivdasan, 2002). Hydrothermal alteration of the calcite carbonatite led to the introduction of euhedral quartz veins and growth of secondary minerals including synchysite [$CaLREE(CO_3)_2F$], baryte and fluorite (Shivdasan, 2002).

This study is based on detailed examination of two diopside-bearing calcite carbonatite pods (e.g. Fig. 3-3A), a pegmatitic calcite carbonatite pod about 11 m wide and 4 m high (Fig. 3-3B), a mafic dyke (sample OKC4) and a fluorite body (Fig. 3-2). Cerium is the dominant lanthanide in all the REE minerals identified at Okorusu; hence, the suffix–(Ce) will be omitted from mineral names for simplicity.

Sample number	Coordinate	Rock type	Igneous mineralogy	Hydrothermal mineralogy
OKC4	20°2'33"S 16°44'22"E	Mafic dyke with chilled margin	Ca-Mg bearing aluminium silicate (5%), diopside (5%), magnesiochromite (<5%), fosterite (<5%)	Actinolite, phlogopite, sodalite, magnetite, pyrite. Total = 80%
OKC4'	20°2'33"S 16°44'22"E	Calcite carbonatite replacing the mafic dyke	Calcite (60%), apatite (<5%)	Calcite, witherite, strontianite, REE-carbonate. Total = 35%
OKA5	20°2'57"S 16°44'39"E	Diopside-bearing calcite carbonatite pod	Calcite (40%), diopside (30%), apatite (15%), phlogopite (5%), pyrite (5%)	Calcite, iron oxide. Total = 5%
OKA1	20°2'57"S 16°44'39"E	Diopside-bearing calcite carbonatite pod	Calcite (25%), diopside (20%), apatite (15%), Ti-bearing magnetite (5%)	Calcite, dolomite, quartz, iron hydroxide, K-feldspar, strontianite, baryte, parisite, witherite, pyrite, REE-carbonate, REE-fluorcarbonate. Total = 35%
OKC17, OKC18, OKC19-1	20°2'34"S 16°44'26"E	Pegmatitic calcite carbonatite pod	Calcite (45%), apatite (<10%), Ti-bearing magnetite (<5%), Nb-bearing mineral (<5%)	Calcite, iron hydroxide, dolomite, pyrite, quartz, K-feldspar, celestine, baryte, strontianite, parisite, REE-carbonate, fluorite. Total = 45% – 65%
OKC19-2	20°2'34"S 16°44'26"E	Intensely hydrothermally altered calcite carbonatite margin	Apatite (<5%)	Calcite (50%), quartz, dolomite, iron hydroxide, baryte, strontianite, celestine-baryte, parisite. Total > 95%
OKC3, OKC6, OKC7, OKC8, OKC10	20°2'31"S 16°44'24"E	Fluorite-rich rock		Fluorite (>60%), calcite, quartz, K-feldspar, dolomite, baryte, parisite. Total = 100%

Table 3-1: Summary of the mineralogy of the samples studied (see Figs 3-2 and 3-3 for locations). The minerals are listed by order of abundance (only the most abundant hydrothermal minerals are listed here). Note that the estimate percentage of the igneous minerals refers to the entire calcite carbonatite rock including the hydrothermal minerals.
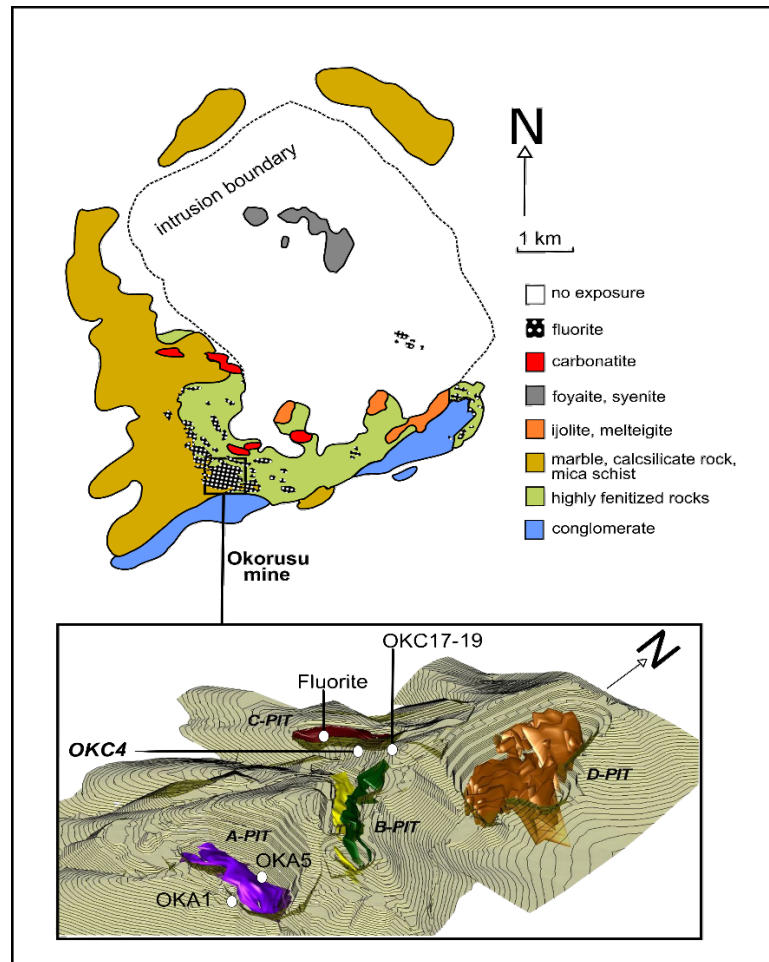
Figure 3-2: Simplified geology of the Okorusu carbonatite complex (after Van Zijl, 1962) with a 3D model of the Okorusu fluorite mine and the locations of samples used in this study (the fluorite ore bodies are represented in different colours only to differentiate fluorite in different pits) (Okorusu Fluorspar, 2014, personal communication).

3.4. Methodology

Samples were collected from the Okorusu Fluorite Mine in October 2015. The mine comprises several pits (outlined in Fig. 3-2), which display differences in fluorite grade, grain size, colour and mineral associations. For the purposes of this study, which focusses on hydrothermal alteration in the carbonatites, these differences in the nature of the fluorite ore are of secondary importance. Samples collected from Pits A and C are labelled as OKA and OKC respectively (Fig. 3-3).

Mineral paragenetic relationships were established using optical petrography of thin sections and corresponding doubly polished wafers together with scanning electron microscopy (SEM), back scattered electron (BSE) and SEM-Cathodoluminescence (SEM-CL) imaging carried out at the University of Leeds using a FEI Quanta 650 Field Emission Gun Scanning Electron Microscope operated at 20 kV.

Mineral compositions were determined with a JEOL JXA8230 Electron Microprobe (EPMA) at the University of Leeds. Beam conditions were: 15 μm spot, 15 kV, 3 nA (calcite); 10 μm, 15 kV, 8 nA (apatite and fluorite); and 1 μm, 20 kV, 30 nA (diopside). The standards and element lists used for the different minerals are summarised in Appendix 1 alongside the detection limit and on-peak and off-peak counting times for each element. Slight fluctuations in detection limits reflect the individual background measurement for each analysis. The selection of standards was aimed to match the structure of the unknown as closely as possible, using available material. Data reduction was made with the Phi-Rho-Z Armstrong matrix correction (Packwood and Brown, 1981).

Complementary trace element data for minerals were obtained by Laser Ablation Inductively Coupled Plasma Mass Spectrometry (LA-ICP-MS) using a 193 nm ArF Excimer laser coupled to an Agilent 7500c ICP-MS instrument at the University of Leeds. Analyses were performed using a spot size from 25 to 51 μm, a 10 J·cm^{-2} laser fluence and a repetition rate of 5 Hz. The analyses were run in reaction cell mode using 2.5 ml·min^{-1} H$_2$ to supress ^{40}Ar$^+$ and ^{40}Ar^{16}O$^+$ interferences on ^{40}Ca$^+$ and ^{56}Fe$^+$ and improve the measurement of ^{39}K by removing the small interferences from ^{39}Ar. The following isotopes were analysed: ^{23}Na, ^{24}Mg, ^{29}Si, ^{39}K, ^{40}Ca, ^{47}Ti, ^{55}Mn, ^{56}Fe, ^{88}Sr, ^{89}Y, ^{238}Th, ^{232}U ^{137}Ba, ^{139}La, ^{140}Ce, ^{141}Pr, ^{146}Nd, ^{147}Sm, ^{153}Eu, ^{157}Gd, ^{159}Tb, ^{163}Dy, ^{165}Ho, ^{166}Er, ^{169}Tm, ^{172}Yb, ^{175}Lu. The element lists used per run alongside the limit of detection for each element are summarised in Appendix 1. The instrument was calibrated using NIST610 and NIST612 silicate glass standards, and these were ablated 6 times each at the beginning and end of each analysis session to monitor instrument drift, which was found to be insignificant. Because the LA-ICP-MS yields wt/wt ratios, the value of Ca (for carbonates, apatite and fluorite) or Si (for silicate minerals) was determined by EPMA in order to quantify the other elements analysed by LA-ICP-MS. Where this was not possible at a particular spot, the median concentrations of Ca or Si determined in nearby areas were used. For parisite [Ca(LREE)$_2$(CO$_3$)$_3$F$_2$], the stoichiometric Ca content was used to normalise analyses, since it was not analysed by EPMA. The ablation locations in each sample were the same as the locations of previous EPMA analyses.

Bulk rock analyses were undertaken by Activation Laboratories Ltd. with the sample preparation undertaken at the University of Leeds. Samples were powdered using a steel pestle and mortar and an agate TEMA barrel, and sieved to < 200 μm. The methods 4Litho and 4F-ISE were used on the calcite carbonatite and mafic dyke samples and the method 4Litho was used for the fluorite ore samples. The detection limits are detailed in Appendix 2.

3.5.   Field relationships and mineral paragenesis

Diopside-bearing and pegmatitic calcite carbonatites are the two main carbonatite types sampled for this study (Table 3-1). They record evidence of both magmatic crystallisation of the carbonatite magma and subsequent hydrothermal activity which led to the development of the present REE minerals. The mineralogy of the samples investigated is detailed in Table 3-1 and outlined below.

Diopside-bearing calcite carbonatites locally intrude marble country rock, and where this occurs they exhibit a magnetite aureole (Fig. 3-3A). Sample OKA5 is referred to as "least altered diopside-bearing calcite carbonatite" owing to its high percentage of magmatic minerals. "Altered, diopside-bearing calcite carbonatite" (sample OKA1; Fig. 3-3A) is a diopside-bearing calcite carbonatite which has undergone partial replacement of magmatic minerals by hydrothermal phases.

Pegmatitic calcite carbonatites occur as small pods within diopside-bearing calcite carbonatite, cementing brecciated diopside-bearing calcite carbonatite and in contact with fenite (Hagni and Shivdasan, 2001; Shivdasan, 2002), making it the last carbonatite type to form. Four samples and sub-samples are from a pegmatitic calcite carbonatite pod (Fig. 3-3B). The highly altered margins of this pod comprise ~95% of hydrothermal minerals (sample OKC19-2) and is referred to as "intensely altered calcite carbonatite" in the rest of this study (Fig. 3-3B). The degree of alteration is less intense in the interior of the pod.

Four phases of mineral growth have been identified: magmatic (stage 1), late magmatic (stage 2), hydrothermal (stage 3) and late hydrothermal fluorite mineralisation (stage 4). The textural relationships that determine the sequence of mineral growth are illustrated in Figs 3-4 and 3-5, while the mineral paragenesis is summarised in Fig. 3-6.
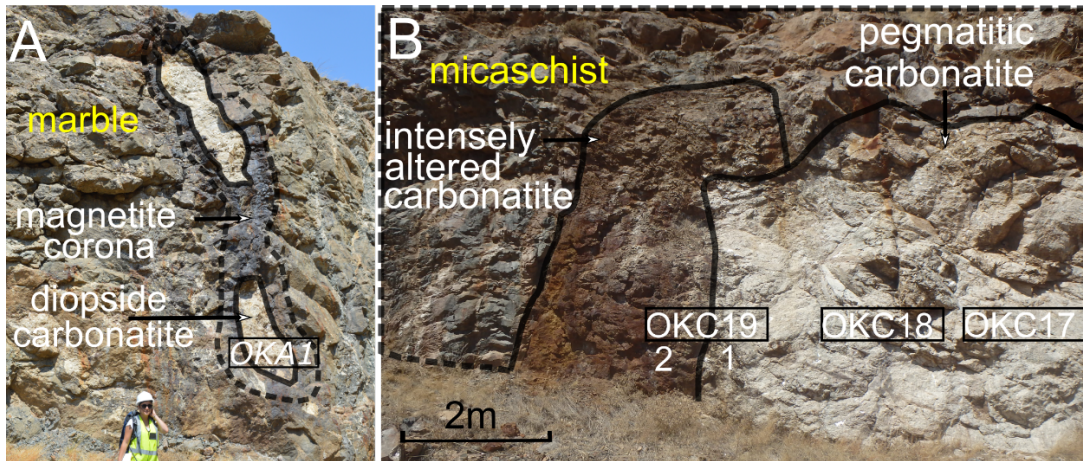
Figure 3-3: Field relationships at the sample sites. Note that 'calcite' from calcite carbonatite was omitted in the figure (A) OKA1 altered diopside-bearing calcite carbonatite occurs as two elongated pods with a magnetite aureole. (B) Pegmatitic calcite carbonatite pod with highly altered margin referred to the intensely altered calcite carbonatite (OKC19-2). Samples OKC17 was taken from the middle of the pod, sample OKC19 at the contact with the altered margin.
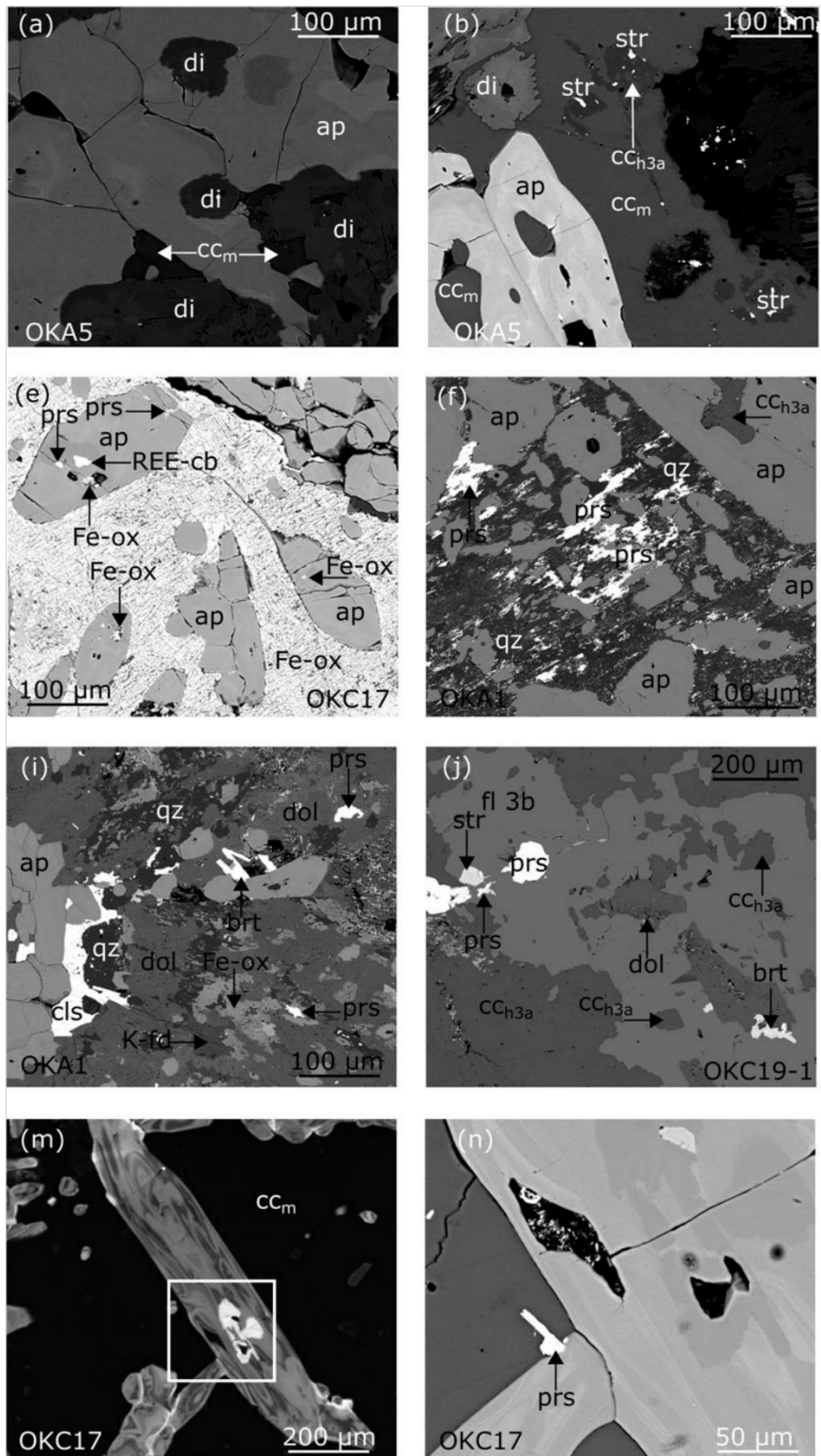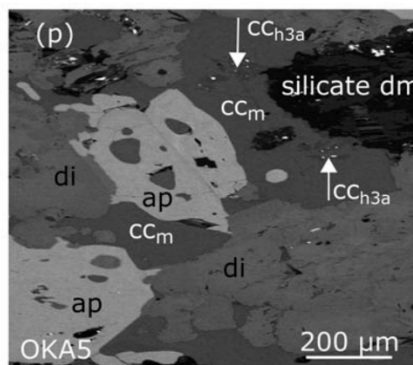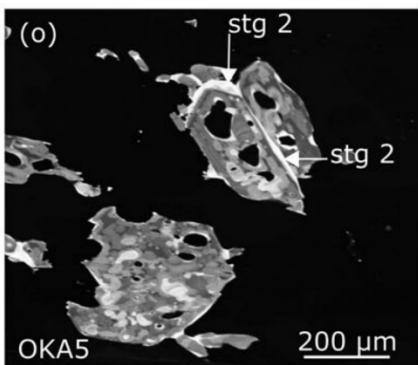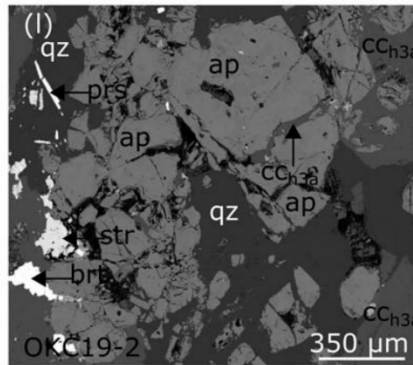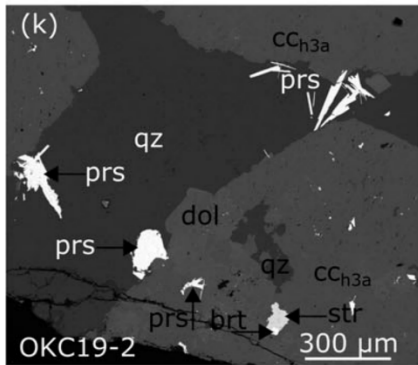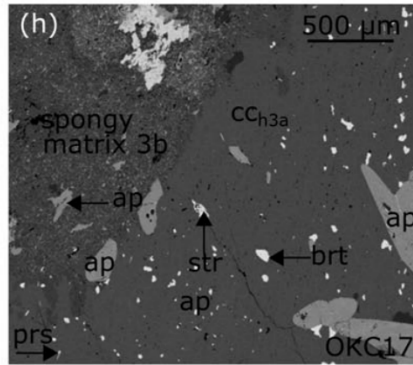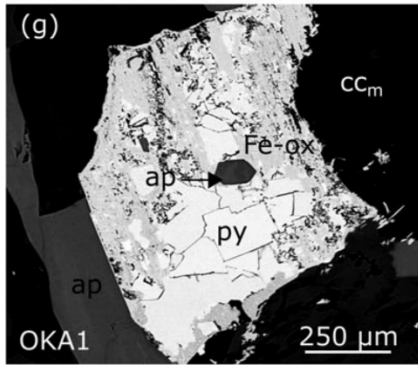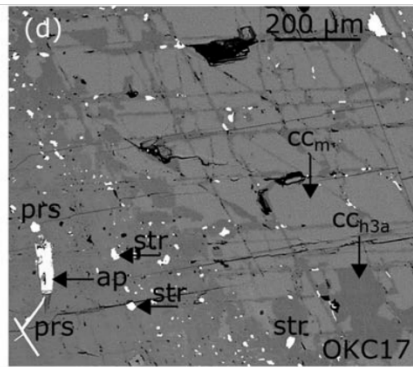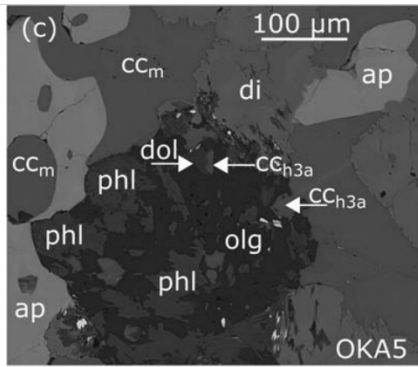
Figure 3-4: Back scattered electron (BSE) (image A to L + N + P) and cathodoluminescence (CL) (image M + O) images of magmatic and hydrothermal alteration textures of the Okorusu calcite carbonatites. (A) Sample OKA5 showing early diopside displaying irregular zoning with corroded crystal edge enclosed in later magmatic apatite; (B) Sample OKA5 with magmatic calcite forming rounded inclusions in apatite, early corroded diopside enclosed in magmatic calcite and hydrothermal calcite (dark grey-stage 3a) containing strontianite inclusions; (C) Sample OKA5 with a silicate domain of intergrown plagioclase and phlogopite; (D) Sample OKC17 showing magmatic calcite replaced along cleavage planes by hydrothermal calcite, strontianite and parisite (stage 3a); (E) Sample OKC17 with subhedral to euhedral apatite enclosed in iron hydroxide with parisite and other alteration minerals along the apatite fractures. (F) Sample OKA1 with variably replaced magmatic apatites in a quartz matrix; parisite occurs as fine grains in the matrix and as replacement of apatite; (G) Sample OKA1 with partially oxidised pyrite and euhedral apatite inclusion; (H) Sample OKC17 showing recrystallised calcite (stage 3a), strontianite and baryte inclusions, corroded by a spongy assemblage (stage 3b), magmatic apatite occurs in both hydrothermal assemblages; (I) Sample OKA1 with magmatic apatite in extensively recrystallised matrix (stage 3a) consisting of dolomite, iron hydroxide, K-feldspar, quartz, celestine, baryte and parisite; (J) Sample OKC19-1 with stage 3b fluorite partially replacing stage 3a calcite; (K) Sample OKC19-2 with coarse euhedral parisite intergrown with stage 3a quartz and calcite; (L) Sample OKC19-2 with relict of igneous apatite fractured by stage 3a calcite associated with quartz, strontianite, baryte and parisite mineralisation; (M) SEM-CL image of apatite in sample OKC17. Stage 1 apatite exhibits complex zoning in lower intensity greys while stage 2 apatite is the distinctive bright material on rims, in late cracks and in an irregular central pore-filling; (N) BSE image of the area shown in M, with a euhedral parisite embedded at the edge of the apatite, note that the stage 2 apatite corresponds here to the darkest zone, (O) SEM-CL image of apatite in sample OKA5 showing stage 2 apatite; (P) BSE image of the area shown in (O) showing that stage 1 and 2 are enclosed in magmatic calcite. Abbreviations: ccm—magmatic calcite; cch3a –hydrothermal calcite; di—diopside; ap—apatite; str—strontianite; phl—phlogopite; olg—oligoclase; dol—dolomite; prs—parisite; REE-cb—REE-carbonate; Fe-ox—unidentified Fe- hydroxide; qz—quartz; py—pyrite; brt—baryte; K-fd—K-feldspar; cls—celestine; fl—fluorite, stg 2—stage 2 apatite; silicate dm—silicate domain.
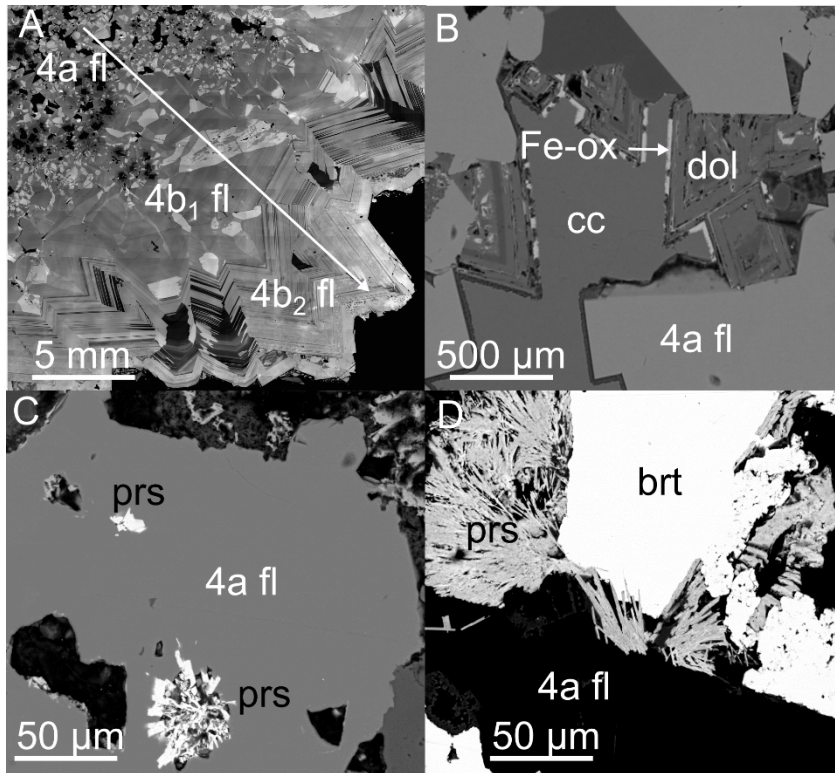
Figure 3-5: CL and BSE images illustrating stage 4 textures (sample OKC6, OKC3 and OKC8). (A) SEM-CL image showing the sequential crystallisation represented by the arrow of type 4a and type 4b fluorite (OKC6); (B) BSE image demonstrating the sequential crystallisation of type 4a fluorite, quartz, dolomite, iron hydroxide and stage 4 calcite, note that the Fe and Mg content of dolomite varies (OKC3); (C) BSE image of parisite mineralisation embedded in a cavity lining in type 4a fluorite (OKC8); (D) BSE image of radiating parisite crystals growing into baryte in type 4a fluorite (OKC8).

3.5.1. Stage 1 and 2—Magmatic to late magmatic minerals in the calcite carbonatites

The Okorusu calcite carbonatites predominantly exhibit magmatic textures typical of carbonatites (Chakhmouradian *et al.,* 2016). Magmatic calcite occurs as very large (0.5 cm to > 7 cm) twinned crystals and makes up the bulk of all carbonatite types. Magmatic calcite is distinguished from stage 3 hydrothermal calcite because it appears brighter in BSE images due to its higher level of Sr (Fig. 3-4B,D), and does not contain inclusions of baryte, strontianite or other sulfates or carbonates.

Clinopyroxenes in the diopside-bearing calcite carbonatite are diopside and occur as clusters of subhedral to euhedral crystals. Euhedral grains often display growth zoning while zoning in subhedral grains is less regular (Fig. 3-4A,B). Diopside commonly exhibits resorption along

its edges, and occurs in two forms: evenly distributed through the least altered diopside-bearing calcite carbonatite (Fig. 3-4A,B) or segregated as diopside-rich clusters in the altered diopside-bearing calcite carbonatite. Diopside inclusions with resorbed edges occur in magmatic apatite and calcite suggesting that diopside was early to crystallise from the carbonatite magma (Fig. 3-6).

Apatite is the most significant magmatic REE-bearing mineral in the Okorusu calcite carbonatites. Stage 1 and 2 apatite occurs as medium-grained subhedral crystals (Fig. 3-4A,E), locally radiating in clusters within apatite-rich zones typical of the diopside-bearing calcite carbonatite, but also as individual grains in contact with calcite (Fig. 3-4D), as inclusions in Ti-bearing magnetite (Fig. 3-4E) and Nb-bearing phases, or as vein-like clusters in the pegmatitic calcite carbonatite. The grains consistently exhibit similar textures, including complex zoning (Fig. 3-4B,M,O), with SEM-CL imaging revealing a pill-like shape typical of plutonic carbonatite (Chakhmouradian *et al.,* 2017, their fig. 5b), calcite inclusions (Fig. 3-4B,C). Magmatic apatites host inclusions of magmatic calcite and vice versa, indicating these minerals are cogenetic (Fig. 3-6).

Apatite records a complex growth history revealed by SEM-CL imaging. Some oscillatory growth zoning is present (Fig. 3-4M-O) and the apatite SEM-CL patterns indicate that dissolution was interspersed with periods of growth (Fig. 3-4M,O). Dissolution made stage 1 apatite (dull CL), porous, and the pores were then infilled with stage 2 apatite (bright CL) which truncates stage 1 zoning (Fig. 3-4M,O).

Similar textures in fluorapatite have been generated in hydrothermal experiments and have been ascribed to simultaneous dissolution–reprecipitation which creates porosity allowing enhanced transport and new growth (Harlov *et al.,* 2003; Harlov *et al.,* 2005). Harlov *et al.,* (2005) describe topotaxial replacement of REE-bearing fluorapatite by a REE-depleted fluorapatite triggered by dissolution-reprecipitation in a $HCl-H_2SO_4$ solution. Chakhmouradian *et al.,* (2017) also describe very similar dissolution–reprecipitation texture in magmatic apatite, interpreted as apatite re-equilibration with a fluid. The Okorusu stage 1 and 2 apatites similarly have uniform extinction. Stage 2 growth is a 3D process, which creates the irregular patches observed in SEM-CL imaging (Fig. 3-4M,O). SEM-CL patterns show that stage 1–stage 2 apatite relationships are consistent across the sample suites, irrespective of later alteration.

A few parisite crystals have developed on the edges of some magmatic apatites where it appears that part of the apatite was dissolved to crystallise parisite (Harlov *et al.,* 2003; Harlov *et al.,* 2005; Fig. 3-4N). Stage 2 apatite therefore has a cogenetic parisite generation.

Stage 2 apatite dissolution–reprecipitation may be driven by fluid exsolved from the crystallising carbonatite (Feng *et al.,* 2016) or might be post magmatic. While evidently formed after almost all the magmatic minerals, stage 2 apatite can occur entirely enclosed in magmatic calcite, with no post-magmatic hydrothermal calcite nearby, especially in the least altered calcite carbonatite (Fig. 3-4O,P). The lack of any later modification of adjacent magmatic calcite suggests that stage 2 apatite formed at the final magmatic stage while magmatic calcite was still stable. Both stage 1 and 2 apatites are replaced during later stage 3 hydrothermal alteration (Fig. 3-4E,L). In view of these observations, we believe that stage 2 apatite growth (and the associated parisite, Fig. 3-4N) did not form during the later stage 3 hydrothermal event.

Additional magmatic phases in the calcite carbonatites include phlogopite (which may host apatite and diopside inclusions), pyrite, which occurs as medium sized (~400 µm) subhedral crystals with apatite inclusions in sample OKA5 (< 5%, Fig. 3-4G) and Ti-bearing magnetite. A few crystals of a heavily-altered euhedral Nb-bearing mineral with oscillatory zoning were also observed in the pegmatitic calcite carbonatite. The centres of the Nb-bearing crystals are heavily altered and porous, but Nb is present throughout the grain. The least altered parts give an EDS spectrum dominated by Nb with associated peaks for Sr, Ti, Ca, Th and Fe.

The association of calcite, apatite and iron oxide is typical of carbonatites (Le Bas and Srivastava, 1989; Kapustin, 1980; Chakhmouradian *et al.,* 2016). Based on textures such as those illustrated in Fig. 3-4, we infer that the sequence of crystallisation was diopside joined by calcite, apatite and finally phlogopite (Fig. 3-6) (cf. Weidendorfer *et al.,* 2017).

Silicate domains of intergrown plagioclase (ranging from albite to oligoclase in composition) and phengite with minor phlogopite, dolomite and calcite occur in the least altered diopside-bearing calcite carbonatite (Fig. 3-4C). At the edges of the silicate domains, coarser-grained diopside and calcite tend to be intergrown with the plagioclase (Fig. 3-4C). It is likely that these silicate domains are wall rock xenoliths which have reacted with the carbonatite magma (c.f. Anenburg *et al.,* 2018a; Chebotarev *et al.,* 2019).

	magmatic	late magmatic	hydrothermal (h)		late hydrothermal (h)
	stage 1	stage 2	stage 3a	stage 3b	stage 4
diopside	—				
calcite	▆ grey CL	▆ bright CL	▆		—
apatite	▆	—			
phlogopite	—				
Ti-magnetite	—				
Nb-bearing phase	—				
pyrite	—				
strontianite			—		
witherite			—		
celestine				—	
baryte				—	—
parisite		—	▆	—	—
REE-carbonate			—		
fluorite				—	4a ▆ 4b 4c ▆▆
quartz				—	— —
dolomite			⋯⋯ spongy		—
Fe-hydroxide				—	—
K-feldspar			spongy		—
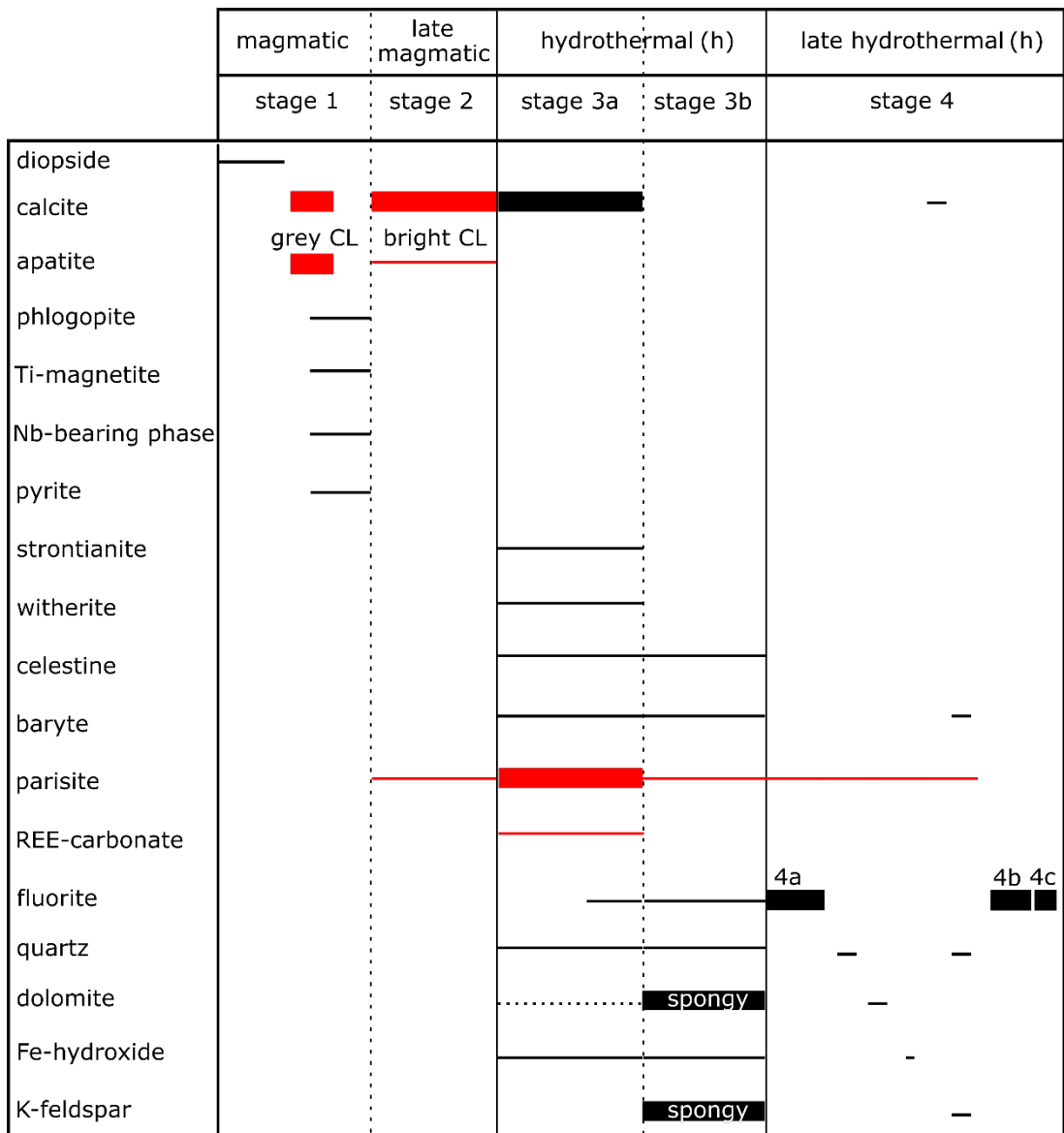
Figure 3-6: Simplified paragenetic diagram of the Okorusu carbonatite deposit illustrating the REE reworking from magmatic (associated to gangue minerals) to hydrothermal as REE minerals. Bar thickness represents mineral abundance. Red bars represent the main REE-bearing minerals in each stage. Abbreviation: late m– late magmatic.

3.5.2. Stage 3— Hydrothermal alteration

All carbonatite samples show some degree of secondary overprinting from hydrothermal fluids. In less-altered examples (e.g. OKA5, Fig. 3-4B,C), significant magmatic calcite remains, while in the most altered, OKC19-2, the magmatic calcite is fully replaced by coarse hydrothermal calcite with distinctive Ba, Sr and REE-bearing mineral inclusions (Fig. 3-4D). In detail, hydrothermal calcite is designated as stage 3a since it is, in turn, partially replaced by a spongy matrix of hydrothermal phases assigned to stage 3b (Fig. 3-4H). Apatite is also brecciated in altered areas and stage 3 calcite and quartz have crystallised in the gaps. In the most altered carbonatites, only minor magmatic apatite remains (Fig. 3-4L). Parisite is an integral part of stage 3 alteration, occurring in stage 3b spongy intergrowths as well as in stage 3a.

Hydrothermal (stage 3) calcite appears dark in BSE images compared to magmatic calcite as a result of low Sr and Ba contents (Table 3-2). In the least altered samples, stage 3 calcite is confined to secondary replacement of magmatic calcite along cleavage planes and grain margins (Fig. 3-4B,D). Where alteration is more extensive, stage 3a calcite pseudomorphs stage 1 calcite (Fig. 3-4D). In all cases, stage 3a calcite contains small inclusions (from < 40 µm to < 10 µm for the least altered samples) of strontianite, witherite, parisite, baryte, celestine and unidentified REE-fluorcarbonate and REE-carbonate (Figs 3-4B,D, 3-6). In the pegmatitic calcite carbonatite, stage 3a calcite is more abundant and the inclusions are coarser (50 µm to 300 µm) towards the contact with the intensely altered calcite carbonatite (OKC19-2) where the magmatic calcite was fully replaced by stage 3a calcite.

The stage 3a inclusion phases, such as celestine, baryte and parisite (Fig. 3-6), can also occur with iron hydroxides (Fig. 3-4E) and quartz in the rock matrix. The hydrothermal iron hydroxide may be goethite or limonite. Iron hydroxides occur infilling fractures and replacing magmatic apatite (Fig. 3-4E). In the altered diopside-bearing calcite carbonatite, medium-grained apatite is locally brecciated and infilled with stage 3 quartz and parisite (Figs 3-4F, 3-6). Apatite is the only magmatic mineral remaining in the intensely altered calcite carbonatite (OKC19-2; Fig. 3-3B); it is brecciated and in-filled by stage 3a calcite with minor baryte, strontianite, celestine and iron hydroxide (Fig. 3-4L). Apatites are locally dissolved where stage 3a parisite has crystallised (Fig. 3-4F). Despite stage 3 alteration, some apatite crystals

which were extensively altered still have unaltered regions which retain the CL pattern of stage 1 (oscillatory grey SEM-CL) and stage 2 apatite (bright SEM-CL) seen in less altered samples.

Stage 1 pyrite and Ti-bearing magnetite are partially replaced by stage 3 iron hydroxide minerals (Fig. 3-4E,G) while the Nb-bearing phases in the pegmatitic calcite carbonatites are heavily overprinted by stage 3 alteration, including growth of celestine in the rims. Minor fluorite occurs in stage 3, where it appears to be cogenetic with iron hydroxide, replacing stage 1 pyrite and partially replacing stage 3a calcite in both calcite carbonatite types (Fig. 3-4J).

Stage 3b overprints stage 3a (Fig. 3-4H), and is characterised by the development of a spongy assemblage of porous dolomite and K-feldspar, with quartz, iron hydroxide, celestine, baryte, and accessory parisite, pyrite, Ti-oxide and sphalerite. The texture of the porous dolomite and K-feldspar contrasts with stage 3a calcite which is well crystallised, but it is likely that stage 3 dolomite coexisted with calcite (Fig. 3-4I). Stage 3 REE minerals, mainly parisite and other REE-carbonates, occur as inclusions in stage 3a calcite, in cracks cutting and replacing both stage 1 and 2 apatite (Fig 4E-F), and in altered diopside.

Stage 3 alteration products are coarser grained in the more intensely altered rocks, with parisite forming euhedral crystals up to 400 μm long in OKC19-2 (Fig. 3-4K). Intensely altered calcite carbonatite has the highest content of secondary sulfate minerals, with stage 3 anhedral strontianite commonly hosting baryte inclusions.

3.5.3. Stage 4— Fluorite mineralisation.

Massive fluorite replaces country rock marble as well as carbonatite bodies at Okorusu (Hagni and Shivdasan, 2000) and is described here as stage 4 alteration, although the scale of change in rock composition is much greater than for stage 3 alteration. Optical and SEM-CL imaging indicate three main fluorite generations formed during stage 4. The earliest fluorite, type 4a, occurs as small cubes (average 0.5 mm), typically exhibiting oscillatory growth zoning. Type 4b fluorite comprises coarse euhedral crystals (≥ 1 cm) in voids; which can be divided into an earlier, unzoned stage (type 4b-1) and later (type 4b-2) material with oscillatory euhedral growth zoning (Fig. 3-5A). Type 4a and 4b fluorite often developed sequentially (Fig. 3-5A). Finally, type 4c fluorite seals healed cracks which crosscut the earlier fluorite generations.

Minor amounts of other minerals may accompany stage 4 fluorite, mainly growing between type 4a and type 4b fluorite, although these are not always present (Fig. 3-5). Type 4a fluorite is overgrown by a veneer of quartz, itself overgrown by dolomite, minor iron hydroxide and stage 4 calcite. The coexistence of quartz and dolomite requires a low temperature for this stage. This sequence of minerals was subsequently corroded and partially replaced by quartz, K-feldspar and minor baryte (Figs 3-5B, 3-6) prior to the growth of Type 4b fluorite. Bühn *et al.* (2003) divided the fluorite into types based on hand specimens and fluorite textures, whereas we have categorised them based on SEM-CL images. Type 4a fluorite from this study matches fluorite they observed in the metasomatised wallrock, while type 4b fluorite corresponds to their fluorite II. They also described feldspar and quartz with resorbed grain boundaries, but interpreted these textures as possible relicts of feldspar-bearing protoliths or as fluorite cogenetic phases observed in the metasomatised wall rock. Early fluid inclusion studies of the fluorite ore at Okorusu (Roedder, 1973), and subsequent work (Bühn *et al.,* 2002), yielded fluid salinities up to 5 wt.% NaCl equivalent and homogenisation temperatures between 120 °C to 150 °C.

While the stage 4 mineral assemblage is dominated by fluorite (Table 3-1) it contains a similar mineral suite to stage 3b, with coexisting calcite and dolomite, parisite, fluorite, baryte, quartz, iron hydroxide and K-feldspar in both stages. Stage 4 may fully replace the partially altered stage 3 calcite carbonatites (Hagni and Shivdasan, 2000). Overall, the fluorite orebody replaces calcite. If this process occurred without addition or removal of Ca, it implies a solid volume decrease of 33.5% (Glover and Sippel, 1962), which would likely result in an increase in porosity and so enhance fluid flow via a positive feedback. Some such feedback may explain the formation of the coarse euhedral stage 4b fluorite which crystallised in the voids created by the replacement process.

Rare earth mineralisation during stage 4 alteration occurs solely in association with type 4a fluorite. This contains discrete inclusions and elongate crystals of parisite embedded in cavity linings (Fig. 3-5C), crosscutting quartz and K-feldspar or associated with baryte as radiating crystals locally growing into the baryte (Fig. 3-5D).

3.6. Mineral compositions and trace element abundances

3.6.1. Stage 1 and 2 magmatic phases

3.6.1.1. Calcite

Calcite is the most abundant magmatic phase in the Okorusu carbonatite. In both the diopside-bearing and pegmatitic calcite carbonatites the $CaCO_3$ component > 95%. In detail, magmatic calcite in the least altered diopside-bearing calcite carbonatite has slightly lower Mg and Fe contents than magmatic calcite in other samples (Table 3-2). As with calcite carbonatites elsewhere (Chakhmouradian *et al.,* 2016; Chakhmouradian *et al.,* 2017), magmatic calcite has a high Sr content (usually > 2 wt% SrO; Table 3-2) with Ba as the next most abundant cation. The ∑LREE content tends to be higher in pegmatitic calcite carbonatite than diopside-bearing calcite carbonatites (respectively averaging ∑LREE= 1350 ppm and ∑LREE= 910 ppm, La and Ce are the most abundant lanthanides). Overall, ∑HREE (∑HREE= Eu–Lu) contents are low in magmatic calcite averaging < 20 ppm (Table 3-2), comparable to magmatic calcite from calcite carbonatites elsewhere (Chakhmouradian *et al.,* 2016; Table 3-2). The calcite analyses are presented in Appendix 3.

	OKC4		OKA5		OKA1				OKC17				OKC19-1		OKC19-2	
	m		m		m		stg 3a		m		stg 3a		m		stg 3a	
	n = 15		n = 19		n = 20		n= 7		n= 18		n= 10		n = 5		n = 27	
wt%																
CaO	52.98		52.32		52.34		54.45		53.97		55.77		53.44		54.15	
SrO	1.36		2.05		2.55		0.89		2.49		0.55		2.39		0.29	
BaO	0.43		0.34		0.23		n.d.		0.27		0.01		0.23		n.d.	
MnO	0.19		0.05		0.07		0.16		0.09		0.16		0.05		0.59	
FeO	0.24		0.01		0.07		0.31		0.11		0.32		0.06		0.53	
MgO	0.22		0.01		0.04		0.10		0.05		0.05		0.05		0.15	
pfu																
Ca	0.97		0.98		0.97		0.98		0.97		0.99		0.97		0.98	
Sr	0.01		0.02		0.02		0.01		0.02		0.005		0.02		0.003	
Ba	0.003		0.002		0.002		n.d.		0.002		<0.001		0.002		n.d.	
Mn	0.003		<0.001		0.001		0.00		0.001		0.002		0.001		0.01	
Fe	0.003		<0.001		0.001		0.00		0.001		0.004		0.001		0.01	
Mg	0.01		<0.001		0.001		0.00		0.001		0.001		0.001		0.004	
	avg	SD	avg	SD	avg	SD	avg	SD	avg	SD	avg	SD	avg	SD	avg	SD
ppm																
Na	152	122	n.d.	n.d.	n.d.		123	86	146	60	n.d.	n.d.	146	16	n.d.	n.d.
La	482	372	314	55	344	138	117	27	508	121	19	12	482	32	4	3
Ce	570	450	414	86	468	175	175	44	679	143	32	20	630	37	7	6
Pr	41	33	32	9	34	13	13	3	53	12	3	2	46	3	1	2
Nd	111	89	95	30	103	38	37	7	151	31	9	6	126	8	3	6
Sm	13	11	9	5	10	3	n.d.		12	3	n.d.		11	2	<1	<1
Eu	4	3	2	1	3	1	n.d.		3	1	n.d.		3	<1	<1	<1
Gd	10	8	5	5	9	4	3	<1	8	2	n.d.		8	1	1	1
Tb	1	1	n.d.		1	<1	n.d.		1	<1	n.d.		1	<1	<1	<1
Dy	7	5	n.d.		5	1	2	<1	3	1	1	1	2	<1	4	1
Ho	1	1	n.d.		1	<1	n.d.		<1	<1	<1	<1	1	<1	1	<1
Er	5	3	n.d.		2	1	n.d.		1	1	1	1	1	1	7	3
Tm	1	1	n.d.		n.d.		n.d.		n.d.		n.d.		n.d.		6	5
Yb	6	4	n.d.		n.d.		n.d.		n.d.		2	1	1	<1	19	11
Lu	n.d.		n.d.		n.d.		n.d.		n.d.		n.d.		n.d.		3	2
Y	57	18	15	7	27	5	14	7	19	2	14	12	17	1	51	26
Th	n.d.		n.d.		n.d.		n.d.		n.d.		n.d.		n.d.		n.d.	

Table 3-2: Average LA-ICP-MS analyses of magmatic and stage 3a hydrothermal calcite from the Okorusu calcite carbonatites. Note: the LA-ICP-MS data were calculated using the calcium content determined by EPMA. n.d. = not detected, analysis below LA-ICP-MS detection limit. U is below detection for all analyses. Abbreviations: m-magmatic; stg 3a-stage 3a; SD-one standard deviation.

3.6.1.2. Diopside

Diopsides are formally part of the diopside group and range into ferrian and ferro sodian diopside (Sturm, 2002). Most of the diopsides have Na_2O ranging from 0.75 wt.% to 1 wt.%, although some grain cores of ferro sodian diopside have Na_2O up to 2.25 wt.%. Diopside in the carbonatites is clearly distinct from aegerine which is typical of fenite (Zharikov *et al.,* 2007); this implies that the diopside is magmatic, as indicated by the textures. Diopside EPMA and LA-ICP-MS analyses are presented in Appendix 3. The diopside has low concentrations of REE (∑REE ranging from 11-135 ppm) with the heaviest REE lower than the limit of detection. Compared to the other minerals it shows a LREE enriched profile but the LREE pattern is flattened with Ce(cn) > La(cn), this curvature is characteristic of clinopyroxene from carbonatites (Reguir *et al.*, 2012; Fig. 3-7).

3.6.1.3. Apatite

Semi-quantitative analyses confirm that apatites are fluorapatites which are the main magmatic host for the REE at Okorusu (Fig. 3-7). Apatites from the diopside-bearing and pegmatitic calcite carbonatites are similar in composition and comparable to apatites from other carbonatites (Chakhmouradian *et al.,* 2017; Belousova *et al.,* 2002), although Sr is relatively high (1.5 to 2 wt.% SrO; Table 3-3). In contrast, apatite inclusions hosted in magmatic calcite from the calcite carbonatite replacing the mafic dyke core (OKC4, Table 3-1), are distinctly enriched in Na and the REE but are depleted in Th (Table 3-3).

The narrow textural zonations made it difficult to analyse individual apatite growth stages (Fig. 3-4M,O), especially by LA-ICP-MS, but some individual analyses of stage 1 and 2 apatite are provided in Appendix 3. Stage 2 apatite has lower concentrations of the REE relative to stage 1, especially for the LREE (Fig. 3-8), and this may reflect the crystallisation of cogenetic parisite. Since both stages of apatite have very similar normalised REE trends (Fig. 3-7) despite the differences in concentrations, exchange of REE with an external reservoir can likely be ruled out.
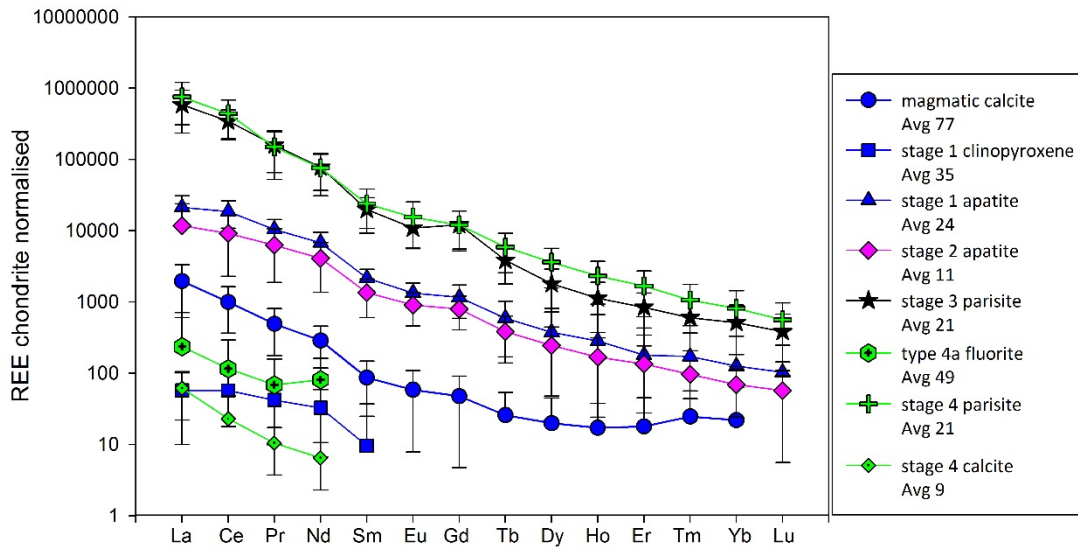
Figure 3-7: REE distribution of the REE-bearing minerals observed in magmatic stages 1 and 2 (blue, pink) and hydrothermal stages 3 and 4 (black and green). Type 3b and 4c fluorite are omitted due to their low REE content (Appendix 3). Data are chondrite normalised (McDonough and Sun, 1995). Data from EPMA and LA-ICP-MS analyses, error bars represent two standard deviations of the average value, some of the error bars are not visible due to the y-axis log scale.
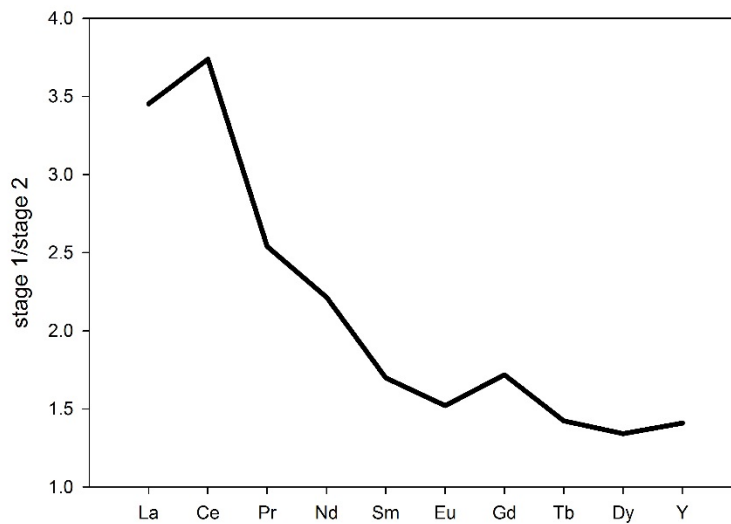
Figure 3-8: Ratio of REE concentration in stage 1 vs stage 2 apatite of sample OKC19-2, stage 1 apatite n = 12 and stage 2 apatite n = 6. Ho-Lu were omitted due to the low concentration (< 30 ppm) of these elements in both apatite types.

	OKC4 n = 4	OKA5 n = 31	OKA1 n = 29	OKC17 n= 52	OKC19-1 n = 9	OKC19-2 n = 31
wt.%						
CaO	53.20	53.75	54.30	53.75	53.13	52.98
SrO	1.84	1.56	1.48	1.89	1.73	2.01
Na2O	0.57	0.06	0.06	0.1	0.14	0.11
MgO	0.17	0.01	<0.01	<0.01	0.01	0.01
SiO2	n.d.	n.d.	n.d.	n.d.	0.26	0.36
P2O5	40.65	39.93	40.06	40.04	40.43	39.95
Cl	0.03	0.01	0.01	< 0.01	0.01	< 0.01
Cations per 25 O						
Ca	9.84	10	10.03	9.97	9.87	9.90
Sr	0.15	0.14	0.16	0.16	0.17	0.20
Na	0.13	0.02	0.02	0.03	0.05	0.04
Si	n.d.	n.d.	n.d.	n.d.	0.06	0.05
P	5.94	5.84	5.84	5.87	5.90	5.93
Average ppm*						
Mn	183 (35)	122 (34)	105 (36)	130 (33)	n.a.	n.a.
Fe	419 (57)	89 (41)	47 (17)	69 (30)	n.a.	n.a.
K	n.d.	n.d.	n.d.	n.d.	n.a.	n.a.
Ba	143 (59)	69 (11)	74 (20)	97 (30)	70 (9)	85 (60)
La	7069 (118)	4469 (1129)	4069 (1282)	4301 (870)	3522 (1173)	4223 (1973)
Ce	11473 (1599)	7778 (2302)	7123 (2419)	8291 (1676)	8955 (3834)	9987 (4328)
Pr	960 (143)	691 (196)	574 (214)	789 (172)	763 (185)	773 (256)
Nd	2962 (426)	2260 (640)	1838 (698)	2546 (579)	2425 (479)	2449 (743)
Sm	358 (54)	238 (65)	197 (77)	238 (55)	259 (28)	264 (69)
Eu	89 (19)	56 (17)	47 (20)	55 (13)	61 (6)	63 (18)
Gd	260 (41)	159 (39)	137 (59)	148 (37)	217 (32)	221 (69)
Tb	28 (4)	16 (5)	13 (6)	13 (3)	17 (3)	18 (9)
Dy	127 (29)	72 (26)	58 (26)	51 (10)	66 (14)	83 (56)
Ho	21 (5)	12 (5)	9 (4)	8 (2)	10 (2)	14 (11)
Er	45 (16)	30 (13)	23 (9)	16 (5)	22 (7)	34 (31)
Tm	5 (1)	3 (1)	2 (1)	2 (1)	3 (1)	4 (4)
Yb	15 (2)	17 (10)	14 (6)	9 (4)	10 (3)	17 (17)
Lu	n.d.	2 (1)	2 (1)	1 (<1)	1 (0)	2 (2)
Y	447 (7)	282 (116)	221 (100)	201 (46)	290 (78)	419 (380)
Th	697 (123)	3097 (1558)	1584 (817)	1322 (423)	815 (305)	995 (676)
U	n.d.	18 (18)	15 (7)	12 (10)	2 (< 2)	9 (13)

Table 3 3: Average apatite analyses for the Okorusu igneous rocks. Note: CaO, and P2O5 and Cl were determined by EPMA and Ca was used to calculate the LA-ICP-MS analyses. n.d. = not detected, analysis below LA-ICP-MS detection limit; SD-one standard deviation in brackets.

3.6.2. Stage 3: chemical changes accompanying hydrothermal alteration of calcite

3.6.2.1. Calcite

Stage 3a calcite is chemically distinct from magmatic calcite (Table 3-2). Being very pure ($CaCO_3$ component > 98%) the hydrothermal calcite is depleted in the major additional cations, Sr, Ba and in REE (Fig. 3-9; Table 3-2). Overall, Mg, Mn and Fe, while still very low, are slightly enriched compared to the magmatic calcite (Fig. 3-9A; Table 3-2) and stage 3a calcite exhibits Mn-Fe zonation observed in SEM imaging in the intensely altered calcite carbonatite. Only yttrium does not show the intense depletion of the other REE (Fig. 3-9B), and is within error of the concentrations in magmatic calcite.

Stage 3 alteration involved the growth of a suite of hydrothermal minerals, including strontianite, witherite, baryte and parisite (Fig. 3-4B,D), and these are likely to be repositories for the elements released during hydrothermal alteration of magmatic minerals.
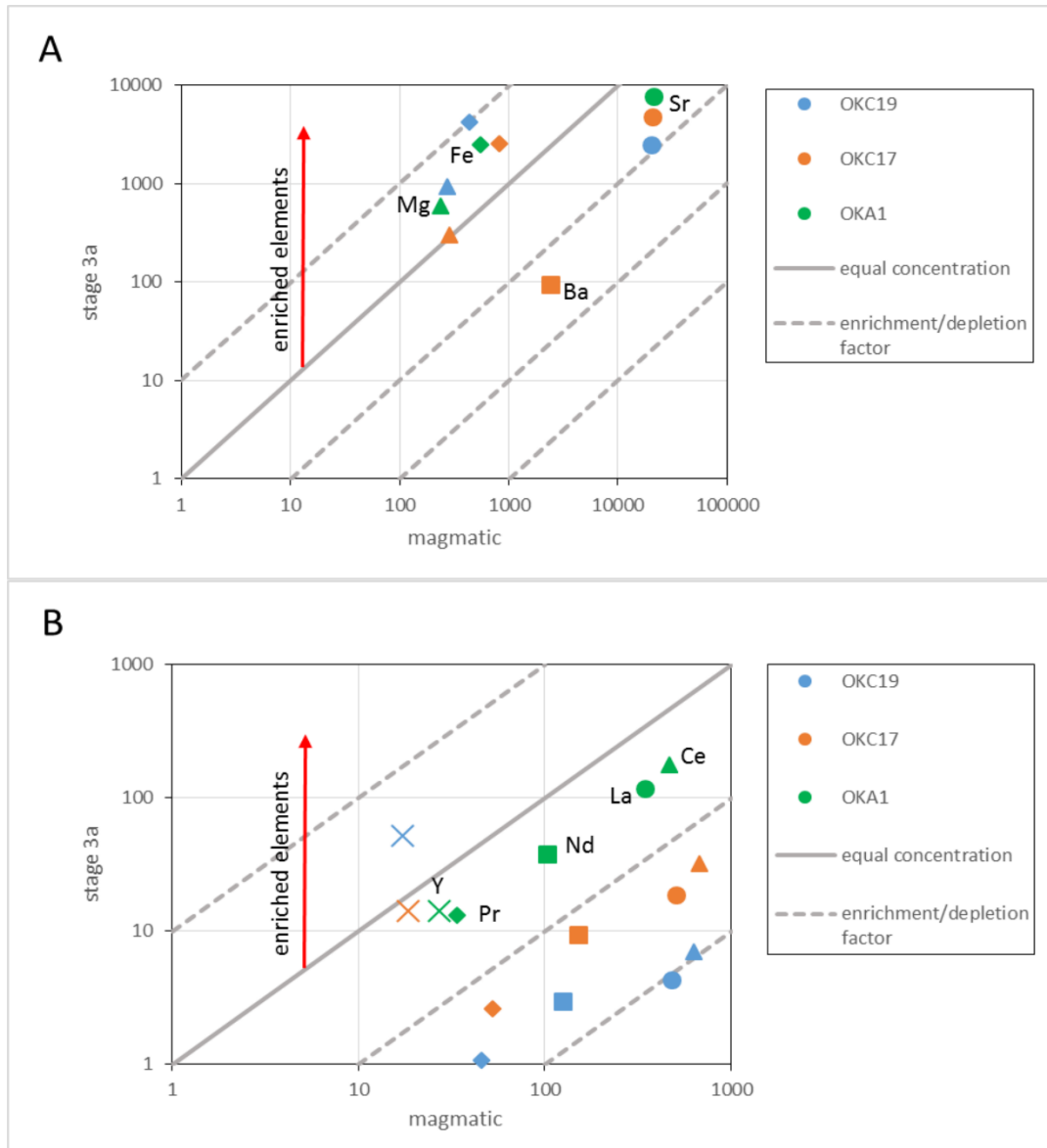
Figure 3-9: Comparisons of the composition of magmatic and hydrothermal (stage 3a) calcite to illustrate the changes accompanying recrystallisation. Compositions plotted are element ppm. The calcite carbonatite samples are described in Table 3-1. (A) Major elements including Sr and Ba (Table 3-2); (B) Binary plot of the average trace element of the magmatic and stage 3a calcite of the diopside-bearing and pegmatitic calcite carbonatites. Data are in ppm from EPMA and LA-ICP-MS analyses. The different samples are colour coded, and each shape represent one element.

3.6.2.2. Parisite

Parisite is the principal REE mineral in the calcite carbonatite sample suite (average $\sum RE_2O_{3tot}$ in stage 3 parisite from the calcite carbonatite ~47 wt.%) (Fig. 3-7; Appendix 3). The parisite REE pattern is broadly similar to those of the magmatic phases (Fig. 3-7) but shows even stronger LREE enrichment than apatite.

71

3.6.3. Stage 4 alteration: REE behaviour in fluorite mineralisation

LA-ICP-MS analyses of stage 3b and stage 4 fluorite are given in Appendix 3. All fluorite generations have low concentrations of REE, with the HREE below detection except for Y, and a positive Y anomaly of a few ppm to a few hundred ppm, as is common for fluorite (Williams-Jones and Palmer, 2002; Nadoll *et al.,* 2018). Stage 4a fluorite coexists with parisite (Fig. 3-5C-D) and has the highest LREE contents, averaging $\sum$LREE ~145 ppm; type 4c fluorite has an average $\sum$LREE slightly higher than type 4b fluorite ($\sum$LREE ~ 60 ppm).

The composition of stage 4 parisite was difficult to quantify because of fine scale intergrowth with Fe-hydroxides and other phases. It apparently has a somewhat higher REE content than stage 3 parisite (average $\sum RE_2O_{3tot}$ = 58 wt.%), although this could be an artefact of the associated Fe-hydroxides. Associated stage 4 calcite has a very low LREE content (average $\sum REE_{tot(La-Nd)}$ < 40 ppm) with no detectable HREE, even though both stage 3a and stage 4 calcite coexist with parisite (Appendix 3).

3.6.4. Minor and trace element redistribution during hydrothermal alteration of calcite carbonatite

3.6.4.1. Primary magmatic variation:

The suite of rocks studied shows a broad increase in REE contents from mafic rocks to carbonatites. Most of the major element variations reflect the different proportion of calcite and silicate minerals (Table 3-4) in the different rock types. The margin of the mafic dyke (OKC4) has the lowest REE content, but all REE patterns are similar (Fig. 3-10). The mafic dyke core, which was subsequently intruded by calcite carbonatite, shows LREE depletion compared to the magmatic calcite carbonatites because apatite and calcite are less abundant. The mafic dyke core is also depleted in HREE, but to a lesser extent than the LREE, compared to the other calcite carbonatites. This reflects the higher total HREE content of apatite and calcite from the mafic dyke (Tables 3-2, 3-3). In contrast, the least altered diopside-bearing calcite carbonatite (OKA5) has a distinctly higher HREE content compared to other magmatic calcite carbonatites (Fig. 3-10; OKA1, OKC17, 18, 19-1), although no specific mineralogical host for the HREE has been identified.

	OKC4m	OKC4c	OKA5	OKA1	OKC18	OKC17	OKC19-1	OKC19-2
Major elements (wt%)								
F	0.11	0.58	0.49	0.46	0.42	0.37	0.31	0.13
SiO_2	41.38	27.49	35.94	24.07	3.62	0.79	1.00	19.03
Al_2O_3	10.44	6.91	4.14	0.49	0.18	0.03	0.07	0.06
$Fe_2O_3(T)$	8.72	7.29	9.10	19.65	2.28	1.75	1.41	1.42
MnO	0.16	0.22	0.47	0.67	0.13	0.11	0.15	0.51
MgO	13.25	9.71	6.55	5.44	0.83	0.22	0.34	0.21
CaO	14.45	21.28	26.24	27.99	49.29	51.93	51.29	36.58
BaO	0.13	0.72	0.09	0.13	0.26	0.29	0.35	4.55
SrO	0.14	0.69	0.49	0.86	> 1.18	> 1.18	> 1.18	> 1.18
Na_2O	3.55	4.75	2.21	0.55	0.10	0.04	0.01	< 0.01
K_2O	1.76	1.60	0.80	0.28	0.10	0.02	0.01	0.03
TiO_2	1.06	0.75	0.85	1.34	0.08	0.07	0.03	0.01
P_2O_5	0.42	0.91	6.75	4.56	4.95	2.82	2.85	0.11
LOI	4.82	17.39	6.79	13.69	34.91	38.41	38.77	30.55
BaO/CaO	0.009	0.034	0.003	0.005	0.005	0.006	0.007	0.124
SrO/CaO	0.01	0.03	0.02	0.03	n.a.	n.a.	n.a.	n.a.
Total - (BaO+SrO)	**100.12**	**98.88**	**100.33**	**99.19**	**96.89**	**96.56**	**96.24**	**88.64**
Trace elements (ppm)								
V	207	149	244	517	50	50	36	36
Ba	1183	6442	783	1119	2349	2605	3093	40720
Sr	1180	5804	4266	7242	> 10000	> 10000	> 10000	> 10000
Zr	118	68	84	92	28	4	10	< 2
Cr	780	510	30	< 20	< 20	< 20	< 21	< 20
Ni	310	220	30	< 20	< 20	< 20	< 21	< 20
Cu	100	50	50	20	10	20	30	< 10
Zn	60	90	145	340	< 30	30	< 31	< 30
Nb	51	67	199	43	38	30	35	13
Pb	6	26	13	47	12	15	12	138
Th	20	42	180	64	130	50	112	270
La	52	386	759	632	933	671	861	> 2000
Ce	100	554	1445	1070	1620	1090	1440	> 3000
Pr	11	47	148	100	153	97	133	375
Nd	42	130	467	297	445	276	382	1140
Sm	7	14	58	32	43	26	37	115
Eu	2	4	16	8	10	6	9	26
Gd	5	8	34	15	19	12	16	47
Tb	1	1	4	2	2	1	2	4
Dy	4	6	24	8	9	6	8	21
Ho	1	1	4	1	1	1	1	4
Er	2	3	12	4	4	3	4	11
Tm	<1	<1	2	<1	<1	<1	1	2
Yb	1	2	9	3	2	2	3	12
Lu	<1	<1	1	<1	<1	<1	<1	2
Y	20	33	113	40	43	30	46	130
∑LREE	211	1131	2877	2131	3194	2160	2852	> 6630
∑HREE	15	25	106	41	48	30	43	128

Table 3-3: Bulk rock analyses of the Okorusu igneous rocks described in Table 3-1, OKC4 is a mafic dyke with OKC4m = OKC4 dyke margin and OKC4c = OKC4 dyke core. LREE= La to Sm, HREE= Eu to Lu + Y. Ge, Sn, In, Ag, Ti, Cs and Bi are under 2 ppm; Sb, Be, Hg, Ta and U are under 10 ppm and Ga, As, W, Sc, Rb, Mo and Co are under 60 ppm. BaO and SrO were calculated from the trace element values.
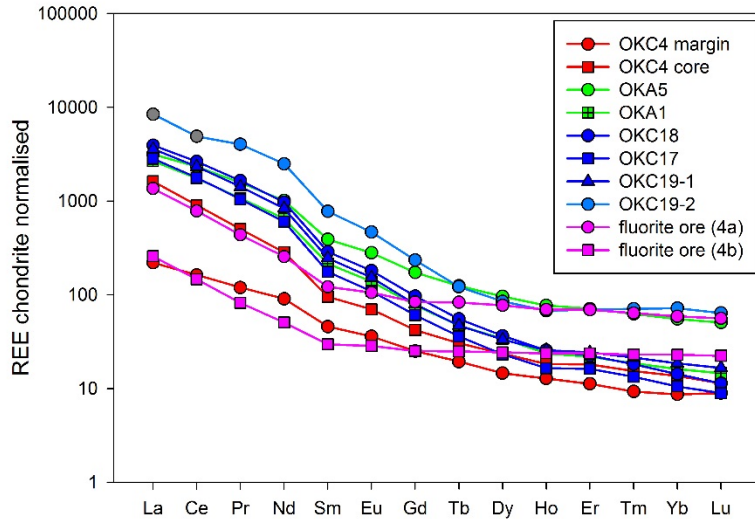
Figure 3-10: Whole rock data showing REE chondrite normalised pattern of the Okorusu igneous rocks and fluorite body (McDonough and Sun, 1995). Note that the true Ce and La value of the intensely altered calcite carbonatite (OKC19-2) are higher than the recorded ones (grey) due to the instrument saturation (respectively 2000 ppm and 3000 ppm) and the symbol colours are independent from Fig. 3-7.

3.6.4.2. Variation with hydrothermal alteration:

In order to evaluate the scale of element redistribution during hydrothermal alteration, we carried out bulk analyses on a range of relatively altered to relatively unaltered calcite carbonatites (Table 3-4). A simplified mass balance illustrates that for the less altered, pegmatitic calcite carbonatite (sample OKC17) there is no significant change in total REE content due to hydrothermal alteration. Calcite and apatite are respectively 95% and 5% of the original REE-bearing minerals in sample OKC17 (Table 3-4) and together made up approximately 95% of the sample initially. Based on their ∑REE concentrations prior to hydrothermal alteration (Tables 3-2, 3-3) we can calculate the original ∑REE concentration of the rock prior to alteration as 2090 ppm. The analysed bulk ∑REE content of the sample after alteration is 2190 ppm (Table 3-4). These values are effectively identical within uncertainty and we conclude that, during alteration, the REE released from magmatic minerals were retained in the rock but no additional REE were added.

In contrast, a similar calculation for the more altered pegmatitic calcite carbonatite sample OKC19-1 and the intensely altered pegmatitic carbonatite sample OKC19-2, shows addition of REE. In sample OKC19-1, calcite and apatite represent respectively 95% and 5% of the original REE-bearing minerals, and together they made up approximately 95% of the rock (Table 3-4). Based on the magmatic mineral compositions (Tables 3-2, 3-3), the ∑REE content

74

of the original rock was 1989 ppm whereas the ∑REE of the present, altered sample is 2943 ppm (Table 3-4), suggesting that REE may have been added during alteration. In the intensely altered calcite carbonatite (OKC19-2), calcite and apatite represent respectively 99% and 1% of the original REE-bearing minerals and the sample now has approximately 18% of added secondary silicates. No magmatic calcite remains in this sample, so we have assumed that it had the same composition as the magmatic calcite in sample OKC19-1, which was adjacent. Assuming there were no other minerals in the original rock, the magmatic calcite and apatite compositions (Tables 3-2, 3-3) allow us to estimate an original ∑REE content of 1501 ppm for the rock prior to alteration. This is markedly lower than the ∑REE content of the present rock, which is at least 6758 ppm (Table 3-4, note that Ce and La values are minima). Allowing for dilution by added hydrothermal silicates, the ∑REE content of the altered carbonatite is now at least 8241 ppm, i.e. much higher than that of the original rock. The present REE concentrations in OKC19-2 reflect the abundant parisite in this intensely altered carbonatite (Figs 3-4K, 3-10). We conclude that, although the mineralogical changes characteristic of hydrothermal alteration did not always lead to increased REE levels, the more intensely altered samples are rich in parisite and have enhanced levels of REE compared to their magmatic precursors.

Barium and strontium exhibit similar behaviour to the REE. Magmatic calcite is the main repository of Ba and Sr in the least altered rocks (Table 3-2), and stage 3 hydrothermal recrystallisation to a low-Ba, low-Sr calcite was accompanied by growth of Ba and Sr hydrothermal phases including baryte, witherite, strontianite and celestine. Table 3-4 shows that the Ba/Ca ratio of the calcite carbonatites increases with increasing degree of stage 3 alteration, with the markedly higher values for sample OKC19-2. As for the REE, the least altered samples show little evidence for enrichment in Ba, despite the appearance of baryte, but there was significant enrichment in Ba in the most altered sample, OKC19-2. The true Sr concentrations of the pegmatitic calcite carbonatites are above the calibrated range of the whole rock analyses (> 10000 ppm; Table 3-4), but based on the modal abundance of Sr-bearing minerals in these samples it is likely that Sr, like Ba, was also enriched during stage 3 alteration.

The enrichment in REE and Ba suggests that stage 3 alteration involves not just redistribution of minor and trace elements from magmatic minerals to hydrothermal phases on the hand specimen scale, but also some movement on a larger scale. The diopside-bearing carbonatites (OKA5 and OKA1) and pegmatitic calcite carbonatites (OKC17, 18, 19) have the

same suite of stage 3 hydrothermal alteration phases and similar REE patterns (Fig. 3-10; Table 3-1). The absence of Eu and Ce anomalies from all samples are distinctive (Figs 3-7, 3-10). We infer that the most altered carbonatites accumulated trace elements through growth of secondary phases, but these may well have been released from ongoing alteration nearby (Fig. 3-11).

An alternative hypothesis, which merits consideration, is that these enrichments are a residual effect due to net dissolution of calcite during stage 3. However, the way in which hydrothermal calcite pseudomorphs magmatic calcite in the sample suite, and the lack of comparable enrichment in elements such as Al (Table 3-4), make this less likely.

In summary, stage 3 hydrothermal alteration resulted in modest changes in the composition of the calcite carbonatites, principally involving minor and trace elements which were initially present in magmatic calcite (Fig. 3-11). Although magmatic apatite has higher REE contents than magmatic calcite (by one order of magnitude), it is much less altered during hydrothermal alteration (< 10%), and it is considerably less abundant than calcite, hence it released a smaller amount of REE and the major part of the REE, together with Ba and Sr for hydrothermal minerals, was derived from magmatic calcite. Nevertheless, more altered samples are enriched in Ba, Sr and REE relative to Ca, reflecting the growth of the hydrothermal stage 3 minerals in which they are concentrated, and this suggests that these elements migrated to the areas of most intense alteration on a modest scale. In contrast, stage 4 hydrothermal alteration resulted in wholesale replacement of calcite by fluorite in the ore zones, with addition of F but removal of LREE, Ba and Sr as well as CO_2.
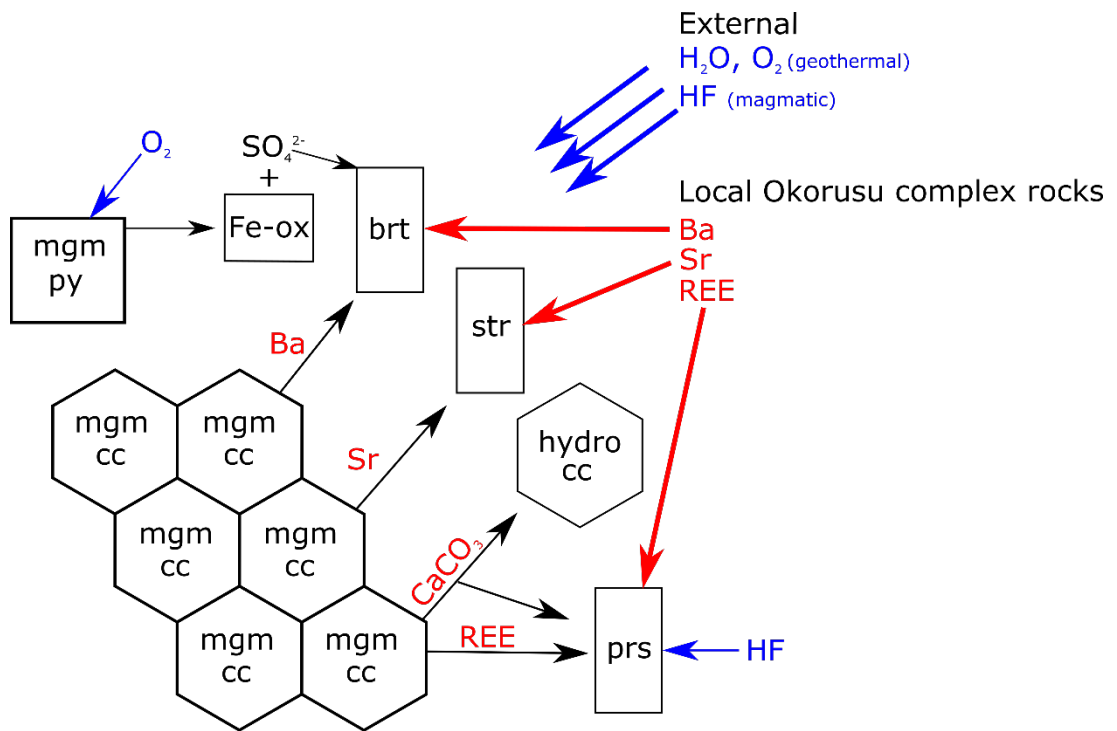
Figure 3-11: Schematic presentation of the formation of the main hydrothermal assemblage observed in the altered Okorusu calcite carbonatites. Abbreviations: Fe-ox–unidentified Fe- hydroxide; cc–calcite; mgm–magmatic; hydro—hydrothermal; str—strontianite; prs—parisite; py—pyrite; brt—baryte.

3.7. Discussion

Hydrothermal reworking has played an important role in determining the composition and mineralogy of the Okorusu carbonatite body. Hydrothermal changes are potentially significant for future exploitation of carbonatites for REE, because they dictate the REE mineralogy.

3.7.1. Hydrothermal reworking of the calcite carbonatites

We have argued above that the growth of parisite and other hydrothermal stage 3a phases in the calcite carbonatites resulted from breakdown of magmatic minerals, mainly calcite, releasing REE, Ba and Sr. While there is a qualitative match between the elements released from magmatic minerals and those taken up in stage 3 hydrothermal phases, the most altered samples show some enrichment, implying redistribution on a larger scale than the outcrops sampled (e.g. Fig. 3-3B). In particular, remobilisation gave rise to a greater local LREE enrichment in the most intensely altered calcite carbonatite (OKC19-2) reflecting abundant stage 3 parisite mineralisation (Figs 3-4K, 3-10). The most intense hydrothermal alteration of the pegmatitic calcite carbonatite pod is close to the contact with the country rock, which may reflect enhanced fluid flow at the margin of the carbonatite body (Fig. 3-3B).

Local LREE enrichment in the intensely altered calcite carbonatite is accompanied by accumulation of Ba and Sr, mainly as sulfates (Table 3-3, 3-4). These are a key feature of stage 3 hydrothermal alteration at Okorusu. Since baryte and celestine are nearly insoluble (Blount, 1977; Monnin, 1999), we infer that the Ba and Sr released from the breakdown of magmatic calcite and apatite were fixed by interaction with sulfate. A small percentage of magmatic pyrite (< 5%) was present in the calcite carbonatites initially, but is now partially altered to Fe-hydroxides (Fig. 3-4G) and so the reaction of pyrite with an introduced hydrothermal fluid is a likely source of local sulfate (Fig. 3-11).

The stage 3 fluid is inferred to have been oxidising because of the production of sulfate and the association of Fe-hydroxides with the stage 3b assemblages, however it was not sufficiently oxidising for Ce to be fractionated from the rest of the REE as Ce^{4+}, as described in a similar setting by Anenburg *et al.,* (2018b). Assuming that all the Ba and Sr in the intensely

altered calcite carbonatite (OKC19-2) are present in sulfate minerals, approximately 13000 ppm of sulfur was needed to fix them. Oxidation of 3% modal pyrite, a typical level for the magmatic calcite carbonatites, will release around 16000 ppm sulfur as sulfate and so it is likely that sufficient sulfur is available in-situ to fix the elevated Ba and Sr levels present in this sample.

There was probably an excess of Ba and Sr available, since they also form carbonate minerals, and in this case sulfate would not have been available in solution to enhance REE mobility (Migdisov and Williams-Jones, 2008).

3.7.2. Conditions of REE mineralisation and hydrothermal reworking

By analogy to experimental work on carbonatite systems by Weidendorfer *et al.,* (2017) it is likely that the temperature of the magmatic stage of the Okorusu carbonatites was between 700 °C and 1050 °C, although late-magmatic stage 2 crystallisation may have been somewhat cooler. Bühn *et al.,* (2002) estimated that stage 4 alteration and fluorite growth took place at 150 °C ± 30 °C from fluid inclusion studies. Stage 3 and stage 4 hydrothermal alterations result in a similar hydrothermal mineral suite, although stage 4 is dominated by fluorite. In particular, calcite is present coexisting with dolomite in both stage 3 and stage 4. The Mg content of calcite coexisting with dolomite is the basis for the calcite-dolomite solvus geothermometer calibrated by Anovitz and Essene (1987). In practice, the Mg content of stage 3a and stage 4 calcite is too low ($XMg < 0.001$, Table 3-2) to apply this geothermometer except to give an upper temperature limit. The data indicate that both stages 3 and 4 developed at temperatures < 200 °C, in agreement with the earlier fluid inclusion results.

3.7.3. The relation between carbonatite evolution and hydrothermal reworking

High-temperature hydrothermal activity commonly affects the rocks around carbonatite complexes, notably through the formation of fenites (Zharikov *et al.,* 2007; Elliott *et a*l., 2018), and so it is reasonable to ask if such magmatic fluids played a role in the hydrothermal alteration described here. Carbonatite melts are low viscosity (Jones *et al.,* 2013) and rich in chloride salts and volatiles, predominantly CO_2 and H_2O (Mitchell, 2005; Rankin, 2005). Salts and volatiles which are not retained in the carbonatite rocks give rise to fenitizing fluid (Elliott *et al.,* 2018). A minimum fenitization temperature of 500 °C ± 30 °C is indicated by

experimental work (Zaraiskii, 1989). The upper temperature limit of fenites in natural systems is > 700 °C, measured at Amba Dongar (Williams-Jones and Palmer, 2002). These are very different from the conditions of the hydrothermal alteration observed at Okorusu (Table 3-1), which indicate a distinct break between magmatic and hydrothermal conditions. In the absence of evidence of high-T alteration in the studied rocks it unlikely that late stage magmatic fluids were the only source responsible (cf. Trofanenko *et al.,* 2016). Furthermore, the fluid inclusions hosted in the fluorite lack a CO_2 component and show low salinities (Bühn *et al.*, 2002), unlike carbonatite fluid inclusions observed in other carbonatite bodies (e.g. Rankin, 2005; Shu and Liu, 2019; Zheng and Liu, 2019). Instead, the alteration observed is consistent with a maximum temperature of 200 °C and the oxidising character of the hydrothermal fluid is suggestive of a geothermal system involving surface waters, although a magmatic origin for the added F seems very likely. A link between geothermal systems and hydrothermal mineralisation is widely documented from many settings, with water of meteoric origin interacting with components derived from magmatic fluids and gases to produce a wide range of epithermal ores (e.g. White, 1981; Krupp and Seward, 1987). In this example, the development of hydrothermal massive fluorite points to continued magmatic vapor contributions to the geothermal fluid system down to low temperatures (Bühn *et al.*, 2002, 2003).

3.8. Conclusions

The REE-rich carbonatites at Okorusu are originally of magmatic origin, but hydrothermal reworking has served to redistribute the REE into new minerals. Three alteration stages redistributed the REE at Okorusu. Stage 2 mineral growth is late magmatic and results in minor growth of REE-depleted apatites after magmatic (stage 1) apatite. Stage 2 apatites exhibit lower REE contents than the stage 1 grains across the full lanthanide series (Fig. 3-7) but were accompanied by cogenetic parisite. Stages 3 and 4 are two distinct low temperature hydrothermal events. Stage 3 involves partial breakdown of apatite and extensive recrystallisation of more abundant, trace element-rich magmatic calcite, to purer hydrothermal calcite. Elements released from stage 1 magmatic minerals during alteration precipitated as parisite, baryte and celestine with lesser amounts of strontianite, witherite and other minor phases. Overall, stage 3 alteration is widespread in the different carbonatite pods and dykes, and is dominated by redistribution of REE without significant change in the bulk rock composition. Nevertheless, there is evidence of enrichment in Sr, Ba and REE during alteration in the most altered calcite carbonatites (Fig. 3-11). In contrast, stage 4 alteration

resulted in widespread replacement of calcite carbonatite bodies (including those affected by stage 2 and stage 3 alteration) and country rock marbles by fluorite, and is accompanied by much more extensive metasomatic change than stage 3. Fluorite ore is low in Ba, Sr and REE irrespective of precursor lithology and only the earliest fluorite, type 4a, has associated parisite. The REE profiles of minerals from all alteration stages are close to that of the main REE-bearing magmatic phases (Fig. 3-7). Likewise, the REE bulk rock patterns of the different rocks (from mafic to fluorite ore) are comparable (Fig. 3-10). This suggests that the REE-bearing minerals developed in stages 2, 3 and 4 formed by redistribution of the REE from stage 1 magmatic minerals without a major external source of REE (Fig. 3-11).

Stage 3 alteration is responsible for the most abundant REE mineralisation at Okorusu, with REE derived from magmatic phases being concentrated into hydrothermal parisite. It developed at a temperature less than 200 °C and the associated baryte and celestine indicate an oxidising hydrothermal fluid, with sulfate likely derived from oxidation of magmatic pyrite. The most altered calcite carbonatite (OKC19-2) appears to have been enriched in Ba, Sr and REE during the alteration.

The stage 3 and stage 4 hydrothermal alteration at Okorusu developed under low temperature, mildly oxidising conditions typically associated with geothermal systems. It is likely that surface-derived waters played an important role, but the extensive development of fluorite in stage 4 is indicative of an important contribution of F-rich fluid, likely of magmatic origin (Bühn *et al.*, 2002, 2003).

Although Okorusu does not have economic potential for REE at present, this study demonstrates that hydrothermal alteration can serve to concentrate REE, forming hydrothermal REE minerals. The hydrothermal alteration of the main magmatic gangue mineral at Okorusu (calcite) has proven to be able to concentrate a significant amount of REE to form parisite-rich areas. Small amounts of hydrothermal alterations are sufficient to facilitate recrystallisation and the accompanying concentration of trace and minor elements into their own discrete secondary minerals, but more extensive alteration appears to be necessary to achieve significant overall enrichment.

Acknowledgements

References

Alderton, D.H.M., Pearce, J.A. and Potts, P.J. (1980) Rare earth element mobility during granite alteration: evidence from the southwest England. *Earth and Planetary Science Letters,* **49**, 149-165.

Anenburg, M., and Mavrogenes, J.A. (2018a) Carbonatitic versus hydrothermal origin for fluorapatite REE-Th deposits: Experimental study of REE transport and crustal "antiskarn" metasomatism. *American Journal of Science*, **318**, 335-366.

Anenburg, M., Burnham, A.D. and Mavrogenes, J.A. (2018b) Ree redistribution textures in altered fluorapatite: Symplectites, veins, and phosphate-silicate-carbonate assemblages from the Nolans bore preeth deposit, Northern Territory, Australia. *Canadian Mineralogist*, **56**(3), 331-354.

Anovitz, L.M. and Essene, E.J. (1987) Phase equilibria in the system $CaCO_3$-$MgCO_3$-$FeCO_3$. *Journal of Petrology,* **28**, 389-414.

Banks, D.A., Yardley, B.W.D., Campbell, A.R. and Jarvis, K.E. (1994) REE composition of an aqueous magmatic fluid: A fluid inclusion study from the Capitan Pluton, New Mexico, U.S.A. *Chemical Geology*, **113**, 259-272.

Belousova, E.A., Griffin, W.L., O'Reilly, S.Y., and Fisher, N.I. (2002) Apatite as an indicator mineral for mineral exploration: trace-element compositions and their relationship to host rock type. *Journal of Geochemical Exploration*, **76**, 45-69.

Blount, C. (1977) Baryte solubilities and thermodynamic quantities up to 300°C and 1400 bars. *American Mineralogist,* **62**, 942-957.

Broom-Fendley, S., Styles, M.T., Appleton, J.D., Gunn, G. and Wall, F. (2016) Evidence for dissolution-reprecipitation of apatite and preferential LREE mobility in carbonatite-derived late-stage hydrothermal processes. *American Mineralogist*, **101**, 596-611.

Broom-Fendley, S., Aoife, B.E., Wall, F., Gunn, G. and Dawes, W. (2017a) REE minerals at the Songwe Hill carbonatite, Malawi: HREE-enrichment in late-stage apatite. *Ore Geology Reviews,* **81**, 23-41.

Broom-Fendley, S., Wall, F., Spiro, B. and Ullmann, C.V. (2017b) Deducing the source and composition of rare earth mineralising fluids in carbonatites: insights from isotopic (C, O, ^{87}Sr/^{86}Sr) data from Kangankunde, Malawi. *Contributions to Mineralogy and Petrology*, **172**, 96.

Bühn, B., Rankin, A.H., Schneider, J. and Dulski, P. (2002) The nature of orthomagmatic, carbonatitic fluids precipitating REE, Sr-rich fluorite: fluid-inclusion evidence from the Okorusu fluorite deposit, Namibia. *Chemical Geology,* **186**, 75-98.

Bühn, B., Schneider, J., Dulski, P. and Rankin, A.H. (2003) Fluid-rock interaction during progressive migration of carbonatitic fluids, derived from small-scale trace element and Sr, Pb isotope distribution in hydrothermal fluorite. *Geochimica et Cosmochimica Acta*, **67**, 4577-4595.

Chakhmouradian, A.R., Reguir, E.P. and Zaitsev, A.N. (2016) Calcite and dolomite in intrusive carbonatites. I. Textural variations. *Mineralogy and Petrology*, **110**, 333-360.

Chakhmouradian, A.R., Reguir, E.P., Zaitsev, A.N., Couëslan, C., Xu, C., Kynický, J., Mumin, A.H. and Yang, P. (2017) Apatite in carbonatitic rocks : Compositional variation, zoning, element partitioning and petrogenetic significance. *Lithos*, **275**, 188-213.

Chakhmouradian, A.R. and Wall, F. (2012) Rare earth elements: Minerals, mines, magnets (and more). *Elements*, **8**, 333-340.

Chakhmouradian, A.R. and Zaitsev, A.N. (2012) Rare earth mineralization in igneous rocks: Sources and processes. *Elements*, **8**, 347-353.

Chebotarev, D.A., Veksler, I.V., Wohlgemuth-Ueberwasser, C., Doroshkevich, A.G., and Koch-Müller, M. (2019) Experimental study of trace element distribution between calcite, fluorite and carbonatitic melt in the system $CaCO_3 + CaF_2 + Na_2CO_3 \pm Ca_3(PO_4)_2$ at 100 MPa. *Contributions to Mineralogy and Petrology*, **174**(1), 1-13.

Elliott, H.A.L., Wall, F., Chakhmouradian, A.R., Siegfried, P.R., Dahlgren, S., Weatherley, S., Finch, A.A., Marks, M.A.W., Dowman, E., and Deady, E. (2018) Fenites associated with carbonatite complexes: A review. *Ore Geology Reviews*, **93**, 38-59.

European Commission (2017) Communication from the commission to the European parliament, the council. *The European economic and social committee and the committee of the regions on the 2017 list of Critical Raw Materials for the EU*. COM(2017) 490.

Feng, M. Xu, C., Kynicky, J., Zeng, L. and Song, W. (2016) Rare earth element enrichment in Palaeoproterozoic Fengzhen carbonatite from the North China block. *International Geology Review*, **58**(15) 1940-1950.

Giebel, R.J., Gauert, C.D.K., Marks, M.A.W., Costin, G. and Markl, G. (2017) Multi-stage formation of REE minerals in the Palabora Carbonatite Complex, South Africa. *American Mineralogist,* **102**, 1218-1233.

Glover, E.D. and Sippel, R.F. (1962) Experimental pseudomorphs: Replacement of calcite by fluorite. *American Mineralogist,* **47**, 1156-1165.

Gysi, A.P. and Williams-Jones, A. (2013) Hydrothermal mobilization of pegmatite-hosted REE and Zr at Strange Lake, Canada: a reaction path model. *Geochimica et Cosmochimica Acta,* **122**, 324-352.

Hagni, R.D. and Shivdasan, P.A. (2000) Characterizing megascopic textures in flurospar ores at Okorusu mine. *Microtextural Mineralogy*, 17-19.

Hagni, R.D. and Shivdasan, P.A. (2001) Application of cathodoluminescence microscopy to the study of carbonatite-related fluorspar ores, host rock carbonatites and beneficiation products at Okorusu, Namibia. *Minerals and Metallurgical Processing*, **18**(4), 203-208.

Harlov, D.E., Förster, H.J., and Schmidt, C. (2003) High P-T experimental metasomatism of a fluorapatite with significant britholite and fluorellestadite components: implications for LREE mobility during granulite-facies metamorphism. *Mineralogical Magazine*, **67**, 61-72.

Harlov, D.E., Wirth, R. and Förster, H.J. (2005) An experimental study of dissolution-reprecipitation in fluorapatite: Fluid infiltration and the formation of monazite. *Contributions to Mineralogy and Petrology*, **150**(3), 268-286.

Holtstam, D. and Andersson, U.B. (2007). The REE minerals of the Bastnäs-type deposits, South-Central Sweden. *Canadian Mineralogist*, **45**, 1073-1114.

Holtstam, D., Andersson, U.B., Broman, C. and Mansfeld, J. (2014) Origin of REE mineralization in the Bastnäs-type Fe–REE-(Cu–Mo–bi–Au) deposits, Bergslagen, Sweden. *Mineralium Deposita*, **49**, 933-966.

Jones, A.J., Genge, M. and Carmody, L. (2013) Carbonate melts and carbonatites. *Reviews in Mineralogy and Geochemistry*, **75,** 289-322**.**

Kapustin, I. (1980) *Mineralogy of carbonatites.* Amerind Publ Co, New Delhi.

Krupp, R.E. and Seward, T.M. (1987) The Rotokawa geothermal system, New Zealand: An active epithermal gold-depositing environment. *Economic Geology*, **82**, 1109-1129.

Le Bas, M.J. and Srivastava, R.K. (1989) The mineralogy and geochemistry of the Mundwana carbonatite dykes, Sirohi District, Rajasthan, India. *Journal of Mineralogy and Geochemistry*, **160**, 207-227.

Lewis, A.J., Komninou, A., Yardley, B.W.D. and Palmer, M.R. (1998) Rare earth element speciation in geothermal fluids from Yellowstone National Park, Wyoming, USA. *Geochimica et Cosmochimica*, **62**, 657-663.

Linnen, R.L., Samson, I.M., Williams-Jones, A.E. and Chakhmouradian, A.R. (2014) Geochemistry of the rare-earth element, Nb, Ta, Hf, and Zr deposits. Pp 543-569 in: *Treatise on Geochemistry*: Second Edition, Elsevier

McDonough, W.F. and Sun, S. (1995) The composition of the earth. *Chemical Geology,* **120**, 223-253.

Migdisov, A., Williams-Jones, A.E., Brugger, J. and Caporuscio, F.A. (2016) Hydrothermal transport, deposition, and fractionation of the REE: Experimental data and thermodynamic calculations. *Chemical Geology,* **439**, 13-42.

Migdisov, A.A. and Williams-Jones, A.E. (2008) A spectrophotometric study of Nd(III), Sm(III) and Er(III) complexation in sulfate-bearing solutions at elevated temperatures. *Geochimica et Cosmochimica Acta,* **72**, 5291-5303.

Milner, S.C., Le Roex, A.P. and O'Connor, J.M. (1995) Age of Mesozoic igneous rocks in northwestern Namibia, and their relationship to continental breakup. *Journal of the Geological Society*, **152**, 97-104.

Mitchell, R.H. (2005) Carbonatites and carbonatites and carbonatites. *Canadian Mineralogist*, **43**, 2049-2068.

Monnin, C. (1999) A thermodynamic model for the solubility of baryte and celestine in electrolyte solutions and seawater to 200°C and to 1 kbar. *Chemical Geology*, **153**, 187-209.

Moore, M., Chakhmouradian, A.R., Mariano, A.N. and Sidhu, R. (2015) Evolution of rare-earth mineralization in the Bear Lodge carbonatite, Wyoming: Mineralogical and isotopic evidence. *Ore Geology Reviews,* **64**, 499-521.

Nadoll, P. Rehm, M., Duschl, F., Klemd, R., Kraemer, D., and Sośnicka, M. (2018) REY and trace element chemistry of fluorite from Post-Variscan hydrothermal veins in Paleozoic units of the North German Basin. *Geosciences*, **8**(8), 283-312.

Packwood, R.H. and Brown, J.D. (1981) A Gaussian expression to describe Φ(ρz) curves for quantitative electron probe microanalysis. *X-RAY Spectrometry,* **10**, 138-146.

Perry, P. and Gysi, A. (2018) Rare earth elements in mineral deposits: speciation in hydrothermal fluids and partitioning in calcite. *Geofluids, 2018*, 1-19.

Rankin, A.H. (2005) Carbonatite-associated rare metal deposits—Composition and evolution of ore-forming fluids-The fluid inclusion evidence. pp. 299-314 in: Rare-element geochemistry and mineral deposits (Linnen, R.L. and Samson, I.M. editors) Quebec: Geological Association of Canada, Short Course Notes 17.

Reguir, E.P. Chakhmouradian, A.R., Pisiak, L.H., Halden,N.M., Yanng, P. Xu, C., Kynický, J. and Couëslan, C.G. (2012) Trace-element composition and zoning in clinopyroxene- and amphibole-group minerals: Implications for element partitioning and evolution of carbonatites. *Lithos*, **128-131**, 27-45.

Roedder, E. (1973) Fluid inclusions from the fluorite deposits associated with carbonatite of Amber Dongar, India and Okorusu, South West Africa. *Transaction of the Institution of Mining and Metallurgy*, **82**, 35-39.

Schreiber, U.M., Minlners, S.C. and Goscombe, B.G. (1977) Geological map of Namibia: 1:250 000 geological series.

Shivdasan, P. (2002) *Petrology, geochemistry, and mineralogy of pyroxene and pegmatite carbonatite and the associated fluorspar deposit at Okorusu alkaline igneous carbonatite complex, Namibia*. PhD dissertation, University of Missouri-Rolla, USA.

Shu, X. and Liu, Y. (2019) Fluid inclusion constraints on the hydrothermal evolution of the Dalucao Carbonatite-related REE deposit, Sichuan Province, China. *Ore Geology Reviews*, **107**, 41-57.

Smith, M.P., Henderson, P. and Campbell, L.S. (2000) Fractionation of the REE during hydrothermal processes: constraints from the Bayan Obo Fe-REE-Nb deposit, Inner Mongolia, China. *Geochimica et Cosmochimica Acta,* **64**, 3141-3160.

Smith, M.P., Moore, K., Finch, A.A., Kynicky, J. and Wall, F. (2016) From mantle to critical zone, a review of large and giant sized deposits of the rare earth elements. *Geoscience Frontiers,* **7**, 315-334.

Sturm, R. (2002) PX-NOM - An interactive spreadsheet program for the computation of pyroxene analyses derived from the electron microprobe. *Computers and Geosciences*, **28**, 473-483.

Trofanenko, J., Williams-Jones, A.E., Simandl, G.J. and Migdisov, A.A. (2016) The nature and origin of the REE mineralization in the Wicheeda carbonatite, British Columbia, Canada. *Economic Geology,* **111**, 199-223.

U.S. Geological Survey (2018) Mineral commodity summaries 2018, U.S. *Geological Survey*, 1-204.

Van Zijl, P (1962) *The geology, structure and petrology of the alkaline intrusions of Kalkfeld and Okorusu and the invaded Damara rocks*. PhD dissertation, University of Stellenbosch, South Africa.

Verplanck, P.L., Mariano, A.N. and Mariano, A. (2016) Rare earth element ore geology of carbonatites. pp. 5-32 in: *Rare earth and critical elements in ore deposits* (Hitzman, M.W. editors. Review of Economic Geology, **18**.

Wall, F., Niku-Paavola, V.N., Storey, C.M. and Axel, J.T. (2008) Xenotime-(Y) from carbonatite dykes at Lofdal, Namibia: Unusually low LREE:HREE ratio in carbonatite, and the first dating of xenotime overgrowths on zircon. *Canadian Mineralogist,* **46**, 861-877.

Wall, F. (2014) Rare Earth Elements. pp. 312-340 in: *Critical Metals Handbook* (Gunn, A. editor). Wiley, New York, USA.

Weidendorfer, D., Schmidt, M.W. and Mattsson, H.B. (2017) A common origin of carbonatite magmas. *Geology*, **45**(6), 507-510.

White, D.E. (1981) Active geothermal systems and hydrothermal ore deposits. *Economic Geology*, **75**, 392-423.

Williams-Jones, A.E. and Palmer, D.A.S. (2002) The evolution of aqueous-carbonic fluids in the Amba Dongar carbonatite, India: Implications for fenitisation. *Chemical Geology*, **185**, 283-301.

Williams-Jones, A.E., Migdisov, A.A. and Samson, I.M. (2012) Hydrothermal mobilisation of the rare earth elements-a tale of "ceria" and "yttria"'. *Elements,* **8**, 13-42.

Zaitsev, A.N., Wall, F. and Le Bas, M.J. (1998) REE-Sr-Ba minerals from the Khibina carbonatites, Kola Peninsula, Russia: their mineralogy, paragenesis and evolution. *Mineralogical Magazine*, **62**, 225-250.

Zaitsev, A., Demény, A., Sindern, S. and Wall, F. (2002) Burbankite group minerals and their alteration in rare earth carbonatites: source of elements and fluids (evidence from C-O and Sr-Nd isotopic data). *Lithos,* **62**, 15-33.

Zaraiskii, G.P. (1989) Zonation and Conditions of Metasomatic Rocks Formation. Nauka Publishing, Moscow.

Zharikov, V.A., Pertsev, N.N., Rusinov, V.L., Callegari, E., Fettes, D.J. (2007) Metasomatism and metasomatic rocks. In: Recommendations by the IUGS Subcommision of the Systematics of Metamorphic Rocks. British Geological Survey.

Zheng, X. and Liu, Y. (2019) Mechanisms of element precipitation in carbonatite-related rare-earth element deposits: Evidence from fluid inclusions in the Maoniuping deposit, Sichuan Province, southwestern China. *Ore Geology Reviews*, **107**, 218-238.

CHAPTER 4.

The role of sulfate-rich fluids in Heavy Rare Earth enrichment at the Dashigou carbonatite deposit, Huanglongpu, China

Cangelosi, D.A., Smith, M.P; Banks, D.A. and Yardley, B.W.D. (2019b) The role of sulfate-rich fluids in Heavy Rare Earth enrichment at the Dashigou carbonatite deposit, Huanglongpu, China. *Mineralogical Magazine*, (n.d.).

4.1. Abstract

The Huanglongpu carbonatites are located in the north-western part of the Qinling orogenic belt in central China. Calcite carbonatite dykes at the Dashigou open pit are unusual due to their enrichment in HREE relative to LREE, leading to a flat REE pattern, and in that the majority of dykes have a quartz core. They also host economic concentrations of molybdenite. The calcite carbonatite dykes show two styles of mineralogy according to the degree of hydrothermal reworking, and these are reflected in REE distribution and concentration. The REE in the little-altered calcite carbonatite occur mostly in magmatic REE minerals, mainly monazite-(Ce), and typically have $\sum$LREE/(HREE+Y) ratios from 9.9 to 17. In hydrothermally altered calcite carbonatites, magmatic monazite-(Ce) is partially to fully replaced by HREE-enriched secondary phases and the rocks have $\sum$LREE/(HREE+Y) ratios from 1.1 to 3.8. The fluid responsible for hydrothermal REE redistribution is preserved in fluid inclusions in the quartz lenses. The bulk of the quartz lacks fluid inclusions but is cut by two

later hydrothermal quartz generations, both containing sulfate-rich fluid inclusions with sulfate often present as multiple trapped solids, as well as in solution. The estimated total sulfate content of fluid inclusions ranges from 6 to > 33 wt.% K_2SO_4 equivalent. We interpret these heterogeneous fluid inclusions to be the result of reaction of sulfate-rich fluids with the calcite carbonatite dykes. The final HREE enrichment is due to a combination of factors: a) the progressive HREE enrichment of later magmatic calcite created a HREE-enriched source; b) REE-SO_4^{2-} complexing allowed the REE to be redistributed without fractionation; c) secondary REE mineralisation was dominated by minerals such as HREE-enriched fluorcarbonates, xenotime-(Y) and churchite-(Y) whose crystal structures tends to favour HREE.

4.2. Introduction

The light rare earth elements (LREE; La to Sm) and the heavy rare earth elements (HREE; Eu to Lu) are now classified as critical raw materials by the European Commission (European Commission, 2017) due to the growing demand for these strategic elements. This has created a heightened interest in understanding the origin of economic REE deposits (Williams-Jones *et al.,* 2012; Wall, 2014).

Currently the largest and highest grade REE deposits are associated with carbonatite rocks (Chakhmouradian and Wall, 2012; Chakhmouradian and Zaitsev, 2012; Verplanck, 2017). Carbonatite deposits are commonly LREE-enriched (Woolley and Kempe, 1989; Rankin, 2005; Verplanck *et al.,* 2014), but a few carbonatite deposits, such as Huanglongpu, (central Shanxi Province, China), the Lofdal complex, (north-western Namibia) and Bear Lodge, (USA) show relative HREE enrichment (Xu *et al.,* 2007; Wall *et al.,* 2008; Andersen *et al.,* 2016). Many REE carbonatite deposits display evidence of hydrothermal reworking which can influence the final REE distribution and mineralogy (e.g. Smith *et al.,* 2000; Smith *et al.,* 2015; Shu and Liu,

2019; Cangelosi *et al.,* 2019). Economic concentrations of REE are often hosted by minerals precipitated during hydrothermal alteration, rather than the early magmatic REE minerals (Wall, 2014).

This study follows from the recent work of Smith *et al.,* (2018) on the Huanglongpu calcite carbonatites. They investigated the HREE enrichment of the carbonatites by looking at the progression from magmatic REE-bearing minerals to later hydrothermal REE-bearing minerals. They demonstrated that each subsequent REE-bearing mineral stage resulted in preferential leaching of the LREE and enrichment in the HREE. This is associated with a shift to more silica-rich hydrothermal conditions leading to quartz growth, and finally with sulfate mineralisation. They documented magmatic HREE enrichment seen in late stage magmatic calcite. Subsequently, hydrothermal alteration of magmatic REE phases, notably monazite-(Ce), was accompanied by growth of secondary REE minerals, in particular britholite-(Ce) and Ca-REE fluorcarbonate, which show relative HREE enrichment compared to magmatic phases.

The Huanglongpu carbonatite is mined as a molybdenum deposit, but is considered to be part of a key REE-producing area of China, although its REE reserves and grades are unpublished (Kynicky *et al.,* 2012). The presence of quartz with associated fluid inclusions, together with hydrothermal HREE-rich minerals, make it suitable to investigate the role of secondary hydrothermal fluid in the REE enrichment of carbonatites.

4.3. The Huanglongpu carbonatite deposit

4.3.1. Geological setting

The Huanglongpu deposit lies in the north-western part of the Qinling orogenic belt in central China (Xu *et al.*, 2007; Fig. 4-1). This orogenic belt hosts numerous ore deposits and is divided

by the Shangdan suture into two parts: North and South Qinling. The northern border of the North Qinling belt is defined by a normal fault associated with the Cenozoic rift basin to the north. The southern Qinling belt is further divided by the Mianlue suture which was extensively reworked by Late Mesozoic thrusting (Xu *et al.*, 2010). A comprehensive summary of the North and South Qinling belt lithologies is given in Xu *et al.,* (2010). The Qinling orogenic belt was incorporated into Rodinia during the Grenvillian orogeny, followed by rifting, then subduction-related tectonics in the Palaeozoic and early Mesozoic, leading to Cretaceous to Palaeogene reactivation, and finally Neogene extension. The detailed tectonic history can be found in Ratschbacher *et al.*, (2003).

The Qinling orogenic belt is an important metallogenic belt, hosting the most important Mo ore camp in China and including several world-class Mo deposits (Mao *et al.*, 2008). The mineralisation is mostly hosted by granitic porphyry bodies with a few porphyry-skarn deposits. However, in the Huanglongpu area (Fig. 4-1) the Mo mineralisation is associated with unusual carbonatite veins. The Huanglongpu area contains an extensional structure hosting ore bodies that extend over a distance of 6 km, mainly controlled by a northwest-striking fault zone (Xu *et al.,* 2010; Fig. 4-1A). There are five ore fields currently being mined (Fig. 4-1A): Yuantou, Dashigou, Shijiawan I and II and Taoyuan, with a total reserve of 0.18 million tonnes of MoS_2. Apart from Shijiawan I, which is hosted by porphyry and has intruded into the Neoarchean Taihua gneiss, these are associated with carbonatite dykes. Most of the carbonatite ore fields are also spatially related to porphyry and porphyry skarn Mo deposits which yield Re-Os ages ranging from 148 Ma to 112 Ma (Mao *et al.*, 2008). However, the carbonatite molybdenite yields Re-Os ages from 209 Ma to 221 Ma and monazite-(Ce) U-Pb and Th-Pb ages from 208.9 ± 4.6 Ma and 213.6 ± 4.0 Ma (Huang *et al.,* 1994; Stein *et al.,* 1997; Song *et al.,* 2016) indicating that the mineralisation of the carbonatites is not related

to overprinting by the porphyry-related systems. The samples analysed in this study are from the Dashigou open pit.
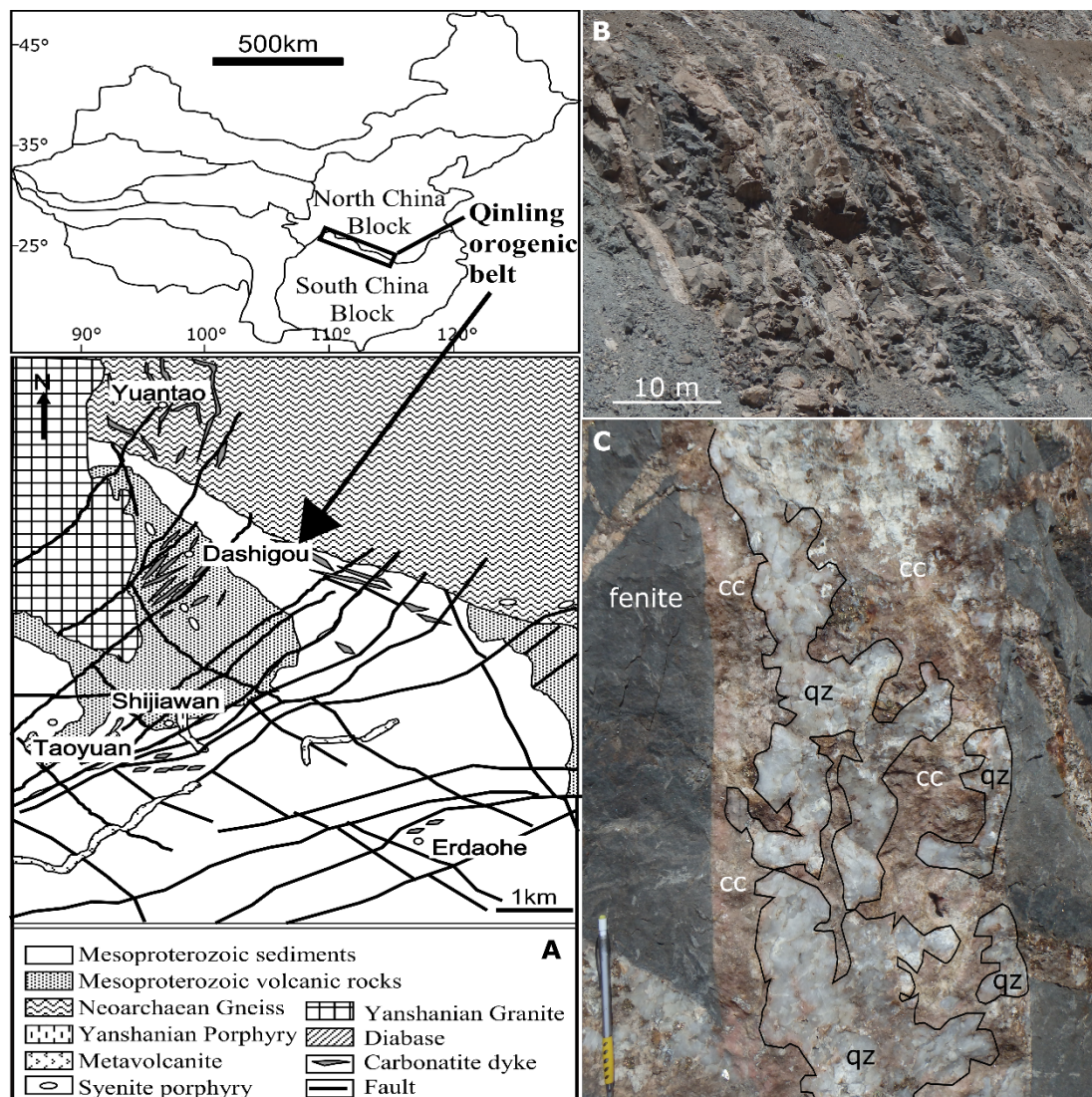
Figure 4-1: (A) Geological map of the Huanglongpu Mo-district from Smith et al., (2018). (B,C) Examples of Dashigou open pit dykes, located around WGS84 410530 49S 3803439. (B) Set of parallel calcite carbonatite dykes at the Dashigou open pit. (C) Calcite carbonatite dyke with central quartz lenses and fenetised margins

4.3.2. The Dashigou open pit

Individual molybdenite-bearing calcite carbonatite dykes at Dashigou are generally between 0.1 and 1 metre in width, and extend for several tens of meters (Fig. 4-1B). The main set of

dykes predominantly dips N to NNW at steep angles, 50-88 °N, (Smith *et al.,* 2018; Fig. 4-1B). Despite the range of dyke orientations observed by Smith *et al.,* (2018), including some east-dipping conjugate dykes, they are understood to be closely contemporaneous (Smith *et al.,* 2018; their fig.3E). The country rock gneiss has been fenitised next to the carbonatites (Fig. 4-1C), and now consists mainly of K-feldspar, phlogopite, pyrite and calcite, with minor amounts of monazite-(Ce) and titanite. However, the fenite was apparently unaffected by the later hydrothermal alteration which corroded and altered monazite-(Ce) in the samples we studied.

4.3.3. Mineralogy of the calcite carbonatites

The carbonatite dykes are dominated by calcite and are referred to here as calcite carbonatite. The majority of the dykes contain central quartz lenses (Fig. 4-1C). A few dykes show evidence for multiple opening events (Table 4-1). The calcite carbonatite dykes consist of 50 to 80 vol.% calcite, with typical individual crystals ranging from less than 0.1 cm to 2 cm in size, together with sulfates (celestine-baryte), sulphides (molybdenite, pyrite, galena and sphalerite), K-feldspar, phlogopite, albite, REE minerals and apatite. Quartz only occurs as lenses and is only observed in the calcite carbonatite dykes and not the surrounding fenite. The lenses are composed of quartz grains, ranging from less than 100 µm up to 3 cm, containing micron sized birefringent inclusions discussed later in this manuscript. Smith *et al.,* (2018) described the paragenesis of the calcite carbonatite minerals. Molybdenite can occur as disseminated grains, as fracture infill within the calcite carbonatite, with other sulphides, or in fracture infill within the fenitised gneiss. Celestine-baryte was inferred to be hydrothermal in origin and Smith *et al.,* (2018) documented a crosscutting relationship with the calcite carbonatite dykes. Pyrite and sphalerite are later than cogenetic molybdenite and pyrite.

The REE mineral assemblages of the calcite carbonatite dykes (Smith *et al.,* 2018) preserve a range of replacement textures making it possible to establish a history of REE mineral growth. The initial, magmatic stage associated with the calcite carbonatites consists of monazite-(Ce), bastnäsite-(Ce), parisite-(Ce) and aeschynite-(Ce) possibly with magmatic burbankite-(Ce); all these minerals are relatively enriched in LREE. Subsequent hydrothermal events first led the monazite-(Ce) to be altered to produce a second generation of apatite, and this was in turn replaced and overgrown by britholite-(Ce) accompanied by the crystallisation of allanite-(Ce). Bastnäsite-(Ce) and parisite-(Ce) were replaced by synchysite-(Ce) and röntgenite-(Ce). Aeschynite-(Ce) was altered to uranopyrochlore and then pyrochlore with uraninite inclusions (Smith *et al.,* 2018). These hydrothermal replacement minerals show HREE enrichment relative to the magmatic precursors.

The magmatic calcite shows some late HREE enrichment indicating that the Dashigou magmatic carbonatite system evolved to HREE-richer conditions (Xu *et al.,* 2007; Smith *et al.,* 2018). The composite dykes observed in the field suggest a sequence of calcite carbonatite pulses.

There is significant variation in the extent of hydrothermal alteration between calcite carbonatite samples, with magmatic REE phases well preserved in some but largely overprinted in others. Smith *et al.,* (2018) concluded that the hydrothermal alteration was linked to the deposition of some of the quartz including the fluid inclusions which they host.

Sample number	Field relationship	Dyke orientation	Alteration category
DSG 002	70 cm width calcite carbonatite dyke	252/77 N	altered
DSG 004	50 cm width calcite carbonatite dyke	255/80 N	altered
DSG 431	6 samples transect across complex 75 cm width multi-opening calcite carbonatite dyke. DSG 431 and DSG 436 are in contact with the fenite on each side	264/88 N	little-altered
DSG 432			little-altered
DSG 433			altered
DSG 434			altered
DSG 435			little-altered
DSG 436			altered
DSG 437	10 cm width calcite carbonatite dyke	306/58 NE	altered
DSG 437f	fenite in direct contact with the calcite carbonatite dyke DSG 437	empty cell	little-altered
DSG 005	50 cm width composite calcite carbonatite dyke	358/68 E	altered
DSG 006	6 cm width calcite carbonatite dyke	355/84 S	altered
DSG 007	4 cm width calcite carbonatite dyke	216/54 W	little-altered
ND 430-1	3 samples from the same calcite carbonatite dyke showing transition from the wall rock. ND 430-1 and ND 430-3 are in contact with the fenite on each side	ex-situ boulder	altered
ND 430-2			altered
ND 430-3			altered
ND 001f	fenite in direct contact with the calcite carbonatite dyke ND 001		little-altered

Table 4-1: Summary of the Dashigou open pit samples used in this study. The alteration categories are based on the predominant REE minerals. Little-altered refers to samples with predominantly magmatic REE minerals and altered refers to those with significant hydrothermal REE minerals (Smith et al., 2018). Only DSG 007 and DSG 434 samples do not host quartz lenses.

4.4. Methodology

Samples were collected from the Dashigou open pit in June 2016, within a 100 m radius around location WGS84 49S 410530 3803439 (Fig. 4-1A). The open pit exposes calcite carbonatite dykes intruded into country rock gneiss (Fig. 4-1). Four samples were also collected from the Yuantao mine dump a few km north of the Dashigou open pit (WGS84 49S

409886 3804124); they are labelled as ND. The two fenite samples used in this study were in direct contact with the associated calcite carbonatite samples.

Mineral and fluid inclusion parageneses were established using optical petrography followed by SEM-Back Scattered Electron (BSE) and SEM-Cathodoluminescence (SEM-CL) imaging at the University of Leeds using a FEI Quanta 650 Field Emission Gun Scanning Electron Microscope (FEG-SEM) operated at 20 kV.

Oxygen isotope measurements were undertaken on selected polished areas of some carbonatite samples mounted in an epoxy block. Prior to being mounted, the selected samples were SEM-BSE mapped. Stable oxygen isotope measurements were carried out at the Edinburgh Ion Microprobe Facility (EIMF) using a Cameca 1270 mass spectrometer operating with a primary Cs+ beam, in multi collector mode, operating at conditions of ~5 nA with a net impact energy of 20 KeV (+10 kv primary and -10 kv secondary). The beam size was about 12 μm. A EIMF calcite and a Stern S0237 baryte standard. The instrument was calibrated before each session and its drift was corrected by starting and finishing a session by analysing 5 to 10 points of the reference standards and then 5 points every 10 analyses. Linear least squares was applied as drift correction. Reproducibility of the calcite and baryte standards can be found in Appendix 4.

Raman spectroscopy was carried out in the GeoResources Laboratory, at the University of Lorraine, France. The fluid inclusion phases were analysed separately to identify solids and Raman-active solution and gas components. Analyses were performed using a LabRAM Raman microspectrometer (Horiba Jobin Yvon) equipped with a Linkam THMS600 microthermometry stage. The excitation beam was a monochromatic green laser at 514 ηm (ionised argon 74.53 ηm, with a working temperature of -128 °C and a Pn of 500 mW). For each solid and gas analysis a spectrum was taken directly next to the fluid or solid inclusion to allow subtraction of the quartz and air N_2 peaks from the analysed spectrum. The

subtractions were made in LabSpec software, and CrystalSleuth was used to identify the solids. The gas proportions within the fluid inclusions were estimated using the method of Dubessy *et al.,* (1989).

Microthermometry measurements were carried out at the University of Leeds using a Linkam MDS600 Heating Freezing Stage attached to a TMS93 temperature programmer and controller and an LNP cooling system mounted on an Olympus BX50 microscope. Double polished wafers were between 200 μm to 300 μm thick. The stage was calibrated using synthetic fluid inclusion wafers containing pure water fluid inclusions (0 °C and 374.1 °C) and H_2O-CO_2 fluid inclusions (-56.6 °C and 31.1 °C) provided by Ronald Bakker, Leoben University, Austria.

Bulk rock analyses were carried out by Activation Laboratories Ltd. with the sample preparation undertaken at the University of Leeds. Samples were powdered using a steel pestle and mortar and an agate TEMA barrel and sieved to < 200 μm. The methods 4Litho and 4F-Total sulfur were used on the calcite carbonatite and country rock samples. The detection limits are detailed in Appendix 2.

4.5.   Results

4.5.1. Calcite carbonatites

The calcite carbonatite samples have been divided into two broad alteration categories, little-altered and altered, based on the extent to which new REE minerals have replaced the original magmatic ones (Table 4-1). No correlation of alteration with the different dyke orientations was observed. The little-altered samples host predominantly magmatic REE minerals. Monazite-(Ce) is the main primary magmatic REE mineral in the calcite carbonatite samples, and is usually fairly pristine in the little-altered samples (Fig. 4-2A), although in

some instances it can show overgrowth and fracture-fill of late magmatic molybdenite (Fig. 4-2B). In the altered samples (Table 4-1) monazite-(Ce) is at least partially corroded and is sometimes fully replaced by new HREE-enriched phases (Fig. 4-2C), with later HREE-enriched phases in fractures (Fig. 4-2D). The HREE-enriched phases are predominantly Ca-REE-fluorcarbonates, uraninite, xenotime-(Y) and churchite-(Y) together with unidentified Y and REE-bearing silicate minerals with a variable amount of Ca and Fe, and unidentified Ti, Nb, U, Y, REE-bearing oxide phases with a variable amount of Fe and Ca (Fig. 4-2C; Table 4-2). Smith *et al.,* (2018) described the REE mineral paragenesis, demonstrating that the hydrothermal REE mineralisation becomes more HREE enriched with each subsequent hydrothermal event.

Xu *et al.,* (2007) first reported that the Huanglongpu carbonatites are anomalously rich in the HREE, exhibiting a distinctive flat REE pattern. Xu *et al.*, (2010) investigated calcite carbonatites from the Yuantou, Shijiawan and the Dashigou deposits and reported that total REE concentrations could exceed 3000 ppm. They found that ∑LREE/(HREE+Y) ratios ranged from 0.6 to 2.8. We have obtained a wider range of ∑(LREE/HREE+Y) ratios in this study, from 1.1 to 17.3, correlated with the alteration categories described above, with the little-altered calcite carbonatite samples showing ∑LREE/HREE ratios ranging from 9.9 up to 17.3 and the altered calcite carbonatite samples ratios ranging from 1.1 to 3.8 (Table 4-3). ∑HREE+Y values also overlap with those reported by Xu *et al.,* (2007, 2010).

The four little-altered calcite carbonatite samples in this study (DSG 431, DSG 431-2, DSG 007 and DSG 435; Tables 4-1, 4-3) are shown by blue lines on Fig. 4-3 and do not show the HREE-enrichment documented by Xu *et al.,* (2010). Instead, they exhibit a LREE-enriched pattern typical of carbonatites worldwide (Woolley and Kempe, 1989) and similar to that of the fenites (Fig. 4-3-green lines). The fenite REE pattern reflects its REE mineralisation mainly consisting of unaltered monazite-(Ce) which has been observed in other carbonatite

associated fenites (e.g. Thair and Olli, 2013; Midende *et al.,* 2014; Trofanenko *et al.,* 2016). In contrast, the altered calcite carbonatites in this study (Table 4-1, shown in red on Fig. 4-3) are HREE-enriched and plot close to the samples described by Xu *et al.,* (2010) with the most HREE-enriched samples showing a positive Y anomaly (Fig. 4-3).

Mineral	Formula	Occurrence
REE minerals		
monazite-(Ce)	$CePO_4$	carbonatite rock
uraninite	UO_2	carbonatite rock
xenotime-(Y)	YPO_4	carbonatite rock
churchite-(Y)	$YPO_4.2H_2O$	carbonatite rock
HREE enriched fluorcarbonate	n.a.	carbonatite rock
HREE enriched silicate	n.a.	carbonatite rock
HREE enriched oxide	n.a.	carbonatite rock
Sulfate		
celestine	$SrSO_4$	carbonatite rock/fluid inclusion
baryte	$BaSO4$	carbonatite rock/fluid inclusion
arcanite	K_2SO_4	fluid inclusion
anhydrite	$CaSO_4$	fluid inclusion
aphthilatite	$(K,Na)_3Na(SO_4)_2$	fluid inclusion
glauberite	$Na_2Ca(SO_4)_2$	fluid inclusion
thenardite	Na_2SO_4	fluid inclusion
anglesite	$PbSO_4$	fluid inclusion
Sulphides		
pyrite	FeS_2	carbonatite rock
galena	PbS	carbonatite rock
sphalerite	$(Zn,Fe)S$	carbonatite rock
molybdenite	MoS_2	carbonatite rock/fluid inclusion
Others		
calcite	$CaCO_3$	carbonatite rock/fluid inclusion
dolomite	$CaMg(CO_3)_2$	fluid inclusion
gypsum	$CaSO. 2H_2O$	fluid inclusion
apatite	$Ca_5(PO_4,CO_3)_3(OH,F)$	carbonatite rock
quartz	SiO_2	carbonatite rock
K-feldspar	$KAlSi_3O_8$	carbonatite rock
phlogopite	$KMg_3(Si_3Al)O_{10}(F,OH)_2$	carbonatite rock
albite	$NaAlSi_3O_8$	carbonatite rock
muscovite	$KAl_2(AlSi_3O_{10})(OH)_2$	fluid inclusion
whewellite	$Ca(C_2O_4) \cdot H_2O$	fluid inclusion

Table 4-2: List of minerals encountered in this study and their occurrences.

	DSG 002	DSG 004	DSG 431	DSG 431-2	DSG 432	DSG 433	DSG 434	DSG 435	DSG 436	DSG 005	DSG 437	DSG 437f	DSG 007	DSG 006
Major elements (wt%)														
Total S	2.44	1.00	4.46	3.28	2.64	5.60	7.57	2.63	0.24	3.00	7.59	0.84	2.63	1.33
SiO_2	19.15	5.42	9.53	65.54	69.43	13.20	13.57	77.54	6.61	13.67	14.03	46.96	74.84	13.41
Al_2O_3	0.14	0.15	0.85	0.35	0.03	0.06	0.14	0.15	0.05	0.02	0.02	12.43	0.15	0.20
$Fe_2O_3(T)$	0.75	1.12	0.71	0.78	0.41	0.45	0.36	1.94	0.76	0.39	5.78	10.19	1.89	1.96
MnO	1.82	2.16	1.84	0.43	0.40	1.11	1.08	0.40	2.23	1.38	1.22	0.25	0.40	2.51
MgO	0.37	0.63	0.44	0.09	0.08	0.24	0.22	0.08	0.49	0.31	0.24	2.96	0.08	0.41
CaO	33.53	46.16	29.58	8.10	7.69	23.83	20.31	8.18	48.34	36.18	31.90	8.24	8.23	44.73
Na_2O	0.03	0.03	0.03	0.01	0.01	0.02	0.02	0.01	0.04	0.03	0.02	0.17	0.01	0.03
K_2O	0.10	0.13	0.73	0.30	0.03	0.05	0.13	0.13	0.04	0.02	0.01	10.65	0.12	0.14
TiO_2	0.01	0.05	0.03	0.01	< 0.01	< 0.01	0.03	0.01	< 0.01	< 0.01	< 0.01	1.50	0.01	0.01
P_2O_5	0.06	0.09	0.27	0.04	< 0.01	0.01	0.01	0.06	< 0.01	< 0.01	< 0.01	0.57	0.07	< 0.01
LOI	26.91	36.33	24.95	5.86	5.55	9.93	15.51	6.09	38.43	28.68	23.62	5.17	6.08	34.11
Partial total	**82.88**	**92.28**	**68.95**	**81.51**	**83.63**	**48.89**	**51.39**	**94.59**	**97.00**	**80.69**	**76.84**	**99.09**	**91.88**	**97.51**
Trace elements (ppm)														
Sc	3	7	5	1	1	4	2	1	5	2	1	21	1	3
V	< 5	< 5	< 5	< 5	< 5	< 5	< 5	< 5	< 5	< 5	< 5	159	< 5	< 5
Ba	32930	14230	51050	46240	39820	29220	114700	16860	391	59480	53600	1562	19570	1551
Sr	> 10000	> 10000	> 10000	> 10000	> 10000	> 10000	> 10000	> 10000	6094	> 10000	> 10000	746	> 10000	4472
Zr	4	< 2	< 2	< 2	< 2	< 2	< 2	< 2	< 2	< 2	< 2	180	< 2	< 2
Cr	< 20	< 20	< 20	< 20	< 20	< 20	< 20	< 20	< 20	< 20	< 20	120	< 20	< 20
Co	< 1	< 1	< 1	< 1	< 1	< 1	< 1	< 1	< 1	< 1	< 1	26	< 1	< 1
Ni	< 20	< 20	< 20	< 20	< 20	< 20	< 20	< 20	< 20	< 20	< 20	40	< 20	< 20
Cu	10	20	30	< 10	< 10	40	< 10	< 10	< 10	< 10	< 10	60	10	20
Zn	< 30	< 30	< 30	< 30	< 30	< 30	910	170	90	260	90	130	170	< 30
Ga	< 1	4	11	7	2	1	< 1	6	5	5	< 1	25	2	2
Rb	< 2	3	7	3	< 2	3	< 2	< 2	< 2	< 2	< 2	186	< 2	< 2

Nb	10	44	19	2	< 1	2	85	10	11	4	9	16	9	1
Mo	> 100	> 100	> 100	> 100	37	> 100	> 100	> 100	> 100	> 100	> 100	4	> 100	17
La	508	531	1750	455	167	282	582	541	148	453	454	181	561	179
Ce	760	867	2620	589	125	387	476	794	385	617	522	321	810	422
Pr	69	80	221	49	9	37	37	68	51	65	53	32	68	52
Nd	235	271	658	142	32	140	123	197	223	251	212	110	199	218
Sm	40	48	73	18	8	31	27	21	61	52	42	18	19	46
Eu	13	15	19	7	5	12	15	5	18	17	15	5	5	14
Gd	43	50	45	12	9	36	30	12	66	43	36	13	12	44
Tb	7	8	6	2	2	6	6	2	11	6	5	2	1	7
Dy	46	51	37	10	10	39	36	8	67	35	30	10	8	40
Ho	11	11	8	2	2	8	8	2	14	7	6	2	2	9
Er	38	37	29	7	7	26	26	6	47	23	19	5	6	29
Tm	7	6	5	1	1	4	4	1	8	4	3	1	1	5
Yb	50	43	37	9	8	32	32	7	57	25	21	5	7	38
Lu	8	7	6	1	1	4	5	1	9	4	3	1	1	6
Y	466	437	318	75	73	244	235	54	472	217	198	53	53	348
Pb	30	19	116	178	3510	> 10000	396	656	7210	857	80	173	528	46
Bi	< 0.4	< 0.4	1	< 0.4	4	138	2	2	4	1	0	< 0.4	3	1
U	15	59	16	3	0	6	97	13	9	3	17	8	13	1
∑LREE	1611	1797	5322	1252	342	877	1244	1621	868	1438	1283	662	1657	917
∑HREE+Y	689	664	511	126	118	411	396	96	769	381	336	96	96	539
∑LREE/HREE	2.3	2.7	10.4	9.9	2.9	2.1	3.1	16.9	1.1	3.8	3.8	6.9	17.3	1.7

Table 4-3: Bulk rock analyses of the Dashigou open pit rocks described in Table 1, DSG 437f is the fenitised country gneiss associated to sample 437. '<' below detection limit of the instrument (detailed in Appendix 1). LREE = La to Sm, HREE = Eu to Lu + Y. Ge, Sb, In, TI and Ta are under 2 ppm; As, Be, Sn, Cs and Hf are under 10 ppm and Ag and Th are under 20 ppm. Note that the total below 100% reflects the lack of data for Mo, Sr and F, which can be important component of some samples. ND sample's analyses are detailed in Appendix 5
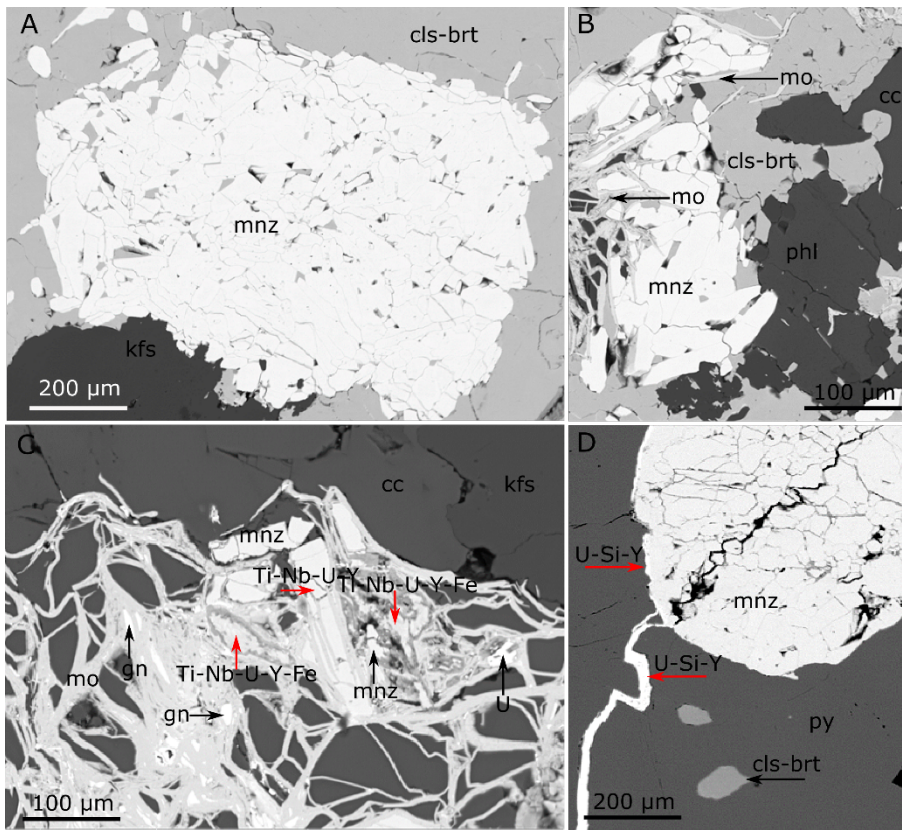
Figure 4-2: BSE images of magmatic monazite-(Ce) with different degrees of alteration. (A) Magmatic monazite-(Ce) and K-feldspar enclosed by hydrothermal celestine-baryte in a little-altered calcite carbonatite (DSG 431). (B) Magmatic phlogopite and monazite-(Ce) with overgrowth and fracture fill of molybdenite (DSG 431). (C) Magmatic monazite-(Ce) partially replaced by late magmatic molybdenite and an unidentified HREE-rich phase in an altered calcite carbonatite (DSG 434). (D) Magmatic monazite-(Ce) hosted by pyrite with a hydrothermal Y-rich phase in fractures and at the interface of monazite-(Ce) and pyrite grains, note associated hydrothermal celestine-baryte. Altered calcite carbonatite (DSG 004). The red arrows in (C) and (D) indicate analysed points where the listed elements were the dominant constituents of unidentified hydrothermal phases. Abbreviation: cls-brt-celestine-baryte; mnz-monazite-(Ce); kfs-K-feldspar; mo-molybdenite; phl-phlogopite; cc-calcite; U-uraninite; gn-galena; py-pyrite.
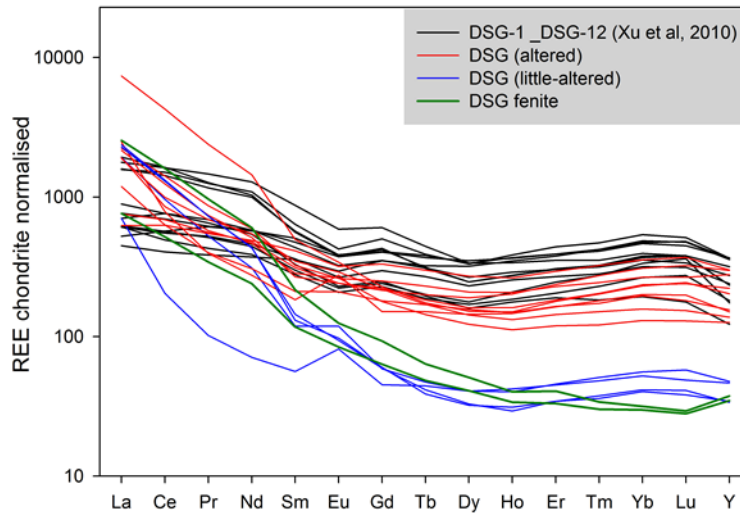
Figure 4-3: REE chondrite-normalised patterns (McDonough and Sun, 1995) for calcite carbonatites (little hydrothermal alteration in blue and altered in red) and associated fenites (green lines). Samples with results from Xu et al., (2010) for the Dashigou open pit (alteration not specified) (black lines) are shown for comparison.

4.5.2. Quartz lenses within calcite carbonatite dykes

Irrespective of the host dyke's orientation, SEM-CL imaging reveals the presence of three quartz generations making up the quartz lenses that occur within them (Fig. 4-4). The dominant generation is the earliest, Qz-1; it is moderately luminescent and shows some poorly-defined growth zonation. Quartz 2 occurs as non-luminescent overgrowths and porosity infills, merging into fracture fills cutting grains of Qz-1. The last generation, Qz-3, is also a non-luminescent quartz and occurs as thread-like fracture fills cutting both earlier generations. Qz-1 lacks fluid inclusions and appears patchy and strained in cross polars. Quartz 2 and Qz-3 are both cloudy and contain fluid inclusions.
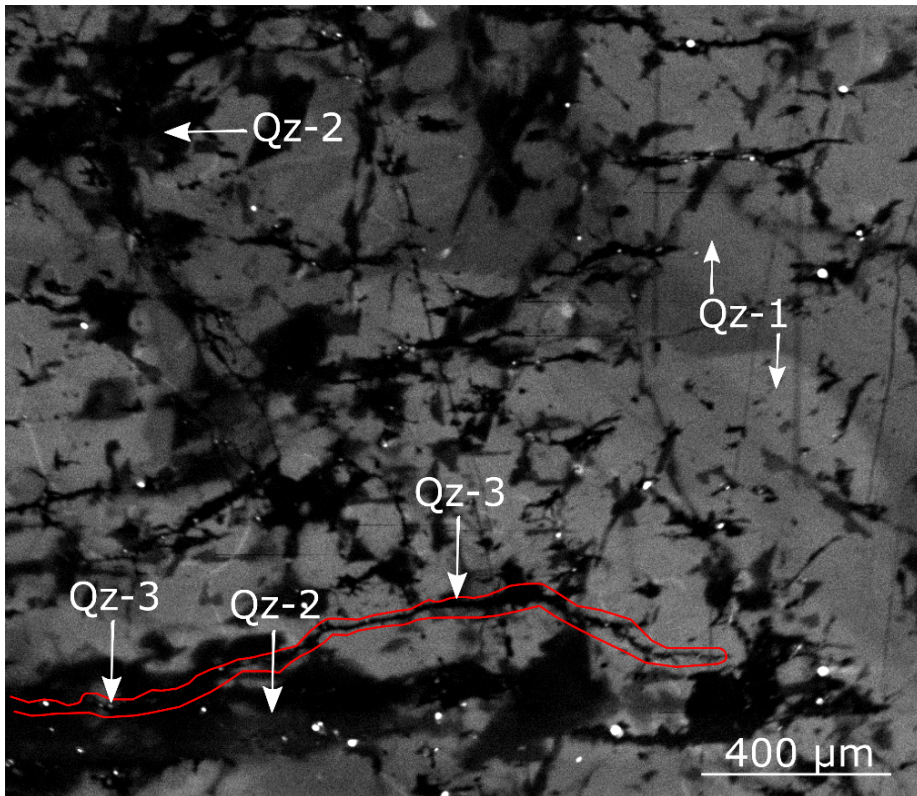
Figure 4-4: SEM-CL image showing the paragenesis of the three quartz generations within a calcite carbonatite dyke, note the irregular zoning of the primary quartz (Qz-1) (DSG 005 001).

4.5.3. Fluid inclusion paragenesis and hydrothermal HREE mineralisation

Smith *et al.,* (2018) showed that secondary quartz grew at the same time as the later hydrothermal REE minerals that are enriched in the HREE. Figure 4-5 shows the relationship between HREE minerals and Qz-2 and Qz-3 partially replacing magmatic calcite. HREE phases occur at the interface between calcite and Qz-2 (Fig. 4-5A) and in calcite fractures associated with celestine-baryte mineralisation related to Qz-3 (Fig. 4-5B).
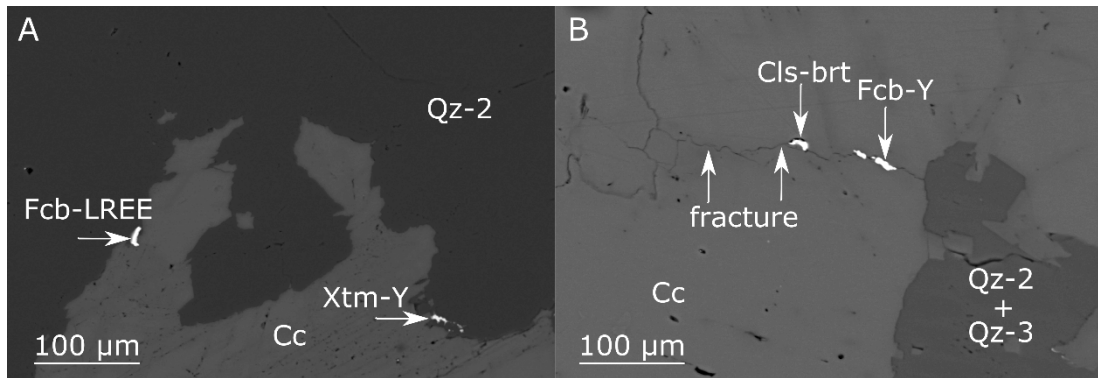
Figure 4-5: BSE images of HREE enriched calcite carbonatite sample DSG 433. (A) HREE mineral hosted in hydrothermal Qz-2 at the interface with earlier calcite. (B) Mineralisation of a fracture in calcite by hydrothermal HREE minerals and celestine-baryte, inferred to be associated with the partial replacement of the calcite by quartz. Abbreviation: Fcb-LREE: fluorcarbonate-(LREE); Xtm-Y: Xenotime-(Y); Cc: calcite; Cls-brt: celestine-baryte.

4.5.4. Calcite and quartz stable oxygen isotope data

The samples analysed are from two distinct dykes and data is presented in Table 4-4. Secondary quartz data is from both Qz-2 and Qz-3 (non-luminescent quartz, Fig. 4-4) since these could not be distinguished during the analyses. Because of the difficulty in finding exact points for analysis in the ion probe, traverses were made across areas with all quartz generations to ensure that primary and secondary generations would be analysed. It is clear from the results that both Qz-1 and secondary quartz (Qz-2 and Qz-3) have similar compositions with tightly constrained populations of data that differ by no more than the analytical uncertainty (c. 0.25‰). Average compositions are close to 10‰ SMOW (e.g. DSG 002 Qz-1 $\delta^{18}O$ ranges from 9.72‰ to 10.43‰ and secondary quartz $\delta^{18}O$ ranges from 9.57‰ to 10.18‰; Table 4-4). Magmatic calcite has similar $\delta^{18}O$ values to quartz, averaging to 9.66‰ for sample DSG 437 and 10.34‰ for sample DSG 002. These values are similar to calcite analysed by Bai *et al.,* (2019) from the Huanglongpu and the Huangshui'an carbonatites of the Lesser Qinling Orogen ($\delta^{18}O$ ranges from 7.10‰ to 9.48‰).

sample	DSG 437			DSG 002		
mineral	calcite (‰)	Qz-1 (‰)	Qz-2/Qz-3 (‰)	calcite (‰)	Qz-1 (‰)	Qz-2/Qz-3 (‰)
$\delta^{18}O$ min	7.00	9.30	9.44	9.93	9.72	9.57
$\delta^{18}O$ max	10.14	11.03	10.32	10.81	10.43	10.65
average	**9.66**	**9.82**	**9.87**	**10.34**	**9.98**	**10.18**
stdev	0.54	0.36	0.30	0.23	0.27	0.80
n	30	24	6	20	10	10

Table 4-4: Summary of the oxygen isotope data from calcite and quartz, all as $\delta^{18}O$ SMOW.

4.5.5. Fluid inclusion petrography and microthermometry

Three samples of quartz lenses from altered carbonatites were selected for fluid inclusion study (Fig. 4-4-3; Table 5): DSG 002, DSG 437 and DSG 433 (Table 4-1). Fluid inclusions range in size from less than 5 µm up to 70 µm but are commonly between 10 µm to 40 µm. Due to the cloudiness of the Qz-2 and Qz-3, we were unable to collect freezing measurements such as Tm_{CO2} and Tm_{CLA}. Fluid inclusions are abundant in Qz-2 and mainly occur as clusters or in fluid inclusion-rich zones in cloudy quartz (Fig. 4-6A), more rarely in planar arrays and linear trails. The fluid inclusions usually have quite irregular shapes (Fig. 4-6A,B,D) and are predominantly LCO_2+VCO_2+Lw and $LCO_2+VCO_2+Lw+S(s)$ type fluid inclusions (where LCO_2 = liquid CO_2, VCO_2 = gas CO_2, Lw = aqueous liquid and S(s) = from one to five solids). They show variable proportions of CO_2 relative to the aqueous liquid, even within the same fluid inclusion cluster (Fig. 4-6A). Some inclusions have a homogenized CO_2 bubble at room temperature and are referred to as LCO_2+Lw fluid inclusions (Fig. 4-6A; Table 4-5; Appendix 6). About 15% of the fluid inclusions in Qz-2 contain one or more solids (Fig. 4-6A-F; Tables 4-2,4-5). These solids are often birefringent and individual fluid inclusions may contain up to five different solids, but there is only ever one opaque solid (Fig. 4-6D). On rare occasions, fluid inclusions are not CO_2-bearing and only comprise an aqueous solution and solid(s) (Lw+S) with the solid taking up most of the inclusion volume. Qz-2 may also contain small (< 15 µm) birefringent solid inclusions near the fluid inclusions, within the same cluster or fluid

inclusion trail. These solid inclusions are of comparable size to the solids observed within the fluid inclusions (Fig. 4-6A).

Microthermometric analysis of Qz-2 fluid inclusions show a scatter of Th_{CO_2} from + 12 °C to + 30.9 °C, yielding a density of the CO_2 phase of 0.85 $g \cdot cm^{-3}$ to 0.47 $g \cdot cm^{-3}$ (Valakovich and Altunin, 1968). CO_2 always homogenised to the liquid phase.

In Qz-3, fluid inclusions occur in planar arrays decorating healed fractures (Fig. 4-6G-I) or as linear fluid inclusions trails in finer healed fractures (< 50 μm). Overall, the Qz-3 fluid inclusions are smaller than those in Qz-2 ranging from less than 5 μm to 25 μm. These fluid inclusions tend to have similar shapes within a single array, either elongate or with a more rounded shape (Fig. 4-6H-I). Quartz 3 hosts a wider variety of fluid inclusion types (Table 4-5) but they are predominantly of LCO_2+VCO_2+Lw type, similar to those in Qz-2, but with more variability in the relative proportion of the CO_2 and aqueous phase (Fig. 4-6H). Some of these fluid inclusions have a homogenised CO_2 bubble below room temperature. In aqueous inclusions (Lw+V) there is a reasonably constant liquid/vapour ratio (c. 80:20). Lastly, there are monophase Lw inclusions which are small (< 15 μm) and tend to occur in wider healed fractures, typically from 100 μm to 400 μm (Fig. 4-6I). They are clearly secondary. Lw and Lw+V type fluid inclusions can occur in the same fluid inclusion trail and in this instance the vapour bubble proportion is usually lower at around 10% (Fig. 4-6I). Quartz 3 also hosts small (< 15 μm) birefringent solid inclusions, however they tend to be less abundant than in Qz-2.

For Qz-3, only 5 measurements of Th_{CO_2} on the LCO_2+VCO_2+Lw inclusions could be performed; values range from 26.4 °C to 29.8 °C corresponding to CO_2 densities of 0.70 $g \cdot cm^{-3}$ to 0.56 $g \cdot cm^{-3}$ (Valakovich and Altunin, 1968). Twenty Lw+V fluid inclusions show a temperature of total homogenisation (Th_{TOT}) ranging from about 120 °C to 222 °C. The Lw inclusions fail to nucleate a vapour bubble despite cooling to a temperature of -130 °C for 5 minutes, something that is often indicative of low trapping temperature.

The sequence of the different types of fluid inclusions within Qz-3 is often ambiguous as cross-cutting relationships have not been observed. Nonetheless, in Qz-3 the Lw+V inclusions show a max Th_{TOT} of 222 °C, and this is likely to be higher than the trapping temperature of the Lw inclusions, suggesting that they are likely not contemporaneous. The non CO_2-bearing fluid inclusions are inferred to be the youngest population (Fig. 4-7).
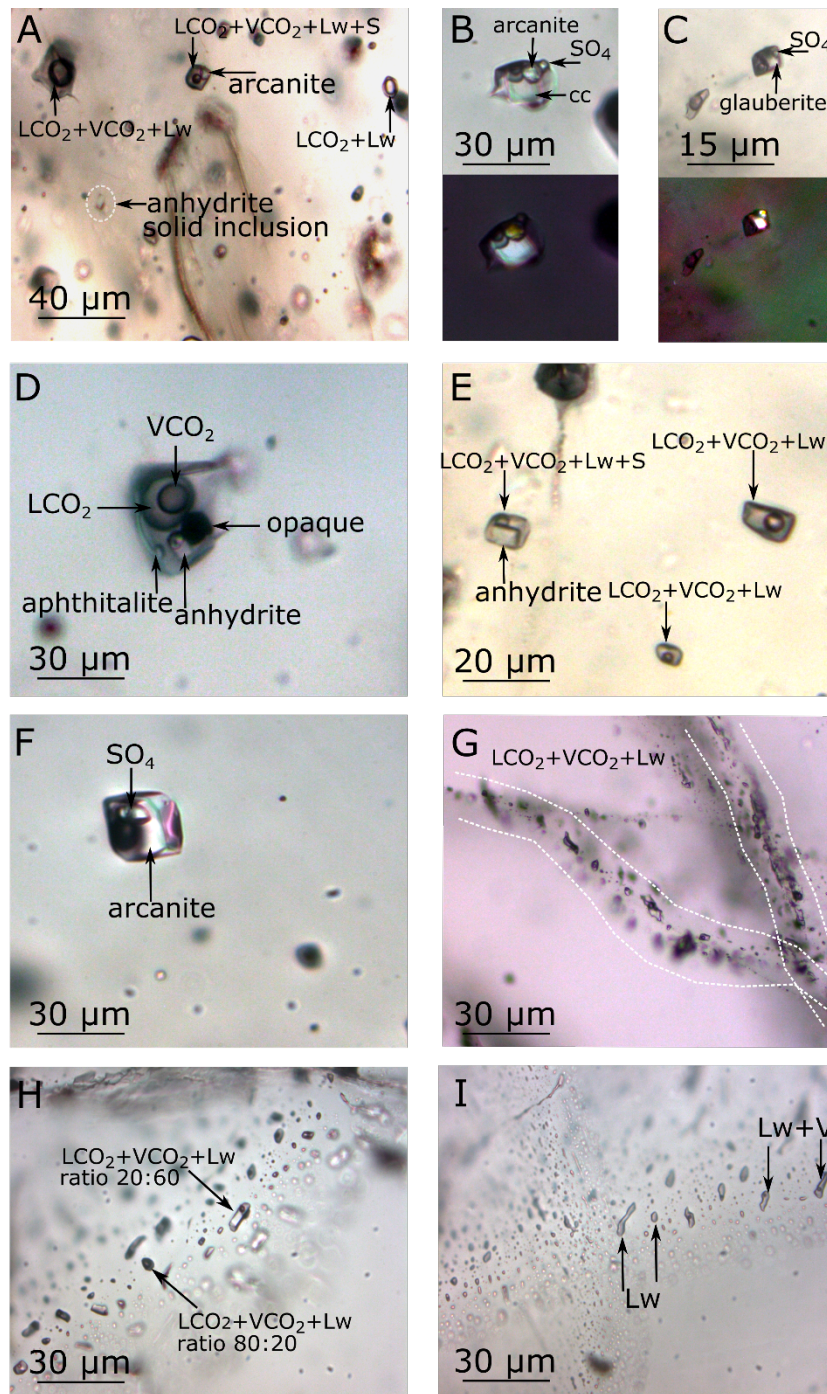
Figure 4-6: Photomicrographs of fluid inclusions hosted in Qz-2 (E-F) and Qz-3 (G-I). (A)
$LCO_2+VCO_2\pm Lw\pm S$ fluid inclusions hosted in cloudy quartz showing variation of the CO_2 and aqueous
phase ratio, the fluid inclusion on the top right show the gas bubble taking up most of the fluid
inclusions volume while the fluid inclusion in the top middle show a rather small gas bubble, with a
homogenised CO_2-bearing fluid inclusions ($LCO_2\pm Lw$). The $LCO_2+VCO_2\pm Lw+S$ inclusion contains an
arcanite solid. Note the anhydrite solid inclusion in the quartz has a similar size to the trapped solid
(DSG 002 4). (B) $LCO_2+VCO_2\pm Lw+3S$ fluid inclusion hosting sulfate and calcite solids (DSG 433 2f) with
the corresponding cross polar image. (C) $LCO_2+VCO_2\pm Lw+2S$ fluid inclusion hosting two sulfate solids

and a LCO$_2$±Lw fluid inclusion (DSG 437 8i) with the corresponding cross polar image. (D) LCO$_2$+VCO$_2$±Lw+4S fluid inclusions clearly showing the CO$_2$ vapour bubble within the CO$_2$ liquid. The fluid inclusion hosts two identified sulfates, one unidentified solid and one opaque (DSG 433 2a). (E) Three LCO$_2$+VCO$_2$±Lw±S fluid inclusions cluster with one with a trapped anhydrite solid (DSG 002 13a). (F) LCO$_2$+VCO$_2$±Lw+2S fluid inclusion hosting two sulfate solids like for (B) most of the space is taking up by the solids (DSG 433 4d). (G) Thin healed fractures hosting LCO$_2$+VCO$_2$±Lw fluid inclusions cross cutting fluid inclusion free Qz-1 (DSG 437). (H) LCO$_2$+VCO$_2$±Lw fluid inclusions in a planar array showing variation of the CO$_2$ and aqueous phase ratio (DSG 433 33b). (I) Wide healed fracture hosting Lw and Lw+V in the same planar array (DSG 433 29). Abbreviations: cc-calcite, SO$_4$-unidentified sulfate phase.

		Magmatic stage	Qz-2	Qz-3
			early hydrothermal	late hydrothermal
REE minerals (after Smith et al., 2018)	Monazite			
	Bastnasite			
	Parisite			
	Burbankite			
	Apatite			
	Britholite			
	Allanite			
	Synchysite			
	Rontgenite			
Fluid inclusion types	LCO$_2$+VCO$_2$+Lw			
	LCO$_2$+VCO$_2$±Lw±S(s)			
	Lw+V/Lw			
Sulphate occurence	SO$_4$ in sol			
	SO$_4$ solid in FI			
	SO$_4$ inclusion in qz			
Major gangue minerals	Calcite			
	Celestine-baryte			

Figure 4-7: Simplified paragenetic diagram illustrating the paragenetic sequence associated to the later quartz generations in the Huanglongpu carbonatites. The REE minerals paragenesis is after Smith et al., (2018). Bar thickness represents minerals and fluid inclusions abundance. Abbreviation: FI-fluid inclusion, qz-quartz.

112

Fluid inclusion type	Occurrence	Microthermometry	Anion in solution	Solid within fluid inclusion	Gas component
LCO_2+VCO_2+Lw/LCO_2+Lw	Qz-2			n.a.	
$LCO_2+VCO_2+Lw+S(s)$	Qz-2	Th_{CO2} = 12.0 °C to 30.9 °C	SO_4^{2-}	Mainly: arcanite, anhydrite, celestine, glauberite, aphthilatite, unidentified sulfate, calcite. Few: whewellite, thenardite, anglesite, dolomite, molybdenite, gypsum, muscovite, unidentified phosphate.	CO_2 varies from 68% to 100% with N_2; trace of H_2S, CH_4 and H_2
$LCO2+VCO2+Lw/LCO_2+Lw$	Qz-3	Th_{CO2}= 26.4 °C to 29.8 °C	SO_4^{2-} in 55%	n.a.	CO_2 > 99 % with trace of N_2
Lw+V	Qz-3	Th_{TOT} = 120.0 °C to 222.3 °C	SO_4^{2-} in 65%	n.a.	n.a.
Lw	Qz-3	n.a.	SO_4^{2-} in 75%	n.a.	n.a.

Table 4-5: Summary of the different fluid inclusion types and their characteristics measured by microthermometry and Raman spectroscopy.

4.5.6. Raman spectroscopy

About 200 fluid inclusions were analysed from Qz-2 and Qz-3 in the three samples investigated (Table 4-5; Appendix 6). Compared to Qz-2, Qz-3 fluid inclusions are less suitable for Raman spectroscopy and microthermometric analysis as the majority are smaller than 20 µm. A summary of the fluid inclusion Raman spectroscopy data is provided in Appendix 6. When possible, the same fluid inclusions were analysed for solution, solid and gas. Both solid-bearing and solid-absent inclusions were analysed for solution components and gave comparable results.

4.5.6.1. Quartz-2 fluid inclusions

The aqueous liquid phase of approximately 100 CO_2-bearing fluid inclusions was analysed by Raman spectroscopy. Sulfate (SO_4^{2-}) ions were detected in solution in 90% of the fluid inclusions, from the peak at 981 cm^{-1}. A few inclusions without detectable sulfate in solution have sulfate solids and it is likely that where sulfate was not found this was a result of the small volume of liquid available. HSO_4^- was not detected during the analysis (1050 cm^{-1}), precluding very acidic conditions (pH < 2).

In approximately 52 CO_2-bearing fluid inclusions, the vapour phase composition was determined. It is dominated by CO_2 and N_2 with CO_2 between 68% to 100%. Ninety percent of the fluid inclusions have a CO_2 content ≥ 95%. H_2S, CH_4 and H_2 were only detected as trace constituents (< 1%) of the vapour phase. No difference in vapour phase composition was detected between solid-bearing inclusions and the inclusions without solids.

The majority of the solids hosted in the fluid inclusion in Qz-2 are sulfates (Figs 4-8, 4-9). They include arcanite, anhydrite, celestine, aphthilatite and some other unidentified sulfates (Table 4-2); a few calcite crystals were also found (Fig. 4-8). Note that celestine and glauberite have very similar Raman spectra and they can be hard to differentiate; when this

was the case they are noted as celestine/glauberite in Appendix 6. Whewellite, thenardite, anglesite, dolomite, molybdenite, gypsum, muscovite and an unidentified phosphate mineral were also detected in fluid inclusions (Table 4-2). The opaque solids could not be identified as they moved under the laser beam.

Solid inclusions also occur directly hosted in the quartz and these are predominantly sulfates (mainly anhydrite with one unidentified sulfate) and calcite.
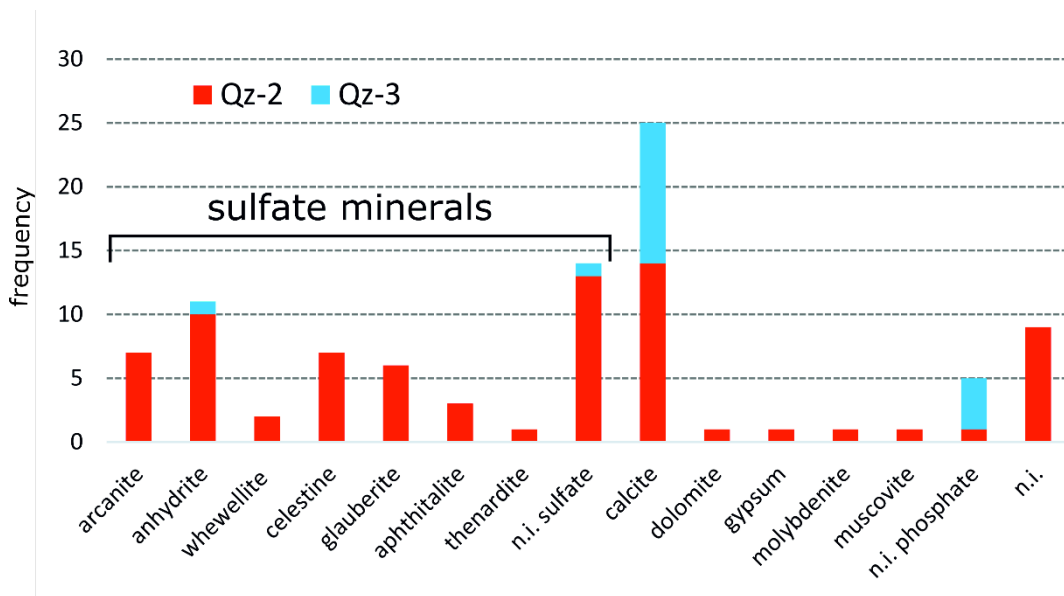
Figure 4-8: Frequency histogram showing the different minerals identified by Raman spectroscopy within the fluid inclusions and hosted as solid inclusion in the quartz in Qz-2 and Qz-3. Abbreviation: n.i. is non-identified. Note that the celestine/glauberite spectra are counted in the n.i. sulfate bar.
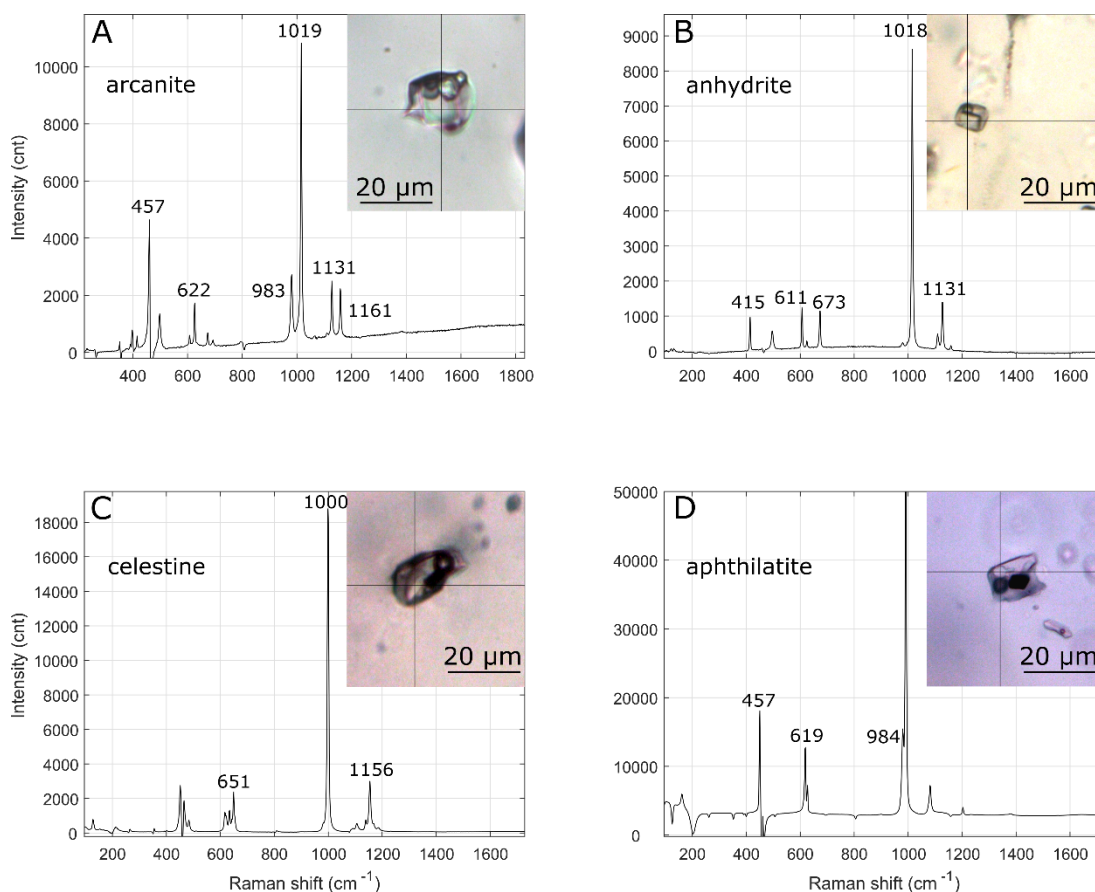
Figure 4-9: Laser Raman spectroscopy spectra of some trapped solids hosted in Qz-2 fluid inclusions from the Dashigou calcite carbonatites note that the background signal from the quartz were subtracted. (A) Arcanite spectrum of a $LCO_2+VCO_2+Lw+3S$, the solid on the right is calcite and the solid in the middle is an unidentified sulfate solid (DSG 433 2f-1). (B) Anhydrite spectrum of a LCO_2+VCO_2+Lw+S (DSG 002 13a-1). (C) Celestine spectrum of a $LCO_2+VCO_2+Lw+2S$, the celestine crystal is accompanied with an unidentified opaque (DSG 437 8b-1). (D) Aphthilatite spectrum in a $LCO_2+VCO_2+Lw+3S$, the opaque and the small transparent solid are unidentified (DSG 433 6a).

4.5.6.2. Quartz-3 fluid inclusions

Sulfate was only detected in about half of the 27 LCO_2+VCO_2+Lw fluid inclusions analysed from Qz-3 (Table 4-5) and, as with Qz-2, fluid inclusions with and without detectable sulfate in solution occur within the same inclusion trails. Like Qz-2, CO_2 is the main component of the vapour phase, but in these inclusions is always > 99%, with N_2 occurring in trace amounts only. The majority of the solid inclusions hosted directly in Qz-3 are calcite with some unidentified phosphate and sulfate particles (Fig. 4-8).

116

The aqueous portions of two Lw fluid inclusions were analysed and SO_4 was detected in both. About 75% of the 16 Lw fluid inclusions also had detectable sulfate in solution (Table 4-5).

Compared to Qz-2 fluid inclusions, Qz-3 fluid inclusions lack sulfate solids and sulfate is not always detected in solution. Likewise, there are fewer solid sulfate inclusions in Qz-3.

4.5.7. Fluid inclusions origin and reconstructed composition

The $LCO_2+VCO_2\pm Lw\pm S(s)$ fluid inclusions in the Qz-2 and Qz-3 generations have variable CO_2/aqueous phase ratios (Fig. 4-6A,H), from some that are nearly pure CO_2 inclusions to others than contain multiple solids, occurring in the same inclusions trails. This suggests that the fluid inclusions result from heterogeneous trapping of different phases that coexisted at the time of fluid inclusion formation, including an aqueous liquid, supercritical CO_2 and sulfate solids. Although the solids could be daughter minerals, formed after trapping during cooling of a homogeneous fluid, the compositional variability (Figs 4-8; 4-9; Table 4-5) and the fact that they show no signs of dissolution during heating before the inclusions decrepitate between 225 °C to 325 °C, makes this unlikely. Accidental trapping is the preferred interpretation, particularly since some of the same solid phases also occur in the quartz as solid inclusions of similar size (Fig. 4-6A). We infer that these solids were present in the fluid while Qz-2 was being precipitated. Hence, the composition of these inclusions does not represent any single fluid. Despite this limitation, we have attempted to estimate the compositions of a number of the individual inclusions.

Due to the chemically complex sulfate-rich fluid and sulfate solids within the fluid inclusions, interpretation of the microthermometric measurements is problematic due to the lack of knowledge of the precise chemical system. The presence of sulfate crystals in these fluid inclusions precludes conventional estimation of their dissolved load as NaCl equivalent salinity. Instead, we used visual proportion estimates to calculate the bulk composition of

individual solid-bearing fluid inclusions (Shepherd *et al.,* 1985; Fig. 4-6A; Appendix 7). Due to the clear evidence of heterogeneous trapping, these estimates represent the composition of the material trapped in the fluid inclusions, not a true fluid composition.

Fluid inclusion DSG 002 4 (Fig. 4-6A) is a LCO_2+VCO_2+Lw+S fluid inclusion hosting a single crystal of arcanite comprising 15% of the inclusion by volume, with 15% CO_2-rich vapour phase and 70% arcanite-saturated aqueous phase (the volumes were estimated using visual proportion estimates as presented in Appendix 7). These proportions give a bulk fluid inclusion composition of 33 wt.% K_2SO_4 equivalent or ~3 molal K_2SO_4. Some other solid-bearing fluid inclusions have multiple sulfate crystals taking up more than 15% of the fluid inclusion volume and must therefore have an even higher sulfate content (Fig. 4-6). The sulfate-bearing LCO_2+VCO_2+Lw fluid inclusions hosted in Qz-2 have similar petrographic characteristics to the $LCO_2+VCO_2\pm Lw\pm S(s)$ fluid inclusions. Hence, their salinities have also been estimated as equivalent K_2SO_4 using the visual estimate proportion method assuming a K_2SO_4 saturated solution. The majority of these fluid inclusions have the CO_2 bubble occupying from 10% to 60% of the fluid inclusion. This corresponds to a salinity between 6 - 10 wt.% K_2SO_4 equivalent, or < 0.7 molal K_2SO_4.

4.6. Interpretation and Discussion

4.6.1. Origin of the quartz lenses

The systematic localisation of the quartz lenses within the dyke cores (Fig. 4-1) indicates they are genetically linked to the calcite carbonatite and formed in the same stress field, which is consistent with the lack of quartz lenses in the surrounding rocks. The quartz lenses are not intergrown with the calcite indicating they are not conventional magmatic phases.

Qz-2 and Qz-3 are believed to be of hydrothermal origin due to the volume for volume replacement texture observed, their characteristic non-luminescent CL emission (Fig. 4-4) and the presence of fluid inclusions. Qz-3 Lw + V fluid inclusions Th_{TOT} temperatures point to low hydrothermal temperatures (120 °C to 222 °C).

The origin of the original quartz (Qz-1 in this study) from the Huanglongpu calcite carbonatites, which accounts for just over 50% of the quartz lenses in our samples overall, has been discussed by Song *et al.,* (2015). They suggested a magmatic origin of the quartz from Si enriched carbonatitic liquids which may have been produced by intense fractional crystallization of non-silicate minerals. Bai *et al.,* (2019) expanded on the work of Song *et al.,* (2015) and concluded that quartz mainly precipitated before calcite, which is consistent with the calcite veins locally crosscutting the quartz lenses observed in this study, but must also be reconciled with the fact that quartz lenses only occur within calcite carbonatite dykes. Bai *et al.,* (2019) also favoured a magmatic origin, but they ascribed the coarse, nearly monomineralic quartz grains to a supercritical C-H-O-Si magmatic fluid intermediate between a hydrous melt and an aqueous solution. Our stable oxygen isotope data (Table 4-4) indicates very small fractionation between quartz and calcite, which is indicative of temperatures in excess of 500 °C (Zheng *et al.,* 1999) and is consistent with a magmatic environment (Table 4-4). We conclude that the quartz veins formed from a fluid of magmatic origin, but were subsequently reworked by hydrothermal activity.

4.6.2. Conditions of hydrothermal activity

There is no direct measurement of the temperature of Qz-2 and Qz-3 precipitation but the quartz luminescence and the fluid inclusions can provide some indications. The brighter luminescence of Qz-1 compared to the later quartz generations indicates a higher temperature for growth. The later quartz generations exhibit low CL emission typical of

hydrothermal quartz (Rusk and Reed, 2002; Rusk *et al.,* 2006). Quartz-2 and Qz-3 show very similar luminescence (Fig. 4-4) and based on the literature on non-luminescent hydrothermal quartz precipitation, they have likely precipitated at temperatures below ~450 °C.

The CO_2-bearing fluid inclusions hosted in Qz-2 and Qz-3 decrepitated upon heating before homogenisation. It is likely that decrepitation only occurs above the temperature of trapping and if so the maximum trapping temperature is below the range 225 °C to 325 °C. The homogenisation temperature Th_{TOT} of the Lw+V fluid inclusions hosted in Qz-3 give a temperature range from 120 °C to 220 °C which may be close to the true trapping temperature since the system was experiencing significant fluid flow. This is consistent with the low luminescence from Qz-2 and Qz-3 (Fig. 4-4) and with the association of hydrothermal bastnäsite-(Ce) with them. Shu and Liu (2019) estimated that, in the Dalucao carbonatites, hydrothermal bastnäsite-(Ce) formed between 147 °C and 323 °C while the pervasive hydrothermal bastnäsite-(Ce) stage of the Maoniuping carbonatite deposit also crystallised at low temperature, between 160 °C to 240 °C (Zheng and Liu, 2019). Both these studies invoke a fluid with high $(SO_4)^{-2}$ content, alongside Cl^- and F^-. It should be noted that the similarity in oxygen isotope composition between different quartz generations (Table 4-4) suggests that the hydrothermal fluid from which they grew had an oxygen composition dominated by interaction with magmatic silicates under similar conditions to those at which the hydrothermal quartz was precipitated.

4.6.3. Possible sources of hydrothermal fluids and their dissolved components

This study has demonstrated that the fluid inclusions in the hydrothermal quartz (Qz-2 and Qz-3) are very variable. Where solids are present they vary in both abundance and mineralogy between adjacent inclusions. The ratio of CO_2 vapour phase to aqueous fluid is

also variable. We also note that the sulfate-rich fluid could not have also transported all the associated cations, since baryte and celestine are nearly insoluble (Blount, 1977; Monnin, 1999). We conclude from these lines of evidence that the population of solid-bearing inclusions results from heterogeneous trapping, but the issue of how such a complex, multi-phase fluid came to be present must still be explained.

We note however that similar CO_2-bearing fluid inclusions with sulfate solids and opaque crystals hosted in quartz and calcite from a quartz-bearing carbonatite deposit in the north Qinling region were attributed by Song *et al.,* (2016) to trapping of a carbonatite fluid exsolved at subsolidus conditions. Sulfate-rich fluids have also been found in the Maoniuping REE deposit, from the Himalayan orogenic belts, China within a similar carbonatite setting (Xie *et al.,* 2009, 2015). They described extremely sulfate-rich melt-fluid inclusions in fluorite and suggested a sulfate-rich supercritical orthomagmatic fluids originated from the unmixing of the carbonatite melt. Alkali-sulfate salt melt inclusions have been identified in carbonatites by Panina and Motorina (2008).

There are two difficulties in applying these models to the examples described here. Firstly the heterogeneous character of the inclusions makes it very unlikely that their contents correspond to any single fluid. Secondly, at Dashigou, no melt inclusions or other sulfate-rich phases are present in the early, high temperature Qz-1. Instead, we infer that the variety of the fluid inclusions provides evidence for at least three different types of fluids associated with hydrothermal Qz-2 and Qz-3: a sulfate-rich aqueous fluid, a more dilute aqueous fluid and a carbonic fluid. Although the sulfate content of these hydrothermal fluids may have been derived directly from a carbonatite parent, this cannot be demonstrated, and it is possible that the sulfate is derived from oxidation of reduced sulfur under surface conditions. Acid sulfate geothermal waters are common in many modern volcanic geothermal systems formed at similar temperatures to those inferred for the hydrothermal activity here (Lewis

et al., 1997; Smith *et al.,* 2010). Boiron *et al.,* (1999) described sulfate-rich fluid inclusions associated with retrograde quartz veins from Ouro Fino (Brazil) and pointed out that the composition of the fluid was similar to some present day geothermal systems where feldspars have been destroyed and so cannot buffer the Na/K ratio. However, S isotope data from sulphides and sulfates are consistent with a magmatic sulfur source with $\delta^{34}S$ of around 1‰ (Huang *et al.,* 1984; Song *et al.,* 2016).

The more dilute fluid present in many Qz-3 fluid inclusions is also consistent with the introduction of a fluid of geothermal origin, since it is common in modern geothermal fields for fluids with different ligand concentrations to occur within the same system (Henley and Hedenquist, 1986; Lewis *et al.,* 1997).

The carbonic fluid observed in the majority of the fluid inclusions hosted in Qz-2 and Qz-3 could have resulted from the dissolution of calcite within the carbonatite (Fig. 4-10, model 1). Nonetheless, CO_2-rich fluids have also been commonly described as orthomagmatic fluids resulting from carbonatite magma unmixing (Rankin, 2005; Bühn *et al.,* 2002).

It is unlikely that metal and sulfate ions now present in Qz-2 inclusions were introduced in a single fluid. It is clear from the varied mineralogy of the inclusions that the proportions of major cations in sulfate inclusions are very variable, and in any case the bulk fluid composition cannot have existed as a single phase under the conditions inferred for the hydrothermal activity, if at all. The Maoniuping REE carbonatite deposit host sulfate-rich multisolid daughter crystal fluid inclusions (Xie *et al.,* 2015; e.g. ADC and ADV fluid inclusions), which behaved differently as they did meet the expectations for a single-phase origin but unlike these fluid inclusions, none of the CO_2-bearing fluid inclusions at Dashigou homogenised upon heating which is evidence for heterogeneous trapping.

4.6.4. Model for the hydrothermal alteration at Huanglongpu

Figure 4-10 presents two possible models for the hydrothermal alteration and HREE enrichment of the calcite carbonatites at Dashigou, based on inclusion mineralogy and fluid inclusion results. They are intended to demonstrate how a sulfate-rich fluid is able to interact with a source of cations to produce a multi-phase fluid.

Model 1 is based on the reaction of a single acid sulfate fluid with the calcite carbonatite and its hosts. This generates CO_2 and precipitate sulfates by the neutralisation of the acid fluid by wall rock reactions (e.g. $H_2SO_4 + CaCO_3 = CaSO_4 + CO_2 + H_2O$). The sulfate minerals present in the fluid inclusions and in quartz are mainly salts of K (arcanite), Ca (anhydrite), Sr (celestine) and Na (aphthilatite) (Fig. 4-9), and these cations are readily available within wallrock calcite carbonatite dykes or the surrounding fenite (e.g. $H_2SO_4 + 2KAlSi_3O_8 = K_2SO_4$ + Al-silicates). In this model, local production of CO_2 explains why it is closely associated with the sulfate fluid.

Model 2 involves the mixing of two externally-derived fluids, one sulfate-rich and one CO_2-rich, with cations carried by the carbonic fluid, and does not explicitly require chemical interaction with the carbonatite or fenite. This model can also result in the precipitation of sulfate salts, but requires cations to be introduced in a carbonic fluid even though they, and the CO_2, are already available in the rocks.

Irrespective of the origin of the initial alteration and precipitation of sulfates, the growth of Qz-3 appears to be associated with the introduction of a more dilute fluid to the system and this is also shown in Figure 4-10.

While Qz-2 occurs as thread-like infills linked by a cobweb texture, Qz-3 always occurs infilling healed fractures (Fig. 4-4). We propose a late fracturing event led to the introduction of the more dilute water, leading to Qz-3 precipitation and the less saline fluid inclusions. Loss of CO_2 at this stage is likely since aqueous Lw+V and Lw fluid inclusions become common (Fig. 4-10).
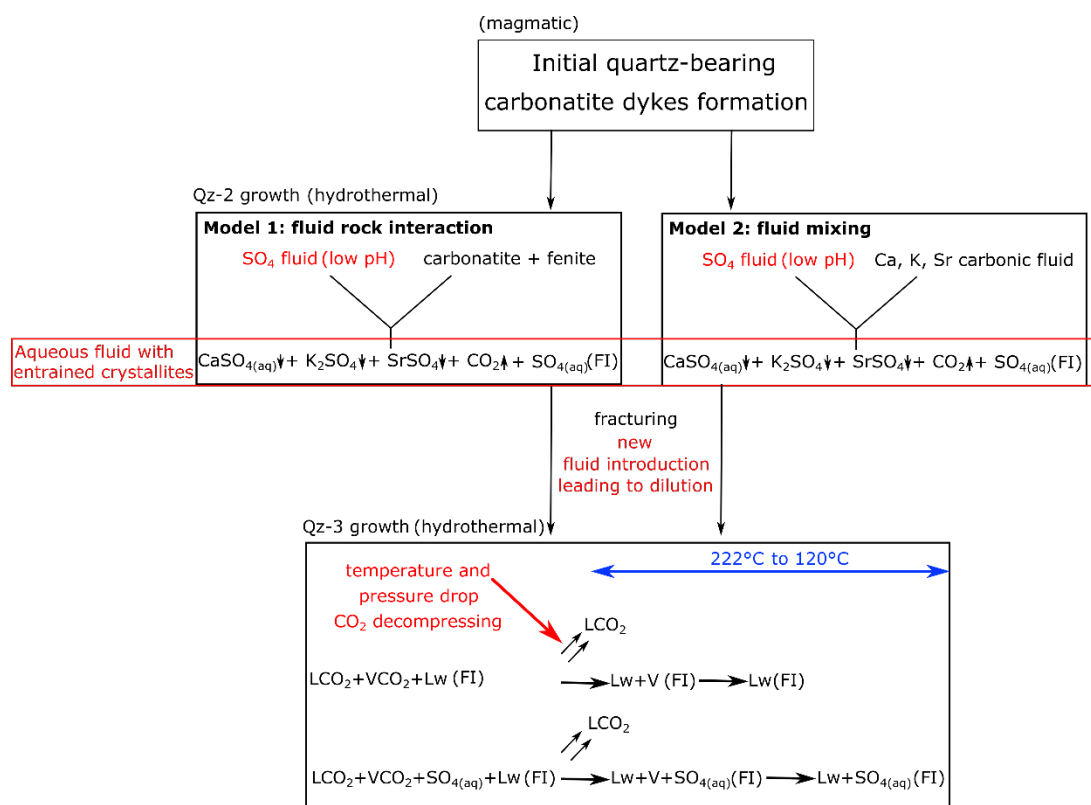
Figure 4-10: Potential models for the origin of the fluid inclusions cogenetic with the HREE mineralisation in the calcite carbonatite dykes at the Dashigou open pit.

4.6.5. Hydrothermal REE enrichment

The HREE enrichment of the Dashigou carbonatite leading to the uncommon flat REE pattern (Fig. 4-3) is believed to be due to a combination of factors. Smith *et al.,* (2018) proposed a HREE-enrichment model in which magmatic, HREE-enriched calcite with a relatively flat REE pattern (their fig. 7a) provided a baseline source for the secondary REE mineralisation. The magmatic calcite has lower REE contents than the magmatic REE phases, but it accounts for

over 50% of the carbonatite deposit and is more reactive than the REE minerals, making calcite a viable HREE-enriched source. The primary magmatic LREE-rich mineralisation consisted of monazite-(Ce) (e.g. sample HLP15, $\sum$LREE/(HREE+Y)= 587470, their table 4) and fluorcarbonates (bastnäsite-(Ce) and parisite-(Ce)) mineralisation. These early REE minerals show steep, LREE enriched, chondrite-normalised patterns as demonstrated by their high $\sum$LREE/(HREE+Y) ratio (Smith *et al.,* 2018; their fig. 8A-B). The sulfate-rich fluid leached the REE from the magmatic carbonatite without fractionation and then precipitated secondary HREE-enriched phases with flat REE patterns (e.g. britholite-(Ce), Smith *et al.,* 2018; sample HLP10, $\sum$LREE/(HREE+Y)= 11, fig. 8C-E; their table 6). The hydrothermal REE minerals are still Ce-dominant but have much higher HREE content than typically found in carbonatite related systems.

Hydrothermal Qz-2 and Qz-3 grew alongside secondary REE minerals as the carbonatites became enriched in HREE (Smith *et al.,* 2018), suggesting that the fluid inclusions contain information about the fluid responsible for the REE transport and deposition. The associated fluid inclusions have high sulfate contents and Qz-2 and Qz-3 emplacement correlates overall with widespread growth of sulfate minerals and deposition of secondary quartz in the calcite carbonatite dykes.

REE transport is also likely to be an important factor for HREE-enrichment. Migdisov and Williams-Jones (2008, 2014, 2016) identified two categories, ligands leading to REE transportation (Cl^- and SO_4^{2-}) and ligands leading to REE deposition (F^-, OH^-, CO_3^{2-}, HCO_3^- and PO_4^{2-}). At Dashigou, sulfate is inferred to be the main complexing agent for REE transport from the fluid inclusion analyses. The flat REE profile of the hydrothermally altered calcite carbonatites (Fig. 4-3) is consistent with experimental studies on the REE-SO_4^{2-} complexes at hydrothermal temperatures from 100 °C to 400 °C (Migdisov and Williams-Jones, 2008, 2014, 2016). These studies agree that sulfate is a non-selective ligand as it does not fractionate the

LREE from the HREE. The stability of REE-SO_4^{2-} complexes is not strongly dependent on atomic number and they have similar formation constants across the lanthanide series. In contrast, HREE-Cl^{2+} complexes show an overall lower stability than REE-sulfate complexes and since this decreases along the lanthanide series, a chloride-dominated fluid will fractionate the LREE from the HREE. In contrast a sulfate fluid is able to transport the LREE and the HREE equally. One case study on a natural carbonatite system has previously demonstrated the importance of REE sulfate transport at low temperature below 240 °C (Zheng and Liu, 2019). Sulfate transport has also been observed in sedimentary basin systems at low hydrothermal temperature between 100 °C and 120 °C (Richter *et al.,* 2019).

The chloride content of the Dashigou fluids were not measured but no trace of Cl-bearing salts were observed suggesting only a minor amount of this ligand is present in the fluids. The precipitation of sulfate minerals within the calcite carbonatite dyke as the sulfate fluid encountered Ca, Na and K is inferred to have destabilised the REE-SO_4^{2-} complexes and triggered the deposition of the hydrothermal REE minerals. While sulfate transport does not account for the HREE enrichment specifically, it plays an important role in linking REE mineralisation to the growth of sulfate minerals.

The final HREE enrichment factor is thought to be the stabilisation of secondary minerals whose crystal structures tend to favour HREE, in particular HREE-enriched fluorcarbonate, uraninite, xenotime-(Y) and churchite-(Y) and other minerals that were not always possible to identify; Smith *et al.,* (2018) also reported britholite-(Ce) and Ca-REE fluorcarbonate mineralisation. These fractionate the HREE out of the fluid they are crystallising from. An additional mechanism that could also have concentrated the HREE is the co-precipitation of hydrothermal gangue LREE enriched phase such as sulfate minerals.

In summary, a HREE-enriched source is probably important for the final HREE enrichment. The late-stage magmatic HREE enrichment of the calcite, the main gangue mineral of the

carbonatite, provides a source baseline allowing a potential secondary HREE enrichment (Xu *et al.,* 2007; Smith *et al.,* 2018; Bai *et al.,* 2019). However, it is also possible that HREE-enrichment is enhanced at the hydrothermal stage. This might have happened indirectly, by selective removal of LREE in a Cl-fluid (Smith *et al.,* 2018), although no evidence for such a fluid has been seen, or directly through transport and precipitation of REE. Sulfate-REE complexation facilitates non-selective transport of the REE, and precipitation of REE minerals may then occur in response to precipitation of sulfate minerals. Stabilisation of secondary HREE-enriched minerals in the hydrothermal environment may have selectively concentrated HREE.

4.7. Conclusions

The calcite carbonatites at Dashigou can be divided into two groups on the basis of hydrothermal alteration of magmatic minerals, including monazite-(Ce); little-altered calcite carbonatites exhibit a normal carbonatite LREE-enriched REE pattern, but more altered dykes have enhanced levels of HREE and show an unusual flat REE pattern (Fig. 4-3). These observations suggest that the rocks became enriched in HREE in the course of the hydrothermal alteration which was accompanied by the growth of secondary minerals which favoured incorporation of HREE (Smith *et al.,* 2018). Alteration took place in at least two phases whose conditions are not well-defined but are between 450 °C and 120 °C. The hydrothermal fluid responsible for the alteration was remarkably sulfate-rich, and the bulk composition of heterogeneously-trapped fluid inclusions can exceed 30 wt.% K_2SO_4 equivalent. The REE were transported as sulfate complexes and likely precipitated due to the precipitation of sulfate gangue minerals. The simplest model for the process involves interaction of an externally-derived acid sulfate hydrothermal fluid with carbonatite and fenite (Fig. 4-10). Calcite and silicates neutralised the acidity of the sulfate-rich fluid,

generating CO_2 and acquiring cations (K, Ca, Na) which precipitated sulfates. Late fracturing was accompanied by renewed quartz precipitation from a more dilute fluid lacking CO_2.

Overall, the HREE enrichment of the Dashigou carbonatite is believed to be due to a combination of factors. Late-magmatic HREE enrichment of the calcite, the main mineral of the carbonatite, provided a source baseline. Secondary HREE-enrichment was made possible by a fluid rich in sulfate, a non-selective REE ligand able to transport and concentrate the REE equally but in complexes that are destabilised by the precipitation of sulfate minerals. Final HREE-enrichment was achieved by the growth of secondary REE minerals which favour HREE, notably HREE-enriched fluorcarbonates, uraninite, xenotime-(Y) and churchite-(Y).

Acknowledgements

References

Andersen, A.K,. Clark, J.G., Larson, P.B. and Neill, O.K. (2016) Mineral chemistry and petrogenesis of a HFSE(+HREE) occurrence, peripheral to carbonatites of the Bear Lodge alkaline complex, Wyoming. *American Mineralogist*, **101**(7), 1604-1623.

Blount, C. (1977) Baryte solubilities and thermodynamic quantities up to 300°C and 1400 bars. *American Mineralogist,* **62**, 942-957.

Bai, T., Chen, W. and Jiang, S. (2019) Evolution of the carbonatite Mo-HREE deposits in the Lesser Qinling Orogen: Insights from in situ geochemical investigation of calcite and sulfate. *Ore Geology Reviews*, **113**, 1-14.

Boiron, M.-C., Moissette, A., Cathelineau, M., Banks, D., Monin, C. and Dubessy, J. (1999) Detailed determination of paleofluid chemistry: an integrated study of sulfate-volatile rich brines and aqueo-carbonic fluids in quartz veins from OuroFino (Brazil). *Chemical Geology*, **154**, 179-192.

Bühn, B., Rankin, A.H., Schneider, J. and Dulski, P. (2002) The nature of orthomagmatic, carbonatitic fluids precipitating REE, Sr-rich fluorite: fluid-inclusion evidence from the Okorusu fluorite deposit, Namibia. *Chemical Geology,* **186**, 75-98.

Cangelosi, D.A., Broom-Fendley, S., Banks, D.A., Morgan, D.J. and Yardley, B.W.D. (2019) LREE redistribution during hydrothermal alteration at the Okorusu carbonatite complex, Namibia. *Mineralogical Magazine, (n.d.)* 1-54.

Chakhmouradian, A.R. and Wall, F. (2012) Rare earth elements: Minerals, mines, magnets (and more). *Elements*, **8**, 333-340.

Chakhmouradian, A.R. and Zaitsev, A.N. (2012) Rare earth mineralisation in igneous rocks: Sources and processes. *Elements*, **8**, 347-353.

Dubessy, J., Poty, B. and Ramboz, C., (1989) Advances in C-O-H-N-S fluid geochemistry based on micro-Raman spectrometric analysis of fluid inclusions. *European Journal of Mineralogy* **1**, 517-534.

European Commission (2017) Communication from the commission to the European parliament, the council. *The European economic and social committee and the committee of the regions on the 2017 list of Critical Raw Materials for the EU*. COM(2017) 490.

Henley, R.H. and Hedenquist, J.W. (1986) Introduction to the geochemistry of active and fossil geothermal systems. Pp. 1-22 in: *Guide to the active epithermal (geothermal) systems and precious metal deposits of New Zealand* (R.W. Henley, J.W. Hedenquist and P.J. Roberts, editors). Monograph Series Mineral Deposits, Berlin-Stuttgart, Gerbruder Borntrager.

Huang, D.H., Wang, Y., Nie, F. and Jiang, X. (1984) Isotopic composition of sulfur, carbon and oxygen and source material of the Huanglongpu carbonatite vein-type of molybdenum (lead) deposits. *Acta Geologica Sinica,* **63**, 252-264 (in Chinese with English abstract).

Huang, D.H., Wu, C.Y., Du, A.D. and He, H.L. (1994) Re–Os isotope age of molybdenum deposits in East Qinling and their significance. *Mineral Deposits*, **13**, 221-230 (in Chinese with English abstract).

Kynicky, J., Smith, M.P. and Xu, C. (2012) Diversity of rare earth deposits: The key example of China, *Elements*, **8**, 361-367.

Lewis, A.J., Palmer, M.R., Sturchio, N.C. and Kemp, A.J. (1997) The rare earth element geochemistry of acid-sulfate and acid-sulfate-chloride geothermal systems from Yellowstone National Park, Wyoming, USA. *Geochimica et Cosmochimica Acta*, **61**(4), 695-706.

Mao, J.W., Xie, G.Q., Bierlein, F., Qu, W.J., Du, A.D., Pirajno, F., Guo, B.J., Li, Y.F. and Yang, Z.Q. (2008) Tectonic implications from Re-Os dating of Mesozoic molybdenum deposits in the East Qinling-Dabie orogenic belt. *Geochimica et Cosmochimica Acta*, **72**(18), 4607-4626.

McDonough, W.F. and Sun, S. (1995) The composition of the earth. *Chemical Geology,* **120**, 223-253.

Midende, G., Boulvais, P., Tack, L. Melcher, F., Gerdes, A., Dewaele, S., Demaiffe, D. and Decrée, S. (2014) Petrography, geochemistry and U–Pb zircon age of the Matongo carbonatite Massif (Burundi): Implication for the Neoproterozoic geodynamic evolution of Central Africa. *Journal of African Earth Sciences*, **100**, 656-674.

Migdisov, A.A. and Williams-Jones, A.E. (2008) A spectrophotometric study of Nd(III), Sm(III) and Er(III) complexation in sulfate-bearing solutions at elevated temperatures. *Geochimica et Cosmochimica Acta*, **72**, 5291-5303.

Migdisov, A.A. and Williams-Jones, A.E. (2014) Hydrothermal transport and deposition of the rare earth elements by fluorine-bearing aqueous liquids. *Mineralium Deposita*, **49**, 987-997.

Migdisov, A.,Williams-Jones, A.E., Brugger, J. and Caporuscio, F.A., (2016) Hydrothermal transport, deposition, and fractionation of the REE: experimental data and thermodynamic calculations. *Chemical Geology,* **439**, 13-42.

Monnin, C. (1999) A thermodynamic model for the solubility of baryte and celestine in electrolyte solutions and seawater to 200°C and to 1 kbar. *Chemical Geology*, **153**, 187-209.

Panina, L.I. and Motorina, I.V. (2008) Liquid immiscibility in deep-seated magmas and the generation of carbonatite melts. *Geochemistry International,* **46**, 448-464.

Rankin, A. (2005) Carbonatite-associated rare metal deposits: composition and evolution of ore-forming fluids—the fluid inclusion evidence. *The Geological Association of Canada*, Short Course Notes, **17**, 299-314.

Ratschbacher, L., Hacker, B.R., Calvert, A., Webb, L.E., Grimmer, J.C., McWilliams, M.O., Ireland, T., Dong, S. and Hu, J. (2003) Tectonics of the Qinling (Central China): Tectonostratigraphy, geochronology, and deformation history. *Tectonophysics*, **366**(1-2), 1-53.

Richter, L., Diamond, L.W., Atanasova, P., Banks, D.A. and Gutzmer, J. (2019) Hydrothermal formation of heavy rare erath (HREE)- xenotime deposits at 100 °C in a sedimenatry basin. *Geology*, **46**(3), 263-266.

Rusk, B.G., Reed, M.H., Dilles, J.H. and Kent, A.J.R. (2006) Intensity of quartz cathodoluminescence and trace-element content in quartz from the porphyry copper deposit at Butte, Montana. *American Mineralogist*, **91**(8-9), 1300-1312.

Rusk, B. and Reed, M. (2002) Scanning electron microscope-cathodoluminescence analysis of quartz reveals complex growth histories in veins from the Butte porphyry copper deposit, Montana. *Geology*, **30**, 727-730.

Shepherd, T.J., Rankin, A.H. and Alderton, D.H.M. (1985) A Practical Guide to Fluid Inclusion Studies. Blackie, Glasgow and London.

Shu, X. and Liu, Y. (2019) Fluid inclusion constraints on the hydrothermal evolution of the Dalucao Carbonatite-related REE deposit, Sichuan Province, China. *Ore Geology Reviews*, **107**, 41-57.

Smith, D.J., Jenkin, G.R.T., Naden, J., Boyce, A.J., Petterson, M.G., Toba, T., Darling, W.G., Taylor, H. and Millar, I.L. (2010) Anomalous alkaline sulfate fluids produced in a magmatic hydrothermal system - Savo, Solomon Islands. *Chemical Geology*, **275**(1-2), 35-49.

Smith, M.P., Henderson, P. and Campbell, L.S. (2000) Fractionation of the REE during hydrothermal processes: Constraints from the Bayan Obo Fe-REE-Nb deposit, Inner Mongolia, China. *Geochimica et Cosmochimica,* **64**(18), 3141-3160.

Smith, M.P., Campbell, L.S. and Kynicky, J. (2015) A review of the genesis of the world class Bayan Obo Fe-REE-Nb deposits, Inner Mongolia, China: Multistage processes and outstanding questions. *Ore Geology Reviews*, **64**, 459-476.

Smith, M., Kynicky, J., Xu, C., Song, W., Spratt, J., Jeffries, T., Brtnicky, M., Kopriva, A. and Cangelosi, D. (2018) The origin of secondary heavy rare earth element enrichment in carbonatites: Constraints from the evolution of the Huanglongpu district, China. *Lithos*, **308-309**, 65-82.

Song, W., Xu, C., Qi, L., Zhou, L., Wang, L., and Kynicky, J. (2015) Genesis of Si-rich carbonatites in Huanglongpu Mo deposit, Lesser Qinling orogen, China and significance for Mo mineralization. *Ore Geology Reviews*, **64**(C),756-765.

Song,W., Xu, C., Smith, M.P., Kynicky, J., Huang, K.,Wei, C., Li, Z. and Shu, Q. (2016) Origin of the unusual HREE-Mo-rich carbonatites in the Qinling Orogen, China. *Scientific Reports,* **6**, 1-10.

Stein, H.J., Markey, R.J., Morgan, M.J., Du, A. and Sun, Y. (1997) Highly precise and accurate Re–Os ages for molybdenite from the East Qinling–Dabie molybdenum belt, Shaanxi province, China. *Economic Geology,* **92**, 827-835.

Thair, A.A. and Olli, S. (2013) Geochemistry and mineral phases of REE in Jammi carbonatite veins and fenites, southern end of the Sokli complex, NE Finland. *Geochemistry: Exploration, Environment, Analysis,* **13,** 217-224.

Trofanenko, J., Williams-Jones, A.E., Simandl, G.J., and Migdisov, A.A. (2016) The Nature and Origin of the REE Mineralization in the Wicheeda Carbonatite, British Columbia, Canada. *Economic Geology*, **111**, 199-223.

Valakovich, M.P. and Altunin, U.V. (1968) *Thermophysical properties of carbon dioxide*. Collets, London.

Verplanck, P.L., Farmer, G.L., Kettler, R.M., Lowers, H.A., Koenig, A.E. and Blessington, M.J. (2014) Rare Earth Element Enrichments in the Elk Creek Carbonatite. *Acta Geologica Sinica*, **88**, 466-467.

Verplanck, P.L. (2017) The Role of Fluids in the Formation of Rare Earth Element Deposits. *Procedia Earth and Planetary Science*, **17**(39), 758-761.

Wall, F. (2014) Rare Earth Elements. Pp. 312-340 in: *Critical Metals Handbook* (A. Gunn, editor). Wiley, New York, USA.

Wall, F., Niku-Paavola, V.N., Storey, C.M. and Axel, J.T. (2008) Xenotime-(Y) from carbonatite dykes at Lofdal, Namibia: Unusually low LREE:HREE ratio in carbonatite, and the first dating of xenotime overgrowths on zircon. *Canadian Mineralogist,* **46**, 861-877.

Williams-Jones, A.E., Migdisov, A.A. and Samson, I.M. (2012) Hydrothermal mobilisation of the rare earth elements-a tale of "ceria" and "yttria". *Elements*, **8**, 355-360.

Woolley, A.R. and Kempe, D.R.C. 1989. Carbonatites: nomenclature, average chemical composition. Pp. 1-14 in: *Carbonatites: Genesis and evolution (*K. Bell, editor). Unwin Hyman, London.

Xie, Y., Hou, Z., Yin, S., Dominy, S., Xu, J., Tian, S. and Xu, W. (2009) Continuous carbonatitic melt–fluid evolution of a REE mineralization system: Evidence from inclusions in the Maoniuping REE Deposit, Western Sichuan, China. *Ore Geology Reviews*, **36**(1), 90-105.

Xie, Y., Li, Y., Hou, Z., Cooke, D., Danyushevsky, L., Dominy, S. and Shuping Yin, S. (2015) A model for carbonatite hosted REE mineralisation — the Mianning–Dechang REE belt, Western Sichuan Province, China. *Ore Geology Reviews*, **70**, 595-612.

Xu, C., Campbell, I.H., Allen, C.M., Huang, Z., Qi, L., Zhang, H. and Zhang, G. (2007) Flat rare earth element patterns as an indicator of cumulate processes in the Lesser Qinling carbonatites, China. *Lithos*, **95**, 267-278.

Xu, C., Kynicky, K, Chakhmouradian, A.R., Qi, L. and Song, W. (2010) A unique Mo deposit associated with carbonatites in the Qinling orogenic belt, central China. *Lithos*, **118**, 50-60.

Zheng, Y.F. (1999) Oxygen isotope fractionation in carbonate and sulfate minerals. *Geochemical journal*, **33**, 109-126.

Zheng, X. and Liu, Y. (2019) Mechanisms of element precipitation in carbonatite-related rare-earth element deposits: Evidence from fluid inclusions in the Maoniuping deposit, Sichuan Province, southwestern China. *Ore Geology Reviews*, **107**, 218-238.

CHAPTER 5.

Pulsed hydrothermal inputs during reworking of a REE carbonatite deposit, the Okorusu complex, Namibia

Cangelosi, D.A., Broom-Fendley, S., Jamieson, R.A. and Yardley, B.W.D. (ready for submission) Pulsed hydrothermal inputs during reworking of a REE carbonatite deposit, the Okorusu complex, Namibia.

5.1. Abstract

The Okorusu calcite carbonatites are part of the Cretaceous Damaraland Igneous Province (~137 to 124 Ma) of Northern Namibia. They show a common LREE enrichment for carbonatites. Even though, the carbonatites do not hold economic concentrations of REE, the main hydrothermal stage hosts parisite mineralisation. This hydrothermal stage is marked by partial breakdown of the magmatic minerals, mainly calcite with growth of hydrothermal calcite and a range of other minerals, often present as inclusions in the hydrothermal calcite such as baryte, celestine and parisite, with lesser amounts of strontianite, witherite and other minor phases.

Bulk powder (isotope ratio mass spectrometry) and in-situ (secondary ionisation mass spectrometry) techniques were used to measure the oxygen isotope compositions of baryte and calcite from magmatic and hydrothermal stages, the latter being associated with the deposition of hydrothermal REE minerals. Similar $\delta^{18}O$ compositions of both the magmatic and recrystallized hydrothermal calcite make determination of the hydrothermal fluid source impossible due to local control of the fluid composition. Nonetheless, the widely varying $\delta^{18}O$ compositions of the baryte inclusions hosted by hydrothermal calcite (ranging from 1.4‰ to

17‰) suggest a dynamic fluid system with frequent introduction of fresh fluid reacting with the calcite carbonatite to varying degrees.

The calculated oxygen isotopic compositions of water in equilibrium with each of the calcite and baryte grains as a function of temperature, point to low temperature growth of the baryte (around 100 °C). However, the amount of fluid introduced to the system was not sufficient to shift the altered carbonatite $\delta^{18}O$ composition, unlike that observed in some economic carbonatite REE deposits (e.g. Bear Lodge carbonatites). But, the occasional pulses of oxidising low-T hydrothermal fluid entering the system and reacting with the host calcite carbonatite locally reworking the magmatic phases was enough to precipitate secondary REE mineralisation.

5.2. Introduction

Carbonatite deposits host the largest volume and highest grade light rare earth elements (LREE) deposits globally, and are the principal economic source of these elements (U.S. Geological Survey, 2019). The initial control on the high LREE contents is via magmatic processes, such as low degree partial melting (Chakhmouradian and Zaitsev, 2012), fractional crystallisation (Giebel *et al.,* 2017) and, potentially, silicate-carbonatite immiscibility (Veksler *et al.,* 2012). Nonetheless, textural evidence, such as the formation of REE pseudomorphs, veins and stringers, strongly indicates that hydrothermal activity transports, enriches and fractionates the rare earth elements (REE) into new phases (e.g. Zaitsev *et al.,* 1998; Smith *et al.,* 2000; Wall and Zaitsev, 2004; Broom-Fendley *et al.,* 2017a; Cangelosi *et al.,* 2019a). These commonly include secondary REE minerals such as monazite-(Ce) or REE fluorcarbonates (e.g. synchysite-(Ce), bastnäsite-(Ce), parisite-(Ce)) with cogenetic secondary gangue minerals such as strontianite, baryte, quartz and low-Sr secondary calcite replacing Sr-rich magmatic calcite (e.g. Wall and Zaitsev, 2004; Cangelosi *et al.,* 2019a). Such hydrothermal activity is supported by fluid inclusion microthermometry (Cangelosi *et al.,* 2019b; Shu and Liu, 2019), stable isotope data (Ray and Ramesh, 2006; Moore *et al.,* 2015) and direct measurement of natrocarbonatite fumaroles (Genge *et al.,* 2001). Nonetheless, the role of hydrothermal activity in the formation of economic REE mineralisation probably varies between deposits (Smith *et al.*, 2000; Smith *et al.,* 2015; Shu and Liu, 2019; Cangelosi *et al.,* 2019a; Cangelosi *et al.,* 2019b).

Little is known about the evolution of the hydrothermal fluids associated with the secondary REE mineralisation. The aim of this study is to get information on the fluid(s) that drove

hydrothermal alteration in a carbonatite body which has experienced varying degrees of hydrothermal modification.

Carbonate oxygen isotope analysis is commonly used to attempt to identify and understand carbonatite evolution and alteration (Ray and Ramesh, 2006; Moore *et al.,* 2015; Broom-Fendley *et al.,* 2016, 2017a; Simandl and Paradis, 2018). Calcite from carbonatites typically have an initial, mantle-derived bulk rock $\delta^{18}O$ composition of 5-10‰ and $\delta^{13}C$ ranging from -7‰ to -3‰ (Taylor *et al.,* 1967; Deines, 1989; Keller and Hoefs, 1995; Demény *et al.,* 2004; Jones *et al.,* 2013). This signature can be changed by a number of mechanisms, including Rayleigh fractionation (principally of calcite), which leads to an increase in $\delta^{18}O$ and $\delta^{13}C$ in the residual fluid (Ray and Ramesh, 2000), wall-rock interaction, including sediment assimilation, which tends to increase the $\delta^{18}O$ and $\delta^{13}C$ composition of the carbonatite (Santos and Clayton, 1995; Demény *et al.,* 1998), and sub-solidus alteration by fluids such as meteoritic/geothermal waters which may increase or decrease $\delta^{18}O$ depending on the temperature of alteration (Hoefs, 2008; Deines, 1989; Broom-Fendley *et al.,* 2016). Recently, Broom-Fendley *et al.,* (2016, 2017a) highlighted that the bulk oxygen isotope composition of carbonates in a REE mineralised rock is typically not in equilibrium with minerals associated with REE mineralisation. In these cases, considerable care is required to establish the textural relationships between phases and, commonly well spatially resolved analyses are required in order to confidently link $\delta^{18}O$ with a specific process.

In this study, we present spatially-constrained oxygen isotope analyses of magmatic and hydrothermal calcite as well as hydrothermal baryte, to report on the evolution of fluid infiltration associated with the deposition of REE minerals at Okorusu, Namibia. Our spatially constrained analyses include both conventional isotope ratio mass spectrometry methods with small drilled samples (c. 1 mg), and secondary ionisation mass spectrometry (SIMS) for in-situ analysis, in order to report on the evolution of fluid infiltration associated with the deposition of hydrothermal minerals.

5.3.   Hydrothermal alteration of the Okorusu calcite carbonatites

The Okorusu carbonatite complex is part of the Cretaceous Damaraland Igneous Province (~137 to 124 Ma) of Northern Namibia (Milner *et al.,* 1995). Carbonatite here exhibits LREE enrichment, as is observed in most carbonatites (Woolley and Kempe, 1989; Rankin, 2005; Verplanck *et al.,* 2014). The Okorusu complex does not hold economic concentrations of REE, but REE minerals are present. Parisite-(Ce) ($[Ca(LREE)_2(CO_3)_3F_2]$) is the principal REE mineral,

and Cangelosi *et al.,* (2019a) showed from textural evidence that it is of hydrothermal origin, coeval with hydrothermal calcite, baryte and other REE-bearing minerals. Okorusu has been an important commercial source of fluorite and the samples investigated here come from existing mine pits (Cangelosi *et al.,* 2019a). Based on the textural relationships of the minerals, Cangelosi *et al.,* (2019a) described four phases of mineral growth: magmatic (stage 1), late magmatic (stage 2), hydrothermal (stage 3) and late hydrothermal fluorite mineralisation (stage 4). In this study we focus on the hydrothermal stage 3, responsible for the main REE minerals at Okorusu.

5.3.1. Hydrothermal stages

Stage 3 alteration affects a range of carbonatite varieties and is widespread. It is marked by partial breakdown of the magmatic minerals, mainly calcite and to a lesser extent apatite, with growth of hydrothermal calcite and a range of other minerals, often present as inclusions in the hydrothermal calcite. Minor and trace elements, including REE, Sr and Ba were released from magmatic minerals during alteration and precipitated as parisite-(Ce), baryte and celestine with lesser amounts of strontianite, witherite and other minor phases accompanied by low-Ba, low-Sr hydrothermal calcite (Fig. 5-1). Since the magmatic phases were relatively rich in this suite of elements, the hydrothermal alteration mostly occurred without significant change in the bulk rock composition (Cangelosi *et al.,* 2019a). Stage 3 alteration is believed to have developed at relatively low temperatures because calcite coexisting with dolomite is too low in Mg to apply calcite-dolomite solvus thermometry (Anovitz and Essene, 1997). Instead, it is only possible to give a maximum temperature limit of < 200 °C. Calcite and dolomite also coexist in stage 4 assemblages and calcite composition is similar to stage 3 calcite, suggesting a similar temperature. This is in agreement with Bühn *et al.,* (2002) who estimated that stage 4 alteration and fluorite growth took place at 150 °C ± 30 °C from fluid inclusion studies.

The presence of neo-formed baryte and celestine in the stage 3 mineral assemblage supports the inference that an oxidising hydrothermal fluid interacted with the magmatic mineral assemblage (Cangelosi *et al.,* 2019a). The formation of these minerals is coincident with oxidation of pyrite in the carbonatite, although input of sulfur from an external source may also be a possibility.

This study is focussed on a pegmatitic calcite carbonatite pod about 11 m wide and 4 m high, intruded into country rock marble. The margin of the pod is extensively altered and has a brown appearance due to the presence of secondary Fe oxy-hydroxides. Four samples and sub-samples were collected, (sample OKC19, 18, 17; Cangelosi *et al.,* 2019a; Fig. 3-3B). Sample OKC17 was taken from the middle of the pod while sample OKC19 was collected approximately 4 m away, at the contact with the altered margin; sample OKC18 was taken between the two other samples. For reference, two other samples have also been analysed: OKA1, a diopside-bearing calcite carbonatite dyke, about 2 m wide intruding marble country rock (Fig. 3-3A) and OKC4, a calcite carbonatite intruding the core of a 70 cm wide mafic dyke with chilled margin (Cangelosi *et al.,* 2019a).

5.3.2. Calcite and baryte within the calcite carbonatites

Cangelosi *et al.,* (2019a) investigated the compositional and paragenetic evolution of the calcite and baryte generations. Depending on the degree of alteration of the calcite carbonatites, stage 3 calcite can be confined to secondary replacement of magmatic calcite along cleavage planes and grain margins or can completely pseudomorph stage 1 calcite (Fig. 5-1). Stage 3 calcite invariably contains cogenetic inclusions of baryte, celestine, strontianite, witherite, and parisite-(Ce).

Stage 3 hydrothermal calcite (cc_h) is chemically distinct from magmatic calcite (cc_m) (Fig. 5-1). The hydrothermal calcite is depleted in Sr (often over 2% in magmatic calcite), Ba and the REE, but may be enriched in Mn and Fe, (Cangelosi *et al.,* 2019a; Table 5-1). BSE images (Fig. 5-2B) show subtle zoning in stage 3 hydrothermal calcite hosting baryte inclusions, and the form of the darker bands (designated cc_{h2}), suggests that they are likely to reflect growth zoning and are therefore coeval with baryte. Electron microprobe analysis (Table 5-1) shows that the darker calcite (cc_{h2}) has a lower content of Mn and Fe than the brighter (in BSE images, designated cc_{h1}), and so the alternating bands may reflect fluctuations in the redox state of the fluid. Both, cc_{h1} and cc_{h2} from both analysed areas (P1 and P3) have distinctive low Sr content of hydrothermal calcite at Okorusu (Table 5-1; Fig. 5-3).

Figure 5-2D similarly illustrates chemical variation in a calcite crystal from P3, but here the darker calcite is later and is associated with cleavage fractures in cc_{h1}. Calcite$_{h1}$ measurements in area P3, are from the same crystal and are slightly more enriched in Mn and Fe than the cc_{h1} from area P1 (Table 5-1).

Sample area	OKC19-1 P1		OKC19-1 P1		OKC19-1 P3		OKC19-1 P3		OKC19-1 (hydrothermal) average		OKC19-1 (magmatic) average	
calcite type	CC_{h1}		CC_{h2}		CC_{h1}		CC_{h1}		hydrothermal		magmatic	
	average	stdev	average	stdev	average	stdev	average	stdev	average	stdev	average	stdev
MnO	**0.33**	0.07	**0.06**	0.04	**1.06**	0.18	**1.09**	0.17	**0.59**	0.22	**0.05**	0.01
FeO	**0.48**	0.05	**0.17**	0.04	**0.62**	0.06	**0.70**	0.10	**0.53**	0.30	**0.06**	0.01
CaO	**54.36**	0.30	**54.49**	1.18	**53.24**	0.29	**53.26**	0.25	**54.15**	0.70	**53.44**	0.13
SrO	**0.25**	0.09	**0.31**	0.12	**0.22**	0.07	**0.25**	0.05	**0.29**	0.11	**2.39**	0.29
n	16	n.a.	15	n.a.	10	n.a.	14	n.a.	**27**	n.a.	**5**	n.a.

Table 5-1: Comparison of the average composition of two hydrothermal calcite generations from Fig. 5-2 to the hydrothermal and magmatic calcite from the same sample (OKC19) from Cangelosi et al., (2019a). The data were obtained by EPMA analysis.
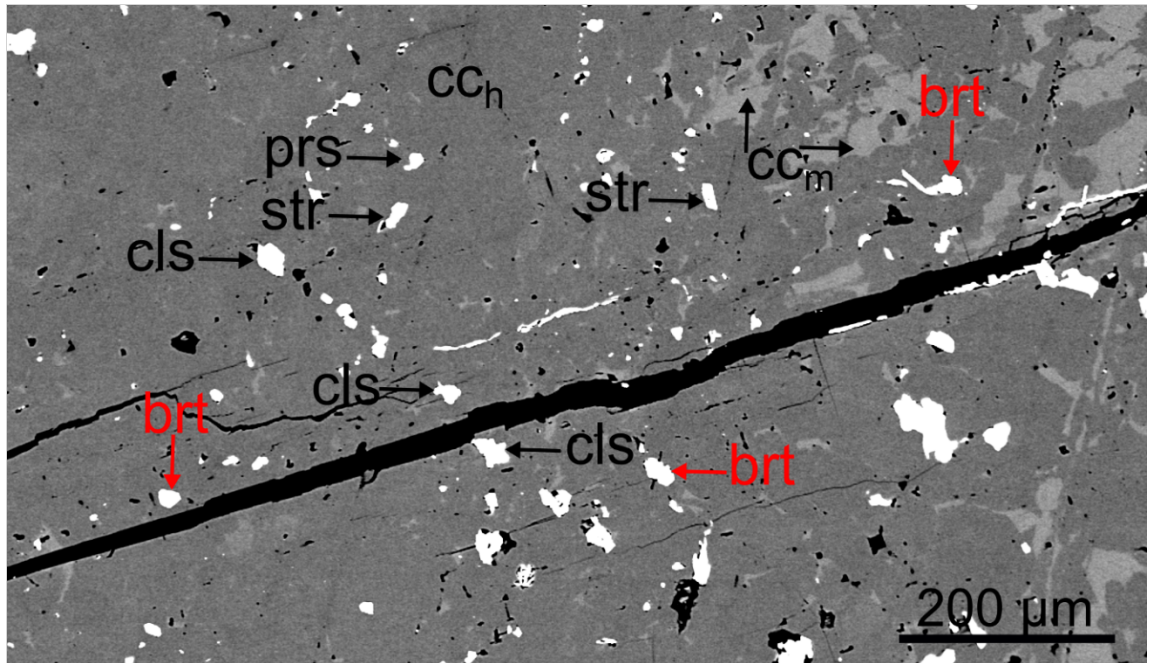
Figure 5-1: Back scattered electron (BSE) image of darker grey stage 3 hydrothermal calcite (cc_h) largely replacing brighter magmatic calcite (cc_m). Cogenetic inclusions are widespread in the hydrothermal calcite and some are identified: brt – baryte, cls – celestine, str – strontianite, prs - parisite. The black diagonal line is an opened cleavage fracture, sample OKC17.
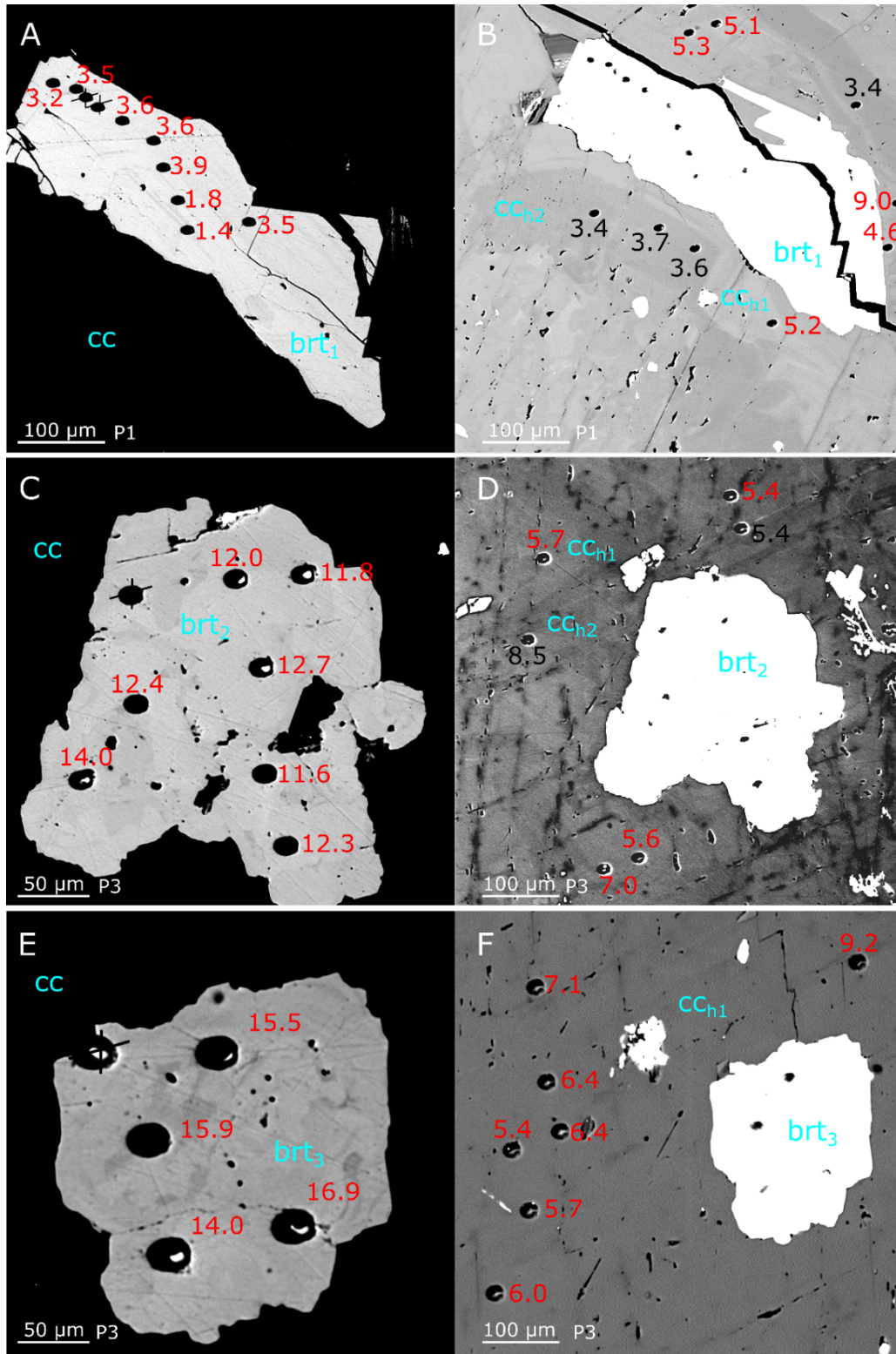
Figure 5-2: Back scattered images of the stable oxygen isotope points analysed (‰) from baryte and cc_{h1} of sample OKC19-1 from area P1 and P3, analysed by SIMS all as $\delta^{18}O$ SMOW. The black data points represent cc_{h2} analyses. Numbers are $\delta^{18}O_{SMOW}$‰. The black cross on some pits represent the dismissed analyses, either due to a location issue such as too near from surface defects or due to the instrument low count.
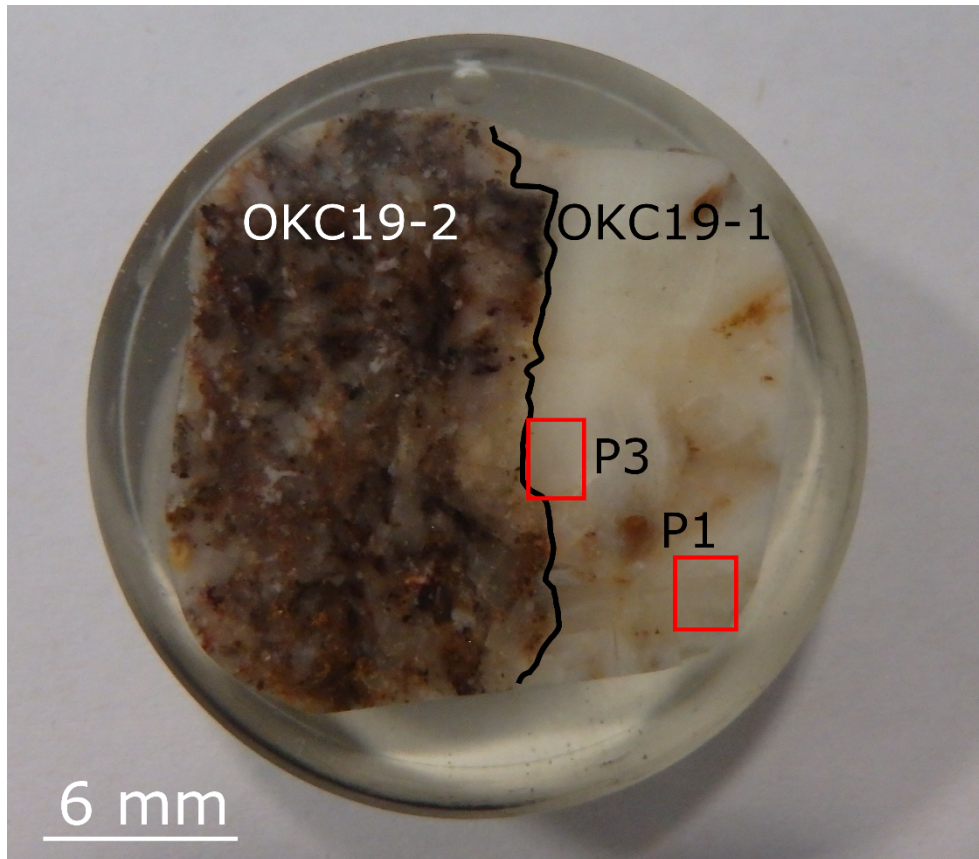
Figure 5-3: Pegmatitic calcite carbonatite sample OKC19, prepared for analysis by SIMS. The specimen spans the contact with the marginal, more altered, carbonatite. The two areas analysed are identified (cf Fig. 5-2).

5.4. Analytical techniques

Two approaches were used to analyse the oxygen stable isotope of the minerals. Drilled calcite powders, were dissolved and analysed by conventional isotope ratio mass spectrometry. Both magmatic and hydrothermal calcite grains were sampled with this technique. In-situ analyses of hydrothermal calcite and baryte were performed by Secondary Ion Mass Spectrometry (SIMS). This allowed individual inclusions of baryte and their host calcite to be analysed.

The drilled calcite stable isotope measurements were carried out at the University of Leeds on calcite carbonatite samples: OKC19-1, OKC18, OKC17, OKA1 and OKC4. The samples were micro-drilled, due to the hydrothermal calcite replacing the magmatic calcite along cleavages planes, there is some risk of contamination from hydrothermal calcite in the magmatic

calcite samples. The stable isotope ratios from calcite were analysed using an Elementar Isoprime™ isotope ratio mass spectrometer (IRMS) with a Dual Inlet Multiprep system. Each sample analysed weighed between 50 μg to 100 μg and was reacted at 90 °C with 103% phosphoric acid. The standard used was a powdered Carrara Marble (-2.01‰ $_{VPDB}$) from Elemental Microanalysis, its reproducibility (as one standard deviation) during analysis for run 1 = 0.14 and run 2 = 0.11 (Appendix 8). Isotopic compositions in this study (SIMS and Mass spectrometry technique) are quoted in ‰ relative to standard mean ocean water (SMOW); individual analyses have an uncertainty of ± 0.11‰ (based on one standard deviation of the standard repeat analyses for the drift correction).

SIMS measurements were undertaken on selected polished areas of a calcite carbonatite sample (OKC19-1, Fig. 5-3) alongside standards mounted in the same epoxy block. Prior to mounting, the selected samples were imaged using SEM-BSE. The blocks were gold coated prior to SIMS analysis. Measurements were carried out at the Edinburgh Ion Microprobe Facility (EIMF) using a Cameca 1270 mass spectrometer operating with a primary Cs+ beam, in multi collector mode, operating at conditions of ~5 nA with a net impact energy of 20KeV (+10 kv primary and -10 kv secondary). The beam has generated pits of about 12 μm. EIMF calcite and Stern S0237 baryte were used as standards. The instrument was calibrated before each session and its drift was corrected by analysing 5 to 10 points of the reference standards at the beginning and end of the session and after every 10 unknowns. Linear least squares was applied as drift correction. The uncertainty in individual data points is estimated to be ± 0.04‰ for baryte and 0.03‰ for calcite and the reproducibility of the calcite and baryte standards are found in Appendix 8.

5.5. Results

5.5.1. Dissolution - Mass spectrometry measurements

Analyses of calcite powders are presented in Appendix 8 and summarised in Table 5-2. It was only possible to obtain pairs of magmatic and hydrothermal calcite for three of the samples: OKA1, OKC4 and OKC17; the other analyses are likely to be of mixed material. Overall, the average analyses in Table 5-2 are between 7.7‰ to 9.4‰ except for sample OKC4, which yields heavier values (av. magmatic = 11.1‰ and av. hydrothermal = 12.6‰). The full range for each of these average compositions is included in Fig. 5-4, and the data points are still closely constrained. It is notable that the hydrothermal and magmatic calcite compositions

for each sample where pairs of values are available, are very similar (Fig. 5-4). This is true of sample OKC4 also, even though the values are both significantly heavier than those from the other samples. This is in accordance with the published fractionation factors for these minerals (Zheng, 1999).

In some samples the analyzed powders were drilled from points which could not be classified texturally (sample OKC19-1, 18 and 17; Table 5-2); however these lie within the same range as the calcites identified as magmatic or hydrothermal in samples OKC17 and OKA1 (Table 5-2, Fig. 5-4), with very similar average $\delta^{18}O$ values and little variability (Table 5-2). Hydrothermal calcite tends to be slightly isotopically heavier than magmatic calcite from the same sample, although this is not the case in OKA1 (Fig 5-4). Nevertheless, the difference between calcites from the different stages is small compared to the difference between OKC4 and the other samples.

sample stage	OKC19-1 (‰) unidentified	OKC18 (‰) unidentified	OKC17 (‰) unidentified	OKC17 (‰) magmatic	OKC17 (‰) hydrothermal	OKA1 (‰) magmatic	OKA1 (‰) hydrothermal	OKC4 (‰) magmatic	OKC4 (‰) hydrothermal
$\delta^{18}O$ min	7.81	7.45	8.17	7.76	8.40	7.62	8.17	11.25	11.70
$\delta^{18}O$ max	9.17	7.85	8.59	8.60	10.46	9.23	8.50	11.40	13.31
average	**8.60**	**7.74**	**8.38**	**8.08**	**9.40**	**8.38**	**8.39**	**11.31**	**12.58**
stdev	0.50	0.17	0.20	0.46	1.03	0.81	0.17	0.06	0.60
n	5	5	5	3	3	3	4	4	5

Table 5-2: Summary of the drilled calcite powder oxygen isotope data measured by Mass spectrometry, all as $\delta^{18}O$ SMOW.
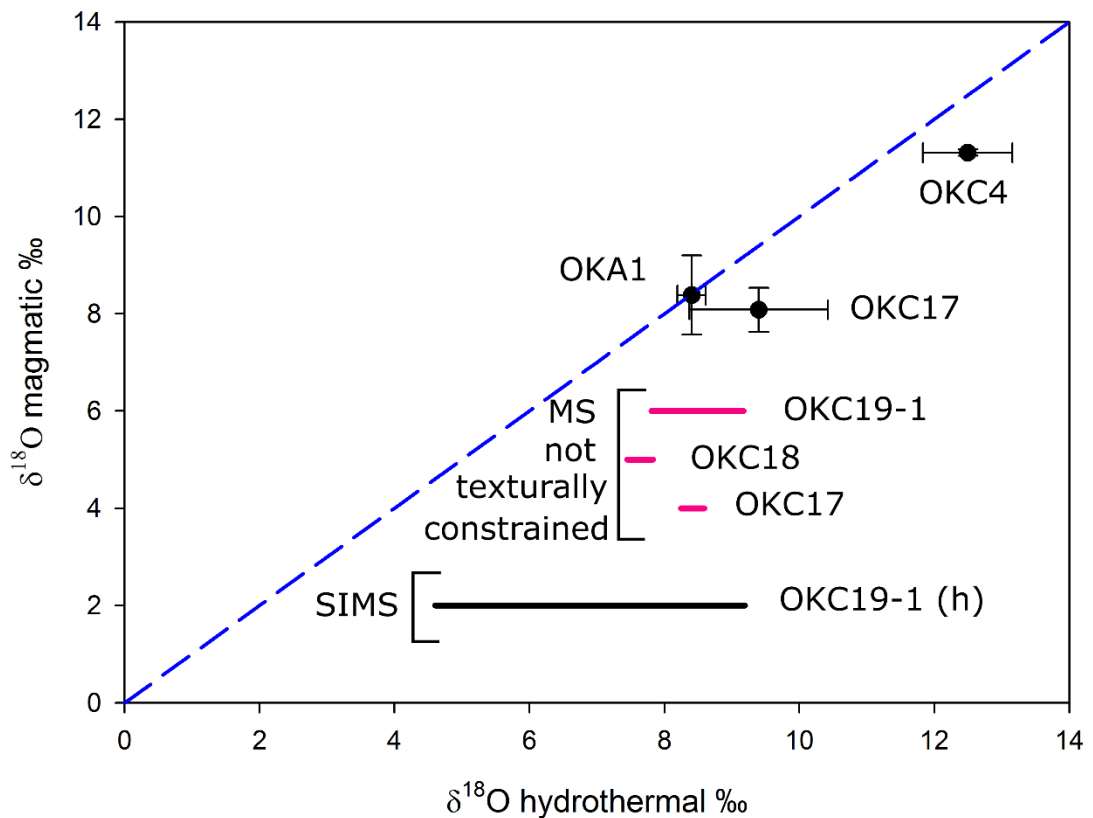
Figure 5-4: Oxygen isotope composition of pairs of magmatic and hydrothermal calcite from samples OKC4, OKA1 and OKC17. The plotted point is the data mean (Table 5-2) and the error bars show one standard deviation. The pink lines correspond to analyses of calcite which were not texturally constrained, MS – mass spectrometry. The black line is the range of compositions of hydrothermal calcite measured by SIMS (sample OKC19-1).

5.5.2. SIMS measurements

Calcite and baryte were analysed in two areas of sample OKC19-1, shown in Fig. 5-3, P1 and P3, which are about 6 mm apart. Baryte 1 is hosted by hydrothermal calcite and is in area P1, while barytes 2 and 3 are hosted by hydrothermal calcite in area P3. The hydrothermal calcite analysed hosting baryte 2 and 3 are part of the same single crystal.

Stage 3 calcite (cc$_{h1}$, hydrothermal) δ^{18}O composition shows a large spread in δ^{18}O values over the three areas analysed, with maximum composition near 9‰ and minimum composition around 5‰ and all averaging around 6‰ (Figs 5-2, 5-5; Table 5-3). This variation is much larger than the analytical uncertainty (0.03‰) and is likely to reflect heterogeneity

in the grains. The calcite cc_{h2} bands in area P1 are however distinctly lighter (average 3.5‰), so the total range in this calcite grain is around 3.4‰ to 9.0‰ (Fig. 5-2B; Table 5-3).

In contrast to the stage 3 calcite, each small stage 3 baryte crystal is rather homogenous with a narrow spread of $\delta^{18}O$ values (Table 5-3; Fig. 5-2), but each crystal analysed has a distinct $\delta^{18}O$ composition with no overlap in the data range (Fig. 5-5), even for barytes 2 and 3 from within the same calcite crystal (Table 5-3; Fig. 5-5).

mineral	baryte 1 (‰)	baryte 2 (‰)	baryte 3 (‰)	cc_{h1} (‰)	cc_{h2} (‰)	cc_{h1} (‰)	cc_{h2} (‰)	cc_{h1} (‰)
area	P1	P3	P3	P1	P1	P3	P3	P3
$\delta^{18}O$ min	1.41	11.25	14.04	4.60	3.41	5.41	5.44	5.37
$\delta^{18}O$ max	3.90	13.98	16.94	9.03	3.66	8.50	8.50	9.19
average	**3.05**	**12.25**	**15.60**	**5.68**	**3.53**	**5.91**	**6.97**	**6.59**
stdev	0.92	0.90	1.20	1.66	0.12	0.74	2.16	1.28
n	8	7	6	6	4	4	2	7

Table 5-3: Summary of the SIMS oxygen isotope data from cogenetic calcite and baryte, and later calcite cc_{h2} from area P3 sample OKC19-1, all as $\delta^{18}O_{SMOW}$‰.
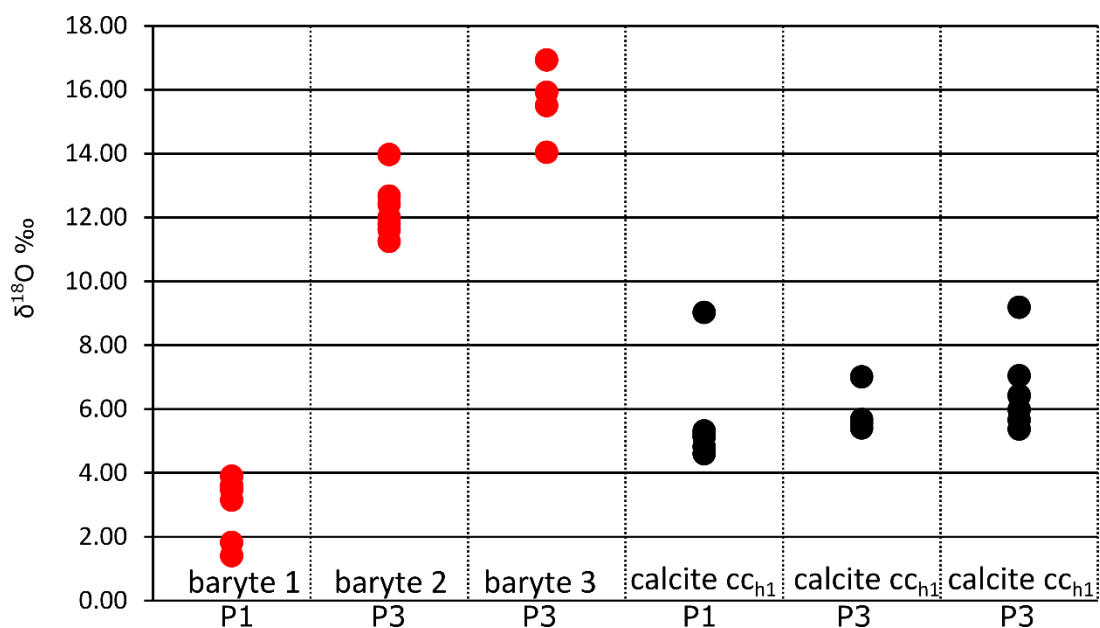
Figure 5-5: $^{18}\delta O$ composition of the hydrothermal baryte 1, baryte 2 and baryte 3 and its host calcite cc_{h1} analysed by SIMS.

5.6. Discussion

The oxygen isotope composition of the micro-drilled hydrothermal calcites at Okorusu broadly reflects the composition of nearby magmatic calcite across a range of primary compositions from different magmatic stages, and this suggests that they are dominated by oxygen derived from their magmatic precursors, rather than oxygen introduced by the hydrothermal fluid (Fig. 5-4; Table 5-2). The very similar values for the magmatic and the hydrothermal generations are indicative of local rock buffering of the hydrothermal fluid which equilibrated with the local rock as it recrystallized magmatic calcite. This is a pattern of behaviour which is common in modern geothermal systems and means that the fluid composition no longer reflects the fluid source. It also indicates that the oxygen isotopic composition of hydrothermal calcite is predominantly controlled by the composition of the magmatic calcite which is being replaced, rather than the composition of the hydrothermal fluid. This would be expected in a system which experienced only limited fluid ingress.

Local buffering of hydrothermal calcite is however in contrast with results from the Bear Lodge carbonatite (Moore *et al.,* 2015 and Andersen *et al.,* 2017), which also shows secondary REE mineralization but experienced an increase of $\delta^{18}O$ from a typical mantle-like value (e.g. between 5‰ and 8‰; Jones *et al.,* 2013) for the magmatic calcite up to 18‰, for

calcite from the more altered and REE enriched zones, this is interpreted as the reaction between the carbonatite and a low temperature meteoric fluid.

In more detail however, the SIMS study of OKC19-1 hydrothermal calcite reveals local variability in calcite composition, and this is likely to reflect incomplete buffering of the introduced hydrothermal fluid during calcite recrystallisation. The baryte analyses provide additional insights into this dynamic aspect of the hydrothermal alteration. Two of the three analysed barytes have significantly heavier oxygen than the adjacent calcite (baryte 2 avg. 12.25‰ and baryte 3 avg. 15.60‰), despite the fact that at equilibrium baryte has a lower $\delta^{18}O$ value than coexisting calcite (Zheng, 1999). There is no possibility that the baryte grains from area P3 grew in equilibrium with their host calcite, although this is a possibility for baryte 1 from area P1. Instead, the data point to a dynamic system in which an incoming fluid with a distinctive fluid composition is modified by reaction with the host carbonatite, precipitating material with different oxygen isotope compositions according to the degree of interaction. This process is consistent with the magmatic redistribution mechanism described by Cangelosi *et al.,* (2019a, Fig. 3-11). Baryte crystallisation is triggered by release of Ba from magmatic calcite into a sulfate-bearing hydrothermal fluid, possibly arising through oxidising the local pyrite. Where the baryte precipitates before the system has equilibrated, it has a heavier oxygen isotope composition, making it distinct from the magmatic phases. Temperature variation is unlikely to be an important factor influencing the spread in the data, since calcite-baryte fractionation of oxygen is not strongly temperature dependent (Zheng, 1999).

In order to explore the implications of the data for water composition, we have calculated the oxygen isotopic composition of water in equilibrium with each of the calcite and baryte grains summarized in Table 5-3 as a function of temperature (Fig. 5-6). For the calcite-baryte pairs in area P3, it is clear that, irrespective of temperature, the baryte and its host were not in equilibrium with the same fluid. In contrast, curves for cc_{h1} and baryte 1 from area P1 are identical within error and indicate that for this part of the sample the fluid was already equilibrated for oxygen before baryte precipitated. Baryte 1 is hosted by cc_{h1} which has a slightly heavier composition than the baryte, this is consistent with equilibrium at hydrothermal temperature (Zheng, 1999).

Although, the oxygen isotope data cannot be used directly to estimate temperature, as the fractionation factors between the two phases are within uncertainty of the analytical techniques over the range of temperatures of interest, the results are indicative of low

temperature baryte growth. It is apparent from Fig. 5-6 that barytes 2 and 3 grew from fluids that were heavier than water equilibrated with local carbonatite. It is unusual for geothermal fluids to have $\delta^{18}O$ compositions much heavier than 0‰ and so if the incoming oxidised fluid had a composition of around 0‰ or lower, it is clear from Fig. 5-6 that these barytes must have grown at low temperatures, around or even below 100 °C. Heavy baryte composition can also be caused by a disequilibrium in the hydrothermal fluid between the oxygen hosted by the sulfate (from pyrite oxidation) and the oxygen from the meteoric water (McKenzie and Truesdell, 1975). This oxygen isotope disequilibrium also requires low crystallisation temperature, e.g. for a neutral pH, the upper limit temperature is 140 °C (Lloyd, 1968). Finally, it is of course possible for water to become heavier through interaction with appropriate country rocks at elevated temperatures, so this option cannot be ruled out, but a low temperature origin is consistent with the fluid inclusion evidence for late stage hydrothermal origin of fluorite (Bühn *et al.,* 2003). This also agrees with the upper temperature limit from the calcite-dolomite geothermometer of 200 °C and so supports the idea that the hydrothermal reworking of the REE mineralisation at Okorusu took place at low temperature conditions, consistent with many contemporary geothermal systems.
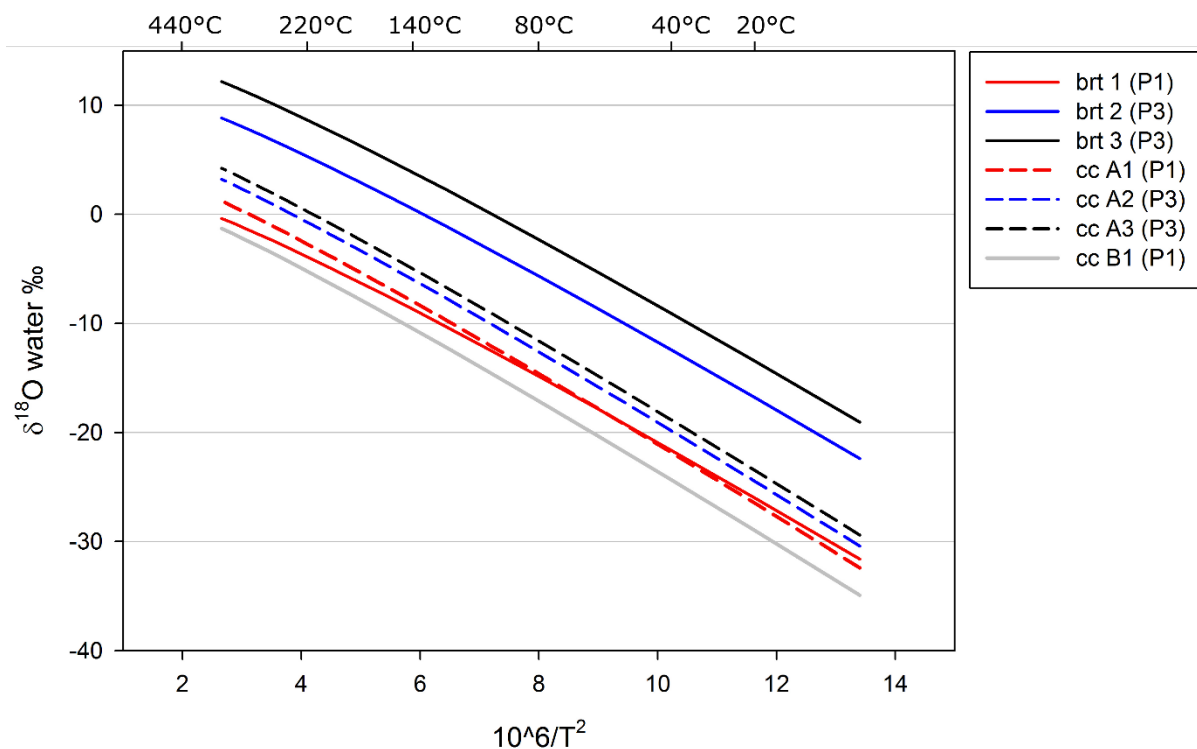
Figure 5-6: Hypothetical hydrothermal fluid composition versus the temperature as a function of the mean value of the baryte and calcite crystals analysed by SIMS.

5.7. Conclusion

The hydrothermal stage 3 fluid responsible for the main alteration stage in the calcite carbonatite at Okorusu does not reflect its source due to the magmatic and recrystallised hydrothermal calcite having very similar $\delta^{18}O$ compositions, suggesting local buffering. Nonetheless, the hydrothermal calcite local $\delta^{18}O$ composition variability reflects an incomplete buffering of the introduced hydrothermal fluid. The amount of fluid introduced to the system was not sufficient to shift the altered carbonatite $\delta^{18}O$ composition, unlike that observed in the economic REE carbonatite deposit Bear Lodge. The crystallisation of stage 3 hydrothermal calcite, sulfate and REE minerals observed in the calcite carbonatite was induced by a low temperature (less than 200 °C) dynamic fluid system with the introduction of small volumes of fluid locally reworking the magmatic phases.

Acknowledgments

References

Anovitz, L.M. and Essene, E.J. (1987) Phase equilibria in the system $CaCO_3$-$MgCO_3$-$FeCO_3$. *Journal of Petrology,* **28**, 389-414.

Andersen, A.K., Clark, J.G., Larson, P.B., and Donovan, J.J. (2017) REE fractionation, mineral speciation, and supergene enrichment of the Bear Lodge carbonatites, Wyoming, USA. *Ore Geology Reviews*, **89**, 780-807.

Broom-Fendley, S., Heaton, T, Wall, F. and Gunn, G. (2016) Tracing the fluid source of heavy REE mineralisation in carbonatites using a novel method of oxygen-isotope analysis in apatite: The example of Songwe Hill, Malawi. *Chemical Geology*, **440**, 275-287.

Broom-Fendley, S., Wall, F., Spiro, B. and Ullmann, C.V. (2017a) Deducing the source and composition of rare earth mineralising fluids in carbonatites: insights from isotopic (C, O, $^{87}Sr/^{86}Sr$) data from Kangankunde, Malawi. *Contributions to Mineralogy and Petrology*, **172**, 96.

Broom-Fendley, S., Aoife, B.E., Wall, F., Gunn, G. and Dawes, W. (2017b) REE minerals at the Songwe

Hill carbonatite, Malawi: HREE-enrichment in late-stage apatite. *Ore Geology Reviews,* **81**, 23-41.

Bühn, B., Schneider, J., Dulski, P. and Rankin, A.H. (2003) Fluid-rock interaction during progressive migration of carbonatitic fluids, derived from small-scale trace element and Sr, Pb isotope distribution in hydrothermal fluorite. *Geochimica et Cosmochimica Acta*, **67**, 4577-4595.

Cangelosi, D.A., Broom-Fendley, S., Banks, D.A., Morgan, D.J. and Yardley, B.W.D. (2019a) LREE redistribution during hydrothermal alteration at the Okorusu carbonatite complex, Namibia. *Mineralogical Magazine*, (n.d.) 1-54.

Cangelosi, D.A., Smith, M.P; Banks, D.A. and Yardley, B.W.D. (2019b) The role of sulfate-rich fluids in Heavy Rare Earth enrichment at the Dashigou carbonatite deposit, Huanglongpu, China. *Mineralogical Magazine*, (n.d.).

Deines, P. (1989) Stable isotope variations in carbonatite. In: Bell, K. (Ed.), Carbonatites: Genesis and Evolution. Unwin Hyman, London.

Demény, A., Ahijado, A., Casillas, R. and Vennemann, T. (1998) Crustal contamination and fluid/rock interaction in the carbonatites of Fuerteventura (Canary Islands, Spain): a C, O, H isotope study. *Lithos*, **44**, 101-115.

Demény, A., Sitnikova, M. and Karchevsky, P. (2004) Stable C and O isotope compositions of carbonatite complexes ofthe Kola Alkaline Province: phoscorite-carbonatite relation- ships and source compositions. In: Wall, F., Zaitsev, A. (Eds.), Phoscorites and Carbonatites from Mantle to Mine: The Key Example of the Kola Alkaline Province. Mineralogical Society Series, vol. 10, p. 407.

Genge, M.J., Balme, M. and Jones, A.P. (2001) Salt-bearing fumarole deposits in the summit crater of Oldoinyo Langai, Northern Tanzania: Interaractions between natrocarbonatite lava and meteoric water. *Journal of Volcanology and Geothermal Research*, **106**(1-2), 111-122.

Hoefs, J. (2008) Stable Isotope Geochemistry. Springer

Jones, A.P., Genge, M. and Carmody, L. (2013) Carbonate melts and carbonatites. *Reviews in Mineralogy and Geochemistry*, **75**, 289–322.

Kapustin, I. (1980) Mineralogy of Carbonatites. Amerind Publishing Co., New Dehli.

Keller, J. and Hoefs, J. (1995) Stable isotope characteristics of recent natrocarbonatites from Oldoinyo Lengai. In: Bell, K., Keller, J. (Eds.), Carbonatite Volcanism. Springer, pp. 113-123.

Lloyd, R.M. (1968) Oxygen isotope behaviour in the sulfate water system. *Journal of Geophysical Research,* **73**, 6099-6110.

McKenzie, W.F. and Truesdell, A.H. (1977) Geothermal reservoir temperatures estimated from the oxygen isotope compositions of dissolved sulfate and water from hot springs and shallow drillholes. *Geothermics,* **5** (1–4), 51-61.

Milner, S.C., Le Roex, A.P. and O'Connor, J.M. (1995) Age of Mesozoic igneous rocks in northwestern Namibia, and their relationship to continental breakup. *Journal of the Geological Society*, **152**, 97-104.

Moore, M., Chakhmouradian, A.R., Mariano, A.N. and Sidhu, R. (2015) Evolution of rare-earth mineralization in the Bear Lodge carbonatite, Wyoming: Mineralogical and isotopic evidence. *Ore Geology Reviews,* **64**, 499-521.

Rankin, A.H. (2005) Carbonatite-associated rare metal deposits—Composition and evolution of ore-forming fluids-The fluid inclusion evidence. pp. 299-314 in: Rare-element geochemistry and mineral deposits (Linnen, R.L. and Samson, I.M. editors) Quebec: Geological Association of Canada, Short Course Notes 17.

Ray, J.S., Ramesh, R., 2000. Rayleigh fractionation of stable isotopes from a multicomponent source. *Geochimica and Cosmochimica Acta,* **64**, 299-306.

Ray, J.S., Ramesh R. (2006) Stable carbon and oxygen isotopic compositions of Indian carbonatites. *International Geology Review*, **48**(1), 17-45.

Santos, R.V. and Clayton, R.N. (1995) Variations of oxygen and carbon isotopes in carbonatites: a study of Brazilian alkaline complexes. *Geochimica et Cosmochimica Acta*, **59**, 1339-1352.

Shu, X. and Liu, Y. (2019) Fluid inclusion constraints on the hydrothermal evolution of the Dalucao Carbonatite-related REE deposit, Sichuan Province, China. *Ore Geology Reviews*, **107**, 41-57.

Simandl, G.J. and Paradis, S. (2018) Carbonatites: related ore deposits, resources, footprint, and exploration methods. *Applied Earth Science,* **127**(4), 123-152.

Smith, M.P., Henderson, P. and Campbell, L.S. (2000) Fractionation of the REE during hydrothermal processes: constraints from the Bayan Obo Fe-REE-Nb deposit, Inner Mongolia, China. *Geochimica et Cosmochimica Acta*, **64**, 3141-3160.

Smith, M.P., Campbell, L.S. and Kynicky, J. (2015) A review of the genesis of the world class Bayan Obo Fe-REE-Nb deposits, Inner Mongolia, China: Multistage processes and outstanding questions. *Ore Geology Reviews*, **64**, 459-476.

Shu, X. and Liu, Y. (2019) Fluid inclusion constraints on the hydrothermal evolution of the Dalucao Carbonatite-related REE deposit, Sichuan Province, China. *Ore Geology Reviews*, **107**, 41-57.

Taylor, H.P., Frechen, J. and Degens, E.T. (1967) Oxygen and carbon isotope studies of carbonatites from the Laacher See district, West Germany and the Alnö district, Sweden. *Geochimica Cosmochimica Acta,* **31,** 407-430.

U.S. Geological Survey (2018) Mineral commodity summaries 2018, U.S. *Geological Survey*, 1-204.

Van Zijl, P (1962) *The geology, structure and petrology of the alkaline intrusions of Kalkfeld and Okorusu and the invaded Damara rocks*. PhD dissertation, University of Stellenbosch, South Africa.

Verplanck, P.L., Farmer, G.L., Kettler, R.M., Lowers, H.A., Koenig, A.E. and Blessington, M.J. (2014) Rare Earth Element Enrichments in the Elk Creek Carbonatite. *Acta Geologica Sinica*, **88**, 466-467.

Wall, F. and Zaitsev, A. (2004) Rare earth minerals in Kola carbonatites Phoscorites and Carbonatites from Mantle to Mine: the Key Example of the Kola Alkaline Province. *Mineralogical Society Bulletin*, **10**, 341-373.

Woolley, A.R. and Kempe, D.R.C. 1989. Carbonatites: nomenclature, average chemical composition. Pp. 1-14 in: *Carbonatites: Genesis and evolution (*K. Bell, editor). Unwin Hyman, London.

Zaitsev, A.N., Wall, F. and Le Bas, M.J. (1998) REE-Sr-Ba minerals from the Khibina carbonatites, Kola Peninsula, Russia: their mineralogy, paragenesis and evolution. *Mineralogical Magazine*, **62**, 225-250.

Zheng, Y.F. (1999) Oxygen isotope fractionation in carbonate and sulfate minerals. *Geochemical Journal*, **33**(2), 109–126.

CHAPTER 6.

Discussion, conclusions and further work

6.1. Introduction

This chapter synthesises the work presented in Chapters 3, 4 and 5. In particular, it explores what we have learned about calcite carbonatite deposits in general and the role of hydrothermal activity in enhancing ore grades. Further work building on the results of this thesis is also proposed. Finally, the concluding remarks and main findings of this study are summarised at the end of this chapter.

The main objectives of this thesis have been to investigate the role and extent of hydrothermal alteration in determining the distribution of REE in calcite carbonatite deposits, and hence put some light on natural REE beneficiation in such systems. In order to contrast the behaviour of LREE and HREE, two contrasting deposits were investigated. Both were hydrothermally reworked, but the Okorusu calcite carbonatites retain the LREE-enriched pattern typical of unaltered carbonatites while the Dashigou calcite carbonatites show a flat REE pattern reflecting HREE enrichment relative to the LREE.

6.2. Discussion

6.2.1. Hydrothermal alteration at the Okorusu and Dashigou deposits

As discussed in Chapters 3, 4 and 5 the Okorusu and the Dashigou calcite carbonatites have both been affected by secondary hydrothermal alteration. Despite the differences in the final REE pattern and the grades attained, there are also important similarities in the hydrothermal processes that led to the REE beneficiation observed. The initial REE mineralisation of both calcite carbonatites is of magmatic origin and where the REE distribution has been modified by hydrothermal processes, mobile REE were sourced from the carbonatite complexes themselves, with no evidence of an external source. The hydrothermal alteration evidence associated to the main REE mineralisation stage of both

155

deposits are observed through replacement texture of the magmatic minerals by typical hydrothermal mineral assemblage, fluid inclusion study and other available geothermometer within the carbonatite rocks.

At Okorusu, the main hydrothermal stage is referred to as stage 3 (Chapter 3), it mainly involves partial breakdown of apatite and extensive recrystallisation of more abundant, trace element-rich magmatic calcite, to purer hydrothermal calcite. The REE elements released from the magmatic minerals during alteration concentrated as hydrothermal parisite, and the other trace elements precipitated mostly as sulfate (baryte and celestine) with lesser amounts of strontianite, witherite and other minor phases. The widespread presence of iron hydroxide also indicates hydrothermal conditions. The hydrothermal parisite REE pattern is broadly similar to those of the magmatic phases (Fig. 3-7) but shows even stronger LREE enrichment. The distinct break in temperature between the magmatic and secondary mineralisation stage (Chapter 3) also indicates hydrothermal alteration conditions, with the fluid inclusions hosted by fluorite from stage 4 suggesting its growth took place at 150 °C ± 30 °C (Bühn *et al.,* 2002). Stage 3 and stage 4 hydrothermal alterations result in a similar hydrothermal mineral assemblage, though stage 4 is dominated by fluorite. More indication on the hydrothermal condition of stage 3 is observed through the Mg content of calcite coexisting with dolomite (calcite-dolomite solvus geothermometer, Anovitz and Essene, 1987). The data indicate both stages 3 and 4 developed at temperatures < 200 °C (Table 3-2), in agreement with the fluid inclusion results.

At Dashigou, the magmatic REE minerals have been partially to fully replaced by subsequent hydrothermal REE minerals which are cogenetic to the deposition of secondary quartz (Qz-2 and Qz-3) and abundant sulfate mineralisation. The secondary quartz non-luminescent CL emission and its volume for volume replacement texture observed by SEM-CL are characteristic of hydrothermal conditions (Fig. 4-4). The quartz also hosts Lw + V fluid inclusions with Th_{TOT} measurements pointing to low hydrothermal temperatures (120 °C to 222 °C; Appendix 6). The magmatic REE mineralisation including monazite, bastnäsite and parisite show steep, LREE enriched, chondrite-normalised patterns compared to the magmatic calcite which shows a HREE enrichment toward the late magmatic stage, leading to the late magmatic calcite crystallising with a flat REE pattern. The hydrothermal REE minerals are still Ce-dominant but have much higher HREE content than typically found in carbonatites and broadly match the magmatic calcite REE pattern.

Figure 6-1 and 6-2 summarises the evolution of both systems studied, with the hydrothermal alteration stages in green boxes (Fig. 6-1). It demonstrates that both Dashigou and Okorusu calcite carbonatites show a similar hydrothermal fluid-rock interaction stage which triggered the natural REE beneficiation. Both deposits show calcite recrystallisation with introduction of sulfate. Nonetheless, the final REE patterns are contrasting (Fig. 6-3). This suggests that the REE source and the hydrothermal fluid are the main defining factors associated to the final REE patterns of a carbonatite, rather than the conditions of alteration. The magmatic calcite from Okorusu shows a normal LREE enriched pattern (Fig. 6-3), while the deposition of the magmatic calcite got progressively HREE enriched during the late magmatic stage in the Dashigou calcite carbonatites (Fig. 6-3). Nevertheless, the fluid-rock interaction stages of both deposits show some similarities, such as the hydrothermal sulfate mineralisation, even though the amount of sulfate introduced (Fig. 6-1), and probably its source, are different. We only observed minor sulfate introduction for the Okorusu calcite carbonatite, likely derived from the oxidation of local pyrite. The reworked calcite liberated Ba and Sr, leading to the precipitation of small sulfate inclusions within the recrystallised calcite. At Dashigou, there is a more extensive introduction of external sulfate through a sulfate-rich fluid which has led to the precipitation of sulfate compounds of the major elements (Ca, K, Sr, Ba and Na), both as solids trapped in fluid inclusions and as abundant celestine-baryte mineralisation (Fig. 4-8; Table 4-5).
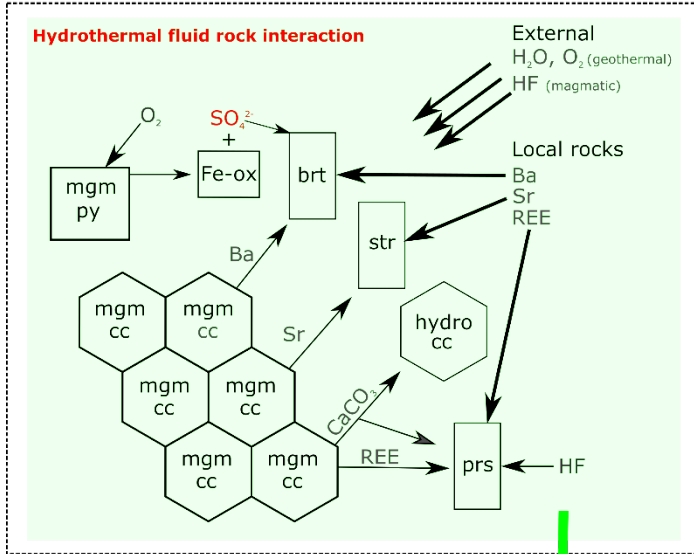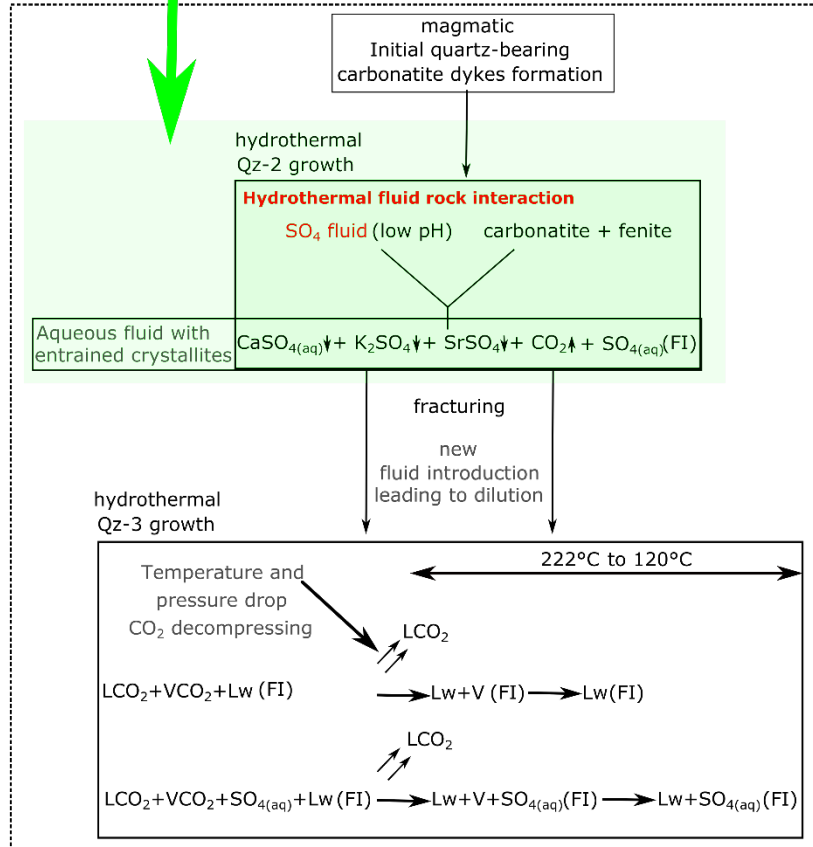
Figure 6-1: Summary of the Okorusu and Dashigou calcite carbonatites hydrothermal alteration stage responsible for the secondary REE mineralisation.
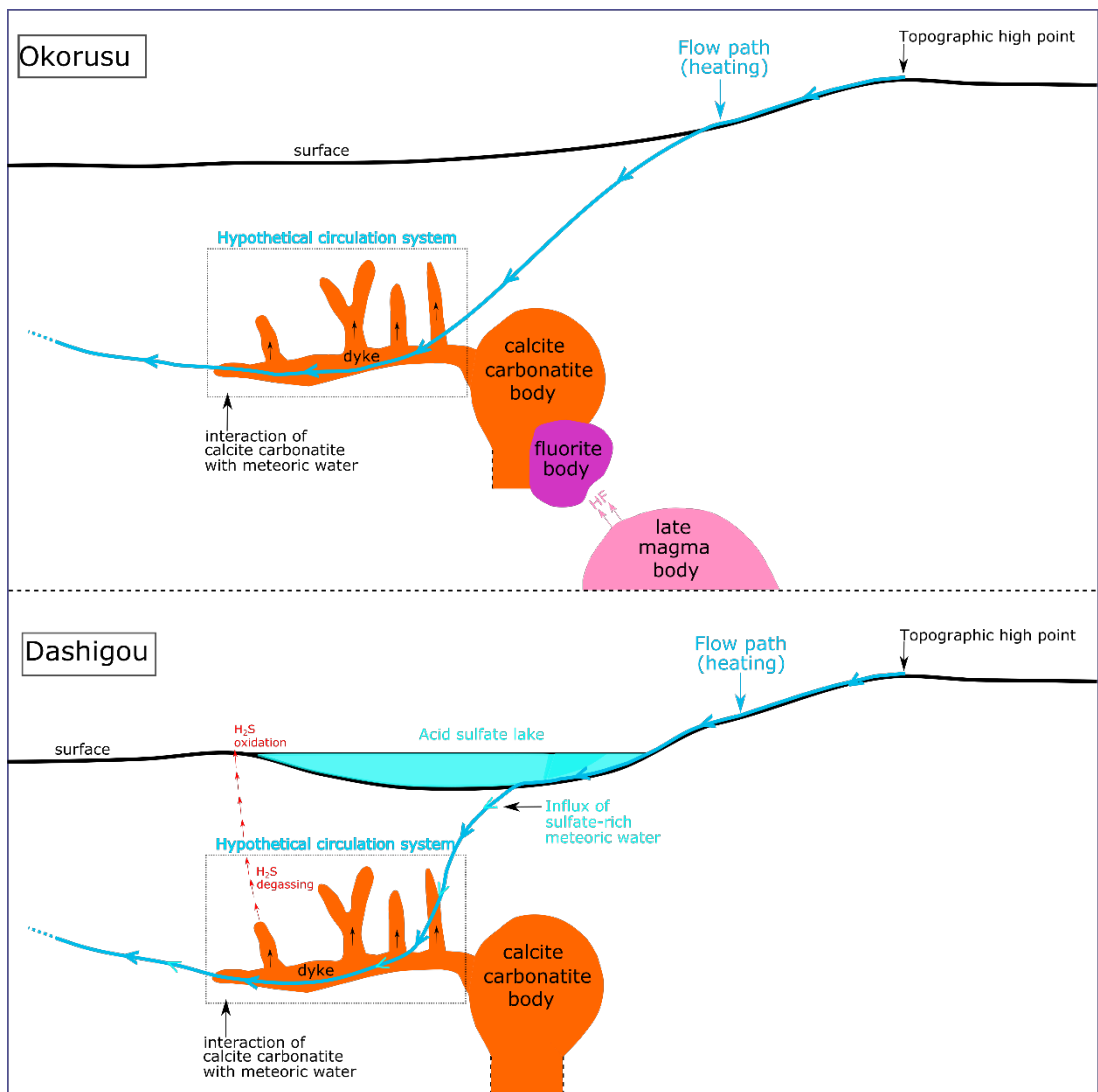
Figure 6-2: Speculative schematic cross section of fluid circulation in geological context for the Okorusu and the Dashigou calcite carbonatite deposits.

6.2.2. Hydrothermal REE beneficiation at the Okorusu and Dashigou calcite carbonatite deposits

The Okorusu and the Dashigou deposits, both show evidence for natural REE beneficiation after hydrothermal reworking of the calcite carbonatites, but to varying degrees. Ultimately, the most important difference is that the Dashigou calcite carbonatite deposit is an economically viable REE deposit, notably for HREE, and is part of a major REE producing area in China (Kynicky *et al.,* 2012), whilst the Okorusu calcite carbonatites do not attain ore grades for REE, even though locally secondary LREE mineralisation is abundant. Figure 6-3 illustrates an example for each deposit. The Okorusu pegmatite calcite carbonatite pod has been significantly less altered toward the middle of the pod (sample OKC17) with around 45% of hydrothermal minerals compared to the pod margin (sample OKC19-2), which consists of 95% of hydrothermal minerals (Fig. 1-3; Table 3-3). The hydrothermal alteration has significantly increased the bulk REE content for the more altered sample (respectively little-altered to altered sample ∑REE from 2190 ppm to > 6758 ppm; Table 3-4). The same process is observed for the Dashigou calcite carbonatites, where the altered calcite carbonatites show an enhanced REE content compared to the little-altered carbonatites (respectively, ∑REE from 1717 ppm to 5833 ppm). For both deposits the carbonatites REE profiles of the altered rocks have broadly similar characteristics to the less altered ones (Fig. 6-3).

Overall, the reworking process consisted of the breakdown of magmatic minerals, mainly calcite but also apatite (Okorusu) and monazite (Dashigou), releasing their REE content, with coupled growth of purer hydrothermal phases including accessory REE minerals. In both cases, the recrystallisation of the dominant mineral, calcite with moderate REE content, dictates the final REE pattern (Fig. 6-3). The primary magmatic calcite does not have a high REE content but its abundant volume and greater susceptibility to alteration than other magmatic minerals, make it the main REE source for secondary REE minerals. As an example, a magmatic calcite (sample HLP5) from the Huanglongpu carbonatite deposit, which includes Dashigou, contains ∑REE = 627 ppm, with ∑LREE = 370 ppm and ∑HREE = 257 ppm (Smith *et al.,* 2018); while the average magmatic calcite composition from sample OKC17 at Okorusu contains ∑REE = 1419 ppm, with ∑LREE = 1403 ppm and ∑HREE = 16 ppm (Table 3-2). Hence,

the differences in the REE pattern of the hydrothermally altered carbonatites at Okorusu and Dashigou reflects that already present in the magmatic calcite (Fig. 6-3).
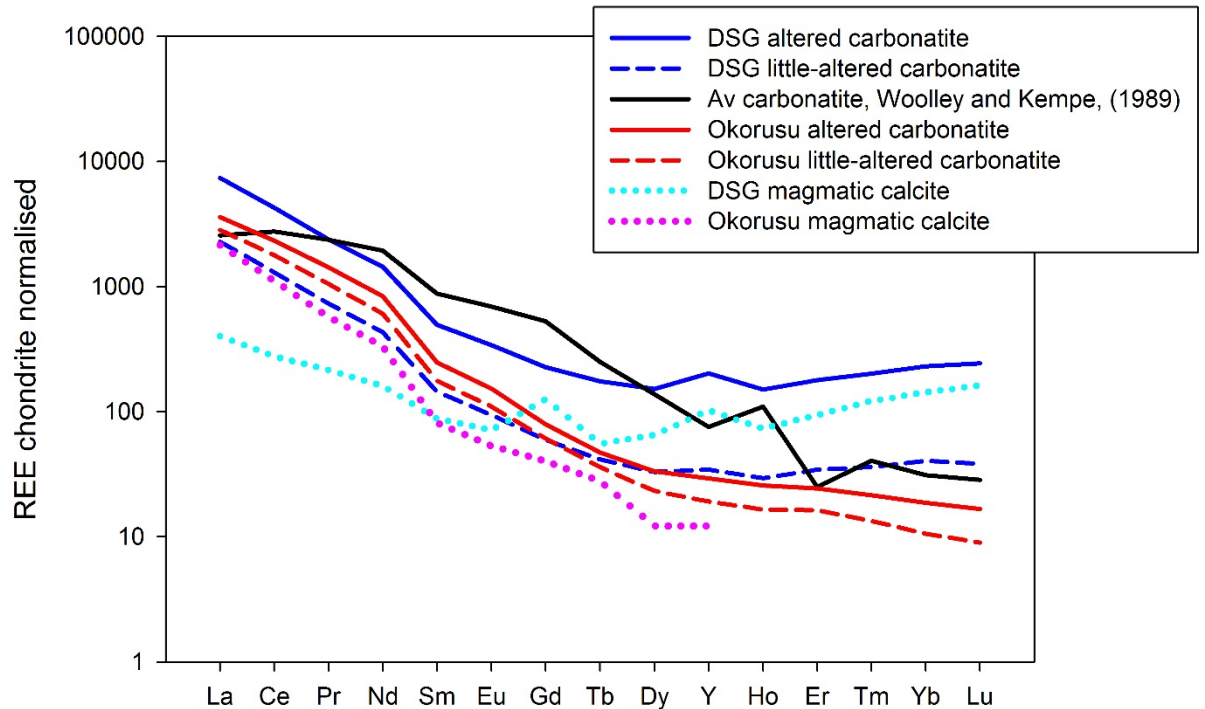
Figure 6-3: Comparison of chondrite normalised (McDonough and Sun, 1995) example of magmatic calcite and bulk rock analyses of the Dashigou (DSG) calcite carbonatites, China and the Okorusu calcite carbonatites, Namibia and the average calcite carbonatites REE patterns (Woolley and Kempe, 1989). DSG altered carbonatite = sample DSG 436; DSG little-altered carbonatite = sample DSG 435; Okorusu altered carbonatite = sample OKC19-2; Okorusu little-altered carbonatite = sample OKC17; DSG magmatic calcite = sample HLP5 (Smith et al., 2019); Okorusu magmatic calcite = sample OKC17.

6.2.3. Effects of the extent of hydrothermal alteration on REE beneficiation in carbonatites.

As discussed previously, the Okorusu and the Dashigou deposits, both show evidence for natural beneficiation after hydrothermal reworking of the calcite carbonatites, but to different extents. The Okorusu calcite carbonatite oxygen compositions suggest a strong influence from magmatic compositions, with occasional pulses of isotopically distinct fluid entering the system and being equilibrated with the local rock. There is no comparable evidence for the relative importance of buffered and infiltrated fluids at Dashigou. Nonetheless, the several REE mineralisation stages described by Smith *et al.,* (2018) and the

precipitation of abundant hydrothermal quartz and sulphates lead to think that infiltration was more important than for the Okorusu calcite carbonatites, and this is likely a cause of the greater REE contents.

The Bear Lodge alkaline complex, Wyoming (USA) hosts stockwork-style calcite carbonatite dykes which are REE mineralised and provide an interesting comparison with the deposits studied here. The central dyke swarm consists of unaltered carbonatites showing already high REE-levels with the common LREE enriched pattern, whilst the peripheral altered carbonatite dyke zones show substantial increase in the REE content (e.g. Bull Hill unaltered carbonatite, sample R25177 $\sum$REO+Y_2O_3 = 5.5 wt.% and Bull Hill altered carbonatite, sample R25340 $\sum$REO+Y_2O_3 =23.5 wt.%; Andersen *et al.,* 2017). The magmatic REE mineralisation mainly consists of bastnäsite, parisite and synchysite in the unaltered carbonatites. This assemblage is replaced by secondary REE mineralisation including fluorcarbonate, ancylite and monazite in the altered carbonatites. The Bear Lodge carbonatites are similar to the Okorusu carbonatites in terms of their LREE-enriched patterns (Fig. 2-2), and they have both been subjected to a low temperature hydrothermal alteration leading to enhanced secondary REE mineralisation. However after hydrothermal alteration, the Bear Lodge carbonatites hold economic REE content comparable to some Chinese REE carbonatite deposits such as the Maoniuping deposit (Moore *et al.,* 2015; Andersen *et al.,* 2017; Zheng and Liu, 2019; Fig. 2-3). The difference is reflected in their oxygen isotopic compositions after hydrothermal alteration. At Okorusu, the similar oxygen isotope compositions of magmatic and hydrothermal calcites point to local rock buffering of the incoming hydrothermal fluid equilibrating. This suggests that the amounts of fluid introduced were insufficient to modify the rock composition, despite the fluid being isotopically distinct initially. In contrast, the Bear Lodge carbonatites show a clear shift in oxygen isotope composition, from mantle-like δ^{18}O values (between 5‰ and 8‰; Jones *et al.,* 2013) to < 18‰ after hydrothermal alteration. The distinct overprint likely reflects a much greater hydrothermal fluid flow.

The REE upgrading factor caused by the hydrothermal reworking in both carbonatite deposits, even though slightly higher for Bear Lodge, are fairly similar. Hence, small volumes of hydrothermal fluid are sufficient to facilitate recrystallisation and low level REE beneficiation, but the original REE magmatic content of a carbonatite seems to be the main factor controlling the economic potential of a deposit. A higher fluid flow (e.g. able to modify the magmatic oxygen isotopic composition of the deposit) can impact positively the REE beneficiation but to a lesser extent.

The only published stable isotope study of the Dashigou carbonatite is by Xu *et al.,* (2010). The sampling, drilling of the powders and the sample size are not detailed in the paper. Six single analyses were performed on six different samples by a similar Mass spectrometer instrument used in this thesis Chapter 5 (IRMS). Their $\delta^{13}C_{PDB}$ and $\delta^{18}O_{SMOW}$ respectively range from -6.9‰ to -6.4‰ and 7.2‰ to 8.8‰, and they concluded that these compositions are consistent with a primary mantle-derived signature unaffected by surface alteration or hydrothermal overprint. The first problem with this interpretation is that they have not distinguished between the different calcite textures observable in the field, with some of the calcite being vuggy, indicative of hydrothermal growth (Fig. 6-3). Likewise, they have neglected the obvious hydrothermal mineralisation present in the samples, including quartz growth (SEM-CL imaging was not performed to check for single or multiple quartz generations), the abundant sulphate mineralisation (Fig 4-2A,D) and the many REE mineral replacement textures observed by Smith *et al.,* (2018). Given the lack of information on sampling, they may only have analysed magmatic calcite and have chosen to disregard the hydrothermal material that is clearly present, or they may have analysed hydrothermal minerals whose composition is similar to the magmatic precursor because of limited fluid infiltration, as at Okorusu. Hence, I conclude that the isotopic arguments of Xu *et al.,* (2010), indicating the carbonatite was not affected by hydrothermal alteration, are not valid, and have shown that textural evidence points unambiguously to hydrothermal activity, as already described by Smith et al (2018). Nevertheless, there is insufficient stable isotope data from this study to evaluate the role of fluid infiltration in the development of the rocks studied.

Figure 6-4: Dashigou calcite carbonatite dyke with transition from magmatic to hydrothermal calcite toward the centre of the dyke with vuggy texture.

6.2.4. The impact of fluid composition on REE mobility during hydrothermal reworking.

The hydrothermal fluids from both calcite carbonatite deposits were analysed by Raman spectroscopy. For Okorusu, the stage associated with the main REE mineralisation (stage 3) did not yield any analysable fluid inclusions, as they were too small, too rare and were hosted in calcite which is very easily cleaved. Fluid inclusions hosted in hydrothermal fluorite which was also associated with stage 4 parisite mineralisation were analysed. However, no Raman peaks were detected from the fluid, indicating that Cl is the main ligand present, as monoatomic ions, if in solution do not have specific peaks on the Raman spectrum (Terpstra *et al.,* 1990) compared to the potential polyatomic anion ligands (Frezzoti *et al.,* 2012). This is consistent with previous fluid inclusion studies on stage 4 fluorite, which show up to 5 wt.% NaCl (Roedder, 1973; Bühn *et al.,* 2002). The microthermometric analyses in this study yielded somewhat higher NaCl contents for stage 4a fluorite, which is the fluorite containing

164

the REE mineralisation, sometimes exceeding 10 NaCl wt.% equivalent (Appendix 9). A few Lw + V fluid inclusions have a small transparent solid, often too small to see a crystal shape (usually < 5 μm), and when analysed by Raman spectroscopy no peak were visible on the spectra, suggesting that these are chloride-salts. The fluids responsible for the hydrothermal REE stages at Okorusu are inferred to have been chloride-dominated. The hydrothermal fluid responsible for the REE mineralisation of the Dashigou calcite carbonatites was remarkably sulfate-rich, with sulfate present both in solution and as solids within fluid inclusions. The estimated total sulfate content of individual fluid inclusions ranging from 6 to more than 33 wt.% K_2SO_4 equivalent. No chloride-salts were detected within the fluid inclusions, suggesting that the hydrothermal fluid was likely chloride-poor. As discussed previously, sulfate-REE complexes have a higher stability than the chloride-REE complexes and their stability is consistent across the lanthanide series. Thus, even if the Dashigou hydrothermal fluids had a small amount of chloride, it would not affect the sulfate-REE complexes dominating the fluid. This implies that if the carbonatite has a magmatic LREE and HREE source, they will be transported within the fluid by sulfate complexes without being fractionated. Chloride forms complexes with the REE which decrease in stability along the lanthanide series implying that if present, the HREE would be fractionated from the LREE, and a HREE enrichment is unlikely. The temperature range of the mineralising fluid for both deposits likely overlap, with the Okorusu mineralising fluid showing a lower range, with a maximum temperature of 200 °C, and estimated temperatures down to 100 °C. The temperature range at Dashigou tends to be higher, from 120 °C to less than 450 °C based on the hydrothermal quartz luminescence (Cangelosi *et al.,* 2019b). Even if temperature plays a role in the REE complexes stability, it does not affect REE transport in our two case studies, as the transporting ligand is dominant.

6.3. Summary and Conclusions

Carbonatite complexes are of particular importance due to their initial elevated REE contents. Normally they are enriched in LREE but in some instances HREE may be relatively enriched. Although the Okorusu and the Dashigou carbonatite deposits are different, their in-depth study has helped to understand fundamental characteristics about hydrothermal REE reworking and natural beneficiation processes in carbonatites that is potentially valuable for exploration. The principal conclusions from this study are as follows:

- Most carbonatite-hosted REE deposits have been hydrothermally reworked and contain predominantly secondary REE ore minerals.

- The hydrothermal reworking involves the recrystallisation of the carbonatite magmatic minerals, notably calcite, which releases REE and other trace and minor elements in turn incorporated into secondary hydrothermal minerals, which is important for ore processing. In the course of the hydrothermal reworking, REE are transported over sufficiently large distances to lead to REE enrichment of the more altered rocks.

- REE transport by a hydrothermal fluid can be effective at temperature as low as 100 °C.

- The final REE pattern depends on both the magmatic REE source and the nature of the hydrothermal fluid. In particular, HREE enrichment in the deposit at Dashigou is associated with a HREE-enrichment at the final magmatic stage as well as unusual sulfate-rich fluids.

- Secondary REE minerals can form in response to a relatively small volume of hydrothermal fluid remobilising REE from magmatic minerals e.g. calcite, such that the magmatic oxygen isotope signature is not greatly modified, but it is likely that enrichment to ore grades requires more extensive alteration documented by the oxygen isotope signature.

- Hydrothermal reworking of carbonatites leading to local concentration of REE takes place under conditions comparable to those of geothermal circulation in the upper crust, as is the case for many epithermal ore deposits. It is possible that many carbonatite-hosted REE deposits are further examples of epithermal ores.

166

6.4. Further work

This study has brought further understanding to the role of hydrothermal alteration on REE beneficiation in carbonatite deposits. However, there are still some uncertainties that need to be addressed, including more accurate estimates of the temperature of REE mineralisation and complete characterisation of the fluid composition responsible for the REE mineralisation.

I have not been able to obtain precise REE mineral precipitation temperatures because of the limited mutual solid solution of mineral pairs such as calcite-dolomite and the lack of data for applicable and well-calibrated oxygen isotope thermometers. Carbonate clumped isotope geothermometry is potentially a technique to obtain better estimates. It is based on the measurement of molecules of similar chemical composition but different isotopic composition (isotopologues). When reacted with othophosphoric acid, calcite produces some CO_2 gas with a mass of 47, where the two heavy rare isotopes (^{13}C and ^{18}O) are substituted in the CO_2 molecule ($^{13}C^{18}O^{16}O$) in isotopic equilibrium with the calcite. This represent the amount of "clumping" of the heavy isotopes in the calcite's crystal lattice analysed. Changes in the Δ_{47} value are directly related to temperature. Due to the isotopic independence of the calcite's clumped isotopic signature from the fluid which it precipitated, this technique would therefore be useful in determining accurate temperature for the different REE stages and give a better insight on the overall story of a deposit.

LA-ICP-MS analyses on the different Dashigou fluid inclusion generations hosted by the hydrothermal quartz would help us quantify the fluid composition responsible for the REE mineralisation. This was planned for the present project but was not possible because of failure of the instrument. Additionally, Raman spectrometry can be used for pH measurements on sulphate-bearing fluid inclusions (Boiron *et al.,* 1999) which would lead to a more accurate fluid chemistry representation for REE transport in hydrothermal systems. This would contribute to better REE transport modelling for natural systems.

I have collected rocks from another carbonatite occurrence (Huayangchuan carbonatite), located in the same region as the Dashigou deposit, China. Few carbonatite dyke outcrops were found and sampled, but these carbonatites are also relatively HREE enriched. No work has been published yet, and it would be interesting to see if the REE reworking is similar to the Dashigou carbonatite or if there are any differences.

Different fields such as exploration geology, mining geology and the mining industry as a whole would greatly benefit from a global carbonatite data base containing all the carbonatite deposits, with information on the REE mineralisation including its origin (hydrothermal, magmatic), and the beneficiation process if any, its associated fluid chemistry etc. This would assist building a global model which would help determine the formation condition of REE carbonatite deposits and ultimately help discover new resources.

References

Andersen, A.K., Clark J.G., Larson P.B. and Donovan J.J. (2017) REE fractionation, mineral speciation, and supergene enrichment of the Bear Lodge carbonatites, Wyoming, USA. *Ore Geology Reviews*, **89**, 780-807.

Anovitz, L.M. and Essene, E.J. (1987) Phase equilibria in the system $CaCO_3$-$MgCO_3$-$FeCO_3$. *Journal of Petrology,* **28**, 389-414.

Boiron, M.-C., Moissette, A., Cathelineau, M., Banks, D., Monin, C. and Dubessy, J. (1999) Detailed determination of paleofluid chemistry: an integrated study of sulfate-volatile rich brines and aqueo-carbonic fluids in quartz veins from OuroFino (Brazil). *Chemical Geology*, **154**, 179-192.

Frezzotti, M.L., Tecce, F., Casagli, A. (2012) Raman spectroscopy for fluid inclusions analysis. *Journal of Geochemical exploration*, **112**, 1-20.

Jones, A.P., Genge, M. and Carmody, L. (2013) Carbonate melts and carbonatites. *Reviews in Mineralogy and Geochemistry*, **75**, 289-322.

McDonough, W.F. and Sun, S. (1995) The composition of the earth. *Chemical Geology,* **120**, 223-253.

Moore, M., Chakhmouradian, A.R., Mariano, A.N., Sidhu, R., 2015. Evolution of rare-earth mineralization in the Bear Lodge carbonatite, Wyoming: Mineralogical and isotopic evidence. *Ore Geology Reviews*, **64**, 499-521.

Smith, M., Kynicky, J., Xu, C., Song, W., Spratt, J., Jeffries, T., Brtnicky, M., Kopriva, A. and Cangelosi, D. (2018) The origin of secondary heavy rare earth element enrichment in carbonatites: Constraints from the evolution of the Huanglongpu district, China. *Lithos*, **308-309**, 65-82.

Terpstra P., Combes, D. and Zwick A.M. (1990) Effect of salts on dynamics of water: A Raman spectroscopy study. *Journal of Chemical Physics,* **92**, 65-70.

Xu, C., Kynicky, K, Chakhmouradian, A.R., Qi, L. and Song, W. (2010) A unique Mo deposit associated with carbonatites in the Qinling orogenic belt, central China. *Lithos,* **118**, 50-60.

Zheng, X. and Liu, Y. (2019) Mechanisms of element precipitation in carbonatite-related rare-earth element deposits: Evidence from fluid inclusions in the Maoniuping deposit, Sichuan Province, southwestern China. *Ore Geology Reviews*, **107**, 218-238.

Appendices

Appendix 1: EPMA and LA-ICP-MS instruments set up

The following tables provide the EPMA and LA-ICP-MS instruments set up per run and mineral analysed, including the standards used and the detection limit per element for Chapter 3.

EPMA instrument

calcite	standard	standard supplier	on peak time (s)	Off peak time (s)	avg LOD (wt% elemental) run 1	
					average n= 67	stdev
Mg	Dolomite	University of Leeds	60	30	0.0234	0.0035
Si	Diopside	P&H developments	60	30	0.0139	0.0014
Mn	Rhodonite	P&H developments	60	30	0.0321	0.0024
Fe	Hematite	P&H developments	60	30	0.0359	0.0016
Ca	Calcite	University of Leeds	60	30	0.0151	0.0006
Ba	Baryte	P&H developments	60	30	0.0507	0.0017
Sr	Celestine	P&H developments	60	30	0.0885	0.0052
apatite	**Standard**	**Std nb**	**on peak time (s)**	**Off peak time (s)**	**average n= 199**	**stdev**
Mg	Diopside	P&H developments	10	5	0.0245	0.0019
Si	Diopside	P&H developments	10	5	0.0245	0.0021
Mn	Rhodonite	P&H developments	20	10	0.0490	0.0033

			on peak time (s)	Off peak time (s)	average	stdev
Fe	Hematite	P&H developments	20	10	0.0507	0.0028
Ca	Apatite	P&H developments	10	5	0.0271	0.0011
Sr	Celestine	P&H developments	30	15	0.0473	0.0088
F	Fluorite	P&H developments	30	15	0.0671	0.0114
P	Apatite	P&H developments	10	5	0.0297	0.0025
Cl	Halite	P&H developments	15	7.5	0.0278	0.0021
Na	Halite	P&H developments	10	5	0.0451	0.0041
fluorite	**standard**	**std nb**	**on peak time (s)**	**Off peak time (s)**	**average n= 527**	**stdev**
Fe	Hematite	P&H developments	20	10	0.0506	0.0024
Mn	Rhodonite	P&H developments	20	10	0.0490	0.0029
Mg	Diopside	P&H developments	15	7.5	0.0268	0.0020
Ca	Fluorite	P&H developments	10	5	0.0224	0.0013
Sr	Celestine	P&H developments	60	30	0.0446	0.0029
Cl	Halite	P&H developments	20	10	0.0291	0.0117

diopside	standard	std nb	on peak time (s)	Off peak time (s)	average n= 74	stdev
F	Fluorite	P&H developments	15	7.5	0.0706	0.0122
Si	Diopside	P&H developments	30	15	0.0117	0.0002
Fe	Almandine	P&H developments	30	15	0.0181	0.0003
Mn	Rhodonite	P&H developments	30	15	0.0169	0.0005
Na	Jadeite	P&H developments	30	15	0.0256	0.0007
Mg	Diopside	P&H developments	30	15	0.0173	0.0005
Al	Almandine	P&H developments	30	15	0.0128	0.0004
K	K-feldspar	P&H developments	30	15	0.0069	0.0003
Ca	Diopside	P&H developments	30	15	0.0066	0.0001
Ti	Rutile	P&H developments	30	15	0.0084	0.0001
Cr	Cr2O3	P&H developments	30	15	0.0158	0.0003

calcite	standard	standard supplier	on peak time (s)	Off peak time (s)	avg LOD (wt% elemental) run 2	
					average n= 62	stdev
Mg	Dolomite	University of Leeds	60	30	0.0185	0.0007
Si	Diopside	P&H developments	60	30	0.0149	0.0005
Mn	Rhodonite	P&H developments	60	30	0.0283	0.0011
Fe	Hematite	P&H developments	60	30	0.0296	0.0011
Ca	Calcite	University of Leeds	60	30	0.0126	0.0003
Ba	Baryte	P&H developments	60	30	0.0486	0.0018
Sr	Celestine	P&H developments	60	30	0.0809	0.0036
calcite	standard	standard supplier	on peak time (s)	Off peak time (s)	avg LOD (wt% elemental) run 3	
					average n= 42	stdev
Mg	Dolomite	University of Leeds	60	30	0.0217	0.0009
Si	Diopside	P&H developments	60	30	0.0215	0.0014
Mn	Rhodonite	P&H developments	60	30	0.0329	0.0014

Fe	Hematite	P&H developments	60	30	0.0353	0.0015
Ca	Calcite	University of Leeds	60	30	0.0149	0.0004
Ba	Baryte	P&H developments	60	30	0.0569	0.0015
Sr	Celestine	P&H developments	60	30	0.0956	0.0054
calcite	**standard**	**standard supplier**	**on peak time (s)**	**Off peak time (s)**	**avg LOD (wt% elemental) run 4**	
					average n= 35	stdev
Mg	Dolomite	University of Leeds	60	30	0.0218	0.0008
Si	Diopside	P&H developments	60	30	0.0213	0.0009
Mn	Rhodonite	P&H developments	60	30	0.0326	0.0013
Fe	Hematite	P&H developments	60	30	0.0349	0.0013
Ca	Calcite	University of Leeds	60	30	0.0147	0.0005
Ba	Baryte	P&H developments	60	30	0.0566	0.0017
Sr	Celestine	P&H developments	60	30	0.0949	0.0054

LA-ICP-MS instrument

			Internal standard = Ca			
Date of the analyses		18/05/2017				
Sample			OKC19-2			
Mineral			calcite	apatite	fluorite	parisite
Ca ppm (EPMA)			384880.6	379828.1	518144.7	74463.9
			LOD ppm			
	Na23	6.5E-05	25.1	24.7	33.7	4.8
	Sr88	9.3E-07	0.4	0.4	0.5	0.1
	Y89	1.1E-06	0.4	0.4	0.6	0.1
	Ba137	2.6E-05	9.9	9.8	13.3	1.9
	La139	7.3E-07	0.3	0.3	0.4	0.1
	Ce140	5.1E-07	0.2	0.2	0.3	0.0
	Pr141	1.2E-06	0.5	0.5	0.6	0.1
	Nd146	2.6E-06	1.0	1.0	1.4	0.2
	Sm147	1.5E-05	5.8	5.7	7.8	1.1
	Eu153	5.2E-06	2.0	2.0	2.7	0.4
	Gd157	3.1E-06	1.2	1.2	1.6	0.2
	Tb159	8.1E-07	0.3	0.3	0.4	0.1
	Dy163	7.1E-06	2.8	2.7	3.7	0.5
	Ho165	1.5E-06	0.6	0.6	0.8	0.1
	Er166	2.6E-06	1.0	1.0	1.3	0.2
	Tm169	1.3E-06	0.5	0.5	0.7	0.1
	Yb172	2.3E-06	0.9	0.9	1.2	0.2
	Lu175	5.4E-07	0.2	0.2	0.3	0.0
	Th232	1.2E-06	0.5	0.5	0.6	0.1
	U238	7.7E-07	0.3	0.3	0.4	0.1

		26/06/2017						
		OKC19-2					OKA1	
		calcite	apatite	parisite			calcite	apatite
		387101.1	376690.6	74455.0			378618.9	388047.3
		LOD ppm					LOD ppm	
Na23	6.2E-04	240.6	234.1	46.3		6.2E-04	235.3	241.1
Mg24	2.9E-05	11.0	10.7	2.1		2.9E-05	10.8	11.1
K39	1.5E-03	573.4	558.0	110.3		1.5E-03	560.8	574.8
Ca40	4.4E-04	168.8	164.2	32.5		4.4E-04	165.1	169.2
Mn55	4.7E-05	18.0	17.5	3.5		4.7E-05	17.6	18.1
Fe56	3.8E-05	14.5	14.2	2.8		3.8E-05	14.2	14.6
Sr88	3.8E-06	1.5	1.4	0.3		3.8E-06	1.4	1.5
Y89	3.0E-06	1.2	1.1	0.2		3.0E-06	1.1	1.2
Ba137	3.2E-05	12.6	12.2	2.4		3.2E-05	12.3	12.6
La139	1.3E-05	5.1	5.0	1.0		1.3E-05	5.0	5.1
Ce140	9.4E-06	3.6	3.5	0.7		9.4E-06	3.6	3.6
Pr141	2.7E-06	1.1	1.0	0.2		2.7E-06	1.0	1.1
Nd146	1.7E-05	6.7	6.5	1.3		1.7E-05	6.5	6.7
Sm147	2.1E-05	8.0	7.8	1.5		2.1E-05	7.8	8.0
Eu153	5.8E-06	2.3	2.2	0.4		5.8E-06	2.2	2.3
Gd157	2.4E-05	9.3	9.1	1.8		2.4E-05	9.1	9.3
Tb159	3.2E-06	1.2	1.2	0.2		3.2E-06	1.2	1.2
Dy163	1.4E-05	5.5	5.3	1.0		1.4E-05	5.3	5.5
Ho165	3.5E-06	1.4	1.3	0.3		3.5E-06	1.3	1.4
Er166	1.1E-05	4.3	4.2	0.8		1.1E-05	4.2	4.3
Tm169	3.6E-06	1.4	1.4	0.3		3.6E-06	1.4	1.4
Yb172	1.9E-05	7.2	7.0	1.4		1.9E-05	7.0	7.2
Lu175	5.0E-06	1.9	1.9	0.4		5.0E-06	1.9	1.9

Th232	6.5E-05	25.4	24.7	4.9		6.5E-05	24.8	25.4
U238	8.2E-05	31.9	31.0	6.1		8.2E-05	31.2	32.0

	27/06/2017						
		OKC17				OKA5	
		calcite	apatite			calcite	apatite
		390771.6	384239.8			373724.0	386375.6
		LOD ppm				LOD ppm	
Na23	1.9E-04	73.8	72.6	1.9E-04	70.6	73.0
Mg24	8.1E-06	3.2	3.1	8.1E-06	3.0	3.1
K39	3.7E-04	146.0	143.5	3.7E-04	139.6	144.3
Ca40	7.2E-05	28.0	27.5	7.2E-05	26.8	27.7
Mn55	1.9E-05	7.2	7.1	1.9E-05	6.9	7.1
Fe56	1.3E-05	5.0	4.9	1.3E-05	4.8	4.9
Sr88	1.0E-06	0.4	0.4	1.0E-06	0.4	0.4
Y89	8.1E-07	0.3	0.3	8.1E-07	0.3	0.3
Ba137	8.2E-06	3.2	3.1	8.2E-06	3.1	3.2
La139	3.2E-06	1.3	1.2	3.2E-06	1.2	1.2
Ce140	2.3E-06	0.9	0.9	2.3E-06	0.9	0.9
Pr141	7.0E-07	0.3	0.3	7.0E-07	0.3	0.3
Nd146	4.5E-06	1.7	1.7	4.5E-06	1.7	1.7
Sm147	5.2E-06	2.0	2.0	5.2E-06	1.9	2.0
Eu153	1.5E-06	0.6	0.6	1.5E-06	0.5	0.6
Gd157	6.0E-06	2.3	2.3	6.0E-06	2.2	2.3
Tb159	8.0E-07	0.3	0.3	8.0E-07	0.3	0.3
Dy163	3.5E-06	1.4	1.4	3.5E-06	1.3	1.4
Ho165	8.9E-07	0.3	0.3	8.9E-07	0.3	0.3
Er166	2.7E-06	1.1	1.1	2.7E-06	1.0	1.1

Tm169	9.0E-07	0.4	0.3		9.0E-07	0.3	0.3
Yb172	4.5E-06	1.8	1.7		4.5E-06	1.7	1.7
Lu175	1.2E-06	0.5	0.5		1.2E-06	0.5	0.5
Th232	1.1E-05	4.3	4.2		1.1E-05	4.1	4.2
U238	1.3E-05	5.2	5.1		1.3E-05	5.0	5.2

		28/06/2017					
		OKC4				OKC3	
		calcite	apatite			calcite	fluorite
		378838.1	380207.3			383335.9	500553.3
		LOD ppm				LOD ppm	
Na23	1.5E-04	56.2	56.4	5.7E-04		219.4	286.5
Mg24	8.9E-06	3.4	3.4	2.7E-05		10.4	13.6
Al27	6.2E-05	23.4	23.5	1.8E-04		70.1	91.5
K39	8.2E-05	31.0	31.1	1.4E-03		529.5	691.4
Ca40	3.0E-04	114.4	114.8	3.6E-04		138.0	180.2
Ti47	2.8E-04	104.8	105.2	6.4E-04		245.9	321.1
Cr53	9.1E-05	34.6	34.7	4.7E-04		181.5	236.9
Mn55	1.2E-05	4.5	4.5	5.7E-05		21.9	28.6
Fe56	7.3E-06	2.8	2.8	2.9E-05		11.1	14.4
Sr88	1.0E-06	0.4	0.4	3.0E-06		1.2	1.5
Y89	8.0E-07	0.3	0.3	2.4E-06		0.9	1.2
Ba137	7.8E-06	3.0	3.0	2.4E-05		9.1	11.9
La139	3.4E-06	1.3	1.3	1.0E-05		4.0	5.2
Ce140	2.3E-06	0.9	0.9	7.2E-06		2.7	3.6
Pr141	6.6E-07	0.3	0.3	2.0E-06		0.8	1.0
Nd146	4.1E-06	1.6	1.6	1.3E-05		4.8	6.3
Sm147	4.9E-06	1.9	1.9	1.5E-05		5.8	7.5

Eu153	1.4E-06	0.5	0.5		4.2E-06	1.6	2.1
Gd157	5.7E-06	2.2	2.2		1.7E-05	6.7	8.7
Tb159	7.5E-07	0.3	0.3		2.3E-06	0.9	1.1
Dy163	3.3E-06	1.2	1.2		1.0E-05	3.8	5.0
Ho165	8.2E-07	0.3	0.3		5.0E-06	1.9	2.5
Er166	2.5E-06	1.0	1.0		7.7E-06	3.0	3.9
Tm169	8.4E-07	0.3	0.3		2.5E-06	1.0	1.3
Yb172	4.2E-06	1.6	1.6		1.3E-05	4.9	6.4
Lu175	1.1E-06	0.4	0.4		3.4E-06	1.3	1.7
Th232	1.3E-05	5.1	5.1		4.1E-05	15.7	20.5
U238	1.6E-05	6.2	6.2		5.0E-05	19.17	25.0

		28/06/2017				OKC6	
		OKC8					
		calcite	parisite	fluorite		fluorite	
		408559.4	74494.5	496975.9		503412.5	
		LOD ppm				LOD ppm	
Na23	6.8E-	27.9	5.1	34.0	6.8E-	34.4	
Mg24	4.2E-	1.7	0.3	2.1	4.2E-	2.1	
Al27	2.6E-	10.8	2.0	13.1	2.6E-	13.3	
K39	1.9E-	75.8	13.8	92.2	1.9E-	93.4	
Ca40	3.9E-	15.7	2.9	19.1	3.9E-	19.4	
Ti47	9.7E-	39.6	7.2	48.1	9.7E-	48.7	
Cr53	4.2E-	17.2	3.1	20.9	4.2E-	21.2	
Mn55	7.6E-	3.1	0.6	3.8	7.6E-	3.8	
Fe56	3.6E-	1.5	0.3	1.8	3.6E-	1.8	
Sr88	4.8E-	0.2	0.0	0.2	4.8E-	0.2	
Y89	3.8E-	0.2	0.0	0.2	3.8E-	0.2	
Ba137	3.8E-	1.5	0.3	1.9	3.8E-	1.9	
La139	1.5E-	0.6	0.1	0.7	1.5E-	0.8	
Ce140	1.1E-	0.4	0.1	0.5	1.1E-	0.5	

Pr141	3.2E-	0.1	0.0	0.2		3.2E-	0.2
Nd146	2.0E-	0.8	0.1	1.0		2.0E-	1.0
Sm147	2.4E-	1.0	0.2	1.2		2.4E-	1.2
Eu153	6.6E-	0.3	0.0	0.3		6.6E-	0.3
Gd157	2.7E-	1.1	0.2	1.3		2.7E-	1.4
Tb159	3.5E-	0.1	0.0	0.2		3.5E-	0.2
Dy163	1.5E-	0.6	0.1	0.8		1.5E-	0.8
Ho165	3.8E-	0.2	0.0	0.2		3.8E-	0.2
Er166	1.2E-	0.5	0.1	0.6		1.2E-	0.6
Tm16	3.9E-	0.2	0.0	0.2		3.9E-	0.2
Yb172	1.9E-	0.8	0.1	0.9		1.9E-	1.0
Lu175	5.1E-	0.2	0.0	0.3		5.1E-	0.3
Th232	3.6E-	1.5	0.3	1.8		3.6E-	1.8
U238	4.4E-	1.8	0.3	2.2		4.4E-	2.2

Internal standard = Si							
Date of the analyses		26/06/2017				27/06/2017	
Sample			OKA1				OKA5
Mineral			diopside				diopside
Si ppm			249981.3				244323.
			LOD ppm				LOD
	Na23	6.4E-04	160.2		Na23	1.2E-02	3042.2
	Mg24	2.9E-05	7.4		Mg24	5.4E-04	131.2
	K39	1.5E-03	381.8		K39	2.5E-02	6017.3
	Ca40	4.5E-04	112.4		Ca40	4.7E-03	1153.7
	Mn55	4.8E-05	12.0		Mn55	1.2E-03	298.1
	Fe56	3.9E-05	9.7		Fe56	8.4E-04	205.4
	Sr88	3.9E-06	1.0		Sr88	6.6E-05	16.1
	Y89	3.1E-06	0.8		Y89	5.3E-05	13.1
	Ba137	3.3E-05	8.4		Ba137	5.4E-04	132.0
	La139	1.4E-05	3.4		La139	2.1E-04	51.9
	Ce140	9.7E-06	2.4		Ce140	1.5E-04	37.4

	Pr141	2.8E-06	0.7		Pr141	4.6E-05	11.3
	Nd146	1.8E-05	4.4		Nd146	2.9E-04	71.9
	Sm147	2.1E-05	5.3		Sm147	3.4E-04	83.3
	Eu153	6.0E-06	1.5		Eu153	9.6E-05	23.5
	Gd157	2.5E-05	6.2		Gd157	3.9E-04	96.2
	Tb159	3.3E-06	0.8		Tb159	5.2E-05	12.8
	Dy163	1.5E-05	3.6		Dy163	2.3E-04	56.8
	Ho165	3.6E-06	0.9		Ho165	5.8E-05	14.3
	Er166	1.1E-05	2.8		Er166	1.8E-04	44.1
	Tm169	3.7E-06	0.9		Tm169	5.9E-05	14.4
	Yb172	1.9E-05	4.8		Yb172	3.0E-04	72.4
	Lu175	5.2E-06	1.3		Lu175	8.0E-05	19.5
	Th232	6.8E-05	16.9		Th232	7.2E-04	176.8
	U238	8.5E-05	21.2		U238	8.8E-04	215.2

Appendix 2: Bulk rock detection limits

Chapter 3 and 4 bulk rock analyses instrument detection limits.

Element	DL (ppm)	Upper Limit (ppm)	Reported by
Ag	0.5	100	ICP/MS
As	5	2,000	ICP/MS
Ba	2	500,000	ICP
Be	1		ICP
Bi	0.4	2,000	ICP/MS
Ce	0.1	3,000	ICP/MS
Co	1	1,000	ICP/MS
Cr	20	10,000	ICP/MS
Cs	0.5	1,000	ICP/MS
Cu	10	10,000	ICP/MS
Dy	0.1	1,000	ICP/MS
Er	0.1	1,000	ICP/MS
Eu	0.05	1,000	ICP/MS
Ga	1	500	ICP/MS
Gd	0.1	1,000	ICP/MS
Ge	1	500	ICP/MS
Hf	0.2	1,000	ICP/MS
Ho	0.1	1,000	ICP/MS
In	0.2	200	ICP/MS
La	0.1	2,000	ICP/MS
Lu	0.01	1,000	ICP/MS

Mo	2	100	ICP/MS
Nb	1	1,000	ICP/MS
Nd	0.1	2,000	ICP/MS
Ni	20	10,000	ICP/MS
Pb	5	10,000	ICP/MS
Pr	0.05	1,000	ICP/MS
Rb	2	1,000	ICP/MS
Sb	0.5	200	ICP/MS
Sc	1		ICP
Sm	0.1	1,000	ICP/MS
Sn	1	1,000	ICP/MS
Sr	2	10,000	ICP
Ta	0.1	500	ICP/MS
Tb	0.1	1,000	ICP/MS
Th	0.1	2,000	ICP/MS
Tl	0.1	1,000	ICP/MS
Tm	0.05	1,000	ICP/MS
U	0.1	1,000	ICP/MS
V	5	10,000	ICP
W	1	5,000	ICP/MS
Y	1	10,000	ICP
Yb	0.1	1,000	ICP/MS
Zn	30	10,000	ICP/MS
Zr	2	10,000	ICP

Oxide	DL (%)
Al_2O_3	0.01
CaO	0.01
Fe_2O_3	0.01
K_2O	0.01
MgO	0.01
MnO	0.001
Na_2O	0.01
P_2O_5	0.01
SiO_2	0.01
TiO_2	0.001
Loss on Ignition	0.01

Analysis	Method	DL
F	FUS-ISE	0.01%
Total S	IR	0.01%

Appendix 3: Chapter 3 minerals EPMA and LA-ICP-MS analyses

Okorusu EPMA diopside analyses

Average EPMA (wt%) and LA-ICP-MS (ppm) analyses of diopside and ferrian diopside analyses for OKA1 and OKA5 from the Okorusu deposit. Note: the LA-ICP-MS data were calculated using the calcium content determined by EPMA.

	n = 28		n = 27	
	OKA5		**OKA1**	
	wt%	SD	**wt%**	SD
SiO2	52.16	0.8	52.68	0.64
TiO2	0.39	0.15	0.37	0.11
Al2O3	0.85	0.31	0.91	0.28
Cr2O3	0.01	0.01	< 0.01	0.01
FeO	11.03	1.09	10.41	0.67
MnO	0.78	0.1	0.70	0.05
MgO	10.82	0.84	11.31	0.56
CaO	23.48	0.27	23.17	0.63
K2O	0.01	0.02	0.01	0.03
Na2O	0.94	0.1	1.06	0.19
	ppm	SD	**ppm**	SD
La	15	7	12	4
Ce	35	14	36	9
Pr	4	2	4	1
Nd	15	7	15	5
Sm	1	2	2	2
Y	5	3	4	3

Representative diopside EPMA analysis hosted in calcite carbonatites from the Okorusu deposit, with assoicated SEM-BSE images.

OKA5										
	point 24	point 25	point 26	point 3	point 7	point 8	point 8'	point 9	point 9'	point 10
SiO2	52.91	52.21	52.49	51.32	52.48	51.77	51.73	51.47	52.29	53.23
TiO2	0.28	0.36	0.13	0.75	0.39	0.47	0.37	0.40	0.27	0.04
Al2O3	0.52	0.84	0.39	1.29	0.90	1.31	0.95	0.93	0.54	0.18
Cr2O3	0.01	< 0.01	0.05	0.01	< 0.01	0.01	0.01	< 0.01	0.02	0.01
FeO	9.93	11.65	15.11	12.25	11.54	11.74	10.50	11.64	9.86	12.03
MnO	0.70	0.88	0.18	0.86	0.86	0.86	0.71	0.85	0.75	1.25
MgO	11.81	10.55	8.67	9.87	10.37	9.95	11.13	10.41	11.75	9.93
CaO	23.72	23.30	22.09	23.30	23.50	23.16	23.62	23.51	23.67	21.45
K2O	n.d.	n.d.	n.d.	n.d.	n.d.	n.d.	n.d.	n.d.	n.d.	0.01
Na2O	0.95	0.90	1.70	1.02	0.91	1.08	0.91	0.89	0.93	2.25
Total	**100.82**	**100.69**	**100.80**	**100.67**	**100.95**	**100.35**	**99.93**	**100.10**	**100.09**	**100.38**
	pfu (6 oxygen)									
Si	1.98	1.98	2.01	1.95	1.98	1.97	1.97	1.96	1.98	2.02
Ti	0.01	0.01	0.00	0.02	0.01	0.01	0.01	0.01	0.01	0.00

Al	0.02	0.04	0.02	0.06	0.04	0.06	0.04	0.04	0.02	0.01
Cr	< 0.01	< 0.01	< 0.01	< 0.01	< 0.01	< 0.01	< 0.01	< 0.01	< 0.01	< 0.01
Fe2+	0.31	0.37	0.48	0.39	0.36	0.37	0.33	0.37	0.31	0.38
Fe3+	0.09	0.08	0.13	0.10	0.07	0.08	0.11	0.11	0.11	0.17
Mn	0.02	0.03	0.01	0.03	0.03	0.03	0.02	0.03	0.02	0.04
Mg	0.66	0.60	0.49	0.56	0.58	0.56	0.63	0.59	0.66	0.56
Ca	0.95	0.94	0.90	0.95	0.95	0.94	0.96	0.96	0.96	0.87
K	n.d.	n.d.	n.d.	n.d.	n.d.	n.d.	n.d.	n.d.	n.d.	n.d.
Na	0.07	0.07	0.13	0.08	0.07	0.08	0.07	0.07	0.07	0.17
pyroxene group	diopside	diopside	diopside	diopside	diopside	diopside	diopside	diopside	diopside	diopside
nomenclature			ferro sodian				ferrian	ferrian	ferrian	ferro sodian
end member calculation	Endmember components were calculated as follows: Di = Mg, Hd = Fe2+ + Mn and Aeg = Na (Halama et al., 2005)									
Ae	6.5	6.3	11.4	7.1	6.4	7.6	6.3	6.2	6.4	14.4
Hd	31.4	37.5	44.1	39.7	37.6	38.4	33.8	37.7	31.5	36.7
Di	62.1	56.2	44.6	53.2	56.0	54.0	59.8	56.0	62.1	48.9

OKA1									
point 1	point 2	point 3	point 4	point 5	point 6	point 7	point 8	point 9	point 10
52.40	52.92	52.61	52.22	52.25	53.60	52.42	52.85	52.30	53.11
0.32	0.30	0.45	0.46	0.47	0.05	0.37	0.28	0.03	0.03
0.66	0.69	1.19	1.16	1.18	0.16	0.92	0.57	0.17	0.03
< 0.01	0.01	0.02	0.01	0.01	0.01	< 0.01	0.01	0.01	< 0.01
10.07	10.04	11.22	11.36	11.54	11.26	10.65	9.77	10.85	9.98
0.70	0.73	0.73	0.73	0.73	0.76	0.72	0.69	0.82	0.65
11.59	11.51	10.56	10.52	10.51	10.78	11.12	11.83	11.01	11.80
23.48	23.38	22.92	22.97	22.94	21.95	23.24	23.70	22.77	22.17
n.d.	< 0.01	n.d.	n.d.	n.d.	< 0.01	< 0.01	< 0.01	0.01	< 0.01
1.00	1.03	1.24	1.23	1.23	1.90	1.11	0.92	1.58	1.91
100.22	**100.62**	**100.92**	**100.65**	**100.84**	**100.47**	**100.55**	**100.63**	**99.55**	**99.68**
pfu (6 oxygen)									
1.98	1.99	1.98	1.97	1.97	2.02	1.98	1.98	2.00	2.01
0.01	0.01	0.01	0.01	0.01	0.00	0.01	0.01	0.00	0.00

0.03	0.03	0.05	0.05	0.05	0.01	0.04	0.03	0.01	0.00
< 0.01	< 0.01	< 0.01	< 0.01	< 0.01	< 0.01	< 0.01	< 0.01	< 0.01	< 0.01
0.32	0.32	0.35	0.36	0.36	0.36	0.34	0.31	0.35	0.32
0.10	0.08	0.08	0.10	0.10	0.13	0.10	0.09	0.17	0.17
0.02	0.02	0.02	0.02	0.02	0.02	0.02	0.02	0.03	0.02
0.65	0.64	0.59	0.59	0.59	0.61	0.63	0.66	0.63	0.67
0.95	0.94	0.92	0.93	0.93	0.89	0.94	0.95	0.93	0.90
n.d.	< 0.01	n.d.	n.d.	n.d.	< 0.01	< 0.01	< 0.01	< 0.01	< 0.01
0.07	0.08	0.09	0.09	0.09	0.14	0.08	0.07	0.12	0.14
diopside	diopside	diopside	diopside	diopside	diopside	diopside	diopside	diopside	diopside
ferrian				ferrian	ferro sodian			ferro sodian	ferro sodian
6.9	7.1	8.5	8.4	8.4	12.4	7.6	6.3	10.5	12.3
31.9	32.0	35.5	35.9	36.3	33.7	33.7	31.1	33.4	29.5
61.2	60.9	55.9	55.7	55.3	53.9	58.7	62.6	56.1	58.3

SEM-BSE image showing stage 1 diopside analysed points by EPMA in OKA5
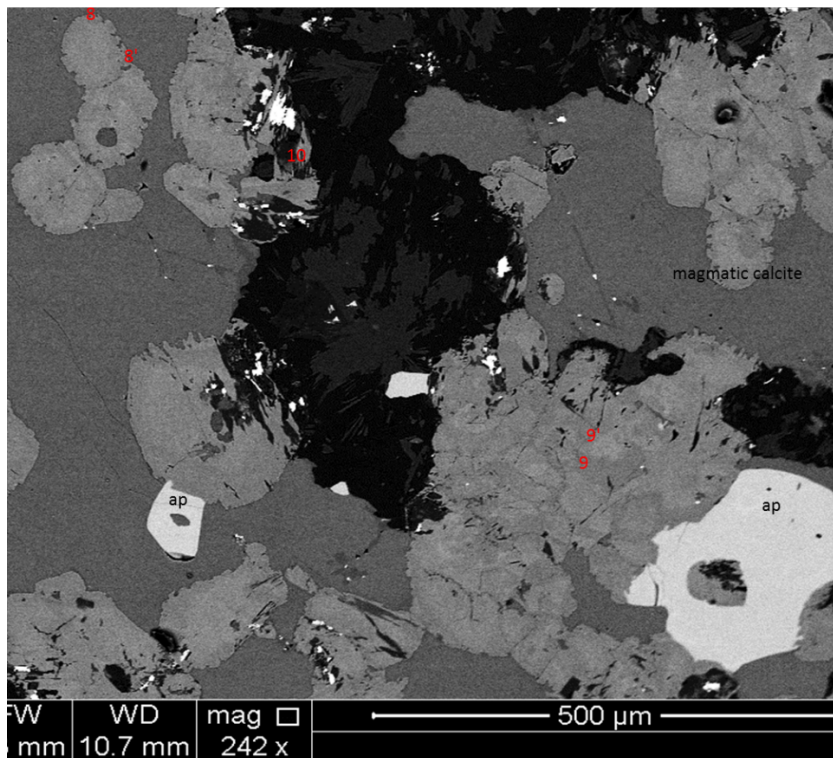
SEM-BSE image showing stage 1 diopside analysed points by EPMA in OKA1
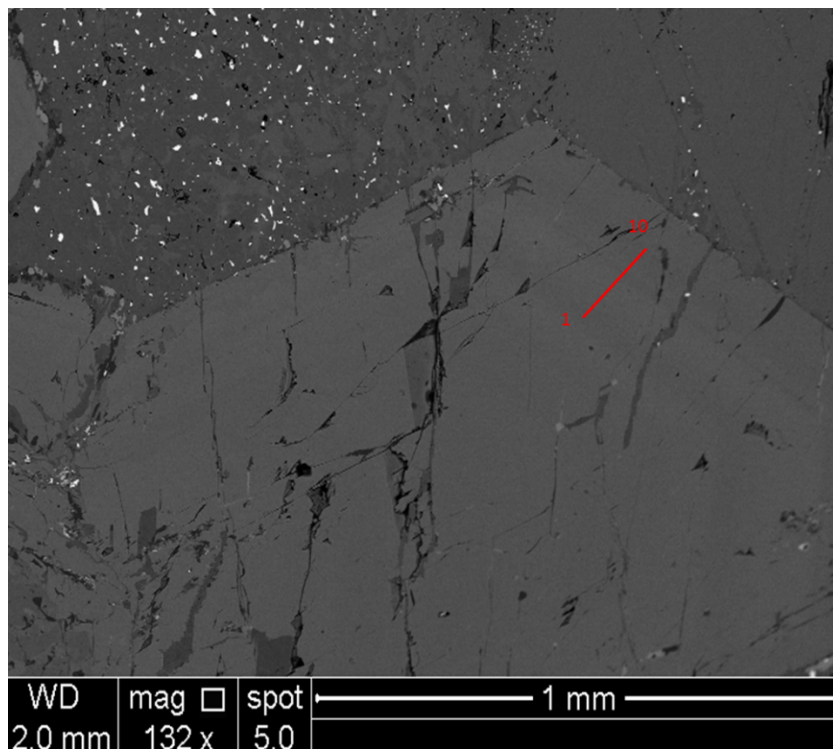
Okorusu LA-ICP-MS apatite analyses

LA-ICP-MS analyses of stage 1 and 2 apatites hosted in calcite carbonatites.

OKA5	stage 1 apatite (ppm)						stage 2 apatite (ppm)			
	point 1	point 2	point 3	point 4	average	stdev	point 5	point 6	average	stdev
Ca	386579	386579	396579	392242	390495	4856	378894	378894	378894	0
Na	709	705	888	562	716	134	622	n.d.		
Mg	65	65	34	n.d.	55	18	106	n.d.		
Si	n.d.	n.d.	n.d.	n.d.			n.d.	n.d.		
K	n.d.	n.d.	n.d.	n.d.			n.d.	n.d.		
Mn	223	152	193	164	183	32	n.d.	n.a.		
Fe	172	159	183	118	158	29	62	n.d.		
Sr	13972	12253	14477	14791	13873	1132	23139	19597	21368	2505
Ba	n.a.	62	83	56	67	14	n.a.	104	104	
Y	394	323	428	356	375	46	20	53	37	23
La	6300	5591	7204	5620	6179	758	495	n.a.	495	
Ce	11084	10380	12996	9665	11031	1432	760	6807	3783	4275
Pr	969	913	1080	823	946	108	50	553	301	355

Nd	3332	2966	3476	2842	3154	299	171	1526	848	959
Sm	314	352	361	282	327	37	20	99	59	56
Eu	77	68	94	74	78	11	n.d.	35		
Gd	202	172	213	212	200	19	24	93		
Tb	25	19	26	14	21	5	n.d.	9		
Dy	120	78	83	90	93	19	n.d.	22		
Ho	10	20	16	13	15	4	n.d.	n.d.		
Er	29	39	36	37	35	4	n.d.	n.d.		
Tm	4	3	4	5	4	1	n.d.	n.d.		
Yb	21	16	19	n.d.	19	3	n.d.	n.d.		
Lu	n.d.	4	n.d.	n.d.			n.d.	n.d.		
Th	7175	6102	7380	4601	6314	1273	n.d.	2532		
U	n.d.	69	n.d.	n.d.			n.d.	n.d.		

OKC17	stage 1 apatite (ppm)										stage 2 apatite (ppm)				
	point 1	point 2	point 3	point 4	point 5	point 6	point 7	point 8	average	stdev	point 9	point 10	point 11	average	stdev
Ca	382242	392242	386579	382242	392242	386579	386579	396579	388161	5096	378894	378894	378894	378894	0
Na	912	1099	1362	1504	815	834	859	917	1038	262	961	1047	746	918	155
Mg	n.d.	n.a.	32	n.a.	13	n.d.	n.d.	n.a.	22	13	40	n.d.	18		16
Si	n.d.	n.d.	n.d.	n.d.	n.d.	n.d.	n.d.	n.d.			n.d.	n.d.	n.d.		
K	n.d.	n.d.	n.d.	n.d.	n.d.	n.d.	n.d.	n.d.			n.d.	n.d.	n.d.		
Mn	171	183	166	n.a.	158	195	174	165	173	12	161	n.a.	94	128	48
Fe	94	n.d.	104	n.a.	72	76	74	n.a.	84	14	143	n.a.	n.a.		
Sr	23132	23859	24161	23303	20071	20617	20805	19080	21879	1949	23516	19899	18610	20675	2543
Ba	116	116	119	99	101	77	122	105	107	15	145	93	114	117	26
Y	352	291	356	249	227	290	240	273	285	48	224	242	220	229	12
La	6157	6032	6785	5076	4622	5974	5449	4468	5570	808	4751	2620	3751	3707	1066
Ce	12276	11511	13705	9838	9057	11773	10594	8955	10963	1659	9441	5541	7288	7423	1954
Pr	1245	1178	1352	956	894	1157	1053	871	1088	173	991	629	742	787	185
Nd	4333	3981	4413	2919	2862	3671	3360	2891	3554	644	3227	1986	2262	2492	651
Sm	412	401	378	326	250	378	321	271	342	60	269	225	224	239	26

Eu	77	89	93	65	59	93	69	65	76	14	65	49	60	58	8
Gd	235	197	296	181	171	201	145	170	199	47	209	158	185	184	25
Tb	21	23	24	19	15	17	19	17	19	3	11	16	17	15	3
Dy	65	59	86	76	43	66	66	63	66	12	73	58	67	66	7
Ho	10	12	15	11	7	13	9	10	11	3	11	7	6	8	3
Er	18	18	35	19	16	22	18	28	22	6	26	21	10	19	8
Tm	n.d.	4	3	2	1	2	3	2	2	1	3	n.d.	2	3	0
Yb	0	21	24	11	5	18	8	6	12	9	n.d.	12	12	12	0
Lu	n.d.	n.d.	n.d.	n.d.	n.d.	n.d.	n.d.	n.d.			n.d.	n.d.	n.d.		
Th	1420	1255	1918	548	1104	1954	1630	1751	1448	473	637	406	936	660	266
U	n.d.	n.d.	n.d.	n.d.	n.d.	n.d.	n.d.	n.d.			n.d.	n.d.	n.d.		

OKC19-2	stage 1 apatite (ppm)													
	point 1	point 2	point 3	point 4	point 5	point 6	point 7	point 8	point 9	point 10	point 11	point 12	average	stdev
Ca	377329	377329	377329	377329	377329	377329	377329	377329	377329	377329	377329	377329	377329	0
Na	1134	1109	747	675	957	996	472	646	918	548	712	1024	828	223
Mg	n.a.	n.a.	n.a.	n.a.	n.a.	n.a.	n.a.	n.a.	n.a.	n.a.	n.a.	n.a.		
Si	n.a.	n.a.	n.a.	n.a.	n.a.	n.a.	n.a.	n.a.	n.a.	n.a.	n.a.	n.a.		
K	n.a.	n.a.	n.a.	n.a.	n.a.	n.a.	n.a.	n.a.	n.a.	n.a.	n.a.	n.a.		
Mn	n.a.	n.a.	n.a.	n.a.	n.a.	n.a.	n.a.	n.a.	n.a.	n.a.	n.a.	n.a.		
Fe	n.a.	n.a.	n.a.	n.a.	n.a.	n.a.	n.a.	n.a.	n.a.	n.a.	n.a.	n.a.		
Sr	31564	20991	23693	20936	18976	26538	21127	20732	18534	20458	20956	19108	21968	3723
Ba	372	113	73	77	87	100	80	79	55	74	85	58	104	86
Y	1017	528	189	245	1339	262	278	258	1097	247	344	1439	604	477
La	4487	5592	3525	4528	4051	5148	5443	4832	2532	4803	3901	2963	4317	956
Ce	12324	10975	8889	13810	10948	11851	16756	14984	6876	14504	11620	7270	11734	3030
Pr	947	1110	724	949	846	1016	1108	996	567	975	776	696	892	171
Nd	3007	3579	2242	2905	2649	3019	3274	3030	1899	2923	2358	2297	2765	484

Sm	371	396	218	278	337	285	312	290	286	280	244	337	303	51
Eu	98	81	50	62	91	62	70	64	80	63	58	101	73	17
Gd	344	303	174	230	327	238	249	227	276	217	200	341	261	57
Tb	35	23	12	16	37	16	17	16	32	15	16	40	23	10
Dy	181	94	46	59	218	60	64	59	176	58	68	235	110	71
Ho	30	16	7	9	40	9	9	9	33	8	11	43	19	14
Er	84	40	14	18	112	21	21	19	85	20	26	118	48	40
Tm	9	4	1	2	13	2	2	2	10	2	3	13	5	5
Yb	38	22	8	9	56	9	9	11	48	9	13	63	25	21
Lu	4	3	1	1	6	1	1	1	5	1	2	5	2	2
Th	1288	1106	654	1076	1248	988	1192	970	732	1070	795	941	1005	200
U	49	2	2	2	35	1	9	2	25	5	6	26	14	16

OKC19-2	stage 2 apatite (ppm)							
	point 13	point 14	point 15	point 16	point 17	point 18	average	stdev
Ca	381257	381257	381257	381257	381257	381257	381257	0
Na	126	796	1066	950	580	626	691	333
Mg	n.a.	n.a.	n.a.	n.a.	n.a.	n.a.		
Si	n.a.	n.a.	n.a.	n.a.	n.a.	n.a.		
K	n.a.	n.a.	n.a.	n.a.	n.a.	n.a.		
Mn	n.a.	n.a.	n.a.	n.a.	n.a.	n.a.		
Fe	n.a.	n.a.	n.a.	n.a.	n.a.	n.a.		
Sr		25814	18711	23113	20142	19705	21497	2918
Ba	7268	58	168	47	39	43	1270	2938
Y	109	130	1313	411	314	294	429	448
La	34	2240	913	1080	1478	1756	1250	763
Ce	125	4501	2813	3124	3618	4653	3139	1647
Pr	17	459	371	407	416	440	352	167

Nd	78	1442	1471	1557	1475	1475	1250	575
Sm	25	151	266	245	208	176	178	86
Eu	10	33	83	65	53	45	48	25
Gd	26	117	258	196	165	149	152	78
Tb	3	8	35	21	16	13	16	11
Dy	21	31	207	99	72	62	82	67
Ho	3	4	40	16	12	9	14	14
Er	8	11	105	34	24	25	34	36
Tm	1	1	12	3	2	3	4	4
Yb	3	5	59	11	10	16	18	21
Lu	0	1	5	1	1	2	2	2
Th	n.d.	n.d.	416	n.d.	n.d.	n.d.		
U	4	0	29	n.d.	1	1		

Okorusu LA-ICP-MS parisite analyses

LA-ICP-MS data average summary of the main cations of stage 3 and 4 parisite.

	n = 21	n = 21
	stage 3 parisite	stage 4 parisite
wt%		
CaO	10.42	10.42
SrO	1.18	0.66
La2O3	16.19	20.96
Ce2O3	24.58	31.42
Pr2O3	1.72	1.69
Nd2O3	4.13	4.04
ThO2	1.39	2.71
∑La2O3-Nd2O3	46.62	58.12

LA-ICP-MS analyses of stage 3 and 4 parisite

						stage 3 parisite (ppm)				
					OKC19-2 intensely altered calcite carbonatite					
	Ca	Na	Sr	Y	La	Ce	Pr	Nd	Sm	Eu
point 1	74436	84	6189	3943	97514	183617	11116	32979	3550	803
point 2	74447	96	6084	2522	111473	206749	11343	34438	3308	699
point 3	74450	78	6795	1892	101764	235141	10632	30816	3057	630
point 4	74443	99	6811	2330	110482	221667	12288	35301	3375	699
point 5	74432	89	6463	4206	98495	184252	13117	34275	3722	845
point 6	74467	48	3922	2075	93666	149962	8006	24021	2458	544
point 7	74486	68	6755	1797	136596	199137	15214	28066	2214	455
point 8	74487	83	6974	1814	140328	204175	15601	28707	2257	458
point 9	74455	85	9158	2561	141615	205827	16717	39611	3485	721
point 10	74491	98	11111	2530	191642	262995	17002	38428	2978	603
point 11	74496	117	12722	1722	193001	255171	16341	37076	2762	515
point 12	74476	119	22162	1995	181493	252689	15742	42820	2740	521
point 13	74485	104	11744	2782	163173	236285	15889	34398	2771	591

point 14	74488	122	11688	2612	178125	251983	15997	36755	3037	604
point 15	74469	97	12752	2472	191770	252555	21108	47600	3607	707
point 16	74463	105	11364	2706	178244	244633	21084	46641	3859	781
point 17	74453	81	9611	3150	161992	231317	18153	46528	3714	750
point 18	74469	205	18849	1649	162609	226074	20072	39796	3236	688
point 19	74456	176	7791	n.a.	70712	103224	7789	19701	1418	303
point 20	74428	202	17647	2386	159881	242337	20478	56001	3082	681
point 21	74472	126	11041	1265	116842	173248	13881	27899	2230	472
average	74464	109	10363	2420	141972	215383	15122	36279	2993	622
stdev	21	40	4648	729	37956	39968	3948	8585	621	136

stage 3 parisite (ppm)									
OKC19-2 intensely altered calcite carbonatite									
Gd	Tb	Dy	Ho	Er	Tm	Yb	Lu	Th	U
2638	201	731	109	202	17	73	9	11608	411
2140	144	510	73	139	15	94	8	11242	266
1966	126	411	54	117	14	90	11	12196	
2249	146	492	65	142	13	90	12	14346	164
2809	215	780	119	215	18	79	9	12212	406
1680	119	446	58	113	12	56	7	14266	202
1352	85	311	49	133	17	107	12	14534	231
1390	85	317	49	134	17	110	12	13690	253
2909	155	462	63	141	16	94	9	10664	82
2859	145	440	58	140	16	94	11	12838	87
2575	120	335	45	103	12	81	10	12413	56
2589	127	370	47	109	14	86	11	10631	38
2564	135	442	67	176	23	136	16	13633	165

2762	151	445	62	159	21	126	14	17625	146
3053	148	435	61	151	19	115	12	8134	23
3169	164	482	67	161	19	102	12	9462	56
2929	160	507	75	170	20	106	12	10503	116
3172	159	435	53	101	10	43	5	18469	158
1464	85	219	29	54	5	21	2	6026	77
3333	189	578	72	133	12	49	5	19201	139
2322	122	350	43	78	7	29	3	9444	88
2473	142	452	63	137	15	85	10	12530	158
607	35	130	20	38	5	31	3	3265	110

stage 4 parisite (ppm)									
OKC8 fluorite-rich rock									
	Ca	Na	Sr	Y	La	Ce	Pr	Nd	Sm	Eu
point 1	74486	n.a.	2441	2667	75436	113671	5978	15923	1771	429
point 2	74500	256	8308	4483	244139	352374	16285	44832	4492	1108
point 3	74482	262	7160	3209	182525	320593	14379	39673	3935	906
point 4	74482	331	12061	3519	194586	327775	14952	42348	4312	1007
point 5	74497	198	8872	4657	249745	354460	17189	47835	4769	1144
point 6	74472	n.a.	2474	2178	52211	94381	n.a.	12212	1224	294
point 7	74502	139	4935	2519	203355	295420	12860	36463	3554	839
point 8	74490	177	6868	3082	200326	316182	14341	40453	4202	1013
point 9	74499	142	5359	4327	198001	295221	15523	35955	3829	973
point 10	74499	128	5265	3938	194380	287149	15580	35486	3766	939
point 11	74503	184	5817	5226	236373	322620	18139	41943	4448	1112
point 12	74496	126	4951	3725	190164	307600	15862	34991	3623	968
point 13	74505	112	4526	3628	164408	211685	11957	28975	3043	760

point 14	74501	116	5657	4436	208862	273817	17495	38248	3883	960
point 15	74507	224	6988	5204	247484	333035	16974	42207	4442	1159
point 16	74489	249	4530	3757	178915	277775	16829	35994	3261	791
point 17	74502	403	8036	3996	195442	302121	13270	34063	3407	859
point 18	74492	270	3584	3164	150202	217460	13441	29515	2820	687
point 19	74495	300	3462	2902	132515	207064	11285	24758	2549	622
point 20	74476	169	3888	3340	150222	280493	14625	34041	2995	741
point 21	74502	118	2483	1675	87017	134671	7232	14948	1472	360
average	74494	206	5603	3601	177919	267884	14210	33851	3419	842
stdev	10	83	2409	938	54629	76329	3199	9779	1003	250

stage 4 parisite (ppm)									
OKC8 fluorite-rich rock									
	Ca	Na	Sr	Y	La	Ce	Pr	Nd	Sm	Eu
point 1	74486	n.a.	2441	2667	75436	113671	5978	15923	1771	429
point 2	74500	256	8308	4483	244139	352374	16285	44832	4492	1108
point 3	74482	262	7160	3209	182525	320593	14379	39673	3935	906
point 4	74482	331	12061	3519	194586	327775	14952	42348	4312	1007
point 5	74497	198	8872	4657	249745	354460	17189	47835	4769	1144
point 6	74472	n.a.	2474	2178	52211	94381	n.a.	12212	1224	294
point 7	74502	139	4935	2519	203355	295420	12860	36463	3554	839
point 8	74490	177	6868	3082	200326	316182	14341	40453	4202	1013
point 9	74499	142	5359	4327	198001	295221	15523	35955	3829	973
point 10	74499	128	5265	3938	194380	287149	15580	35486	3766	939
point 11	74503	184	5817	5226	236373	322620	18139	41943	4448	1112
point 12	74496	126	4951	3725	190164	307600	15862	34991	3623	968
point 13	74505	112	4526	3628	164408	211685	11957	28975	3043	760

point 14	74501	116	5657	4436	208862	273817	17495	38248	3883	960
point 15	74507	224	6988	5204	247484	333035	16974	42207	4442	1159
point 16	74489	249	4530	3757	178915	277775	16829	35994	3261	791
point 17	74502	403	8036	3996	195442	302121	13270	34063	3407	859
point 18	74492	270	3584	3164	150202	217460	13441	29515	2820	687
point 19	74495	300	3462	2902	132515	207064	11285	24758	2549	622
point 20	74476	169	3888	3340	150222	280493	14625	34041	2995	741
point 21	74502	118	2483	1675	87017	134671	7232	14948	1472	360
average	74494	206	5603	3601	177919	267884	14210	33851	3419	842
stdev	10	83	2409	938	54629	76329	3199	9779	1003	250

stage 4 parisite (ppm)									
OKC8 fluorite-rich rock									
Gd	Tb	Dy	Ho	Er	Tm	Yb	Lu	Th	U
1364	126	550	75	136	11	40	5	8576	387
2984	264	1070	148	301	32	158	18	32834	1019
2293	201	767	117	253	25	120	13	25945	719
2787	220	906	119	297	28	138	14	23870	493
3085	253	1083	161	354	39	170	20	31161	992
872	93	442	66	143	14	53	4	9381	227
2262	182	688	87	177	17	86	9	21140	339
2689	213	818	106	202	18	83	10	22087	443
2788	249	1077	149	320	31	160	16	25866	561
2650	242	969	138	269	27	132	14	21538	445
3129	286	1256	183	385	38	194	20	38746	898
2573	230	962	134	278	28	136	13	24144	486
2157	197	862	128	266	27	132	14	22995	725

2683	246	1059	157	330	31	154	16	27208	804
3123	292	1158	177	356	39	175	21	25655	977
2234	206	883	131	269	27	144	14	22985	363
2378	216	924	134	285	29	141	16	29261	381
1946	173	751	108	230	22	107	12	21990	387
1816	164	686	96	198	20	98	11	18073	345
2086	189	829	113	237	23	122	12	16236	
1041	94	398	55	120	12	64	6	13826	239
2330	206	864	123	257	26	124	13	23025	561
646	55	226	34	74	8	41	5	7243	259

Okorusu LA-ICP-MS alcite analyses

LA-ICP-MS analyses of stage 3 and stage 4 calcite.

OKC3	stage 4 calcite										
Fluorite-rich rock	Point 1	Point 2	Point 3	Point 4	Point 5	Point 6	Point 7	Point 8	Point 9	average	stdev
Ca	375082	382122	386974	371108	381321	383299	393299	391668	385150	383336	7145
Na	n.d.	n.d.	n.d.	n.d.	n.d.	n.d.	n.d.	n.d.	n.d.		
Fe	40	5	38	7	17	14	13	46	57	26	19
Mg	7156	8967	5135	9308	8064	5377	6735	6083	5828	6961	1530
Mn	5961	3731	1561	2463	8517	5979	11662	1937	1773	4843	3501
Si	n.d.	n.d.	n.d.	n.d.	n.d.	n.d.	n.d.	n.d.	n.d.		
Sr	2407	2934	1375	2285	2917	1819	1587	2616	3712	2406	740
Ba	n.d.	n.d.	n.d.	n.d.	n.d.	n.d.	n.d.	n.d.	n.d.		
Y	4	0	10	1	4	2	1	8	5	4	3
La	19	n.d.	11	n.d.	11	20	n.d.	64	11	23	20
Ce	15	n.d.	8	n.d.	14	26	n.d.	54	7	21	18
Pr	1	n.d.	1	n.d.	1	1	n.d.	4	1	1	1

Nd	2	n.d.	4	n.d.	3	3	n.d.	7	n.d.		
Sm	n.d.	n.d.	n.d.	n.d.	n.d.	n.d.	n.d.	n.d.	n.d.		
Eu	n.d.	n.d.	n.d.	n.d.	n.d.	n.d.	n.d.	n.d.	n.d.		
Gd	n.d.	n.d.	n.d.	n.d.	n.d.	n.d.	n.d.	n.d.	n.d.		
Tb	n.d.	n.d.	n.d.	n.d.	n.d.	n.d.	n.d.	n.d.	n.d.		
Dy	n.d.	n.d.	n.d.	n.d.	n.d.	n.d.	n.d.	n.d.	n.d.		
Ho	n.d.	n.d.	n.d.	n.d.	n.d.	n.d.	n.d.	n.d.	n.d.		
Er	n.d.	n.d.	n.d.	n.d.	n.d.	n.d.	n.d.	n.d.	n.d.		
Tm	n.d.	n.d.	n.d.	n.d.	n.d.	n.d.	n.d.	n.d.	n.d.		
Yb	n.d.	n.d.	n.d.	n.d.	n.d.	n.d.	n.d.	n.d.	n.d.		
Lu	n.d.	n.d.	n.d.	n.d.	n.d.	n.d.	n.d.	n.d.	n.d.		
Th	n.d.	n.d.	n.d.	n.d.	n.d.	n.d.	n.d.	n.d.	n.d.		
U	n.d.	n.d.	n.d.	n.d.	n.d.	n.d.	n.d.	n.d.	n.d.		

	OKC4											
	magmatic calcite from calcite carbonatite											
	Ca	Na	Fe	Mg	Mn	Si	Sr	Ba	Y	La	Ce	Pr
point 1	379678	265	763	1722	1411	n.d.	13400	5673	52	798	851	51
point 2	379678	203	734	1583	1397	n.d.	14251	5309	52	739	704	43
point 3	379678	136	747	1429	1723	n.d.	13743	3356	58	387	395	27
point 4	381511	196	1234	1930	1730	n.d.	16350	6230	82	640	798	57
point 5	375491	372	1311	2423	1707	n.d.	16579	5750	57	734	908	70
point 6	374975	198	1141	1823	2103	n.d.	15875	4268	87	603	749	58
point 7	377057	229	1070	1819	1596	n.d.	16322	6249	90	851	994	77
point 8	375792	174	933	1835	1285	n.d.	16681	6736	60	754	971	69
point 9	378125	244	919	1609	1245	n.d.	17646	6557	46	841	1102	80
point 10	379678	258	907	1725	1235	n.d.	18199	6708	58	885	1078	79
point 11	379678	n.d.	2879	360	1310	n.d.	1867	54	45	n.d.	n.d.	n.d.
point 12	379678	n.d.	2833	359	1088	n.d.	2376	25	32	n.d.	n.d.	n.d.
point 13	379678	n.d.	4124	498	1227	n.d.	2883	36	39	n.d.	n.d.	n.d.
point 14	379678	n.d.	4511	349	1246	n.d.	3159	38	57	n.d.	n.d.	n.d.
point 15	379678	n.d.	3582	350	1299	n.d.	3617	317	35	n.d.	n.d.	n.d.
average	378670		1846	1321	1440		11530	3820	57			
stdev	1930		1344	720	274		6543	2870	18			

OKC4												
magmatic calcite from calcite carbonatite												
Nd	Sm	Eu	Gd	Tb	Dy	Ho	Er	Tm	Yb	Lu	Th	U
140	16	7	12	2	10	2	3	1	4	n.d	n.d	n.d
122	14	5	10	1	9	1	5	1	4	n.d	n.d	n.d
85	12	5	12	1	8	2	6	1	5	n.d	n.d	n.d
160	18	8	9	2	12	3	9	1	11	n.d	n.d	n.d
165	12	6	13	2	7	1	3	1	n.d.	n.d	n.d	n.d
157	23	5	14	2	17	2	7	1	7	n.d	n.d	n.d
206	31	8	27	2	15	3	8	2	10	n.d	n.d	n.d
193	28	4	11	2	8	1	6	2	5	n.d	n.d	n.d
213	23	5	19	2	10	1	3	1	4	n.d	n.d	n.d
226	19	6	16	1	9	2	4	1	3	n.d	n.d	n.d
n.d.	n.d.	n.d.	n.d.	n.d.	n.d.	n.d.	n.d.	n.d.	9	n.d	n.d	n.d
n.d.	n.d.	n.d.	n.d.	n.d.	7	1	10	n.d.	n.d.	n.d	n.d	n.d
n.d.	n.d.	n.d.	n.d.	n.d.	n.d.	n.d.	n.d.	n.d.	7	n.d	n.d	n.d
n.d.	n.d.	n.d.	n.d.	n.d.	n.d.	n.d.	8	n.d.	16	n.d	n.d	n.d
n.d.	n.d.	n.d.	n.d.	n.d.	n.d.	2	5	n.d.	6	n.d	n.d	n.d

	OKA5									
	magmatic calcite frokm calcite carbonatite									
	point 1	point 2	point 3	point 4	point 5	point 6	point 7	point 8	point 9	point 10
Ca	369682	376945	383538	374506	370648	370648	370648	377147	373082	374894
Na	n.d.	n.d.	n.d.	n.d.	n.d.	n.d.	n.d.	n.d.	n.d.	n.d.
Fe	94	n.a.	96	125	n.a.	56	93	86	52	39
Mg	76	n.a.	72	79	n.a.	68	114	61	65	78
Mn	459	n.a.	420	414	396	378	399	468	410	413
Si	n.d.	n.a.	n.d.	n.d.	n.d.	n.d.	n.d.	n.d.	n.d.	n.d.
Sr	20525	19582	21050	18656	20337	20120	21244	20271	19106	18064
Ba	3452	3136	3968	4778	3149	3043	3101	3225	3415	3386
Y	8	7	2	3	19	19	20	21	24	20
La	286	250	n.a.	n.a.	324	308	361	329	360	261
Ce	344	281	n.a.	n.a.	446	440	512	451	479	363
Pr	26	20	n.a.	n.a.	35	38	39	38	34	37
Nd	67	48	n.a.	n.a.	99	103	121	101	148	99

Sm	7	6	n.a.	n.a.	7	10	11	17	11	11
Eu	1	1	0	0	3	2	3	3	4	2
Gd	3	4	0	0	7	7	7	11	0	18
Tb	n.d.	n.d.	n.d.	n.d.	n.d.	n.d.	n.d.	n.d.	n.d.	n.d.
Dy	n.d.	n.d.	n.d.	n.d.	n.d.	n.d.	n.d.	n.d.	n.d.	n.d.
Ho	n.d.	n.d.	n.d.	n.d.	n.d.	n.d.	n.d.	n.d.	n.d.	n.d.
Er	n.d.	n.d.	n.d.	n.d.	n.d.	n.d.	n.d.	n.d.	n.d.	n.d.
Tm	n.d.	n.d.	n.d.	n.d.	n.d.	n.d.	n.d.	n.d.	n.d.	n.d.
Yb	n.d.	n.d.	n.d.	n.d.	n.d.	n.d.	n.d.	n.d.	n.d.	n.d.
Lu	n.d.	n.d.	n.d.	n.d.	n.d.	n.d.	n.d.	n.d.	n.d.	n.d.
Th	n.d.	n.d.	n.d.	n.d.	n.d.	n.d.	n.d.	n.d.	n.d.	n.d.
U	n.d.	n.d.	n.d.	n.d.	n.d.	n.d.	n.d.	n.d.	n.d.	n.d.

	OKA5										
	magmatic calcite frokm calcite carbonatite										
Ca	point 11	point 12	point 13	point 14	point 15	point 16	point 17	point 18	point 19	average	stdev
Na	368536	369339	377373	374083	376270	373687	371778	380659	374081	374081	3952
Fe	n.d.	n.d.	n.d.	n.d.	n.d.	n.d.	n.d.	n.d.	n.d.		
Mg	187	108	45	85	46	61	72	35	80	80	38
Mn	44	84	62	71	38	60	82	n.d.	66		
Si	383	397	367	395	354	377	352	625	412	412	61
Sr	n.d.	n.d.	n.d.	n.d.	n.d.	n.d.	n.d.	n.d.	n.d.		
Ba	23242	17744	17802	18042	16226	18058	17446	15504	19057	19057	1866
Y	4614	3195	3405	3145	2900	3078	3285	2469	3375	3375	548
La	1	23	14	22	22	14	18	16	15	15	7
Ce	219	424	278	365	243	344	352	n.a.	314	314	55
Pr	201	532	392	517	376	449	459	380	414	414	86
Nd	9	40	28	41	33	33	39	16	32	32	9
Sm	32	133	96	121	87	100	105	55	95	95	30
Eu	0	11	0	13	10	11	12	0	10	9	5

Gd	0	1	2	4	1	1	4	0	2	2	1
Tb	0	8	0	10	5	8	6	0	7	5	5
Dy	n.d.	n.d.	n.d.	n.d.	n.d.	n.d.	n.d.	n.d.	n.d.		
Ho	n.d.	n.d.	n.d.	n.d.	n.d.	n.d.	n.d.	n.d.	n.d.		
Er	n.d.	n.d.	n.d.	n.d.	n.d.	n.d.	n.d.	n.d.	n.d.		
Tm	n.d.	n.d.	n.d.	n.d.	n.d.	n.d.	n.d.	n.d.	n.d.		
Yb	n.d.	n.d.	n.d.	n.d.	n.d.	n.d.	n.d.	n.d.	n.d.		
Ly	n.d.	n.d.	n.d.	n.d.	n.d.	n.d.	n.d.	n.d.	n.d.		
Y	n.d.	n.d.	n.d.	n.d.	n.d.	n.d.	n.d.	n.d.	n.d.		

	OKA1										
	magmatic calcite from calcite carbonatiet										
	point 1	point 2	point 3	point 4	point 5	point 6	point 7	point 8	point 9	point 10	point 11
Ca	372594	370533	372679	370862	371667	371667	371667	371667	371667	377520	375457
Na	143	295	103	115	120	117	123	183	111	n.d.	n.d.
Fe	420	465	415	393	389	367	411	366	634	138	179
Mg	312	314	328	320	314	300	311	288	351	153	137
Mn	540	529	539	530	515	505	505	502	494	535	564
Si	n.d.	n.d.	n.d.	n.d.	n.d.	n.d.	n.d.	n.d.	n.d.	n.d.	n.d.
Sr	30993	30434	30011	30386	30170	29404	28979	29530	28424	20170	19580
Ba	2060	2063	1948	1938	1922	2031	1835	2109	1843	3320	2960
Y	29	28	29	29	28	27	26	28	26	24	29
La	405	395	394	413	404	394	382	389	383	369	392
Ce	574	561	551	558	568	547	526	548	521	498	515
Pr	44	42	41	40	42	41	39	41	38	35	42
Nd	129	129	125	126	126	116	119	117	109	94	144
Sm	13	13	12	12	13	13	10	13	13	8	8

Eu	3	3	3	3	4	3	3	3	3	2	2
Gd	13	10	8	11	9	10	10	11	8	15	0
Tb	1	1	1	1	1	1	1	1	1	1	1
Dy	5	5	4	5	4	3	4	5	4	6	6
Ho	1	1	1	1	1	1	1	1	1	n.d.	n.d.
Er	3	3	2	2	2	2	2	2	2	4	n.d.
Tm	n.d.	n.d.	n.d.	n.d.	n.d.	n.d.	n.d.	n.d.	n.d.	n.d.	n.d.
Yb	n.d.	n.d.	n.d.	n.d.	n.d.	n.d.	n.d.	n.d.	n.d.	n.d.	n.d.
Lu	n.d.	n.d.	n.d.	n.d.	n.d.	n.d.	n.d.	n.d.	n.d.	n.d.	n.d.
Th	n.d.	n.d.	n.d.	n.d.	n.d.	n.d.	n.d.	n.d.	n.d.	n.d.	n.d.
U	n.d.	n.d.	n.d.	n.d.	n.d.	n.d.	n.d.	n.d.	n.d.	n.d.	n.d.

		OKA1									
		magmatic calcite									
	point 12	point 13	point 14	point 15	point 16	point 17	point 18	point 19	point 20	average	stdev
Ca	378436	375873	375873	375873	381400	381400	371667	371667	371667	374092	3427
Na	n.d.	n.d.	n.d.	n.d.	n.d.	n.d.	n.d.	n.d.	n.d.		
Fe	184	113	146	126	356	347	3126	2150	332	553	743
Mg	147	80	120	133	287	303	344	207	66	241	97
Mn	546	536	505	505	474	563	873	646	200	530	115
Si	n.d.	n.d.	n.d.	n.d.	n.d.	n.d.	n.d.	n.d.	n.d.	n.d.	
Sr	19690	20309	19766	19417	18472	16742	2955	1817	3598	21542	9538
Ba	2739	3295	3085	2958	1963	1790	147	72	431	2025	938
Y	26	21	27	25	27	25	36	16	41	27	5
La	518	290	366	386	434	439	102	18	0	344	138
Ce	520	440	494	496	622	585	184	35	14	468	175
Pr	34	30	38	38	41	40	15	3	1	34	13
Nd	129	83	112	100	126	114	55	8	6	103	38
Sm	9	8	12	9	16	13	7	n.d.	n.d.		

Eu	4	2	4	2	4	3	2	n.d.	1		
Gd	12	8	7	5	15	17	6	n.d.	n.d.		
Tb	0	0	1	0	0	0	1	n.d.	1		
Dy	6	3	8	7	4	6	5	n.d.	7		
Ho	n.d.	n.d.	n.d.	2	n.d.	1	2	1	1		
Er	2	2	2	3	n.d.	n.d.	6	2	6		
Tm	n.d.	n.d.	n.d.	n.d.	n.d.	n.d.	n.d.	n.d.	n.d.		
Yb	n.d.	n.d.	n.d.	n.d.	n.d.	n.d.	n.d.	n.d.	n.d.		
Lu	n.d.	n.d.	n.d.	n.d.	n.d.	n.d.	n.d.	n.d.	n.d.		
Th	n.d.	n.d.	n.d.	n.d.	n.d.	n.d.	n.d.	n.d.	n.d.		
U	n.d.	n.d.	n.d.	n.d.	n.d.	n.d.	n.d.	n.d.	n.d.		

OKA1	stage 3a calcite								
calcite carbonatite	point 1	point 2	point 3	point 4	point 5	point 6	point 7	average	stdev
Ca	389135	389135	389135	389135	389135	389135	389134	389134	0
Na	133	n.d.	n.d.	317	136	178	98		
Fe	8668	1866	1355	1324	1420	849	1567	2435	2765
Mg	1549	457	297	308	508	382	555	579	438
Mn	2415	1240	1182	883	926	742	1163	1221	557
Si	n.d.	n.d.	n.d.	n.d.	n.d.	n.d.	n.d.		
Sr	n.a.	7953	n.a.	n.a.	n.a.	8556	6054	7521	1306
Ba	n.a.	n.a.	n.a.	n.a.	n.a.	n.a.	n.a.		
Y	27	10	7	15	9	18	13	14	7
La	n.a.	41	105	285	80	n.a.	74	117	97
Ce	n.a.	49	140	438	144	n.a.	104	175	152
Pr	n.a.	4	12	30	11	n.a.	9	13	10
Nd	n.a.	13	24	95	30	n.a.	24	37	33
Sm	n.a.	n.d.	n.d.	n.d.	n.d.	n.a.	n.d.		

Eu	n.a.	n.d.	n.d.	n.d.	n.d.	n.a.	n.d.		
Gd	n.a.	n.d.	n.d.	10	3	n.a.	4		
Tb	n.a.	n.d.	n.d.	n.d.	n.d.	n.a.	n.d.		
Dy	n.a.	n.d.	2	4	n.d.	n.a.	3		
Ho	n.a.	n.d.	n.d.	n.d.	n.d.	n.a.	n.d.		
Er	n.d.	n.d.	n.d.	n.d.	n.d.	n.d.	n.d.		
Tm	n.d.	n.d.	n.d.	n.d.	n.d.	n.d.	n.d.		
Yb	n.d.	n.d.	n.d.	n.d.	n.d.	n.d.	n.d.		
Lu	n.d.	n.d.	n.d.	n.d.	n.d.	n.d.	n.d.		
Th	n.d.	n.d.	n.d.	n.d.	n.d.	n.d.	n.d.		
U	n.d.	n.d.	n.d.	n.d.	n.d.	n.d.	n.d.		

	OKC17											
	magmatic calcite from calcite carbonatite											
	Ca	Na	Fe	Mg	Mn	Si	Sr	Ba	Y	La	Ce	Pr
point 1	385399	110	898	139	1381	n.d.	21571	2330	18	341	503	38
point 2	387055	130	821	138	1077	n.d.	22336	2613	20	437	582	50
point 3	387055	119	795	173	1018	n.d.	22477	2565	19	448	612	51
point 4	387055	163	739	138	1020	n.d.	22193	2667	18	474	636	48
point 5	387055	153	627	214	599	n.d.	21393	2489	19	497	641	49
point 6	382654	127	493	289	444	n.d.	17656	2013	15	535	666	50
point 7	383843	n.d.	566	340	507	n.d.	15654	1630	18	408	586	44
point 8	383843	195	462	274	427	n.d.	25002	3479	20	724	860	68
point 9	383843	222	487	285	421	n.d.	24716	2981	21	656	886	70
point 10	383843	210	525	313	444	n.d.	25325	3000	21	654	893	67
point 11	383843	233	543	339	450	n.d.	25092	3150	22	672	870	73
point 12	383843	253	505	309	453	n.d.	25082	3101	22	642	886	66
point 13	387275	113	838	351	567	n.d.	19318	1978	18	443	602	45
point 14	387275	114	495	300	443	n.d.	21038	2134	18	445	602	48
point 15	387275	64	n.a.	630	1165	n.d.	9928	1003	13	286	419	31
point 16	387275	161	528	273	506	n.d.	21398	2259	18	546	711	55
point 17	387275	108	n.a.	504	964	n.d.	15309	1694	16	424	589	43
point 18	385630	146	836	294	699	n.d.	20911	2417	19	508	679	53
average	385630		635	294	699		20911	2417	19	508	679	53
stdev	1710		156	124	313		4097	620	2	121	143	12

OKC18												
magmatic calcite from calcite carbonatite												
Nd	Sm	Eu	Gd	Tb	Dy	Ho	Er	Tm	Yb	Lu	Th	U
118	10	2	7	n.d.	3	1	1	n.d.	n.d.	n.d.	n.d.	n.d.
139	7	4	7	<1	2	1	1	n.d.	n.d.	n.d.	n.d.	n.d.
157	12	4	10	1	2	n.d.	2	n.d.	n.d.	n.d.	n.d.	n.d.
142	11	3	7	<1	4	1	2	n.d.	n.d.	n.d.	n.d.	n.d.
140	14	3	8	<1	5	<1	n.d.	n.d.	n.d.	n.d.	n.d.	n.d.
154	12	3	9	<1	3	<1	3	n.d.	n.d.	n.d.	n.d.	n.d.
123	11	3	5	1	5	1	2	n.d.	n.d.	n.d.	n.d.	n.d.
195	11	4	8	1	5	1	1	n.d.	n.d.	n.d.	n.d.	n.d.
206	13	3	5	1	5	1	n.d.	n.d.	n.d.	n.d.	n.d.	n.d.
189	13	3	11	1	3	1	2	n.d.	n.d.	n.d.	n.d.	n.d.
191	17	4	9	1	4	1	n.d.	n.d.	n.d.	n.d.	n.d.	n.d.
174	16	4	8	1	4	n.d.	2	n.d.	n.d.	n.d.	n.d.	n.d.
139	14	4	8	1	2	<1	1	n.d.	n.d.	n.d.	n.d.	n.d.
132	14	3	8	<1	3	1	1	n.d.	n.d.	n.d.	n.d.	n.d.
94	7	2	4	1	3	1	1	n.d.	n.d.	n.d.	n.d.	n.d.
162	11	3	9	1	3	1	n.d.	n.d.	n.d.	n.d.	n.d.	n.d.
117	12	3	6	1	2	n.d.	1	n.d.	n.d.	n.d.	n.d.	n.d.
151	12	3	8	1	3	<1	1	n.d.	n.d.	n.d.	n.d.	n.d.
151	12	3	8	1	3							
31	3	1	2	0	1							

OKC17	stage 3a calcite											
	point 1	point 2	point 3	point 4	point 5	point 6	point 7	point 8	point 9	point 10	average	stdev
Ca	408386	408386	408386	408386	408386	395711	387055	387055	387055	387055	398586	10647
Na	n.d.	n.d.	n.d.	n.d.	n.d.	n.d.	n.d.	n.d.	n.d.	n.d.		
Fe	2411	1750	3419	3255	3549	3273	1529	2046	2331	1308	2487	835
Mg	1239	1133	1398	1463	1232	1059	1229	1184	1081	1442	1246	144
Mn	247	256	346	369	245	204	250	315	283	466	298	78
Si	0	0	0	0	0	0	0	0	0	0		
Sr	5707	16069	2265	4053	1789	3932	2681	3305	2012	4928	4674	4203
Ba	260	n.a.	29	190	5	14	30	65	13	224	92	102
Y	13	12	14	14	8	30	19	8	8	14	14	7
La	14	33	29	35	0	n.a.	14	16	9	n.a.	19	12
Ce	35	45	61	50	1	n.a.	21	28	11	n.a.	32	20
Pr	2	3	6	4	0	n.a.	2	2	1	n.a.	3	2
Nd	10	12	19	14	2	n.a.	6	8	3	n.a.	9	6
Sm	n.d	n.d	n.d	n.d	n.d	n.a.	n.d	n.d	n.d	n.d		
Eu	n.d.	n.d.	n.d.	n.d.	n.d.	n.a.	n.d.	n.d.	n.d.	n.d.		

Gd	n.d.	n.d.	n.d.	n.d.	n.d.	n.a.	n.d.	n.d.	n.d.	n.d.		
Tb	n.d.	n.d.	n.d.	n.d.	n.d.	n.a.	n.d.	n.d.	n.d.	n.d.		
Dy	1	1	n.d.	n.d.	n.d.	n.a.	3	1	2	2		
Ho	<1	<1	<1	1	n.d.	n.a.	1	<1	<1	1		
Er	2	1	2	2	n.d.	n.a.	2	1	1	1		
Tm	n.d.	n.d.	n.d.	n.d.	n.d.	n.a.	n.d.	n.d.	n.d.	n.d.		
Yb	2	2	2	3	5	n.a.	2	1	2	1	2	1
Lu	n.d.	n.d.	n.d.	n.d.	n.d.	n.a.	n.d.	n.d.	n.d.	n.d.		
Th	n.d.	n.d.	n.d.	n.d.	n.d.	n.a.	n.d.	n.d.	n.d.	n.d.		
U	n.d.	n.d.	n.d.	n.d.	n.d.	n.a.	n.d.	n.d.	n.d.	n.d.		

OKC19-1	magmatic calcite						
	point 1	point 2	point 3	point 4	point 5	average	stdev
Ca	382502	382210	382151	380583	382231	381935	768
Na	163	144	148	153	120	146	16
Fe	396	514	401	386	491	438	60
Mg	266	263	261	270	328	278	28
Mn	415	479	402	384	414	419	36
Si	n.d.	n.d.	n.d.	n.d.	n.d.		
Sr	21116	20495	21003	21423	17156	20239	1756
Ba	2289	2050	2028	2116	1727	2042	204
Y	17	18	17	18	18	17	1
La	530	478	492	457	451	482	32
Ce	679	622	655	607	589	630	37
Pr	50	49	46	42	42	46	3
Nd	133	129	133	117	118	126	8
Sm	11	11	13	12	9	11	2
Eu	3	2	3	3	2	3	<1
Gd	8	8	9	7	7	8	1
Tb	1	0	1	1	0	1	<1
Dy	3	2	2	3	3	2	<1
Ho	1	1	1	1	0	1	<1

Er	0	2	1	2	1	1	1
Tm	n.d.	n.d.	n.d.	n.d.	n.d.		
Yb	1	1	1	1	1	1	<1
Lu	n.d.	n.d.	n.d.	n.d.	n.d.		
Th	n.d.	n.d.	n.d.	n.d.	n.d.		
U	n.d.	n.d.	n.d.	n.d.	n.d.		

OKC19-2												
stage 3a calcite from calcite carbonatite												
	Ca	Na	Fe	Mg	Mn	Si	Sr	Ba	Y	La	Ce	Pr
point 1	397430	n.d.	8956	1420	5070	n.d.	2454	n.d.	49	7	10	1
point 2	380162	n.d.	4820	451	5288	n.d.	2440	n.d.	30	5	9	1
point 3	385094	n.d.	4047	444	3262	n.d.	2483	n.d.	51	11	20	2
point 4	396499	n.d.	2823	244	4090	n.d.	1885	n.d.	47	5	13	1
point 5	396499	n.d.	n.a.	3144	n.a.	n.d.	n.a.	n.d.	n.a.	n.a.	n.a.	n.a.
point 6	388231	n.d.	3218	167	3851	n.d.	1922	n.d.	94	4	2	1
point 7	388231	n.d.	3910	377	7963	n.d.	1470	n.d.	n.a.	2	3	0
point 8	388231	n.d.	3316	169	4011	n.d.	1948	n.d.	95	n.d.	n.d.	n.d.
point 9	388231	n.d.	3422	182	4091	n.d.	1935	n.d.	91	1	n.d.	0
point 10	388231	n.d.	3500	208	3973	n.d.	1885	n.d.	65	5	n.d.	0
point 11	388231	n.d.	3171	212	3779	n.d.	1796	n.d.	94	1	n.d.	0
point 12	388231	n.d.	n.a.	1903	n.a.	n.d.	2097	n.d.	21	n.a.	n.a.	n.a.
point 13	388231	n.d.	n.a.	2981	n.a.	n.d.	1332	n.d.	27	n.a.	n.a.	n.a.
point 14	385213	n.d.	n.a.	n.a.	n.a.	n.a.	2300	n.d.	48	8	16	2

point 15	385213	n.d.	n.a.	n.a.	n.a.	n.a.	1626	n.d.	58	7	12	1
point 16	380929	n.d.	n.a.	n.a.	n.a.	n.a.	2426	n.d.	n.a.	n.a.	n.a.	n.a.
point 17	385213	n.d.	n.a.	n.a.	n.a.	n.a.	1552	n.d.	n.a.	n.a.	n.a.	n.a.
point 18	390083	n.d.	n.a.	n.a.	n.a.	n.a.	2061	n.d.	n.a.	n.a.	n.a.	n.a.
point 19	385213	n.d.	n.a.	n.a.	n.a.	n.a.	7217	n.d.	65	n.a.	n.a.	n.a.
point 20	385213	n.d.	n.a.	n.a.	n.a.	n.a.	3102	n.d.	40	1	n.a.	0
point 21	385213	n.d.	n.a.	n.a.	n.a.	n.a.	3097	n.d.	33	3	5	0
point 22	385213	n.d.	n.a.	n.a.	n.a.	n.a.	3281	n.d.	31	2	3	0
point 23	385086	n.d.	n.a.	n.a.	n.a.	n.a.	3182	n.d.	36	5	3	0
point 24	385086	n.d.	n.a.	n.a.	n.a.	n.a.	3015	n.d.	55	n.a.	n.a.	8
point 25	383551	n.d.	n.a.	n.a.	n.a.	n.a.	2070	n.d.	26	5	8	1
point 26	383551	n.d.	n.a.	n.a.	n.a.	n.a.	2986	n.d.	29	2	4	0
point 27	383551	n.d.	n.a.	n.a.	n.a.	n.a.	2708	n.d.	62	9	17	2
average	387032		4119	916	4538		2472		52			1
stdev	4222		1790	1091	1344		1122		24			2

OKC19-2												
stage 3a calcite from calcite carbonatite												
Nd	Sm	Eu	Gd	Tb	Dy	Ho	Er	Tm	Yb	Lu	Th	U
n.d.	n.d.	n.d.	n.d.	n.d.	3	1	6	2	19	2.8	n.d.	n.d.
2	n.d.	n.d.	3	0	4	1	3	1	12	1.1	n.d.	n.d.
n.d.	2	n.d.	n.d.	0	4	1	5	1	8	1.0	n.d.	n.d.
3	1	0	2	1	4	2	10	2	26	3.8	n.d.	n.d.
n.a.	n.a.	n.a.	n.a.	n.a.	n.a.	n.a.	n.a.	n.a.	n.a.	n.a.	n.d.	n.d.
1	n.d.	n.a.	1	0	5	3	n.a.	4	44	5.9	n.d.	n.d.
n.d.	n.d.	n.d.	n.d.	1	n.a.	n.d.	2	0	5	0.4	n.d.	n.d.
1	n.d.	n.d.	n.d.	n.d.	n.a.	3	n.a.	n.a.	n.a.	7.9	n.d.	n.d.
n.d.	n.d.	n.d.	1	1	5	3	14	5	41	5.9	n.d.	n.d.
n.d.	n.d.	n.d.	1	n.d.	5	3	11	3	33	4.9	n.d.	n.d.
n.d.	n.d.	n.d.	2	0	6	3	n.a.	4	35	5.3	n.d.	n.d.
n.a.	n.a.	n.a.	n.a.	n.a.	n.a.	n.a.	n.a.	n.a.	n.a.	n.a.	n.d.	n.d.
n.a.	n.a.	n.a.	n.a.	n.a.	n.a.	n.a.	n.a.	n.a.	n.a.	n.a.	n.d.	n.d.
5	1	0	2	0	4	1	7	1	16	2.4	n.d.	n.d.

3	1	0	1	0	5	2	10	2	24	3.3	n.d.	n.d.
n.a.	n.a.	n.a.	n.a.	n.a.	n.a.	n.a.	n.a.	n.a.	n.a.	n.a.	n.d.	n.d.
n.a.	n.a.	n.a.	n.a.	n.a.	n.a.	n.a.	n.a.	n.a.	n.a.	n.a.	n.d.	n.d.
n.a.	n.a.	n.a.	n.a.	n.a.	n.a.	n.a.	n.a.	n.a.	n.a.	n.a.	n.d.	n.d.
n.a.	n.a.	n.a.	n.a.	n.a.	n.a.	n.a.	n.a.	n.a.	n.a.	n.a.	n.d.	n.d.
1	1	n.d.	1	0	3	1	6	7	16	2.5	n.d.	n.d.
2	1	0	1	0	3	1	5	8	12	2.0	n.d.	n.d.
1	1	0	1	0	2	1	4	9	9	1.7	n.d.	n.d.
1	n.d.	n.d.	0	0	3	1	6	10	13	1.9	n.d.	n.d.
28	4	n.d.	4	1	5	1	7	11	12	1.9	n.d.	n.d.
2	1	0	1	0	2	1	4	12	10	1.6	n.d.	n.d.
2	1	0	1	0	3	1	4	13	10	1.6	n.d.	n.d.
6	1	1	2	1	6	2	9	14	18	2.8	n.d.	n.d.
					4		7	6	19	3		
					1		3	5	11	2		

Okorusu LA-ICP-MS fluorite analyses

Average LA-ICP-MS of stage 3b and 4 fluorite. Note: the LA-ICP-MS data were calculated using the calcium content determined by EPMA. Mg, Th, U and Sm to Lu were under the limit of detection.

	n = 6	n = 49	n = 74	n = 15
	OKC19-2	OKC3-OKC8	OKC6-OKC8	OKC8
	stage 3b	type 4a	type 4b	type 4c
	EPMA (wt%)			
CaO	72.49	69.62	69.95	69.51
	LA-ICP-MS (ppm)			
Na	31	n.d.	n.d.	n.d.
Sr	2713	1516	1976	1935
Ba	5	n.d.	n.d.	n.d.
La	4	53	13	27
Ce	7	71	24	36
Pr	< 1	5	n.d.	n.d.
Nd	1	16	n.d.	n.d.
Y	120	n.d.	120	145

236

LA-ICP-MS analysis of stage 3 and 4 fluorite

OKC19-2								
intensely altered	stage 3b fluorite							
calcite carbonatite	point 1	point 2	point 3	point 4	point 5	point 6	average	stdev
Ca	521601	520997	520323	513952	516844	515151	518145	2973.8
Na	4	n.a.	8	77	18	45	31	27.4
Sr	350	4019	1594	n.a.	5001	2601	2713	1660.4
Ba	1	6	2	n.a.	12	5	5	4
Y	76	214	71	155	70	136	120	53
La	0.16	5	1	12	4	3	4	4
Ce	< 1	4	2	21	7	5	8	7
Pr	< 0.1	1	< 1	n.a.	1	< 1	1	< 0.1
Nd	< 1	2	1	n.a.	2	1	1	1
Sm	n.d.	1	n.d.	1	< 1	n.d.		
Eu	n.d.	< 1	0	1	< 1	< 1		
Gd	n.d.	1	1	1	1	1		

Tb	< 0.1	< 1	< 1	< 1	< 1	< 0.1		
Dy	< 1	2	1	2	4	2	2	1
Ho	< 1	1	1	1	1	1	1	< 1
Er	0.64	9	3	6	9	9	6	3
Tm	< 0.1	4	1	2	2	2	2	1
Yb	0.56	76	7	28	23	30	27	24
Lu	< 0.1	15	1	5	4	6	6	5
Th	< 0.1	3	1	2	1	< 0.1	2	1
U	n.d.	< 0.1	< 0.1	< 0.1	< 0.1	n.d.		

	Ca	Na	Sr	Ba	Y	La	Ce	Pr	Nd	Sm

OKC3/OKC8										
type 4a fluorite from fluorite rich rock										
	Ca	Na	Sr	Ba	Y	La	Ce	Pr	Nd	Sm
point 1	501429	n.d.	256	n.d.	n.d.	41	17	n.d.	n.d.	n.d.
point 2	503053	n.d.	2401	n.d.	n.d.	57	75	6	33	n.d.
point 3	498801	n.d.	2291	n.d.	n.d.	82	61	3	n.d.	n.d.
point 4	498174	n.d.	2337	n.d.	n.d.	107	117	9	17	n.d.
point 5	498981	n.d.	2453	n.d.	n.d.	41	81	5	26	n.d.
point 6	498255	n.d.	2366	n.d.	n.d.	42	43	2	n.d.	n.d.
point 7	502163	n.d.	2978	n.d.	n.d.	72	140	8	21	n.d.
point 8	502574	n.d.	1442	n.d.	n.d.	24	27	n.d.	n.d.	n.d.
point 9	503915	n.d.	157	n.d.	n.d.	n.d.	n.d.	n.d.	n.d.	n.d.
point 10	500967	n.d.	285	n.d.	n.d.	28	24	n.d.	n.d.	n.d.
point 11	494746	n.d.	1198	n.d.	n.d.	41	24	n.d.	n.d.	n.d.
point 12	496764	n.d.	1361	n.d.	n.d.	77	87	7	28	n.d.
point 13	499732	n.d.	2760	n.d.	n.d.	78	107	7	22	n.d.
point 14	501914	n.d.	3250	n.d.	n.d.	183	173	11	38	n.d.
point 15	503483	n.d.	1643	n.d.	n.d.	59	183	9	15	n.d.

point 16	496875	n.d.	1720	n.d.	n.d.	25	58	2	8	n.d.
point 17	498738	n.d.	2767	n.d.	n.d.	109	149	12	13	n.d.
point 18	500108	n.d.	1668	n.d.	n.d.	302	279	12	47	n.d.
point 19	500609	n.d.	2789	n.d.	n.d.	118	79	4	n.d.	n.d.
point 20	500424	n.d.	956	n.d.	n.d.	33	29	1	n.d.	n.d.
point 21	500250	n.d.	230	n.d.	n.d.	9	7	n.d.	n.d.	n.d.
point 22	502210	n.d.	247	n.d.	n.d.	12	12	n.d.	n.d.	n.d.
point 23	499113	n.d.	1501	n.d.	n.d.	25	51	5	n.d.	n.d.
point 24	502190	n.d.	385	n.d.	n.d.	104	101	4	n.d.	n.d.
point 25	503639	n.d.	2161	n.d.	n.d.	35	67	5	n.d.	n.d.
point 26	503915	n.d.	1027	n.d.	n.d.	10	22	4	9	n.d.
point 27	500642	n.d.	1149	n.d.	n.d.	129	153	4	n.d.	n.d.
point 28	502657	n.d.	1106	n.d.	n.d.	25	52	n.d.	n.d.	n.d.
point 29	502171	n.d.	2435	n.d.	n.d.	72	41	n.d.	n.d.	n.d.
point 30	455224	n.d.	3260	n.d.	n.d.	52	87	6	15	n.d.
point 31	496377	n.d.	887	n.d.	n.d.	n.d.	n.d.	n.d.	n.d.	n.d.
point 32	496740	n.d.	1182	n.d.	n.d.	36	n.d.	n.d.	58	n.d.
point 33	491754	n.d.	1365	n.d.	n.d.	n.d.	n.d.	n.d.	89	n.d.

point 34	491835	n.d.	1548	n.d.	n.d.	n.d.	80	13	45	n.d.
point 35	493108	n.d.	946	n.d.	n.d.	n.d.	47	10	43	n.d.
point 36	499383	n.d.	1287	n.d.	n.d.	43	41	12	15	n.d.
point 37	499053	n.d.	1170	n.d.	n.d.	53	55	4	n.d.	n.d.
point 38	497797	n.d.	1231	n.d.	n.d.	56	66	n.d.	n.d.	n.d.
point 39	496433	n.d.	580	n.d.	n.d.	12	17	2	n.d.	n.d.
point 40	496828	n.d.	1090	n.d.	n.d.	7	30	6	11	n.d.
point 41	498860	n.d.	314	n.d.	n.d.	23	21	n.d.	n.d.	n.d.
point 42	492854	n.d.	498	n.d.	n.d.	10	18	2	n.d.	n.d.
point 43	494190	n.d.	691	n.d.	n.d.	13	17	4	n.d.	n.d.
point 44	497074	n.d.	341	n.d.	n.d.	4	26	2	9	n.d.
point 45	491851	n.d.	983	n.d.	n.d.	107	147	3	n.d.	n.d.
point 46	495456	n.d.	1682	n.d.	n.d.	22	47	6	24	n.d.
point 47	493810	n.d.	824	n.d.	n.d.	34	36	2	9	n.d.
point 48	497955	n.d.	3426	n.d.	n.d.	40	46	n.d.	n.d.	n.d.
point 49	494347	n.d.	2154	n.d.	n.d.	59	117	n.d.	n.d.	n.d.
average	497743	n.d.	1485	n.d.	n.d.	57	70	6	27	n.d.
stdev	7088		912							

OKC3/OKC8										
type 4a fluorite from fluorite rich rock										
Eu	Gd	Tb	Dy	Ho	Er	Tm	Yb	Lu	Th	U
n.d.	n.d.	n.d.	n.d.	n.d.	n.d.	n.d.	n.d.	n.d.	n.d.	n.d.
n.d.	n.d.	n.d.	n.d.	n.d.	n.d.	n.d.	n.d.	n.d.	n.d.	n.d.
n.d.	n.d.	n.d.	n.d.	n.d.	n.d.	n.d.	n.d.	n.d.	n.d.	n.d.
n.d.	n.d.	n.d.	n.d.	n.d.	n.d.	n.d.	n.d.	n.d.	n.d.	n.d.
n.d.	n.d.	n.d.	n.d.	n.d.	n.d.	n.d.	n.d.	n.d.	n.d.	n.d.
n.d.	n.d.	n.d.	n.d.	n.d.	n.d.	n.d.	n.d.	n.d.	n.d.	n.d.
n.d.	n.d.	n.d.	n.d.	n.d.	n.d.	n.d.	n.d.	n.d.	n.d.	n.d.
n.d.	n.d.	n.d.	n.d.	n.d.	n.d.	n.d.	n.d.	n.d.	n.d.	n.d.
n.d.	n.d.	n.d.	n.d.	n.d.	n.d.	n.d.	n.d.	n.d.	n.d.	n.d.
n.d.	n.d.	n.d.	n.d.	n.d.	n.d.	n.d.	n.d.	n.d.	n.d.	n.d.
n.d.	n.d.	n.d.	n.d.	n.d.	n.d.	n.d.	n.d.	n.d.	n.d.	n.d.
n.d.	n.d.	n.d.	n.d.	n.d.	n.d.	n.d.	n.d.	n.d.	n.d.	n.d.
n.d.	n.d.	n.d.	n.d.	n.d.	n.d.	n.d.	n.d.	n.d.	n.d.	n.d.
n.d.	n.d.	n.d.	n.d.	n.d.	n.d.	n.d.	n.d.	n.d.	n.d.	n.d.

n.d.	n.d.	n.d.	n.d.	n.d.	n.d.	n.d.	n.d.	n.d.	n.d.	n.d.
n.d.	n.d.	n.d.	n.d.	n.d.	n.d.	n.d.	n.d.	n.d.	n.d.	n.d.
n.d.	n.d.	n.d.	n.d.	n.d.	n.d.	n.d.	n.d.	n.d.	n.d.	n.d.
n.d.	n.d.	n.d.	n.d.	n.d.	n.d.	n.d.	n.d.	n.d.	n.d.	n.d.
n.d.	n.d.	n.d.	n.d.	n.d.	n.d.	n.d.	n.d.	n.d.	n.d.	n.d.
n.d.	n.d.	n.d.	n.d.	n.d.	n.d.	n.d.	n.d.	n.d.	n.d.	n.d.
n.d.	n.d.	n.d.	n.d.	n.d.	n.d.	n.d.	n.d.	n.d.	n.d.	n.d.
n.d.	n.d.	n.d.	n.d.	n.d.	n.d.	n.d.	n.d.	n.d.	n.d.	n.d.
n.d.	n.d.	n.d.	n.d.	n.d.	n.d.	n.d.	n.d.	n.d.	n.d.	n.d.
n.d.	n.d.	n.d.	n.d.	n.d.	n.d.	n.d.	n.d.	n.d.	n.d.	n.d.
n.d.	n.d.	n.d.	n.d.	n.d.	n.d.	n.d.	n.d.	n.d.	n.d.	n.d.
n.d.	n.d.	n.d.	n.d.	n.d.	n.d.	n.d.	n.d.	n.d.	n.d.	n.d.
n.d.	n.d.	n.d.	n.d.	n.d.	n.d.	n.d.	n.d.	n.d.	n.d.	n.d.
n.d.	n.d.	n.d.	n.d.	n.d.	n.d.	n.d.	n.d.	n.d.	n.d.	n.d.
n.d.	n.d.	n.d.	n.d.	n.d.	n.d.	n.d.	n.d.	n.d.	n.d.	n.d.
n.d.	n.d.	n.d.	n.d.	n.d.	n.d.	n.d.	n.d.	n.d.	n.d.	n.d.
n.d.	n.d.	n.d.	n.d.	n.d.	n.d.	n.d.	n.d.	n.d.	n.d.	n.d.
n.d.	n.d.	n.d.	n.d.	n.d.	n.d.	n.d.	n.d.	n.d.	n.d.	n.d.
n.d.	n.d.	n.d.	n.d.	n.d.	n.d.	n.d.	n.d.	n.d.	n.d.	n.d.

n.d.	n.d.	n.d.	n.d.	n.d.	n.d.	n.d.	n.d.	n.d.	n.d.	n.d.
n.d.	n.d.	n.d.	n.d.	n.d.	n.d.	n.d.	n.d.	n.d.	n.d.	n.d.
n.d.	n.d.	n.d.	n.d.	n.d.	n.d.	n.d.	n.d.	n.d.	n.d.	n.d.
n.d.	n.d.	n.d.	n.d.	n.d.	n.d.	n.d.	n.d.	n.d.	n.d.	n.d.
n.d.	n.d.	n.d.	n.d.	n.d.	n.d.	n.d.	n.d.	n.d.	n.d.	n.d.
n.d.	n.d.	n.d.	n.d.	n.d.	n.d.	n.d.	n.d.	n.d.	n.d.	n.d.
n.d.	n.d.	n.d.	n.d.	n.d.	n.d.	n.d.	n.d.	n.d.	n.d.	n.d.
n.d.	n.d.	n.d.	n.d.	n.d.	n.d.	n.d.	n.d.	n.d.	n.d.	n.d.
n.d.	n.d.	n.d.	n.d.	n.d.	n.d.	n.d.	n.d.	n.d.	n.d.	n.d.
n.d.	n.d.	n.d.	n.d.	n.d.	n.d.	n.d.	n.d.	n.d.	n.d.	n.d.
n.d.	n.d.	n.d.	n.d.	n.d.	n.d.	n.d.	n.d.	n.d.	n.d.	n.d.
n.d.	n.d.	n.d.	n.d.	n.d.	n.d.	n.d.	n.d.	n.d.	n.d.	n.d.
n.d.	n.d.	n.d.	n.d.	n.d.	n.d.	n.d.	n.d.	n.d.	n.d.	n.d.
n.d.	n.d.	n.d.	n.d.	n.d.	n.d.	n.d.	n.d.	n.d.	n.d.	n.d.
n.d.	n.d.	n.d.	n.d.	n.d.	n.d.	n.d.	n.d.	n.d.	n.d.	n.d.
n.d.	n.d.	n.d.	n.d.	n.d.	n.d.	n.d.	n.d.	n.d.	n.d.	n.d.

	OKC6/OKC8									
	Type 4b fluorite from fluorite rich rock									
	Ca	Na	Sr	Ba	Y	La	Ce	Pr	Nd	Sm
point 1	495326	n.d.	3011	n.d.	n.d.	n.d.	n.d.	n.d.	n.d.	n.d.
point 2	508020	n.d.	3659	n.d.	n.d.	n.d.	25	n.d.	n.d.	n.d.
point 3	512393	n.d.	2640	n.d.	29	49	63	n.d.	n.d.	n.d.
point 4	496761	n.d.	2993	n.d.	n.d.	n.d.	n.d.	n.d.	n.d.	n.d.
point 5	498795	n.d.	4359	n.d.	n.d.	n.d.	n.d.	n.d.	n.d.	n.d.
point 6	497617	n.d.	4037	n.d.	n.d.	n.d.	24	n.d.	n.d.	n.d.
point 7	493449	n.d.	2778	n.d.	n.d.	36	48	n.d.	n.d.	n.d.
point 8	494507	n.d.	2693	n.d.	n.d.	n.d.	n.d.	n.d.	n.d.	n.d.
point 9	494873	n.d.	4620	n.d.	n.d.	n.d.	n.d.	n.d.	n.d.	n.d.
point 10	496706	n.d.	6206	n.d.	n.d.	n.d.	29	n.d.	n.d.	n.d.
point 11	496018	n.d.	2858	n.d.	n.d.	n.d.	29	5	n.d.	n.d.
point 12	495427	n.d.	3439	n.d.	n.d.	n.d.	n.d.	n.d.	n.d.	n.d.
point 13	494168	n.d.	2539	n.d.	47	n.d.	22	n.d.	n.d.	n.d.
point 14	498463	n.d.	2593	n.d.	n.d.	54	79	29	18	n.d.
point 15	498463	n.d.	1710	n.d.	n.d.	59	93	5	25	n.d.
point 16	502892	n.d.	3224	n.d.	14	n.d.	n.d.	n.d.	n.d.	n.d.
point 17	503384	n.d.	3550	n.d.	19	n.d.	n.d.	n.d.	n.d.	n.d.

point 18	503679	n.d.	2525	n.d.	n.d.	n.d.	n.d.	n.d.	n.d.	n.d.
point 19	504251	n.d.	1879	n.d.	n.d.	n.d.	n.d.	n.d.	n.d.	n.d.
point 20	506026	n.d.	2087	n.d.	22	30	n.d.	n.d.	n.d.	n.d.
point 21	501594	n.d.	2706	n.d.	36	12	37	4	n.d.	n.d.
point 22	506617	n.d.	2290	n.d.	n.d.	15	31	5	n.d.	n.d.
point 23	506122	n.d.	2687	n.d.	n.d.	n.d.	n.d.	n.d.	n.d.	n.d.
point 24	503725	n.d.	1195	n.d.	n.d.	n.d.	n.d.	n.d.	n.d.	n.d.
point 25	504223	n.d.	2552	n.d.	n.d.	n.d.	n.d.	n.d.	n.d.	n.d.
point 26	502769	n.d.	2018	n.d.	50	n.d.	n.d.	n.d.	n.d.	n.d.
point 27	502176	n.d.	3191	n.d.	17	n.d.	n.d.	n.d.	n.d.	n.d.
point 28	501793	n.d.	3611	n.d.	9	n.d.	34	3	n.d.	n.d.
point 29	501145	n.d.	3236	n.d.	n.d.	27	18	n.d.	n.d.	n.d.
point 30	503407	n.d.	3573	n.d.	n.d.	n.d.	13	n.d.	n.d.	n.d.
point 31	500012	n.d.	2971	n.d.	n.d.	n.d.	25	n.d.	n.d.	n.d.
point 32	503053	n.d.	2918	n.d.	n.d.	n.d.	22	n.d.	n.d.	n.d.
point 33	502393	n.d.	2023	n.d.	n.d.	n.d.	n.d.	n.d.	n.d.	n.d.
point 34	503629	n.d.	2345	n.d.	14	20	n.d.	n.d.	n.d.	n.d.
point 35	503672	n.d.	2170	n.d.	76	n.d.	n.d.	n.d.	n.d.	n.d.
point 36	503979	n.d.	1550	n.d.	n.d.	n.d.	n.d.	n.d.	n.d.	n.d.
point 37	505266	n.d.	2011	n.d.	11	n.d.	n.d.	n.d.	n.d.	n.d.

point 38	502196	n.d.	1014	n.d.	n.d.	n.d.	n.d.	n.d.	n.d.	n.d.
point 39	503591	n.d.	3409	n.d.	n.d.	17	17	n.d.	n.d.	n.d.
point 40	503718	n.d.	3076	n.d.	n.d.	27	16	n.d.	n.d.	n.d.
point 41	500622	n.d.	565	n.d.	266	n.d.	17	n.d.	n.d.	n.d.
point 42	496415	n.d.	762	n.d.	280	n.d.	n.d.	n.d.	46	n.d.
point 43	499895	n.d.	714	n.d.	260	n.d.	22	n.d.	37	n.d.
point 44	500484	n.d.	616	n.d.	294	n.d.	29	n.d.	n.d.	n.d.
point 45	493872	n.d.	499	n.d.	262	n.d.	n.d.	n.d.	n.d.	n.d.
point 46	498051	n.d.	502	n.d.	295	n.d.	n.d.	n.d.	n.d.	n.d.
point 47	500240	n.d.	608	n.d.	273	n.d.	32	n.d.	n.d.	n.d.
point 48	498688	n.d.	621	n.d.	228	26	49	n.d.	50	n.d.
point 49	497588	n.d.	609	n.d.	220	36	114	n.d.	36	n.d.
point 50	501124	n.d.	619	n.d.	286	n.d.	17	n.d.	n.d.	n.d.
point 51	501200	n.d.	1636	n.d.	9	50	48	n.d.	n.d.	n.d.
point 52	499129	n.d.	1583	n.d.	8	23	47	n.d.	n.d.	n.d.
point 53	497955	n.d.	1609	n.d.	241	43	71	4	n.d.	n.d.
point 54	500362	n.d.	634	n.d.	272	n.d.	n.d.	n.d.	n.d.	n.d.
point 55	500596	n.d.	589	n.d.	286	n.d.	26	5	n.d.	n.d.
point 56	500620	n.d.	453	n.d.	282	n.d.	15	n.d.	n.d.	n.d.
point 57	497992	n.d.	714	n.d.	229	n.d.	n.d.	7	n.d.	n.d.

point 58	501974	n.d.	318	n.d.	196	n.d.	n.d.	n.d.	n.d.	n.d.
point 59	500601	n.d.	367	n.d.	152	n.d.	n.d.	5	n.d.	n.d.
point 60	496989	n.d.	482	n.d.	n.d.	n.d.	n.d.	n.d.	n.d.	n.d.
point 61	496244	n.d.	664	n.d.	n.d.	n.d.	18	n.d.	n.d.	n.d.
point 62	497827	n.d.	507	n.d.	n.d.	n.d.	45	n.d.	26	n.d.
point 63	495833	n.d.	1010	n.d.	215	27	40	8	24	n.d.
point 64	491755	n.d.	1141	n.d.	191	27	55	6	18	n.d.
point 65	495121	n.d.	1336	n.d.	87	24	66	6	n.d.	n.d.
point 66	499268	n.d.	1519	n.d.	73	51	28	n.d.	n.d.	n.d.
point 67	497986	n.d.	1500	n.d.	64	52	38	n.d.	n.d.	n.d.
point 68	494106	n.d.	1292	n.d.	68	36	48	7	n.d.	n.d.
point 69	495193	n.d.	1666	n.d.	n.d.	62	66	3	n.d.	n.d.
point 70	501386	n.d.	1727	n.d.	n.d.	40	44	7	n.d.	n.d.
point 71	498050	n.d.	772	n.d.	7	25	24	5	16	n.d.
point 72	495551	n.d.	1428	n.d.	9	40	62	4	39	n.d.
point 73	495690	n.d.	1420	n.d.	76	20	113	7	86	n.d.
point 74	498210	n.d.	1766	n.d.	72	52	51	5	n.d.	n.d.
average	499904	n.d.	1976	n.d.	135	35	41	7	n.d.	n.d.
stdev	3885		1217							

OKC6/OKC8										
Type 4b fluorite from fluorite rich rock										
Eu	Gd	Tb	Dy	Ho	Er	Tm	Yb	Lu	Th	U
n.d.	n.d.	n.d.	n.d.	n.d.	n.d.	n.d.	n.d.	n.d.	n.d.	n.d.
n.d.	n.d.	n.d.	n.d.	n.d.	n.d.	n.d.	n.d.	n.d.	n.d.	n.d.
n.d.	n.d.	n.d.	n.d.	n.d.	n.d.	n.d.	n.d.	n.d.	n.d.	n.d.
n.d.	n.d.	n.d.	n.d.	n.d.	n.d.	n.d.	n.d.	n.d.	n.d.	n.d.
n.d.	n.d.	n.d.	n.d.	n.d.	n.d.	n.d.	n.d.	n.d.	n.d.	n.d.
n.d.	n.d.	n.d.	n.d.	n.d.	n.d.	n.d.	n.d.	n.d.	n.d.	n.d.
n.d.	n.d.	n.d.	n.d.	n.d.	n.d.	n.d.	n.d.	n.d.	n.d.	n.d.
n.d.	n.d.	n.d.	n.d.	n.d.	n.d.	n.d.	n.d.	n.d.	n.d.	n.d.
n.d.	n.d.	n.d.	n.d.	n.d.	n.d.	n.d.	n.d.	n.d.	n.d.	n.d.
n.d.	n.d.	n.d.	n.d.	n.d.	n.d.	n.d.	n.d.	n.d.	n.d.	n.d.
n.d.	n.d.	n.d.	n.d.	n.d.	n.d.	n.d.	n.d.	n.d.	n.d.	n.d.
n.d.	n.d.	n.d.	n.d.	n.d.	n.d.	n.d.	n.d.	n.d.	n.d.	n.d.
n.d.	n.d.	n.d.	n.d.	n.d.	n.d.	n.d.	n.d.	n.d.	n.d.	n.d.
n.d.	n.d.	n.d.	n.d.	n.d.	n.d.	n.d.	n.d.	n.d.	n.d.	n.d.
n.d.	n.d.	n.d.	n.d.	n.d.	n.d.	n.d.	n.d.	n.d.	n.d.	n.d.
n.d.	n.d.	n.d.	n.d.	n.d.	n.d.	n.d.	n.d.	n.d.	n.d.	n.d.
n.d.	n.d.	n.d.	n.d.	n.d.	n.d.	n.d.	n.d.	n.d.	n.d.	n.d.

n.d.	n.d.	n.d.	n.d.	n.d.	n.d.	n.d.	n.d.	n.d.	n.d.	n.d.
n.d.	n.d.	n.d.	n.d.	n.d.	n.d.	n.d.	n.d.	n.d.	n.d.	n.d.
n.d.	n.d.	n.d.	n.d.	n.d.	n.d.	n.d.	n.d.	n.d.	n.d.	n.d.
n.d.	n.d.	n.d.	n.d.	n.d.	n.d.	n.d.	n.d.	n.d.	n.d.	n.d.
n.d.	n.d.	n.d.	n.d.	n.d.	n.d.	n.d.	n.d.	n.d.	n.d.	n.d.
n.d.	n.d.	n.d.	n.d.	n.d.	n.d.	n.d.	n.d.	n.d.	n.d.	n.d.
n.d.	n.d.	n.d.	n.d.	n.d.	n.d.	n.d.	n.d.	n.d.	n.d.	n.d.
n.d.	n.d.	n.d.	n.d.	n.d.	n.d.	n.d.	n.d.	n.d.	n.d.	n.d.
n.d.	n.d.	n.d.	n.d.	n.d.	n.d.	n.d.	n.d.	n.d.	n.d.	n.d.
n.d.	n.d.	n.d.	n.d.	n.d.	n.d.	n.d.	n.d.	n.d.	n.d.	n.d.
n.d.	n.d.	n.d.	n.d.	n.d.	n.d.	n.d.	n.d.	n.d.	n.d.	n.d.
n.d.	n.d.	n.d.	n.d.	n.d.	n.d.	n.d.	n.d.	n.d.	n.d.	n.d.
n.d.	n.d.	n.d.	n.d.	n.d.	n.d.	n.d.	n.d.	n.d.	n.d.	n.d.
n.d.	n.d.	n.d.	n.d.	n.d.	n.d.	n.d.	n.d.	n.d.	n.d.	n.d.
n.d.	n.d.	n.d.	n.d.	n.d.	n.d.	n.d.	n.d.	n.d.	n.d.	n.d.
n.d.	n.d.	n.d.	n.d.	n.d.	n.d.	n.d.	n.d.	n.d.	n.d.	n.d.
n.d.	n.d.	n.d.	n.d.	n.d.	n.d.	n.d.	n.d.	n.d.	n.d.	n.d.
n.d.	n.d.	n.d.	n.d.	n.d.	n.d.	n.d.	n.d.	n.d.	n.d.	n.d.
n.d.	n.d.	n.d.	n.d.	n.d.	n.d.	n.d.	n.d.	n.d.	n.d.	n.d.
n.d.	n.d.	n.d.	n.d.	n.d.	n.d.	n.d.	n.d.	n.d.	n.d.	n.d.
n.d.	n.d.	n.d.	n.d.	n.d.	n.d.	n.d.	n.d.	n.d.	n.d.	n.d.

n.d.	n.d.	n.d.	n.d.	n.d.	n.d.	n.d.	n.d.	n.d.	n.d.	n.d.
n.d.	n.d.	n.d.	n.d.	n.d.	n.d.	n.d.	n.d.	n.d.	n.d.	n.d.
n.d.	n.d.	n.d.	n.d.	n.d.	n.d.	n.d.	n.d.	n.d.	n.d.	n.d.
n.d.	n.d.	n.d.	n.d.	n.d.	n.d.	n.d.	n.d.	n.d.	n.d.	n.d.
n.d.	n.d.	n.d.	n.d.	n.d.	n.d.	n.d.	n.d.	n.d.	n.d.	n.d.
n.d.	n.d.	n.d.	n.d.	n.d.	n.d.	n.d.	n.d.	n.d.	n.d.	n.d.
n.d.	n.d.	n.d.	n.d.	n.d.	n.d.	n.d.	n.d.	n.d.	n.d.	n.d.
n.d.	n.d.	n.d.	n.d.	n.d.	n.d.	n.d.	n.d.	n.d.	n.d.	n.d.
n.d.	n.d.	n.d.	n.d.	n.d.	n.d.	n.d.	n.d.	n.d.	n.d.	n.d.
n.d.	n.d.	n.d.	n.d.	n.d.	n.d.	n.d.	n.d.	n.d.	n.d.	n.d.
n.d.	n.d.	n.d.	n.d.	n.d.	n.d.	n.d.	n.d.	n.d.	n.d.	n.d.
n.d.	n.d.	n.d.	n.d.	n.d.	n.d.	n.d.	n.d.	n.d.	n.d.	n.d.
n.d.	n.d.	n.d.	n.d.	n.d.	n.d.	n.d.	n.d.	n.d.	n.d.	n.d.
n.d.	n.d.	n.d.	n.d.	n.d.	n.d.	n.d.	n.d.	n.d.	n.d.	n.d.
n.d.	n.d.	n.d.	n.d.	n.d.	n.d.	n.d.	n.d.	n.d.	n.d.	n.d.
n.d.	n.d.	n.d.	n.d.	n.d.	n.d.	n.d.	n.d.	n.d.	n.d.	n.d.
n.d.	n.d.	n.d.	n.d.	n.d.	n.d.	n.d.	n.d.	n.d.	n.d.	n.d.
n.d.	n.d.	n.d.	n.d.	n.d.	n.d.	n.d.	n.d.	n.d.	n.d.	n.d.
n.d.	n.d.	n.d.	n.d.	n.d.	n.d.	n.d.	n.d.	n.d.	n.d.	n.d.
n.d.	n.d.	n.d.	n.d.	n.d.	n.d.	n.d.	n.d.	n.d.	n.d.	n.d.
n.d.	n.d.	n.d.	n.d.	n.d.	n.d.	n.d.	n.d.	n.d.	n.d.	n.d.

n.d.	n.d.	n.d.	n.d.	n.d.	n.d.	n.d.	n.d.	n.d.	n.d.	n.d.
n.d.	n.d.	n.d.	n.d.	n.d.	n.d.	n.d.	n.d.	n.d.	n.d.	n.d.
n.d.	n.d.	n.d.	n.d.	n.d.	n.d.	n.d.	n.d.	n.d.	n.d.	n.d.
n.d.	n.d.	n.d.	n.d.	n.d.	n.d.	n.d.	n.d.	n.d.	n.d.	n.d.
n.d.	n.d.	n.d.	n.d.	n.d.	n.d.	n.d.	n.d.	n.d.	n.d.	n.d.
n.d.	n.d.	n.d.	n.d.	n.d.	n.d.	n.d.	n.d.	n.d.	n.d.	n.d.
n.d.	n.d.	n.d.	n.d.	n.d.	n.d.	n.d.	n.d.	n.d.	n.d.	n.d.
n.d.	n.d.	n.d.	n.d.	n.d.	n.d.	n.d.	n.d.	n.d.	n.d.	n.d.
n.d.	n.d.	n.d.	n.d.	n.d.	n.d.	n.d.	n.d.	n.d.	n.d.	n.d.
n.d.	n.d.	n.d.	n.d.	n.d.	n.d.	n.d.	n.d.	n.d.	n.d.	n.d.
n.d.	n.d.	n.d.	n.d.	n.d.	n.d.	n.d.	n.d.	n.d.	n.d.	n.d.
n.d.	n.d.	n.d.	n.d.	n.d.	n.d.	n.d.	n.d.	n.d.	n.d.	n.d.
n.d.	n.d.	n.d.	n.d.	n.d.	n.d.	n.d.	n.d.	n.d.	n.d.	n.d.
n.d.	n.d.	n.d.	n.d.	n.d.	n.d.	n.d.	n.d.	n.d.	n.d.	n.d.
n.d.	n.d.	n.d.	n.d.	n.d.	n.d.	n.d.	n.d.	n.d.	n.d.	n.d.
n.d.	n.d.	n.d.	n.d.	n.d.	n.d.	n.d.	n.d.	n.d.	n.d.	n.d.
n.d.	n.d.	n.d.	n.d.	n.d.	n.d.	n.d.	n.d.	n.d.	n.d.	n.d.
n.d.	n.d.	n.d.	n.d.	n.d.	n.d.	n.d.	n.d.	n.d.	n.d.	n.d.

OKC8							
Type 4b fluorite from fluorite rich rock							
	Ca	Na	Sr	Ba	Y	La	Ce
point 1	496341	n.d.	2035	n.d.	333	129	129
point 2	494445	n.d.	1974	n.d.	318	n.d.	44
point 3	491622	n.d.	570	n.d.	50	12	35
point 4	493302	n.d.	1650	n.d.	38	n.d.	n.d.
point 5	495591	n.d.	1606	n.d.	37	15	16
point 6	494310	n.d.	2644	n.d.	27	16	n.d.
point 7	496096	n.d.	3874	n.d.	122	n.d.	23
point 8	498782	n.d.	1750	n.d.	184	n.d.	n.d.
point 9	494616	n.d.	1590	n.d.	29	n.d.	n.d.
point 10	496983	n.d.	1936	n.d.	634	50	36
point 11	500578	n.d.	2673	n.d.	89	51	54
point 12	499822	n.d.	2637	n.d.	120	n.d.	58
point 13	498238	n.d.	1042	n.d.	61	21	50
point 14	501445	n.d.	2428	n.d.	105	55	23
point 15	500196	n.d.	613	n.d.	25	49	67
average	496824		1935		145		
stdev	2832		829		162		

Representative bulk rock analyses of the Okorusu fluorite-rich rocks. Only one fluorite type is present in each sample (stage 4 alteration).

	OKC7 (Type 4a)	OKC3 (Type 4a)	OKC8 (Type 4a)	OKC10 (Type 4b)	OKC8 (Type 4b)	OKC7 (Type 4b)
	Major elements (wt%)					
SiO2	12.94	14.04	10.02	0.21	1.02	0.20
Al2O3	0.33	0.46	0.54	0.02	0.08	< 0.01
Fe2O3(T)	1.56	0.73	1.12	0.04	0.18	0.04
MnO	0.03	0.05	0.02	< 0.01	0.04	< 0.01
MgO	0.03	0.67	0.03	< 0.01	0.11	0.01
CaO	57.73	58.37	59.61	71.71	64.75	70.52
Na2O	0.02	0.02	0.02	< 0.01	< 0.01	< 0.01
K2O	0.13	0.23	0.29	< 0.01	0.03	< 0.01
TiO2	0.02	0.02	0.02	< 0.02	< 0.01	< 0.01
P2O5	0.29	0.07	0.14	0.02	0.03	0.04
LOI	3.88	3.79	3.58	0.18	15.00	0.28
Total	**76.96**	**78.42**	**75.39**	**72.19**	**81.25**	**71.10**
	Trace elements (ppm)					
Ba	8835	78	8693	7	2431	25
Sr	1570	1578	1000	1494	1036	2090
Th	12	14	33	9	6	3
V	73	35	34	5	11	< 5
Cr	30	< 20	30	< 20	< 20	< 20
Ni	20	< 20	40	< 20	< 20	< 20
Cu	20	20	20	< 10	10	< 10

La	197	46	322	30	61	43
Ce	247	53	481	49	90	64
Pr	19	4	41	5	8	6
Nd	49	9	117	16	23	17
Sm	6	1	18	3	4	3
Eu	2	< 1	6	1	2	1
Gd	4	1	17	4	5	3
Tb	1	< 1	3	1	1	1
Dy	4	1	19	5	6	4
Ho	1	< 1	4	1	1	1
Er	2	1	11	4	4	3
Tm	0	< 1	2	1	1	< 1
Yb	2	1	10	5	4	3
Lu	< 1	< 1	1	1	1	< 1
Y	28	13	154	35	52	26
∑LREE	517	113	979	104	186	132
∑HREE	44	17	226	58	75	40

Appendix 4: Chapter 4 SIMS standards reproducibility

Date	Time	No	Y	X	PB(Start)	PB(end)	non correcte d δ18O	δ18O
session 1	QUARTZ						(‰)	(‰)
17/11/2018	17:31:00	std-qz-@1.asc	-1744	4824	6.38E-09	4.45E-09	1.23E+01	12.10
17/11/2018	17:34:00	std-qz-@2.asc	-1744	4782	4.47E-09	4.45E-09	1.24E+01	12.18
17/11/2018	17:38:00	std-qz-@3.asc	-1744	4744	4.47E-09	4.49E-09	1.24E+01	12.20
17/11/2018	17:42:00	std-qz-@4.asc	-1744	4702	4.49E-09	4.46E-09	1.26E+01	12.35
17/11/2018	17:46:00	std-qz-@5.asc	-1744	4664	4.47E-09	4.44E-09	1.24E+01	12.19
17/11/2018	19:12:00	std-qz-@10.asc	-1824	4666	4.33E-09	4.33E-09	1.23E+01	12.17
17/11/2018	18:57:00	std-qz-@6.asc	-1824	4826	4.31E-09	4.32E-09	1.22E+01	12.10
17/11/2018	19:00:00	std-qz-@7.asc	-1824	4784	4.31E-09	4.32E-09	1.20E+01	11.83
17/11/2018	19:04:00	std-qz-@8.asc	-1824	4746	4.31E-09	4.30E-09	1.22E+01	12.04
17/11/2018	19:08:00	std-qz-@9.asc	-1824	4704	4.32E-09	4.31E-09	1.22E+01	12.12

17/11/2018	20:10:00	std-qz-@11.asc	-18644	4826	4.27E-09	4.27E-09	1.23E+01	12.30
17/11/2018	20:13:00	std-qz-@12.asc	-18644	4786	4.27E-09	4.29E-09	1.24E+01	12.36
17/11/2018	20:17:00	std-qz-@13.asc	-18644	4746	4.29E-09	4.29E-09	1.25E+01	12.49
17/11/2018	20:21:00	std-qz-@14.asc	-18644	4706	4.29E-09	4.32E-09	1.26E+01	12.54
17/11/2018	20:25:00	std-qz-@15.asc	-18644	4666	4.32E-09	4.31E-09	1.26E+01	12.58
17/11/2018	21:20:00	std-qz-@16.asc	-19044	4828	4.21E-09	4.23E-09	1.18E+01	11.86
17/11/2018	21:24:00	std-qz-@17.asc	-19044	4786	4.22E-09	4.22E-09	1.20E+01	12.09
17/11/2018	21:28:00	std-qz-@18.asc	-19044	4748	4.24E-09	4.22E-09	1.22E+01	12.27
17/11/2018	21:32:00	std-qz-@19.asc	-19044	4704	4.21E-09	4.22E-09	1.21E+01	12.16
17/11/2018	21:35:00	std-qz-@20.asc	-19044	4666	4.21E-09	4.20E-09	1.21E+01	12.19
17/11/2018	22:30:00	std-qz-@21.asc	-19444	4828	4.14E-09	4.15E-09	1.21E+01	12.28
17/11/2018	22:34:00	std-qz-@22.asc	-19444	4788	4.14E-09	4.14E-09	1.20E+01	12.12

17/11/2018	22:38:00	std-qz-@23.asc	-1944	4748	4.15E-09	4.13E-09	1.21E+01	12.26
17/11/2018	22:41:00	std-qz-@24.asc	-1944	4708	4.14E-09	4.14E-09	1.21E+01	12.24
17/11/2018	22:45:00	std-qz-@25.asc	-1944	4668	4.14E-09	4.13E-09	1.20E+01	12.13
17/11/2018	23:37:00	std-qz-@26.asc	-2011	4826	4.08E-09	4.06E-09	1.19E+01	12.12
17/11/2018	23:41:00	std-qz-@27.asc	-2011	4786	4.07E-09	4.08E-09	1.19E+01	12.10
17/11/2018	23:45:00	std-qz-@28.asc	-2011	4746	4.06E-09	4.06E-09	1.21E+01	12.33
17/11/2018	23:48:00	std-qz-@29.asc	-2011	4706	4.07E-09	4.06E-09	1.18E+01	12.10
						Avg	*12.20*	*12.20*
						Stdev	*0.23*	*0.17*

Date	Time	No	Y	X	PB(Start)	PB(end)	non corrected d18O	δ18O
session 1	CALCITE						(‰)	(‰)
16/11/2018	15:41:00	calcite-standard-1	2203	6092	4.75E-09	4.73E-09	23.04	23.17
16/11/2018	15:45:00	calcite-standard-1@1	2168	6094	4.72E-09	4.69E-09	23.07	23.20
16/11/2018	15:49:00	calcite-standard-1@2	2133	6092	4.71E-09	4.67E-09	23.08	23.20
16/11/2018	15:52:00	calcite-standard-1@3	2133	6058	4.67E-09	4.65E-09	23.15	23.27
16/11/2018	15:56:00	calcite-standard-1@4	2168	6058	4.67E-09	4.65E-09	23.25	23.36
16/11/2018	17:08:00	calcite-standard-6	2064	6010	4.50E-09	4.49E-09	23.39	23.40
16/11/2018	17:12:00	calcite-standard-6@1	2099	6012	4.49E-09	4.50E-09	23.41	23.41
16/11/2018	17:15:00	calcite-standard-6@2	2134	6010	4.50E-09	4.51E-09	23.55	23.54
16/11/2018	17:19:00	calcite-standard-6@3	2169	6012	4.50E-09	4.51E-09	23.36	23.35
16/11/2018	17:23:00	calcite-standard-6@4	2169	5976	4.51E-09	4.47E-09	23.40	23.38
16/11/2018	18:26:00	calcite-standard-10@1	2078	6084	4.48E-09	4.48E-09	23.56	23.43

16/11/2018	18:30:00	calcite-standard-10@2	2078	6048	4.49E-09	4.47E-09	23.46	23.32
16/11/2018	18:34:00	calcite-standard-10@3	2043	6048	4.47E-09	4.47E-09	23.22	23.07
16/11/2018	18:37:00	calcite-standard-10@4	2043	6082	4.47E-09	4.47E-09	23.25	23.09
						Avg	*23.30*	*23.30*
						Stdev	*0.17*	*0.14*

Appendix 5: Chapter 4 boulder waste bulk rock analyses

Dashigou bulk rock analyses of samples collected from a boulder waste few km north of the Dashigou open pit. ND 001f is a fenetised country rock in contact with a calcite carbonatite dyke. LREE= La to Sm, HREE= Eu to Lu + Y. Ge, Sb, Ag, In, TI and Ta are under 3 ppm; As, Be, Sn, Cs and Hf are under 10 ppm

	Nd 430-1	Nd 430-2	Nd 430-3	Nd 001f
	Major elements (wt%)			
Total S	0.55	0.26	0.14	2.02
SiO2	0.85	9.43	7.87	51.39
Al2O3	0.19	2.23	2.09	13.10
Fe2O3(T)	0.83	2.27	1.33	10.47
MnO	1.83	1.52	1.59	0.14
MgO	0.48	3.63	1.35	3.16
CaO	49.88	42.39	46.09	3.59
Na2O	0.02	0.03	0.04	1.50
K2O	0.14	1.96	1.76	8.96
TiO2	0.02	0.25	0.12	1.82
P2O5	0.06	0.46	0.08	0.66
LOI	40.10	33.50	36.60	3.87
Total	94.40	97.68	98.92	98.67
	Trace element (ppm)			
Sc	4	6	4	19
V	< 5	73	22	158
Ba	18730	400	326	1113
Sr	6592	4818	5115	612
Zr	6	85	50	345
Cr	< 20	20	< 20	80
Co	< 1	< 1	< 1	22
Ni	< 20	< 20	< 20	30

Cu	10	< 10	< 10	< 10
Zn	< 30	180	70	260
Ga	3	72	26	38
Rb	< 2	87	46	170
Nb	36	82	32	36
Mo	> 100	46	>100	5
La	493	> 2000	343	603
Ce	815	> 3000	690	981
Pr	77.6	421	74.5	89.5
Nd	275	1190	282	275
Sm	50.1	132	62.6	32
Eu	14.8	27.1	17.1	7.01
Gd	48.4	78.6	62.5	18.5
Tb	7.4	10.6	9.6	2.3
Dy	43.9	57.6	59	12.5
Ho	9.4	11.3	12.1	2.2
Er	29.9	36.1	37.9	6.5
Tm	4.94	5.6	6.21	0.84
Yb	36	38.4	43	5.1
Lu	5.63	6.15	6.71	0.72
Y	395	351	381	59
Pb	654	94	92	143
Bi	4.1	< 0.4	< 0.4	< 0.4
Th	7.7	69.1	5.2	16.1
U	31.6	40.6	18.5	6.6
∑LREE	1710.7	1743.0	1452.1	1980.5
∑HREE	595.4	622.5	635.1	114.7
∑LREE/HREE	2.9	2.8	2.3	17.3

Appendix 6: Chapter 4 fluid inclusions analyses

Chapter 4 Raman spectroscopy and microthermometry analyses of fluid inclusions hosted in quartz.

Cacite carbonatite sample	Quartz type	Fluid inclusion No	Fluid inclusion type	Raman spectroscopy						Microthermometry	
				Anion detected in solution	Solid identification	CO2	N2	Gas trace <1% (H2S, CH4, H2)	ThCO2 in °C (to the liquid phase)	ThTOT in °C
DSG 002	Qz-2	4-1	LCO2+VCO2+Lw+S	SO4	arcanite	97	3	-	29.8	-
DSG 002	Qz-2	4-2	LCO2+Lw	SO4	-	99	1	-	17.9	-
DSG 002	Qz-2	4-3	LCO2+VCO2+Lw	SO4	-	-	-	-	29.8	-
DSG 002	Qz-2	4	solid inclusion	-	anhydrite	-	-	-	-	-
DSG 002	Qz-2	12-a	Lw+2S	-	dolomite, molybdenite	-	-	-	-	-
DSG 002	Qz-2	12-c	LCO2+VCO2+Lw+S	SO4	n.i.	-	-	-	28.0	-
DSG 002	Qz-2	12-x	LCO2+Lw	SO4	-	98	2	-	12.0	-
DSG 002	Qz-2	12	solid inclusion	-	calcite	-	-	-	-	-
DSG 002	Qz-2	13-a1	LCO2+Lw+S	SO4	anhydrite	95	5	-	-	-

DSG 002	Qz-2	13a-2	LCO2+VCO2+Lw	SO4	-	100	-	-	15.0	-
DSG 002	Qz-2	13c-1	LCO2+VCO2+Lw	SO4	-	91	9	-	-	-
DSG 002	Qz-2	13c-2	LCO2+VCO2+Lw	SO4	-	-	-	-	-	-
DSG 002	Qz-2	13	solid inclusion	-	anhydrite	-	-	-	-	-
DSG 002	Qz-2	14a	Lw+2s	n.d.	anhydrite, n.i. sulfate	-	-	-	-	-
DSG 002	Qz-2	14-b1	Lw+S	-	calcite	-	-	-	-	-
DSG 002	Qz-2	14b-2	LCO2+VCO2+Lw+S	SO4	calcite	-	-	-	-	-
DSG 002	Qz-2	14b-3	LCO2+Lw	n.d.	-	94	6	-	-	-
DSG 002	Qz-2	15a	LCO2+Lw+S	-	anhydrite	95	5	-	-	-
DSG 002	Qz-2	15a-2	LCO2+Lw+S	SO4	-	-	-	-	-	-
DSG 002	Qz-2	15b	Lw+2S	SO4	n.i.	-	-	-	-	-
DSG 002	Qz-2	15b-2	LCO2+Lw	SO4	-	-	-	-	-	-
DSG 002	Qz-2	15c	LCO2+VCO2+Lw+S	SO4	whewellite	-	-	-	26.0	-
DSG 002	Qz-2	15c-2	LCO2+VCO2+Lw	SO4	-	-	-	-	25.8	-
DSG 002	Qz-2	15f	Lw+3S	n.d.	anhydrite	-	-	-	-	-
DSG 002	Qz-2	15f-2	LCO2+VCO2+Lw	SO4	-	-	-	-	-	-
DSG 002	Qz-2	15	solid inclusion 1	-	anhydrite	-	-	-	-	-

DSG 002	Qz-2	15	solid inclusion 2	-	anhydrite	-	-	-	-	-
DSG 002	Qz-2	3-b	LCO2+VCO2+Lw	-	-	-	-	-	30.1	-
DSG 002	Qz-2	8b-2	LCO2+VCO2+Lw	n.d.	-	-	-	-	-	-
DSG 002	Qz-2	8b-3	LCO2+VCO2+Lw	SO4	-	-	-	-	29.8	-
DSG 002	Qz-2	8b-4	LCO2+VCO2+Lw	n.d.	-	-	-	-	-	-
DSG 002	Qz-2	8-b1	Lw+S	-	n.i. phosphate	-	-	-	-	-
DSG 002	Qz-2	9-1	LCO2+Lw	SO4	-	99	1	-	-	-
DSG 002	Qz-2	9-2	LCO2+Lw+S	-	calcite	-	-	-	-	-
DSG 002	Qz-2	10-a1	LCO2+VCO2+Lw+S	SO4	-	-	-	-	27.0	-
DSG 002	Qz-2	10-a2	LCO2+Lw	SO4	-	99	1	-	-	-
DSG 002	Qz-2	10-a3	LCO2+VCO2+Lw	SO4	-	-	-	-	26.9	-
DSG 002	Qz-2	10-c1	LCO2+VCO2+Lw+S	SO4	-	-	-	-	25.1	-
DSG 002	Qz-2	10-c2	LCO2+VCO2+Lw	SO4	-	-	-	-	26.7	-
DSG 002	Qz-2	10-c3	LCO2+Lw	SO4	-	99	1	-	24.6	-
DSG 002	Qz-2	10-d1	LCO2+Lw+S	SO4	whewellite	100	< 1	-	18.0	-
DSG 002	Qz-2	10-d2	LCO2+Lw+S	SO4	-	-	-	-	-	-
DSG 002	Qz-2	11-a1	LCO2+VCO2+Lw+S	SO4	calcite	-	-	-	27.0	-

DSG 002	Qz-2	11-a2	LCO2+VCO2+Lw+S	SO4	arcanite	-	-	-	-	-
DSG 002	Qz-2	11-a3	LCO2+VCO2+Lw	SO4	-	-	-	-	-	-
DSG 002	Qz-2	11-a4	Lw	SO4	-	-	-	-	-	-
DSG 437	Qz-2	25-a	LCO2+Lw+2S	SO4	celestine, glauberite	100	< 1	-	-	-
DSG 437	Qz-2	25-a2	LCO2+VCO2+Lw+S	SO4	celestine, calcite	-	-	-	-	-
DSG 437	Qz-2	25-b	Lw+3S	SO4	calcite, anhydrite, n.i. opaque	-	-	-	-	-
DSG 437	Qz-2	25-b2	LCO2+Lw+2S	SO4	arcanite	99	1	-	-	-
DSG 437	Qz-2	3-a	LCO2+Lw+S	SO4	celestine/glauberite	97	3	-	23.6	-
DSG 437	Qz-2	3-b	LCO2+VCO2+Lw+2	SO4	n.i. sulfate	-	-	-	28.3	-
DSG 437	Qz-2	3-b2	LCO2+VCO2+Lw+3 S	SO4	celestine, glauberite, n.i. opaque	-	-	-	-	-
DSG 437	Qz-2	3-b3	LCO2+Lw	SO4	-	-	-	-	27.3	-
DSG 437	Qz-2	3-b4	LCO2+VCO2+Lw+1	SO4	arcanite	-	-	-	26.8	-
DSG 437	Qz-2	5-1	LCO2+Lw	n.d.	-	98	2	-		-
DSG 437	Qz-2	5-2	LCO2+Lw	n.d.	-	-	-	-	-	-
DSG 437	Qz-2	5-3	LCO2+Lw	n.d.	-	-	-	-	-	-

DSG 437	Qz-2	7-a1	LCO2+VCO2+Lw+3 S	SO4	celestine/glauberite, n.i. sulfate, n.i. opaque	-	-	-	-	-
DSG 437	Qz-2	7-a2	LCO2+VCO2+Lw+S	SO4	-	-	-	-	-	-
DSG 437	Qz-2	7-b1	LCO2+VCO2+Lw+3	SO4	n.i.	-	-	-	-	-
DSG 437	Qz-2	7-b2	LCO2+VCO2+Lw+S	SO4	celestine/glauberite	99	1	-	-	-
DSG 437	Qz-2	7-b3	LCO2+VCO2+Lw	SO4	-	-	-	-	-	-
DSG 437	Qz-2	7-c	LCO2+Lw+S	SO4	celestine/glauberite	100	-	-	-	-
DSG 437	Qz-2	7-e2	LCO2+S	-	calcite	100	-	-	-	-
DSG 437	Qz-2	7-e3	LCO2+Lw	SO4	-	100	-	-	-	-
DSG 437	Qz-2	8b-1	LCO2+VCO2+Lw+2	SO4	celestine, n.i. opaque	100	-	-	-	-
DSG 437	Qz-2	8b-2	LCO2+VCO2+Lw	SO4	-	-	-	-	26.2	-
DSG 437	Qz-2	8b-3	LCO2+Lw	SO4	-	97	3	-	-	-
DSG 437	Qz-2	8-c	LCO2+VCO2+Lw	-	-	100	< 1	-	-	-
DSG 437	Qz-2	8-d1	LCO2+Lw	SO4	-	100	< 1	-	14.2	-
DSG 437	Qz-2	8-d3	LCO2+VCO2+Lw+S	SO4	-	100	-	-	23.2	-
DSG 437	Qz-2	8-i	LCO2+VCO2+Lw+2	SO4	glauberite, n.i. sulfate	-	-	-	-	-
DSG 437	Qz-2	8-i2	LCO2+VCO2+Lw+3s	SO4	celestine/glauberite, too small, n.i. sulfate	100	< 1	-	-	-

DSG 437	Qz-2	8-h	Lw+2S	-	celestine, glauberite	-	-	-	-	-
DSG 437	Qz-2	8-h2	Lw+1S	-	muscovite	-	-	-	-	-
DSG 437	Qz-2	8-jx	Lw+4S	-	thenardite, glauberite, celestine, n.i. opaque	-	-	-	-	-
DSG 437	Qz-2	8-k	LCO2+Lw+3s	-	celestine, glauberite, n.i. opaque, too small	-	-	-	-	-
DSG 437	Qz-2	8-k2	LCO2+Lw	SO4	-	99	1	-	-	-
DSG 437	Qz-2	8	solid inclusion	-	n.i. sulfate	-	-	-	-	-
DSG 437	Qz-2	31-a	LCO2+Lw+2s	n.d.	calcite, too small	100	-	-	-	-
DSG 437	Qz-2	31-e	LCO2+VCO2+Lw	SO4	-	-	-	-	30.6	-
DSG 437	Qz-2	16-c	LCO2+Lw	SO4	-	100	< 1	-	-	-
DSG 437	Qz-2	16-a	LCO2+Lw	SO4	-	100	-	-	-	-
DSG 437	Qz-2	17.2	LCO2+Lw	-	-	100	< 1	-	-	-
DSG 437	Qz-2	17-1	LCO2+Lw	-	-	100	< 1	-	-	-
DSG 437	Qz-2	11-a	LCO2+VCO2+Lw+S	SO4	anhydrite	-	-	-	-	-
DSG 437	Qz-2	27-b	LCO2+Lw	-	-	97	3	-	-	-
DSG 437	Qz-2	10-1	Lw	SO4	-	-	-	-	-	-
DSG 433	Qz-2	1-a1	LCO2+VCO2+Lw	SO4	-	-	-	-	-	-

270

DSG 433	Qz-2	1-a2	LCO2+VCO2+Lw	SO4	-	76	24	< 1	24.0	-
DSG 433	Qz-2	1-a3	LCO2+VCO2+Lw	SO4	-	-	-	-	-	-
DSG 433	Qz-2	1-c	LCO2+Lw+2S	SO4	n.i. , n.i. opaque	99	1	-	27.6	-
DSG 433	Qz-2	1	solid inclusion 1	-	calcite	-	-	-	-	-
DSG 433	Qz-2	1	solid inclusion 2	-	calcite	-	-	-	-	-
DSG 433	Qz-2	2-a	LCO2+Lw+3S	SO4	anhydrite, aphthitalite, n.i opaque	99	1	-	26.2	-
DSG 433	Qz-2	2-e	LCO2+Lw+3S	SO4	n.i.	100	< 1	-	-	-
DSG 433	Qz-2	2-b1	LCO2+VCO2+Lw	n.d.	-	-	-	-	24.1	-
DSG 433	Qz-2	2-b2	LCO2+VCO2+Lw	SO4	-	-	-	-	-	-
DSG 433	Qz-2	2-b3	LCO2+VCO2+Lw	SO4	-	-	-	-	25.9	-
DSG 433	Qz-2	2-f1	LCO2+Lw+3S	SO4	arcanite, n.i. sulfate, calcite	100	< 1	-	29.0	-
DSG 433	Qz-2	2-f2	LCO2+VCO2+Lw+3	SO4	n.i.	-	-	-	-	-
DSG 433	Qz-2	3-a1	LCO2+Lw	SO4	-	100	< 1	-	20.0	-
DSG 433	Qz-2	3-a2	LCO2+Lw	SO4	-	-	-	-	30.9	-
DSG 433	Qz-2	4-a	LCO2+VCO2+Lw	SO4	-	-	-	-	30.5	-
DSG 433	Qz-2	4-c1	LCO2+VCO2+Lw+S	SO4	-	99	1	-	23.8	-

271

DSG 433	Qz-2	4-c2	LCO2+VCO2+Lw+S	SO4	n.i.	-	-	-	-	-
DSG 433	Qz-2	4-c3	LCO2+VCO2+Lw+S	SO4	aphthitalite	-	-	-	-	-
DSG 433	Qz-2	4-d1	LCO2+VCO2+Lw+2	SO4	arcanite, n.i. sulfate	-	-	-	-	-
DSG 433	Qz-2	4-d2	LCO2+Lw	SO4	-	99	1	-	-	-
DSG 433	Qz-2	5-a1	LCO2+S	-	gypsum	-	-	-	-	-
DSG 433	Qz-2	5-a2	LCO2+Lw	SO4	-	100	< 1	-	-	-
DSG 433	Qz-2	5-b1	LCO2+VCO2+Lw+S	SO4	-	99	1	-	-	-
DSG 433	Qz-2	5-b2	LCO2+VCO2+Lw+S	SO4	n.i. opaque	-	-	-	-	-
DSG 433	Qz-2	5	solid inclusion	-	calcite	-	-	-	-	-
DSG 433	Qz-2	6a	LCO2+Lw+2S	SO4	aphthitalite, n.i. opaque, n.i.	82	18	< 1	-	-
DSG 433	Qz-2	6-c1	LCO2+VCO2+Lw	SO4	-	-	-	-	-	-
DSG 433	Qz-2	6-c2	LCO2+VCO2+Lw	SO4	-	-	-	-	-	-
DSG 433	Qz-2	6-c3	LCO2+Lw	SO4	-	99	1	-	-	-
DSG 433	Qz-2	9-a1	LCO2+Lw	SO4	-	99	1	-	-	-
DSG 433	Qz-2	9-a2	LCO2+VCO2+Lw	SO4	-	-	-	-	25.5	-
DSG 433	Qz-2	9-a3	LCO2+VCO2+Lw	SO4	-	-	-	-	25.5	-
DSG 433	Qz-2	9-a4	LCO2+Lw	SO4	-	100	1	-	-	-

DSG 433	Qz-2	9-a5	LCO2+Lw	n.d.	-	100	< 1	-	-	-
DSG 433	Qz-2	11-a	LCO2+Lw	SO4	-	-	-	-	-	-
DSG 433	Qz-2	11-b1	LCO2+VCO2+Lw	SO4	-	-	-	-	-	-
DSG 433	Qz-2	11-b2	LCO2+Lw+3S	-	n.i.	99	1	< 1	-	-
DSG 433	Qz-2	13-b1	LCO2+Lw+2S	SO4	calcite, anhydrite	68	32	-	-	-
DSG 433	Qz-2	13-b2	LCO2+VCO2+Lw	SO4	-	-	-	-	-	-
DSG 433	Qz-2	20-b1	LCO2+Lw	SO4	-	100	< 1	-	-	-
DSG 433	Qz-2	20-f2	LCO2+VCO2+Lw	SO4	-	-	-	-	30.0	-
DSG 433	Qz-2	21-b	LCO2+Lw+S	SO4	n.i. opaque	100	-	-	29.1	-
DSG 433	Qz-2	21-a1	LCO2+VCO2+Lw+S	SO4	-	-	-	-	30.0	-
DSG 002	Qz-3	22-c	Lw	-	-	-	-	-	-	-
DSG 002	Qz-3	22-d1	Lw	n.d.	-	-	-	-	-	-
DSG 002	Qz-3	22-d2	Lw+V	SO4	-	-	-	-	-	-
DSG 002	Qz-3	22-d3	Lw+V	n.d.	-	-	-	-	-	-
DSG 002	Qz-3	22	solid inclusion	-	calcite	-	-	-	-	-
DSG 002	QZ-3	18-a	LCO2+Lw+S	-	calcite	-	-	-	-	-
DSG 002	QZ-3	18-c	Lw	SO4	-	-	-	-	-	-

DSG 002	QZ-3	18-c2	Lw	SO4	-	-	-	-	-	-
DSG 002	QZ-3	18-c3	Lw	n.d.	-	-	-	-	-	-
DSG 002	Qz-3	17-a	solid inclusion	-	calcite	-	-	-	-	-
DSG 002	Qz-3	19-1	LCO2+VCO2+Lw	SO4	-	100	-	-	-	-
DSG 002	Qz-3	19	solid inclusion 1	-	phosphate	-	-	-	-	-
DSG 002	Qz-3	19	solid inclusion 2	-	phosphate	-	-	-	-	-
DSG 002	Qz-3	19	solid inclusion 3	-	phosphate	-	-	-	-	-
DSG 002	Qz-3	20a	Lw	SO4	phosphate	-	-	-	-	-
DSG 002	Qz-3	20-b1	Lw+S	-	calcite	-	-	-	-	-
DSG 002	Qz-3	20	solid inclusion 1	-	calcite	-	-	-	-	-
DSG 002	Qz-3	20	solid inclusion 2	-	calcite	-	-	-	-	-
DSG 002	Qz-3	7-1	LCO2+VCO2+Lw	n.d.	-	-	-	-	28.0	-
DSG 002	Qz-3	7-2	LCO2+VCO2+Lw	n.d.	-	-	-	-	26.4	-
DSG 437	Qz-3	10-2	Lw	SO4	-	-	-	-	-	-
DSG 437	Qz-3	10-3	Lw	SO4	-	-	-	-	-	-
DSG 437	Qz-3	10-4	Lw	SO4	-	-	-	-	-	-
DSG 437	Qz-3	14-1	Lw	SO4	-	-	-	-	-	-

DSG 437	Qz-3	14-2	Lw	SO4	-	-	-	-	-	-
DSG 437	Qz-3	14-3	Lw	n.d.	-	-	-	-	-	-
DSG 437	Qz-3	14-4	Lw	n.d.	-	-	-	-	-	-
DSG 437	Qz-3	15-1	LCO2+Lw	n.d.	-	98	-	< 1	-	-
DSG 437	Qz-3	15-2	LCO2+Lw	n.d.	-	-	-	-	-	-
DSG 437	Qz-3	15-3	LCO2+Lw	n.d.	-	-	-	-		-
DSG 437	Qz-3	2-1	LCO2+Lw	n.d.	-	100	< 1	-	29.8	-
DSG 437	Qz-3	2-2	LCO2+Lw	n.d.	-	100	-	-	29.8	-
DSG 437	Qz-3	2-3	LCO2+VCO2+Lw	n.d.	-	-	-	-	-	-
DSG 437	Qz-3	4-1	LCO2+Lw	n.d.	-	100	< 1	< 1	-	-
DSG 437	Qz-3	4-2	LCO2+Lw	n.d.	-	100	-	-	-	-
DSG 437	Qz-3	4-3	LCO2+VCO2+Lw	n.d.	-	-	-	-	-	-
DSG 437	Qz-3	4	solid inclusion 1	-	calcite	-	-	-	-	-
DSG 437	Qz-3	4	solid inclusion 2	-	n.i.sulfate	-	-	-	-	-
DSG 437	Qz-3	21	solid inclusion 3	-	calcite	-	-	-	-	-
DSG 433	Qz-3	8	LCO2+Lw	SO4	-	100	-	-	-	-
DSG 433	Qz-3	8-1	LCO2+VCO2+Lw	SO4	-	-	-	-	-	-

DSG 433	Qz-3	8-2	LCO2+VCO2+Lw	SO4	-	-	-	-	-	-
DSG 433	Qz-3	8-3	LCO2+VCO2+Lw	SO4	-	-	-	-	-	-
DSG 433	Qz-3	8-4	LCO2+VCO2+Lw	SO4	-	-	-	-	-	-
DSG 433	Qz-3	10-a	LCO2+Lw	SO4	-	100	< 1	-	-	-
DSG 433	Qz-3	10	solid inclusion 1	-	anhydrite	-	-	-	-	-
DSG 433	Qz-3	10	solid inclusion 2	-	calcite	-	-	-	-	-
DSG 433	Qz-3	10	solid inclusion 3	-	calcite	-	-	-	-	-
DSG 433	Qz-3	22-c1	LCO2+VCO2+Lw	SO4	-	-	-	-	-	-
DSG 433	Qz-3	22-c2	LCO2+VCO2+Lw	-	-	-	-	-	-	-
DSG 433	Qz-3	22-c3	Lw	SO4	-	-	-	-	-	-
DSG 433	Qz-3	22	solid inclusion	-	calcite	-	-	-	-	-
DSG 433	Qz-3	26-2	LCO2+Lw	SO4	-	100	< 1	-	-	-
DSG 433	Qz-3	26-3	LCO2+Lw	SO4	-	100	< 1	-	-	-
DSG 433	Qz-3	26-4	LCO2+Lw	SO4	-	100	< 1	-	-	-
DSG 433	Qz-3	26-5	LCO2+VCO2+Lw	SO4	-	-	-	-	-	-
DSG 433	Qz-3	29-1	Lw	SO4	-	-	-	-	-	-
DSG 433	Qz-3	29-2	Lw	SO4	-	-	-	-	-	-

DSG 433	Qz-3	29-3	Lw+V	SO4	-	-	-	-	-	132.0
DSG 433	Qz-3	29-4	Lw	SO4	-	-	-	-	-	-
DSG 433	Qz-3	29-a	Lw+V	not	-	-	-	-	-	120.0
DSG 433	Qz-3	29-b	Lw+V	not	-	-	-	-	-	145.4
DSG 433	Qz-3	33-1	LCO2+VCO2+Lw	SO4	-	-	-	-	-	-
DSG 433	Qz-3	33-2	LCO2+Lw	n.d.	-	100	-	-	-	-
DSG 433	Qz-3	33-3	LCO2+VCO2+Lw	n.d.	-	-	-	-	-	-
DSG 433	Qz-3	33-4	LCO2+VCO2+Lw	SO4	-	-	-	-	28.0	-
DSG 433	Qz-3	34-1	LCO2+VCO2+Lw	-	-	-	-	-	-	-
DSG 433	Qz-3	34-2	LCO2+VCO2+Lw	-	-	-	-	-	-	-
DSG 433	Qz-3	34-3	LCO2+VCO2+Lw	-	-	-	-	-	-	-
DSG 433	Qz-3	piece 3-	Lw+V	-	-	-	-	-	-	140.6
DSG 433	Qz-3	piece 3-	Lw+V	-	-	-	-	-	-	147.3
DSG 433	Qz-3	piece 3-	Lw+V	-	-	-	-	-	-	204.1
DSG 433	Qz-3	piece 3-	Lw+V	-	-	-	-	-	-	148.0
DSG 433	Qz-3	piece 3-	Lw+V	-	-	-	-	-	-	158.8
DSG 433	Qz-3	piece 3-	Lw+V	-	-	-	-	-	-	189.0

DSG 433	Qz-3	piece 3-	Lw+V	-	-	-	-	-	-	183.3
DSG 433	Qz-3	piece 3-	Lw+V	-	-	-	-	-	-	156.0
DSG 433	Qz-3	piece 3-	Lw+V	-	-	-	-	-	-	212.6
DSG 433	Qz-3	piece 3-	Lw+V	-	-	-	-	-	-	141.5
DSG 433	Qz-3	piece 3-	Lw+V	-	-	-	-	-	-	206.2
DSG 433	Qz-3	piece 3-	Lw+V	-	-	-	-	-	-	216.9
DSG 433	Qz-3	piece 3-	Lw+V	-	-	-	-	-	-	220.0
DSG 433	Qz-3	piece 3-	Lw+V	-	-	-	-	-	-	222.3
DSG 433	Qz-3	piece 3-	Lw+V	-	-	-	-	-	-	162.8
DSG 433	Qz-3	piece 3-	Lw+V	-	-	-	-	-	-	170.4
DSG 433	Qz-3	piece 3-	Lw+V	-	-	-	-	-	-	195.8

Appendix 7: Chapter 4 visual proportion estimates calculation

Dashigou visual proportion estimates calculation of the CO_2-bearing fluid inclusion (Shepherd *et al.,* 1985).

Solution saturated with arcanite	
Arcanite K2SO4	
Density g.cm-3	2.66
Density in solution g.cm-3	1.0817
Solubility at room temperature	10.71%
Molecular weight	174.257

Visual proportion estimates calculation of the CO2-bearing fluid inclusion (Shepherd *et al.,* 1985)

Fluid inclusion	Measurements in μm		Volume μm-3	incertitude%	volumetric%		ρTOT	W(K2SO4)	Salinity in wt.% K2SO4	Molality per 1000 g of H2O
DSG 002 4-1	FI height	5.7	466.0	19.8	bubble	**14.9**	1.2	0.4	**32.8**	**2.8**
LCO$_2$+VCO$_2$+Lw+S	a	11.2			solid	**15.3**				
s = arcanite	b	7.3			liquid	**69.8**				
Qz-2	bubble	5.1	69.5	2.0						
	solid height	4.2	71.5	28.7						
	a	4.6								
	b	3.7								
	aqueous		325.1	-						
	ThCO2	29.8	0.6							
DSG 002 4-3	height of FI	4.7	452.9	23.5	bubble	**59.2**	0.8	4.7	**6.1**	**0.4**
LCO$_2$+VCO$_2$+Lw	a FI	11.5			liquid	**40.8**				
Qz-2	b FI	8.5								

	bubble	8.0	268.1	0.0						
	aqueous		184.8	-						
	ThCO2	29.8	0.6							
DSG 002 3-b	height of FI	6.4	413.9	18.2	bubble	**10.1**	1.0	10.4	**10.1**	**0.6**
LCO$_2$+VCO$_2$+Lw	a FI	8.9			liquid	**89.9**				
Qz-2	b FI	7.3								
	bubble	4.3	42.0	0.2						
	aqueous		372.0	-						
	ThCO2	30.1	0.5							

Appendix 8: Chapter 5 SIMS and Mass spectrometer standard and analyses

.

SIMS instrument standards reproducibility:

Date	Time	No	Y	X	PB(Start)	PB(end)	non corrected	corrected
session 1	BARYTE							
16/11/2018	09:12:00	baryte-standard-1	1500	3164	4.64E-09	4.61E-09	1.06E+01	11.02
16/11/2018	09:16:00	baryte-standard-2	1465	3166	4.63E-09	4.61E-09	1.06E+01	11.07
16/11/2018	09:19:00	baryte-standard-3	1430	3164	4.63E-09	4.59E-09	1.06E+01	11.00
16/11/2018	09:23:00	baryte-standard-4	1430	3130	4.63E-09	4.59E-09	1.06E+01	10.97
16/11/2018	09:27:00	baryte-standard-5	1465	3130	4.60E-09	4.56E-09	1.06E+01	10.99
16/11/2018	09:30:00	baryte-standard-6	1500	3130	4.58E-09	4.55E-09	1.04E+01	10.75
16/11/2018	09:34:00	baryte-standard-7	1500	3096	4.56E-09	4.54E-09	1.04E+01	10.68
16/11/2018	09:38:00	baryte-standard-8	1465	3094	4.56E-09	4.54E-09	1.09E+01	11.17
16/11/2018	09:41:00	baryte-standard-9	1430	3096	4.56E-09	4.53E-09	1.06E+01	10.88
16/11/2018	09:45:00	baryte-standard-10	1430	3060	4.57E-09	4.55E-09	1.07E+01	10.91
16/11/2018	11:17:00	baryte-standard-11	1342	3028	4.30E-09	4.28E-09	1.13E+01	11.29
16/11/2018	11:21:00	baryte-standard-12	1307	3030	4.30E-09	4.28E-09	1.15E+01	11.43
16/11/2018	11:25:00	baryte-standard-13	1272	3028	4.31E-09	4.31E-09	1.13E+01	11.21
16/11/2018	11:28:00	baryte-standard-14	1272	2994	4.32E-09	4.31E-09	1.10E+01	10.89

16/11/2018	11:32:00	baryte-standard-15	1307	2994	4.30E-09	4.27E-09	1.10E+01	10.89
16/11/2018	12:24:00	baryte-standard-16	1393	3128	4.25E-09	4.19E-09	1.15E+01	11.32
16/11/2018	12:27:00	baryte-standard-17	1358	3126	4.19E-09	4.18E-09	1.15E+01	11.27
16/11/2018	12:31:00	baryte-standard-18	1323	3128	4.20E-09	4.19E-09	1.14E+01	11.16
16/11/2018	12:35:00	baryte-standard-19	1288	3126	4.20E-09	4.20E-09	1.16E+01	11.29
16/11/2018	12:38:00	baryte-standard-20	1288	3092	4.20E-09	4.20E-09	1.12E+01	10.90
16/11/2018	12:42:00	baryte-standard-21	1323	3092	4.20E-09	4.18E-09	1.11E+01	10.79
16/11/2018	12:46:00	baryte-standard-22	1358	3092	4.19E-09	4.16E-09	1.10E+01	10.67
16/11/2018	12:49:00	baryte-standard-23	1393	3092	4.18E-09	4.19E-09	1.12E+01	10.78
16/11/2018	12:53:00	baryte-standard-24	1393	3058	4.17E-09	4.15E-09	1.12E+01	10.83
16/11/2018	12:57:00	baryte-standard-25	1358	3056	4.16E-09	4.14E-09	1.13E+01	10.84
						Avg	*11.00*	*11.00*
						Stdev	*0.39*	*0.22*

session 2						*Std Err*			*0.04*
19/11/2018	11:21:00	baryte-standard-1	1193	2994	4.17E-09	4.14E-09	1.09E+01	23.18
19/11/2018	11:25:00	baryte-standard-2	1158	2992	4.17E-09	4.17E-09	1.09E+01	23.20
19/11/2018	11:29:00	baryte-standard-3	1123	2994	4.18E-09	4.18E-09	1.12E+01	23.54
19/11/2018	11:33:00	baryte-standard-4	1088	2992	4.20E-09	4.19E-09	1.10E+01	23.35
19/11/2018	11:37:00	baryte-standard-5	1053	2994	4.20E-09	4.20E-09	1.13E+01	23.58
19/11/2018	12:42:00	baryte-standard-6	1079	2956	4.13E-09	4.14E-09	1.09E+01	23.21
19/11/2018	12:26:00	baryte-standard-7	1219	2956	4.11E-09	4.10E-09	1.07E+01	22.99
19/11/2018	12:30:00	baryte-standard-8	1184	2954	4.12E-09	4.11E-09	1.10E+01	23.31
19/11/2018	12:34:00	baryte-standard-9	1149	2956	4.10E-09	4.08E-09	1.08E+01	23.12
19/11/2018	12:38:00	baryte-standard-10	1114	2954	4.11E-09	4.14E-09	1.10E+01	23.25
19/11/2018	13:17:00	baryte-standard-11	1219	2886	4.12E-09	4.10E-09	1.10E+01	23.29
19/11/2018	13:21:00	baryte-standard-12	1184	2886	4.12E-09	4.14E-09	1.10E+01	23.31
19/11/2018	13:25:00	baryte-standard-13	1149	2886	4.14E-09	4.13E-09	1.09E+01	23.22
19/11/2018	13:29:00	baryte-standard-14	1114	2886	4.13E-09	4.11E-09	1.11E+01	23.43
19/11/2018	13:33:00	baryte-standard-15	1079	2886	4.12E-09	4.13E-09	1.12E+01	23.52
						Avg	*11.00*		*23.30*
						Stdev	*0.16*		*0.16*
						Std Err			*0.04*

Date	Time	No	Y	X	PB(Start)	PB(end)	non corrected	δ 18O
session 1	CALCITE							
16/11/2018	13:16:00	calcite-standard-1	-2572	2620	4.89E-09	4.87E-	23.18	23.27
16/11/2018	13:19:00	calcite-standard-2	-2607	2620	4.90E-09	4.89E-	23.21	23.29
16/11/2018	13:23:00	calcite-standard-3	-2642	2620	4.89E-09	4.89E-	23.20	23.27
16/11/2018	13:27:00	calcite-standard-4	-2642	2586	4.87E-09	4.85E-	23.25	23.31
16/11/2018	13:30:00	calcite-standard-5	-2607	2584	4.88E-09	4.84E-	23.30	23.35
16/11/2018	14:50:00	calcite-standard-6	-2793	2592	4.69E-09	4.73E-	23.34	23.29
16/11/2018	14:53:00	calcite-standard-7	-2828	2594	4.72E-09	4.76E-	23.55	23.49
16/11/2018	14:57:00	calcite-standard-8	-2863	2592	4.74E-09	4.74E-	23.43	23.36
16/11/2018	15:01:00	calcite-standard-9	-2863	2558	4.73E-09	4.74E-	23.37	23.29
16/11/2018	15:04:00	calcite-standard-	-2828	2558	4.74E-09	4.71E-	23.18	23.10
						Avg	*23.30*	*23.30*
						Stdev	*0.12*	*0.10*
						Std Err		*0.03*
session 2								
19/11/2018	08:58:00	calcite-standard-	-2677	2.86E+03	4.42E-09	4.42E-	23.04	23.13

19/11/2018	09:02:00	calcite-standard-	-2712	2.86E+03	4.44E-09	4.41E-	23.18	23.27
19/11/2018	09:06:00	calcite-standard-	-2747	2.86E+03	4.44E-09	4.42E-	23.32	23.39
19/11/2018	09:10:00	calcite-standard-	-2782	2.86E+03	4.42E-09	4.40E-	23.34	23.41
19/11/2018	09:14:00	calcite-standard-	-2817	2.86E+03	4.41E-09	4.43E-	23.42	23.48
19/11/2018	10:04:00	calcite-standard-	-2677	2.79E+03	4.31E-09	4.28E-	23.20	23.21
19/11/2018	10:08:00	calcite-standard-	-2712	2.79E+03	4.30E-09	4.27E-	23.15	23.15
19/11/2018	10:12:00	calcite-standard-	-2747	2.79E+03	4.28E-09	4.28E-	23.17	23.17
19/11/2018	10:16:00	calcite-standard-	-2782	2.79E+03	4.28E-09	4.28E-	23.39	23.38
19/11/2018	10:20:00	calcite-standard-	-2817	2.79E+03	4.29E-09	4.29E-	23.38	23.37
19/11/2018	10:55:00	calcite-standard-	-2647	2.90E+03	4.14E-09	4.17E-	23.36	23.30
19/11/2018	10:59:00	calcite-standard-	-2682	2.90E+03	4.19E-09	4.10E-	23.35	23.28
19/11/2018	11:03:00	calcite-standard-	-2717	2.90E+03	4.12E-09	4.17E-	23.50	23.42
19/11/2018	11:07:00	calcite-standard-	-2752	2.90E+03	4.17E-09	4.19E-	23.29	23.21
19/11/2018	11:11:00	calcite-standard-	-2787	2.90E+03	4.19E-09	4.17E-	23.43	23.34
						Avg	*23.30*	*23.30*
						Stdev	*0.13*	*0.11*
						Std Err		*0.03*

Mass spectrometry standards reproducibility

run 1	Carrera marble		
Port	**Sample ID**	**δ13C (‰)**	**δ18O (‰)**
2	2019-08-19-S2	24.84	12.03
3	2019-08-19-S3	24.83	12.02
4	2019-08-19-S4	24.86	12.18
5	2019-08-19-S5	24.79	12.10
6	2019-08-19-S6	24.87	12.30
7	2019-08-19-S7	24.90	12.29
8	2019-08-19-S8	24.81	12.06
9	2019-08-19-S9	24.82	12.05
10	2019-08-19-S10	24.75	12.01
27	2019-08-19-S11	24.75	11.89
28	2019-08-19-S12	24.73	12.12
29	2019-08-19-S13	24.68	11.84
30	2019-08-19-S14	24.64	11.96
31	2019-08-19-S15	24.61	11.84
	average	*24.78*	*12.05*
	stdev	*0.09*	*0.14*
run 2			
Port	Sample ID	**δ13C (‰)**	**δ18O (‰)**
2	2019-09-09-S2	24.95	12.00
3	2019-09-09-S3	25.07	12.25
9	2019-09-09-S4	24.97	12.00
10	2019-09-09-S5	25.05	12.14
16	2019-09-09-S6	24.98	12.10
17	2019-09-09-S7	24.87	12.02
23	2019-09-09-S8	24.95	12.23
24	2019-09-09-S9	24.92	12.00
30	2019-09-09-S10	24.89	11.94
32	2019-09-09-S12	24.97	12.08
	average	*24.96*	*12.07*
	stdev	*0.06*	*0.11*

SIMS analyses of calcite and baryte, processed data per mil relative to VSMOW:

Sample	Mineral	Analysis name	Stage	Mineral location	δ18O‰
OKC19-1	baryte 1	161018DC-brt-P1b-1@11.asc	hydrothermal	P1	3.00
	baryte 1	161018DC-brt-P1b-1@1.asc	hydrothermal	P1	3.47
	baryte 1	161018DC-brt-P1b-1@4.asc	hydrothermal	P1	3.61
	baryte 1	161018DC-brt-P1b-1@5.asc	hydrothermal	P1	3.56
	baryte 1	161018DC-brt-P1b-1@6.asc	hydrothermal	P1	3.90
	baryte 1	161018DC-brt-P1b-1@7.asc	hydrothermal	P1	1.83
	baryte 1	161018DC-brt-P1b-1@8.asc	hydrothermal	P1	1.41
	baryte 1	161018DC-brt-P1b-1@9.asc	hydrothermal	P1	3.50
				average	**3.03**
				stdev	**0.92**
	calcite A1	161018DC-cc-P1b-1@10.asc	hydrothermal	P1	4.82
	calcite A1	161018DC-cc-P1b-1@1.asc	hydrothermal	P1	5.32
	calcite A1	161018DC-cc-P1b-1@2.asc	hydrothermal	P1	5.13
	calcite A1	161018DC-cc-P1b-1@4.asc	hydrothermal	P1	9.03
	calcite A1	161018DC-cc-P1b-1@5.asc	hydrothermal	P1	4.60
	calcite A1	161018DC-cc-P1b-1@6.asc	hydrothermal	P1	5.19
				average	**5.68**
				stdev	**1.66**

	calcite B1	161018DC-cc-P1b-1@7.asc	hydrothermal	P1	3.60
	calcite B1	161018DC-cc-P1b-1@8.asc	hydrothermal	P1	3.66
	calcite B1	161018DC-cc-P1b-1@9.asc	hydrothermal	P1	3.41
	calcite B1	161018DC-cc-P1b-1@3.asc	hydrothermal	P1	3.43
				average	**3.53**
				stdev	**0.12**

Sample	Mineral	Analysis name	Stage	Mineral location	δ18O ‰
OKC19-1	baryte 2	191018DC-Nami-P3-brt2@3.asc	hydrothermal	P3 (crystal 1)	12.00
	baryte 2	191018DC-Nami-P3-brt2@1.asc	hydrothermal	P3 (crystal 1)	11.80
	baryte 2	191018DC-Nami-P3-brt1@4.asc	hydrothermal	P3 (crystal 1)	12.67
	baryte 2	191018DC-Nami-P3-brt1@5.asc	hydrothermal	P3 (crystal 1)	11.63
	baryte 2	191018DC-Nami-P3-brt1@6.asc	hydrothermal	P3 (crystal 1)	11.25
	baryte 2	191018DC-Nami-P3-brt1@7.asc	hydrothermal	P3 (crystal 1)	13.98
	baryte 2	191018DC-Nami-P3-brt1@8.asc	hydrothermal	P3 (crystal 1)	12.41
				average	**12.25**
				stdev	**0.90**
	calcite A2	191018DC-Nami-P3-cc@10.asc	hydrothermal	P3	5.67
	calcite A2	191018DC-Nami-P3-cc@12.asc	hydrothermal	P3	7.01
	calcite A2	191018DC-Nami-P3-cc@13.asc	hydrothermal	P3	5.56
	calcite A2	191018DC-Nami-P3-cc@8.asc	hydrothermal	P3	5.41
				average	**5.91**
				stdev	**0.74**
	calcite B2	191018DC-Nami-P3-cc@9.asc	hydrothermal	P3	5.44
	calcite B2	191018DC-Nami-P3-cc@11.asc	hydrothermal	P3	8.50
				average	**6.97**
				stdev	**2.16**

Sample	Mineral	Analysis name	Stage	Mineral location	δ18O ‰
OKC19-1	baryte 3	191018DC-Nami-P3-brt2@13.asc	hydrothermal	P3 (crystal 2)	15.92
	baryte 3	191018DC-Nami-P3-brt2@14.asc	hydrothermal	P3 (crystal 2)	15.51
	baryte 3	191018DC-Nami-P3-brt2@15.asc	hydrothermal	P3 (crystal 2)	16.94
	baryte 3	191018DC-Nami-P3-brt2@16.asc	hydrothermal	P3 (crystal 2)	14.04
				average	**15.60**
				stdev	**1.20**
	calcite A3	191018DC-Nami-P3-cc@1.asc	hydrothermal	P3	7.05
	calcite A3	191018DC-Nami-P3-cc@2.asc	hydrothermal	P3	6.41
	calcite A3	191018DC-Nami-P3-cc@3.asc	hydrothermal	P3	5.37
	calcite A3	191018DC-Nami-P3-cc@4.asc	hydrothermal	P3	6.43
	calcite A3	191018DC-Nami-P3-cc@5.asc	hydrothermal	P3	5.66
	calcite A3	191018DC-Nami-P3-cc@6.asc	hydrothermal	P3	5.99
	calcite A3	191018DC-Nami-P3-cc@7.asc	hydrothermal	P3	9.19
				average	**6.59**
				stdev	**1.28**

Mass spectrometry analyses of calcite, processed data per mil relative to VSMOW

sample	magmatic calcite	δ18O‰
OKC17	2019-08-19-OKC17' mg cc	7.76
OKC17	2019-08-19-OKC17'' mg cc zone 1	8.60
OKC17	2019-08-19-OKC17'' mg cc zone 2	7.88
	average	***8.08***
	stdev	***0.46***
OKA1	2019-08-19-OKA1' mg cc 1	7.62
OKA1	2019-08-19-OKA1' mg cc 2	9.23
OKA1	2019-08-19-OKA1' mg cc 3	8.30
	average	***8.38***
	stdev	***0.81***
OKC4	(av)2019-08-19-OKC4-1 mg cc-1	11.40
OKC4	2019-08-19-OKC4-2 mg cc-1	11.30
OKC4	2019-08-19-OKC4-2 mg cc-2	11.29
OKC4	2019-08-19-OKC4-1 mg cc-3	11.25
	average	**11.31**
	stdev	***0.065***

sample	hydrothermal calcite	δ18O‰
OKC17	(av) 2019-08-19-OKC17' hy cc 1	10.46
OKC17	2019-08-19-OKC17'' hy cc 1	9.33
OKC17	2019-08-19-OKC17' hy cc 2	8.40
	average	***9.40***
	stdev	***1.03***
OKA1	2019-08-19-OKA1' hy cc 4	8.50
OKA1	2019-08-19-OKA1' hy cc 3	8.17
OKA1	2019-08-19-OKA1' hy cc 2	8.55
OKA1	2019-08-19-OKA1' hy cc 1	8.36
	average	***8.39***
	stdev	*0.17*
OKC4	2019-08-19-OKC4 hy cc 3	12.58
OKC4	2019-08-19-OKC4 hy cc 1	11.70
OKC4	(av) 2019-08-19-OKC4-2 hy cc-1	12.38
OKC4	2019-08-19-OKC4-2 hy cc-2	13.31
OKC4	2019-08-19-OKC4-2 hy cc-3	12.91
	average	***12.58***
	stdev	*0.604*

sample	non-specified calcite	δ18O‰
OKC17	2019-09-09-OKC17 mg cc 1	8.24
OKC17	average (x3) 2019-09-09-OKC17 mg cc 4	8.51
OKC17	2019-09-09-OKC17 mg cc 3	8.59
OKC17	*2019-09-09-OKC17 mg cc 2*	*8.18*
	average	***8.38***
	stdev	**0.20**
OKC18	2019-09-09-OKC18 mg cc 5	7.75
OKC18	2019-09-09-OKC18 mg cc 4	7.83
OKC18	average (x3) 2019-09-09-OKC18 mg cc 2	7.45
OKC18	2019-09-09-OKC18 mg cc 3	7.81
OKC18	2019-09-09-OKC18 mg cc 1	7.85
	average	***7.74***
	stdev	***0.17***
OKC19-1	2019-09-09-OKC19-1 mg cc 1	8.77
OKC19-1	2019-09-09-OKC19-1 mg cc 3	9.17
OKC19-1	average (x2) 2019-09-09-OKC19-1 mg cc 2	7.81
OKC19-1	2019-09-09-OKC19-1 mg cc 5	8.50
	2019-09-09-OKC19-1 mg cc 4	8.76
	average	***8.60***
	stdev	***0.50***

Appendix 9: Okorusu fluorite hosted fluid inclusions microthermometry analyses

Microthermometry measurements and corresponding salinity from fluorite-rich rocks from the Okorusu deposit (calculation from Bodnar, 1993).

Microthermometry measurements and corresponding salinity from fluorite-rich rocks					
Sample	Fluorite type	FI	FI type	Tmice	Salinity in NaCl eq.*
OKC3	4a	7-1	Lw+V	-5	7.9
OKC3	4a	7-2	Lw+V	-6.2	9.5
OKC3	4a	7-3	Lw+V	-6.2	9.5
OKC3	4a	7-4	Lw+V	-6	9.2
OKC3	4a	7-5	Lw+V	-6.2	9.5
OKC3	4a	8-1	Lw+V	-4	6.5
OKC3	4a	9-1	Lw+V	-5	7.9
OKC3	4a	9-2	Lw+V	-7	10.5
OKC3	4a	9-3	Lw+V	-5	7.9
OKC3	4a	10-1	Lw+V	-7	10.5
OKC3	4a	10-2	Lw+V	-5.2	8.1
OKC3	4a	1-1	Lw+V	-5.5	8.5
OKC3	4a	1-2	Lw+V	-6.1	9.3
OKC3	4a	1-3	Lw+V	-6.2	9.5
OKC3	4a	13	Lw+V	-4.5	7.2
OKC3	4a	2-2	Lw+V	-7.3	10.9
OKC3	4a	2-3	Lw+V	-7.2	10.7
OKC3	4a	3	Lw+V+s	-5.7	8.8
OKC6	4b-1	8--1	Lw+V	-4	6.5
OKC6	4b-1	8--2	Lw+V	-3.8	6.2
OKC6	4b-1	8--3	Lw+V	-3.8	6.2
OKC6	4b-1	9--1	Lw+V	-6.5	9.9

OKC6	4b-1	9--2	Lw+V	-5	7.9
OKC6	4b-1	9--3	Lw+V	-4.8	7.6
OKC6	4b-1	9--4	Lw+V	-4.6	7.3
OKC6	4b-1	9	Lw+V	-6.8	10.2
OKC6	4b-1	10--1	Lw+V	-6.4	9.7
OKC6	4b-1	10--2	Lw+V	-5.7	8.8
OKC6	4b-1	10--3	Lw+V	-5.7	8.8
OKC6	4b-1	10--4	Lw+V	-4.6	7.3
OKC8	4b-2	54-1	Lw+V	-2.3	3.9
OKC8	4b-2	54-2	Lw+V	-2.3	3.9
OKC8	4b-2	x-3	Lw+V	-2.8	4.6
OKC8	4b-2	55-a	Lw+V	-2	3.4
OKC8	4b-2	55-b	Lw+V	-2.8	4.6
OKC8	4b-2	57	Lw+V	-2.8	4.6
OKC8	4b-2	58	Lw+V	-3	5
OKC8	4c	49	Lw+V	-4.3	6.9
OKC8	4c	47	Lw+V	-8.8	12.6
OKC8	4c	46-1	Lw+V	-5.3	8.3
OKC8	4c	46-5	Lw+V	-6	9.2
OKC8	4c	46	Lw+V	-4.7	7.5
OKC8	4c	46-1	Lw+V	-4.8	7.6
OKC8	4c	44-1	Lw+V	-6	9.2
OKC8	4c	44-2	Lw+V	-4.4	7
OKC8	4c	44-3	Lw+V	-3.5	5.7
OKC8	4c	44-4	Lw+V	-2.5	4.2
OKC8	4c	44-5	Lw+V	-3	5
OKC8	4c	45-1	Lw+V	-4.8	7.6
OKC8	4c	45-2	Lw+V	-5	7.9

The end